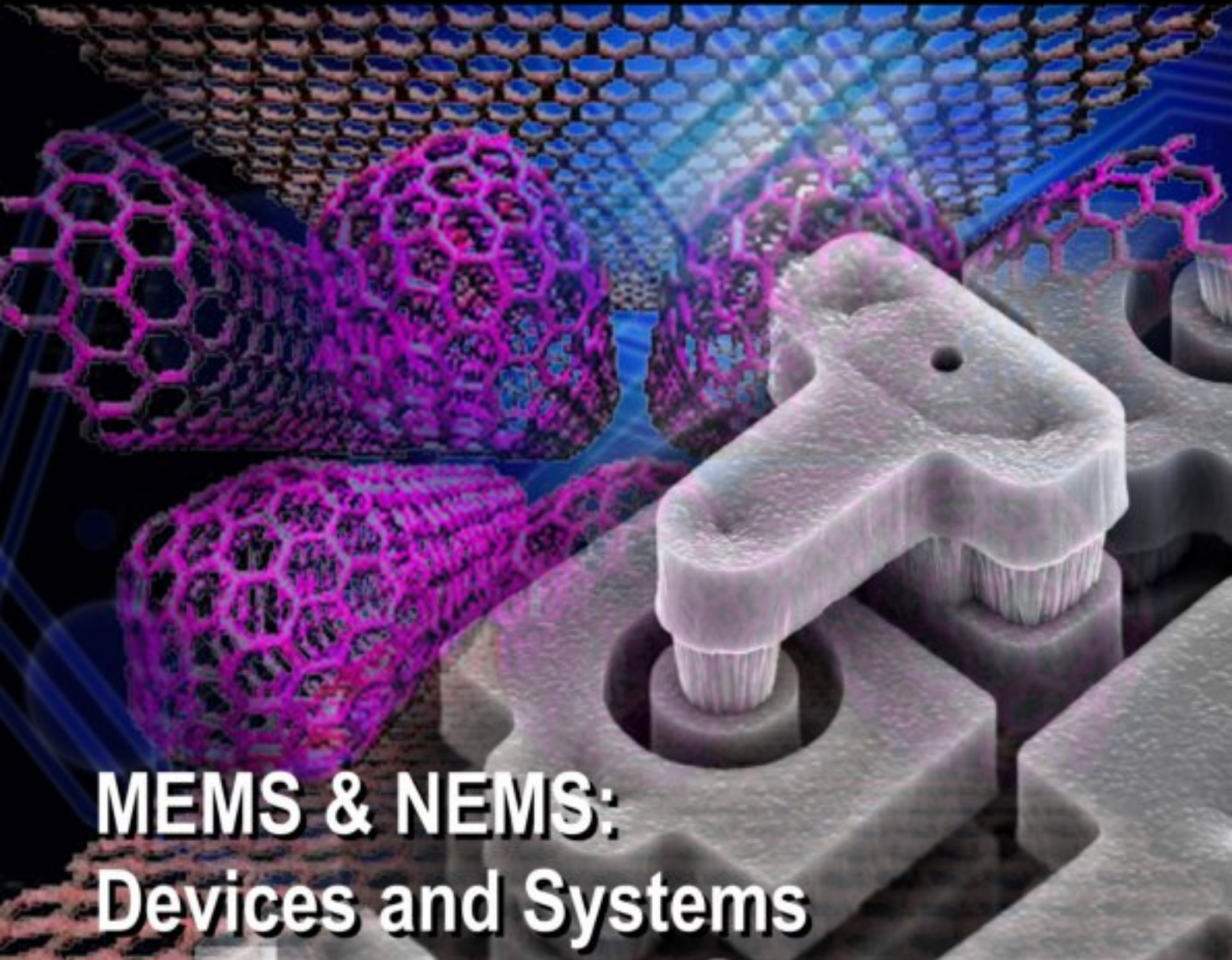


ISSN 1726-5749

# **SENSORS & TRANSDUCERS**

**10** Special  
Issue  
**/07**



**MEMS & NEMS:  
Devices and Systems**

International Frequency Sensor Association Publishing





# Sensors & Transducers

Special Issue  
October 2007

[www.sensorsportal.com](http://www.sensorsportal.com)

ISSN 1726-5479

**Editor-in-Chief:** Sergey Y. Yurish  
**Guest Editors:** Elena Gaura and James P. Brusey

**Editors for Western Europe**

Meijer, Gerard C.M., Delft University of Technology, The Netherlands  
Ferrari, Vittorio, Università di Brescia, Italy

**Editors for North America**

Datskos, Panos G., Oak Ridge National Laboratory, USA  
Fabien, J. Josse, Marquette University, USA  
Katz, Evgeny, Clarkson University, USA

**Editor South America**

Costa-Felix, Rodrigo, Inmetro, Brazil

**Editor for Eastern Europe**

Sachenko, Anatoly, Ternopil State Economic University, Ukraine

**Editor for Asia**

Ohyama, Shinji, Tokyo Institute of Technology, Japan

## Editorial Advisory Board

**Abdul Rahim, Ruzairi**, Universiti Teknologi, Malaysia  
**Ahmad, Mohd Noor**, Nothern University of Engineering, Malaysia  
**Annamalai, Karthigeyan**, National Institute of Advanced Industrial Science and Technology, Japan  
**Arcega, Francisco**, University of Zaragoza, Spain  
**Arguel, Philippe**, CNRS, France  
**Ahn, Jae-Pyoung**, Korea Institute of Science and Technology, Korea  
**Arndt, Michael**, Robert Bosch GmbH, Germany  
**Ascoli, Giorgio**, George Mason University, USA  
**Atalay, Selcuk**, Inonu University, Turkey  
**Atghiaee, Ahmad**, University of Tehran, Iran  
**Augutis, Vygantas**, Kaunas University of Technology, Lithuania  
**Avachit, Patil Lalchand**, North Maharashtra University, India  
**Ayesh, Aladdin**, De Montfort University, UK  
**Bahreyni, Behraad**, University of Manitoba, Canada  
**Baoxian, Ye**, Zhengzhou University, China  
**Barford, Lee**, Agilent Laboratories, USA  
**Barlingay, Ravindra**, Priyadarshini College of Engineering and Architecture, India  
**Basu, Sukumar**, Jadavpur University, India  
**Beck, Stephen**, University of Sheffield, UK  
**Ben Bouzid, Sihem**, Institut National de Recherche Scientifique, Tunisia  
**Binnie, T. David**, Napier University, UK  
**Bischoff, Gerlinde**, Inst. Analytical Chemistry, Germany  
**Bodas, Dhananjay**, IMTEK, Germany  
**Borges Carval, Nuno**, Universidade de Aveiro, Portugal  
**Bousbia-Salah, Mounir**, University of Annaba, Algeria  
**Bouvet, Marcel**, CNRS – UPMC, France  
**Brudzewski, Kazimierz**, Warsaw University of Technology, Poland  
**Cai, Chenxin**, Nanjing Normal University, China  
**Cai, Qingyun**, Hunan University, China  
**Campanella, Luigi**, University La Sapienza, Italy  
**Carvalho, Vitor**, Minho University, Portugal  
**Cecelja, Franjo**, Brunel University, London, UK  
**Cerda Belmonte, Judith**, Imperial College London, UK  
**Chakrabarty, Chandan Kumar**, Universiti Tenaga Nasional, Malaysia  
**Chakravorty, Dipankar**, Association for the Cultivation of Science, India  
**Changhai, Ru**, Harbin Engineering University, China  
**Chaudhari, Gajanan**, Shri Shivaji Science College, India  
**Chen, Rongshun**, National Tsing Hua University, Taiwan  
**Cheng, Kuo-Sheng**, National Cheng Kung University, Taiwan  
**Chiriac, Horia**, National Institute of Research and Development, Romania  
**Chowdhuri, Arijit**, University of Delhi, India  
**Chung, Wen-Yaw**, Chung Yuan Christian University, Taiwan  
**Corres, Jesus**, Universidad Publica de Navarra, Spain  
**Cortes, Camilo A.**, Universidad de La Salle, Colombia  
**Courtois, Christian**, Universite de Valenciennes, France  
**Cusano, Andrea**, University of Sannio, Italy  
**D'Amico, Arnaldo**, Università di Tor Vergata, Italy  
**De Stefano, Luca**, Institute for Microelectronics and Microsystem, Italy  
**Deshmukh, Kiran**, Shri Shivaji Mahavidyalaya, Barshi, India  
**Kang, Moonho**, Sunmoon University, Korea South  
**Kaniusas, Eugenijus**, Vienna University of Technology, Austria  
**Katake, Anup**, Texas A&M University, USA

**Dickert, Franz L.**, Vienna University, Austria  
**Dieguez, Angel**, University of Barcelona, Spain  
**Dimitropoulos, Panos**, University of Thessaly, Greece  
**Ding Jian, Ning**, Jiangsu University, China  
**Djordjevic, Alexandar**, City University of Hong Kong, Hong Kong  
**Donato, Nicola**, University of Messina, Italy  
**Donato, Patricio**, Universidad de Mar del Plata, Argentina  
**Dong, Feng**, Tianjin University, China  
**Drljaca, Predrag**, Instersema Sensoric SA, Switzerland  
**Dubey, Venketesh**, Bournemouth University, UK  
**Enderle, Stefan**, University of Ulm and KTB mechatronics GmbH, Germany  
**Erdem, Gursan K. Arzum**, Ege University, Turkey  
**Erkmen, Aydan M.**, Middle East Technical University, Turkey  
**Estelle, Patrice**, Insa Rennes, France  
**Estrada, Horacio**, University of North Carolina, USA  
**Faiz, Adil**, INSA Lyon, France  
**Fericean, Sorin**, Balluff GmbH, Germany  
**Fernandes, Joana M.**, University of Porto, Portugal  
**Francioso, Luca**, CNR-IMM Institute for Microelectronics and Microsystems, Italy  
**Fu, Weiling**, South-Western Hospital, Chongqing, China  
**Gaura, Elena**, Coventry University, UK  
**Geng, Yanfeng**, China University of Petroleum, China  
**Gole, James**, Georgia Institute of Technology, USA  
**Gong, Hao**, National University of Singapore, Singapore  
**Gonzalez de la Ros, Juan Jose**, University of Cadiz, Spain  
**Grael, Annette**, Goteborg University, Sweden  
**Graff, Mason**, The University of Texas at Arlington, USA  
**Guan, Shan**, Eastman Kodak, USA  
**Guillet, Bruno**, University of Caen, France  
**Guo, Zhen**, New Jersey Institute of Technology, USA  
**Gupta, Narendra Kumar**, Napier University, UK  
**Hadjiloucas, Sillas**, The University of Reading, UK  
**Hashsham, Syed**, Michigan State University, USA  
**Hernandez, Alvaro**, University of Alcala, Spain  
**Hernandez, Wilmar**, Universidad Politecnica de Madrid, Spain  
**Homentcovschi, Dorel**, SUNY Binghamton, USA  
**Horstman, Tom**, U.S. Automation Group, LLC, USA  
**Hsiai, Tzung (John)**, University of Southern California, USA  
**Huang, Jeng-Sheng**, Chung Yuan Christian University, Taiwan  
**Huang, Star**, National Tsing Hua University, Taiwan  
**Huang, Wei**, PSG Design Center, USA  
**Hui, David**, University of New Orleans, USA  
**Jaffrezic-Renault, Nicole**, Ecole Centrale de Lyon, France  
**Jaime Calvo-Galleg, Jaime**, Universidad de Salamanca, Spain  
**James, Daniel**, Griffith University, Australia  
**Janting, Jakob**, DELTA Danish Electronics, Denmark  
**Jiang, Liudi**, University of Southampton, UK  
**Jiao, Zheng**, Shanghai University, China  
**John, Joachim**, IMEC, Belgium  
**Kalach, Andrew**, Voronezh Institute of Ministry of Interior, Russia  
**Rodriguez, Angel**, Universidad Politecnica de Cataluna, Spain  
**Rothberg, Steve**, Loughborough University, UK

**Kausel, Wilfried**, University of Music, Vienna, Austria  
**Kavasoglu, Nese**, Mugla University, Turkey  
**Ke, Cathy**, Tyndall National Institute, Ireland  
**Khan, Asif**, Aligarh Muslim University, Aligarh, India  
**Kim, Min Young**, Koh Young Technology, Inc., Korea South  
**Ko, Sang Choon**, Electronics and Telecommunications Research Institute, Korea South  
**Kockar, Hakan**, Balikesir University, Turkey  
**Kotulska, Malgorzata**, Wroclaw University of Technology, Poland  
**Kratz, Henrik**, Uppsala University, Sweden  
**Kumar, Arun**, University of South Florida, USA  
**Kumar, Subodh**, National Physical Laboratory, India  
**Kung, Chih-Hsien**, Chang-Jung Christian University, Taiwan  
**Lacnjevac, Caslav**, University of Belgrade, Serbia  
**Laurent, Francis**, IMEC, Belgium  
**Lay-Ekuakille, Aime**, University of Lecce, Italy  
**Lee, Jang Myung**, Pusan National University, Korea South  
**Lee, Jun Su**, Amkor Technology, Inc. South Korea  
**Lei, Hua**, National Starch and Chemical Company, USA  
**Li, Genxi**, Nanjing University, China  
**Li, Hui**, Shanghai Jiaotong University, China  
**Li, Xian-Fang**, Central South University, China  
**Liang, Yuanchang**, University of Washington, USA  
**Liawruangrath, Saisunee**, Chiang Mai University, Thailand  
**Liew, Kim Meow**, City University of Hong Kong, Hong Kong  
**Lin, Hermann**, National Kaohsiung University, Taiwan  
**Lin, Paul**, Cleveland State University, USA  
**Linderholm, Pontus**, EPFL - Microsystems Laboratory, Switzerland  
**Liu, Aihua**, Michigan State University, USA  
**Liu Changgeng**, Louisiana State University, USA  
**Liu, Cheng-Hsien**, National Tsing Hua University, Taiwan  
**Liu, Songqin**, Southeast University, China  
**Lodeiro, Carlos**, Universidade NOVA de Lisboa, Portugal  
**Lorenzo, Maria Encarnacio**, Universidad Autonoma de Madrid, Spain  
**Lukaszewicz, Jerzy Pawel**, Nicholas Copernicus University, Poland  
**Ma, Zhanfang**, Northeast Normal University, China  
**Majstorovic, Vidosav**, University of Belgrade, Serbia  
**Marquez, Alfredo**, Centro de Investigacion en Materiales Avanzados, Mexico  
**Matay, Ladislav**, Slovak Academy of Sciences, Slovakia  
**Mathur, Prafull**, National Physical Laboratory, India  
**Maurya, D.K.**, Institute of Materials Research and Engineering, Singapore  
**Mekid, Samir**, University of Manchester, UK  
**Mendes, Paulo**, University of Minho, Portugal  
**Mennell, Julie**, Northumbria University, UK  
**Mi, Bin**, Boston Scientific Corporation, USA  
**Minas, Graca**, University of Minho, Portugal  
**Moghavvemi, Mahmoud**, University of Malaya, Malaysia  
**Mohammadi, Mohammad-Reza**, University of Cambridge, UK  
**Molina Flores, Esteban**, Benemirita Universidad Autonoma de Puebla, Mexico  
**Moradi, Majid**, University of Kerman, Iran  
**Morello, Rosario**, DIMET, University "Mediterranea" of Reggio Calabria, Italy  
**Mounir, Ben Ali**, University of Sousse, Tunisia  
**Mukhopadhyay, Subhas**, Massey University, New Zealand  
**Neelamegam, Periasamy**, Sastra Deemed University, India  
**Neshkova, Milka**, Bulgarian Academy of Sciences, Bulgaria  
**Oberhammer, Joachim**, Royal Institute of Technology, Sweden  
**Ould Lahoucin**, University of Guelma, Algeria  
**Pamidighanta, Sayanu**, Bharat Electronics Limited (BEL), India  
**Pan, Jisheng**, Institute of Materials Research & Engineering, Singapore  
**Park, Joon-Shik**, Korea Electronics Technology Institute, Korea South  
**Pereira, Jose Miguel**, Instituto Politecnico de Seteбал, Portugal  
**Petsev, Dimitar**, University of New Mexico, USA  
**Pogacnik, Lea**, University of Ljubljana, Slovenia  
**Post, Michael**, National Research Council, Canada  
**Prance, Robert**, University of Sussex, UK  
**Prasad, Ambika**, Gulbarga University, India  
**Prateepasen, Asa**, Kingmoungut's University of Technology, Thailand  
**Pullini, Daniele**, Centro Ricerche FIAT, Italy  
**Pumera, Martin**, National Institute for Materials Science, Japan  
**Radhakrishnan, S.**, National Chemical Laboratory, Pune, India  
**Rajanna, K.**, Indian Institute of Science, India  
**Ramadan, Qasem**, Institute of Microelectronics, Singapore  
**Rao, Basuthkar**, Tata Inst. of Fundamental Research, India  
**Reig, Candid**, University of Valencia, Spain  
**Restivo, Maria Teresa**, University of Porto, Portugal  
**Rezazadeh, Ghader**, Urmia University, Iran  
**Robert, Michel**, University Henri Poincare, France  
**Royo, Santiago**, Universitat Politecnica de Catalunya, Spain  
**Sadana, Ajit**, University of Mississippi, USA  
**Sandacci, Serghei**, Sensor Technology Ltd., UK  
**Sapozhnikova, Ksenia**, D.I.Mendeleyev Institute for Metrology, Russia  
**Saxena, Vibha**, Bhabha Atomic Research Centre, Mumbai, India  
**Schneider, John K.**, Ultra-Scan Corporation, USA  
**Seif, Selemani**, Alabama A & M University, USA  
**Seifter, Achim**, Los Alamos National Laboratory, USA  
**Sengupta, Deepak**, Advance Bio-Photonics, India  
**Shearwood, Christopher**, Nanyang Technological University, Singapore  
**Shin, Kyuho**, Samsung Advanced Institute of Technology, Korea  
**Shmaliy, Yuriy**, Kharkiv National University of Radio Electronics, Ukraine  
**Silva Girao, Pedro**, Technical University of Lisbon Portugal  
**Slomovitz, Daniel**, UTE, Uruguay  
**Smith, Martin**, Open University, UK  
**Soleymanpour, Ahmad**, Damghan Basic Science University, Iran  
**Somani, Prakash R.**, Centre for Materials for Electronics Technology, India  
**Srinivas, Talabattula**, Indian Institute of Science, Bangalore, India  
**Srivastava, Arvind K.**, Northwestern University  
**Stefan-van Staden, Raluca-Ioana**, University of Pretoria, South Africa  
**Sumriddetchka, Sarun**, National Electronics and Computer Technology Center, Thailand  
**Sun, Chengliang**, Polytechnic University, Hong-Kong  
**Sun, Dongming**, Jilin University, China  
**Sun, Junhua**, Beijing University of Aeronautics and Astronautics, China  
**Sun, Zhiqiang**, Central South University, China  
**Suri, C. Raman**, Institute of Microbial Technology, India  
**Sysoev, Victor**, Saratov State Technical University, Russia  
**Szewczyk, Roman**, Industrial Research Institute for Automation and Measurement, Poland  
**Tan, Ooi Kiang**, Nanyang Technological University, Singapore  
**Tang, Dianping**, Southwest University, China  
**Tang, Jaw-Luen**, National Chung Cheng University, Taiwan  
**Thumbavanam Pad, Kartik**, Carnegie Mellon University, USA  
**Tsiantos, Vassilios**, Technological Educational Institute of Kaval, Greece  
**Tsigara, Anna**, National Hellenic Research Foundation, Greece  
**Twomey, Karen**, University College Cork, Ireland  
**Valente, Antonio**, University, Vila Real, - U.T.A.D., Portugal  
**Vaseashta, Ashok**, Marshall University, USA  
**Vazques, Carmen**, Carlos III University in Madrid, Spain  
**Vieira, Manuela**, Instituto Superior de Engenharia de Lisboa, Portugal  
**Vigna, Benedetto**, STMicroelectronics, Italy  
**Vrba, Radimir**, Brno University of Technology, Czech Republic  
**Wandelt, Barbara**, Technical University of Lodz, Poland  
**Wang, Jiangping**, Xi'an Shiyou University, China  
**Wang, Kedong**, Beihang University, China  
**Wang, Liang**, Advanced Micro Devices, USA  
**Wang, Mi**, University of Leeds, UK  
**Wang, Shinn-Fwu**, Ching Yun University, Taiwan  
**Wang, Wei-Chih**, University of Washington, USA  
**Wang, Wensheng**, University of Pennsylvania, USA  
**Watson, Steven**, Center for NanoSpace Technologies Inc., USA  
**Weiping, Yan**, Dalian University of Technology, China  
**Wells, Stephen**, Southern Company Services, USA  
**Wolkenberg, Andrzej**, Institute of Electron Technology, Poland  
**Woods, R. Clive**, Louisiana State University, USA  
**Wu, DerHo**, National Pingtung University of Science and Technology, Taiwan  
**Wu, Zhaoyang**, Hunan University, China  
**Xiu Tao, Ge**, Chuzhou University, China  
**Xu, Tao**, University of California, Irvine, USA  
**Yang, Dongfang**, National Research Council, Canada  
**Yang, Wuqiang**, The University of Manchester, UK  
**Ymeti, Aurel**, University of Twente, Netherland  
**Yu, Haihu**, Wuhan University of Technology, China  
**Yuferra Garcia, Alberto**, Seville University, Spain  
**Zagnoni, Michele**, University of Southampton, UK  
**Zeni, Luigi**, Second University of Naples, Italy  
**Zhong, Haoxiang**, Henan Normal University, China  
**Zhang, Minglong**, Shanghai University, China  
**Zhang, Qintao**, University of California at Berkeley, USA  
**Zhang, Weiping**, Shanghai Jiao Tong University, China  
**Zhang, Wenming**, Shanghai Jiao Tong University, China  
**Zhou, Zhi-Gang**, Tsinghua University, China  
**Zorzano, Luis**, Universidad de La Rioja, Spain  
**Zourob, Mohammed**, University of Cambridge, UK

# Contents

Special Issue  
October 2007

[www.sensorsportal.com](http://www.sensorsportal.com)

ISSN 1726-5479

## Research Articles

### Foreword

*Elena Gaura and James P. Brusey*..... 1

### Nano-Structure or Nano-Systems: Opportunities and Pitfalls

*P. J. French and C.-K. Yang*..... 1

### New Trends on MEMS Sensor Technology for Harsh Environment Applications

*Patricia M. Nieva* ..... 10

### Healthcare for the Healthy People: Miniaturization, Sensing and Actuation Trends and Needs in Preventive and Predictive Medicine

*Alberto Sanna, Marco Nalin, Riccardo Serafin*..... 21

### Global Environmental Micro Sensors Test Operations in the Natural Environment (GEMSTONE)

*Mark Adams, John Manobianco and Matthew Buza*..... 30

### Frequency Domain Modeling of SAW Devices for Aerospace Sensors

*William Wilson, Gary Atkinson*..... 42

### Development of Materials and Sensors for the U.S. Army's Active Coatings Technology Program

*James L. Zunino III* ..... 51

### Microfabrication and Characterization of an Integrated 3-Axis CMOS-MEMS Accelerometer

*Hongwei Qu, Deyou Fang and Huikai Xie*..... 60

### Characterization and Optimization Design of the Polymer-based Capacitive Micro-arrayed Ultrasonic Transducer

*De-Yi Chiou, Mu-Yueh Chen, Hsu-Cheng Deng, Ming-Wei Chang*..... 68

### Fabry-Perot Diaphragm Fiber Optic Sensor (DFOS) for Acoustic Detection

*Yan Sun, Guanhua Feng, George Georgiou, Edip Niver, Karen Noe and Ken Chin*..... 76

### Micromechanical GaAs Hot Plates for Gas Sensors

*Jiri Jakovenko, Miroslav Husak, Tibor Lalinky, Milan Drzik*..... 84

### Integration of Microfluidics and Microacoustics Components for Miniature Flow Cytometry Systems

*Surendra K. Ravula, Darren W. Branch, Jennifer Sigman, Paul G. Clem, Igal Brener*..... 93

### Design and Characterization of MEMS Thermal Converter

*Jiri Jakovenko, Miroslav Husak, Tibor Lalinky*..... 101

### Fabrication of a Real Time Reactive Ion Etching Resonant Sensor Using a Low Temperature Sacrificial Polymer

*Bryan G. Morris, Paul J. Joseph and Gary S. May*..... 111

|  |     |
|--|-----|
| <b>Perturbation Stochastic Finite Element Analysis of Thermoelastic Quality Factor of Micro-Resonators</b><br><i>Séverine Lepage and Jean-Claude Golinval</i> .....                  | 124 |
| <b>A Semi-Analytical Model for Calculating Touch-Point Pressure and Pull-in Voltage for Clamped Diaphragms with Residual Stress</b><br><i>Anurekha Sharma and P. J. George</i> ..... | 131 |
| <b>The Development of Chemical Nanosensors</b><br><i>A. J. Jin, J. Li, Y. Lu</i> .....   | 140 |

Authors are encouraged to submit article in MS Word (doc) and Acrobat (pdf) formats by e-mail: [editor@sensorsportal.com](mailto:editor@sensorsportal.com)  
Please visit journal's webpage with preparation instructions: <http://www.sensorsportal.com/HTML/DIGEST/Submission.htm>

## Foreword

The 10<sup>th</sup> annual NSTI Nanotech Conference and Trade Show was held this year during 20-24 May at the Santa Clara Convention Center, in Santa Clara, California. The conference has grown this year to host 3000 attendees and 250 exhibitors, while the resulting proceedings boasts over 3000 pages of peer-reviewed micro and nanotechnology research.

A number of authors publishing in the Joint Electronics and Microsystems Symposia track were invited to submit a revised version of their papers to this special issue. Papers were selected from a number of symposia within the track, including: MEMS & NEMS, Sensors & Systems, Micro & Nano Fluidics, and MSM – Modeling Microsystems. These symposia brought together researchers from a number of disciplines to discuss topics ranging from theoretical developments, to design and fabrication, through to industrial applications of MEMS and NEMS sensors, devices and systems.

The joint symposia are motivated by the dream of smarter, smaller, and more complex systems that integrate micro and nano system technologies with intelligence, power and communication ability at the same micro or nano scale. The resulting increase in complexity poses an enormous challenge to engineers when designing, modeling, and fabricating such integrated micro and nano systems. The joint symposia aimed at bringing together researchers from different disciplines to exchange ideas about how to best develop such systems.

As with the joint symposia, this special issue includes papers ranging from those with a higher level focus to those covering low-level physical aspects of MEMS and NEMS devices and their modeling and fabrication. Four of the papers presented in this special issue correspond to invited talks: Sanna et al., examine miniaturization trends in preventative medicine and include some results from the EU project ANGEL; Adams et al., describe the results of the NASA funded GEMSTONE project, which involved creating and field-testing a small system of atmospheric probes; French and Yang explore the opportunities and pitfalls of scaling, whilst Nieva presents a number of new trends for using MEMS sensors in harsh environments.

We are very thankful both to the NSTI directors and Nanotech chairs (Dr. Matthew Laudon and Dr. Bart Romanovicz) and to the *Sensors & Transducers Journal* for offering the opportunity to publish this special issue.

### Guest Editors:



**Dr. Elena Gaura**

Reader in Pervasive Computing  
Director of Cogent Computing Applied Research Centre  
Faculty of Engineering and Computing  
Coventry University, UK  
e.gaura@coventry.ac.uk  
www.cogentcomputing.org



**Dr. James P. Brusey**

Senior Lecturer in Systems Engineering  
Senior Research Fellow of Cogent Computing Applied  
Research Centre  
Faculty of Engineering and Computing  
Coventry University, UK  
j.brusey@coventry.ac.uk  
www.cogentcomputing.org

## Nano-Structure or Nano-Systems: Opportunities and Pitfalls

**P. J. FRENCH and C.-K. YANG**

EI/EWI-DIMES, Delft University of Technology

Mekelweg 4, 2628 CD Delft, The Netherlands

E-mail: [p.j.french@tudelft.nl](mailto:p.j.french@tudelft.nl),

<http://ei.ewi.tudelft.nl>

*Received: 7 September 2007 /Accepted: 19 September 2007 /Published: 8 October 2007*

---

**Abstract:** Scaling down has revealed many new effects leading to new devices able to measure faster and more accurately than traditional devices. They also present challenges in terms of connecting to the macro-world and in reliability. In some cases the scaling works against us leading to lower performance. We should also consider reducing the size of the system, through integration and optimization. It is therefore important to consider the benefits of miniaturization for each application and either reduce the size of the structures in the system, or integrate the system to reduce size. This paper discusses the effects of scaling at both a device level and also a system level.  
*Copyright © 2007 IFSA.*

**Keywords:** Scaling, Microsystems, Smart sensors

---

### 1. Introduction

Moore predicted the miniaturization in the IC industry in the 1960's and we have seen the dramatic reduction in feature size with the improved performance [1]. For 40 years the IC industry has followed this law.

This scaling is, however, will come to an end requiring a new look at device structure and device physics. Machining has perhaps not seen such a dramatic change but scaling can be found here as well, from fine mechanics to micromachining and later to nano-machining. Fine mechanics was based on assembly technique, whereas micromachining made use of depositions and etching. Moving to nano-machining has involved combinations of micromachining techniques (top-down) and structure growth (bottom-up).

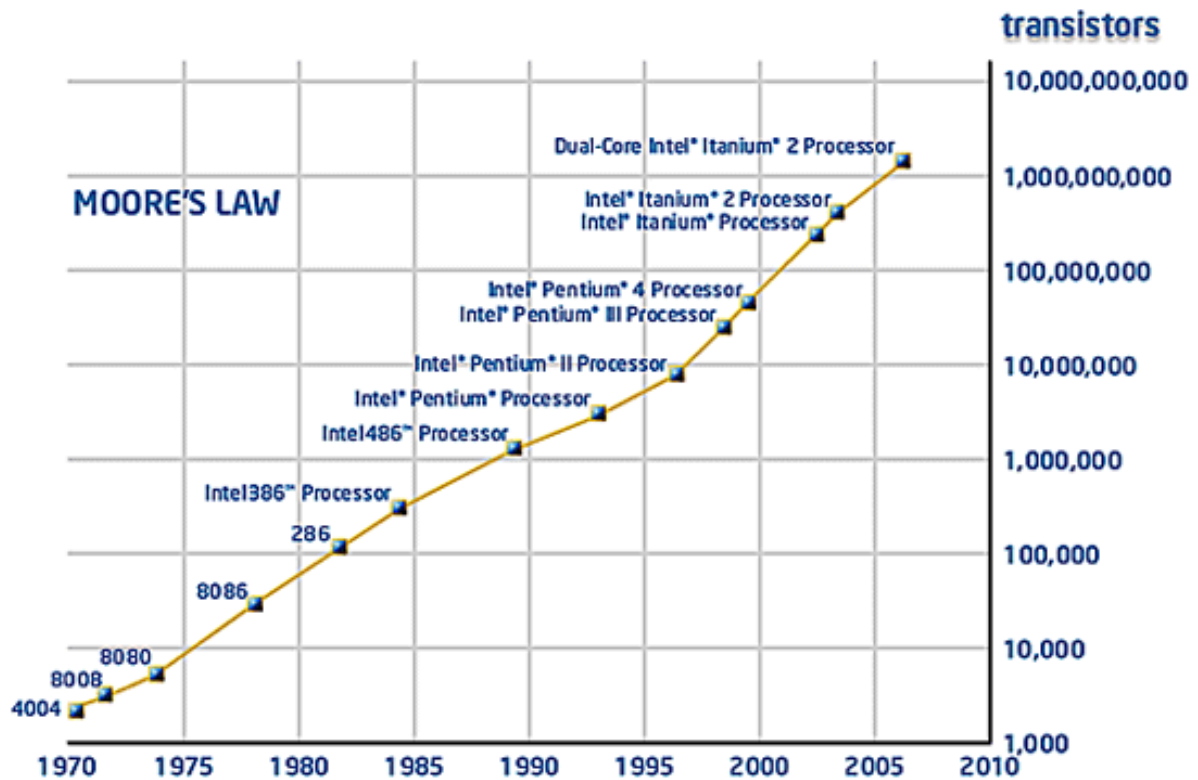


Fig. 1. Moore's law and the IC industry [2].

The benefits, or not, of further scaling depend on the structure and the application and also we should consider not only the feature size of structures, but also the size of the total system. The scaling of pumps from the macro-scale to the micro-scale has led to great benefits in the bio-chemical and medical industries through enabling the pumping of  $\mu\text{l}$  or  $\text{nI}$  of fluid. Further scaling down will probably not benefit many of these applications, due to physical pumping problems. However, nano-fluidics, often using electrophoresis, enables individual cell handling.

## 2. Scaling

The issues of scaling can work in our favour but also against us. In nature we see the adaptation to scale. Smaller creatures often have fine limbs and have to deal with heat loss. Larger creatures need strong limbs and have to be able to lose excess heat. This is a fact often forgotten in films where giant people have normal proportions. If a person were enlarged by a factor of 100 the limbs would have to be proportionally stronger. As we scale down the surface area scales with  $L^2$  and the volume with  $L^3$ , which means that the nano structure have a much larger surface area to volume ratio. We can use this to our advantage if we are using the surface to capture molecules or cells, but on the other hand, this can work against us since changes in the surface (such as oxidation) can considerably change the structure's operation.

When scaling we need to consider both the individual devices and also the system to decide whether we should reduce the size. With an integrated sensor, the sensor itself may be only a small part of the chip and therefore further reduction in size should only be considered if there are benefits in terms of functionality, since there is an increased emphasis on more functionality in the same volume rather than reduced volume.

### 3. Devices

#### 3.1. Accelerometer

An example of a complete micromachined system on a chip is the Analog Devices accelerometer, which contains all the read-out electronics and self-test on a single chip. A photograph of the chip is shown in Fig.3. The functionality has been increased in a miniaturized package, although the accelerometer used micromachining and not nanomachining. Further scaling of the accelerometer would result in a higher resonant frequency but the reduced proof-mass would make it difficult to achieve a high resolution. Although this is an excellent example of a miniaturized system, the high resolution device ( $\mu\text{g}$ ) uses bulk micromachining to achieve the larger mass (milligramme). One device which achieved high sensitivity and low noise, combined surface and bulk micromachined in a highly symmetrical device. This device is illustrated in Fig.2. Improved sensitivity to small movement can also be achieved using readout techniques such as tunneling [4].

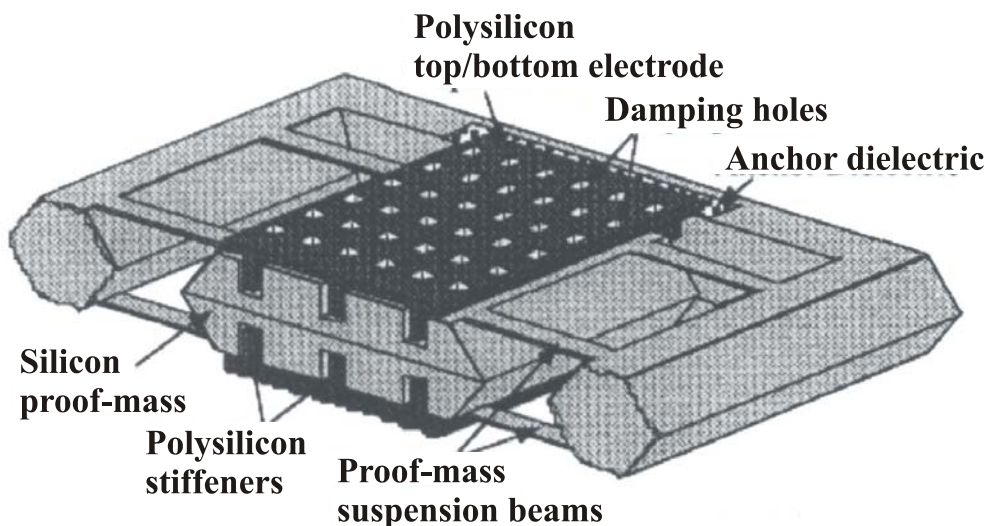


**Fig. 2.** Micro-g accelerometer using bulk and surface micromachining [3].

Surface micromachined accelerometer has proof-masses in the range of sub- $\mu\text{gramme}$  and the measurement range usually  $\pm 1\text{g}$  [5-7]. In this case great benefit can be gained from miniaturization of the system through integration, creating a complete system on a chip (Fig.3) but further miniaturization of the device will not help. Most of the surface micromachined accelerometers are lateral accelerometers, although there are examples of vertical devices [8]. An example of such a device is given in Fig.4.

#### 3.2. Micro-Pump

Miniaturization of pumps has yielded many benefits in chemistry, biology and medicine. The ability to accurately pump  $\mu\text{l}$  or  $\text{nL}$  per minute can reduce cost (by using less sample) and enable studies at cell level. Activation of the pump at this scale can be thermal, piezoelectric or electrostatic, etc. Miniaturization of the system has also enabled implantable systems for medical applications. Early micro-pumps did not perform as expected due to changes in fluid properties which were not taken into account. However, understanding of fluid properties on the microscale has led to a range of applications. Most pumps are fabricated using bulk micromachining with dimensions of a few

millimeters [9-10]. However, there are also examples of surface micromachined pumps [11]. Techniques for activating these pumps include piezoelectric, thermal and electrostatic. These activation techniques all scale well even to sub-micro level.

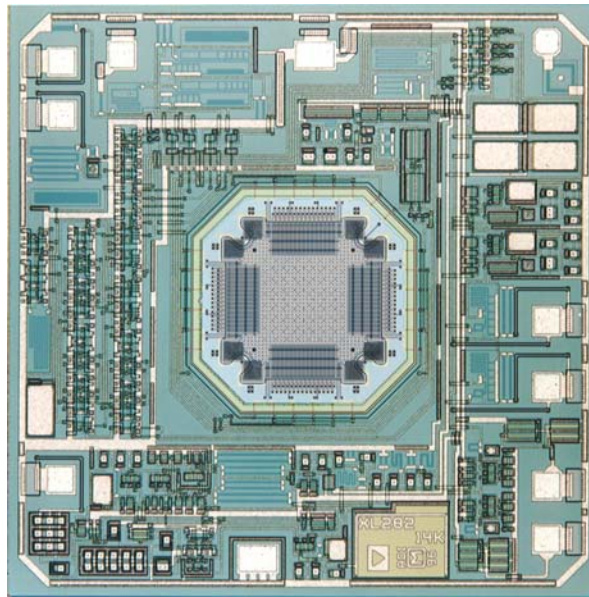


**Fig. 3.** Analog Devices 2 axis accelerometer (reproduced with kind permission).

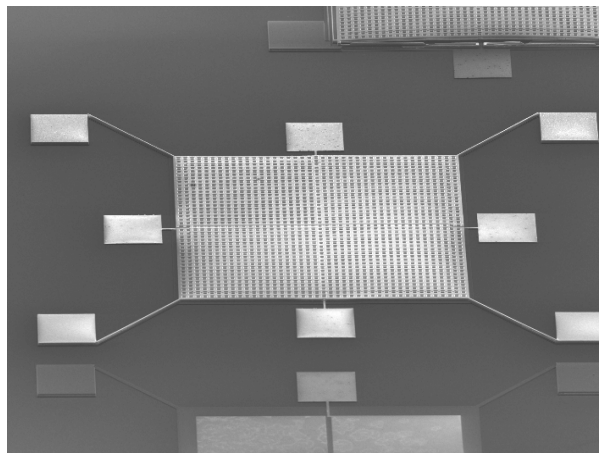


**Fig. 4.** Vertical accelerometer using surface micromachined SiC and Aluminium [8].

### 3.3. Micro-Nano-Fluidics

The challenge with scaling fluid systems further is the increase in resistance with decreasing size. However, if achieved analysis at cell or molecule level can be achieved. Fluids can be drawn through the channels using electro-osmosis. Sub-micron distance between pillars allows DNA to be separated by length [12]. This is achieved by oxidizing macro-pore arrays. The result is shown in Fig.5.

Miniaturization can bring fluid samples down to atto-litre allowing analysis of single molecules [13]. An example of such a device is given in Fig. 6.

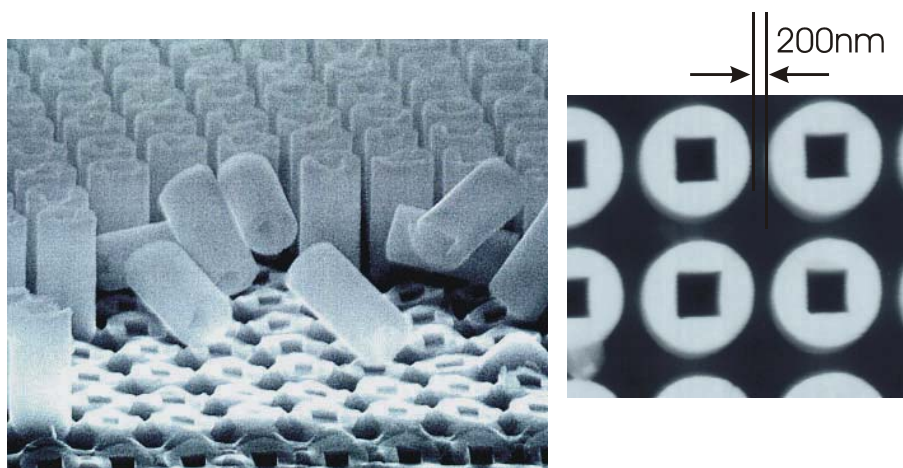


**Fig. 5.** Oxide pillar arrays with sub-micron spacing for DNA separation [12].

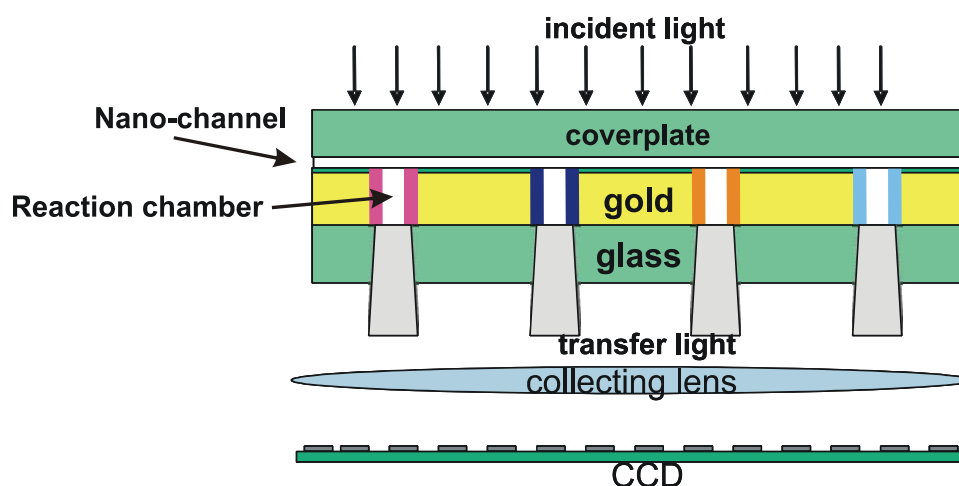


**Fig. 6.** Schematic of the atto-litre plate device [13].

### 3.4. Resonators

Simple cantilevers made from epitaxial silicon can be used as vibration sensors for frequencies into the kHz range [14].

Scaling of resonators leads to higher frequencies and new applications since, for example, molecule attached to the resonator will yield a clear change in resonant frequency, or detecting force with high accuracy [15]. Further reduction in size can lead to MHz and even GHz resonant frequencies [16-18].

There are a number of issues which have to be addressed when developing these devices – reliability, actuation and sensing. Some sensing techniques do not scale well or require large equipment, not permitting a reduction in the size of the system. (Tables 1 and 2).

**Table 1.** Actuation techniques and their scalability.

| <b>Actuation</b> |  |                      |                    |   |
|------------------|--|----------------------|--------------------|---|
| <b>Method</b>    | <b>Scaling limit</b>   | <b>Scalability</b>   | <b>Integration</b> | <b>Other criteria</b>   |
| Piezoelectric    | No fundamental limit for piezoeffect                                     | nano                 | ++                 | Piezoelectric material, parasitic capacitance, frequency bandwidth limit. |
| Electrostatic    | No fundamental limit for coulomb force                                   | nano                 | ++                 |   |
| Magnetomotive    | No fundamental limit for Lorentz force                                   | nano                 | --                 | Conductive double clamped devices. Stable, high magnetic field required.  |
| Optical-thermal  | Heat capacity of the device and its heat dissipation, dimension related. | Micron/<br>submicron | --                 | Limited frequency response, optical system required.                      |

**Table 2.** Detection techniques and their scalability.

| <b>Sensing</b>                  |  |                       |                    |  |
|---------------------------------|--|-----------------------|--------------------|--|
| <b>Method</b>                   | <b>Scaling limit</b>   | <b>Scalability</b>    | <b>Integration</b> | <b>Other criteria</b>  |
| Capacitive                      | Parasitic capacitance from the device and electronics.                 | micron                | ++                 | Frequency dependent on RC time constant  |
| Optical reflection displacement | Effective reflection from the structure. Force constant of the device  | micron                | --                 | Optical device required  |
| Optical interferometer          | Effective reflection from the structure. Force constant of the device  | Micron/<br>nano       | --                 | Complex, precision optics required   |
| Magneto-motive                  | Detectable induced electromotive force                                 | nano                  | --                 | Stable, high magnetic field required. Double clamped device only.                |
| SET charge                      | Detectable SET source-drain current due to Coulomb blockade of the SET | nano                  | +                  | Cryogenic temperature, double clamped devices only                               |
| Piezoelectric                   | Effective piezoelectric signal generated. Dimension related.           | Micron/<br>sub-micron | ++                 | Piezoelectric material required. Multilayer structure for maximum signal output. |
| Piezoresistive                  | Effective piezoresistive change. Dimension related                     | Micron/<br>sub-micron | ++                 | Piezoresistive material required. Multilayer.                                    |
| Tunneling                       | Not device dimension related   | nano                  | ++                 | Small initial electrode distances. High device impedance.                        |

The limitation with piezoresistive techniques when scaling has been noise and long term reliability. When scaling silicon piezoresistors, the surface area to volume plays an increasingly important role. Recently, gold piezoresistors have been applied to the submicron scale. Although the piezoresistive coefficient is low, the low noise and stability of the material, makes it a good option [19].

Field emission can also be an interesting read-out technique since it scales very well. It is able to accurately measure distance over a limited range. An example of this measurement is given in Fig.7 [20].

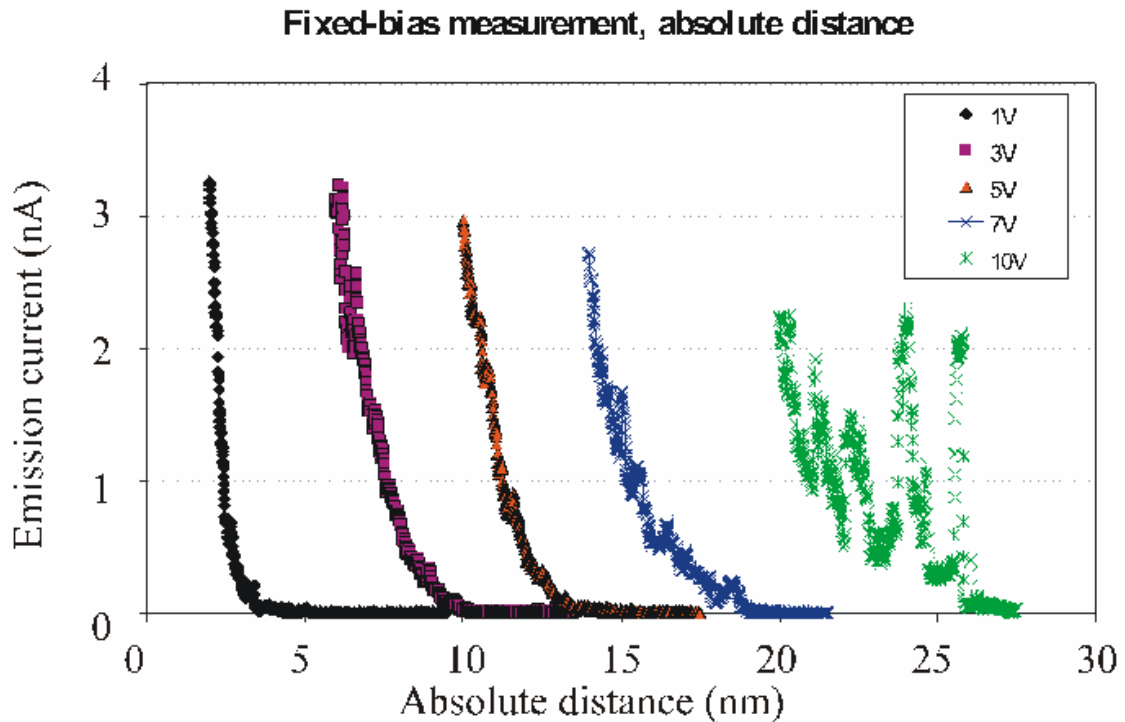


**Fig. 7.** Emission current as a function of absolute distance using field emission [20].

#### 4. Nanotubes/Nanowires

When fabricating cantilevers on the micro-scale, the fabrication techniques are top-down techniques. Further down-scaling often requires the bottom-up approach. Structures such as nano-wires and nano-tubes have shown properties able to detect quantum effects, for fundamental studies and also new sensors [21-22]. An interesting application of nano-tubes, although not in a nano-sensor is to use anodized aluminium oxide as a seed. In this was tubes can be grown in arrays [23-24], as shown in Fig.8. These structures can then be used for applications such as gas and humidity sensors.

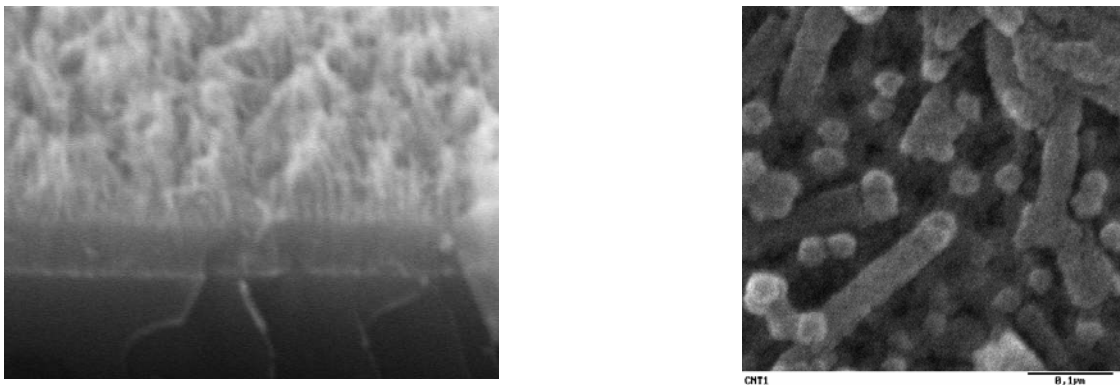


**Fig. 8.** SEM images of CNT's grown on an AAO/Si substrate: a) cross-section; b) top view [23-24].

## 5. Conclusions

Scaling from micro to nano can present many advantages but also many challenges. The advantages are very application specific. In some cases scaling can lead to greater accuracy, but in others it can actually reduce sensitivity. Therefore for each application the benefits and pitfalls of scaling need to be examined. The second aspect is that in many applications the size of the sensing device is not the issue, but the size of the system.

## Acknowledgements

The authors would like to thank the members of the DIMES research school who have contributed to this work and the authors who have given permission for the use of figures.

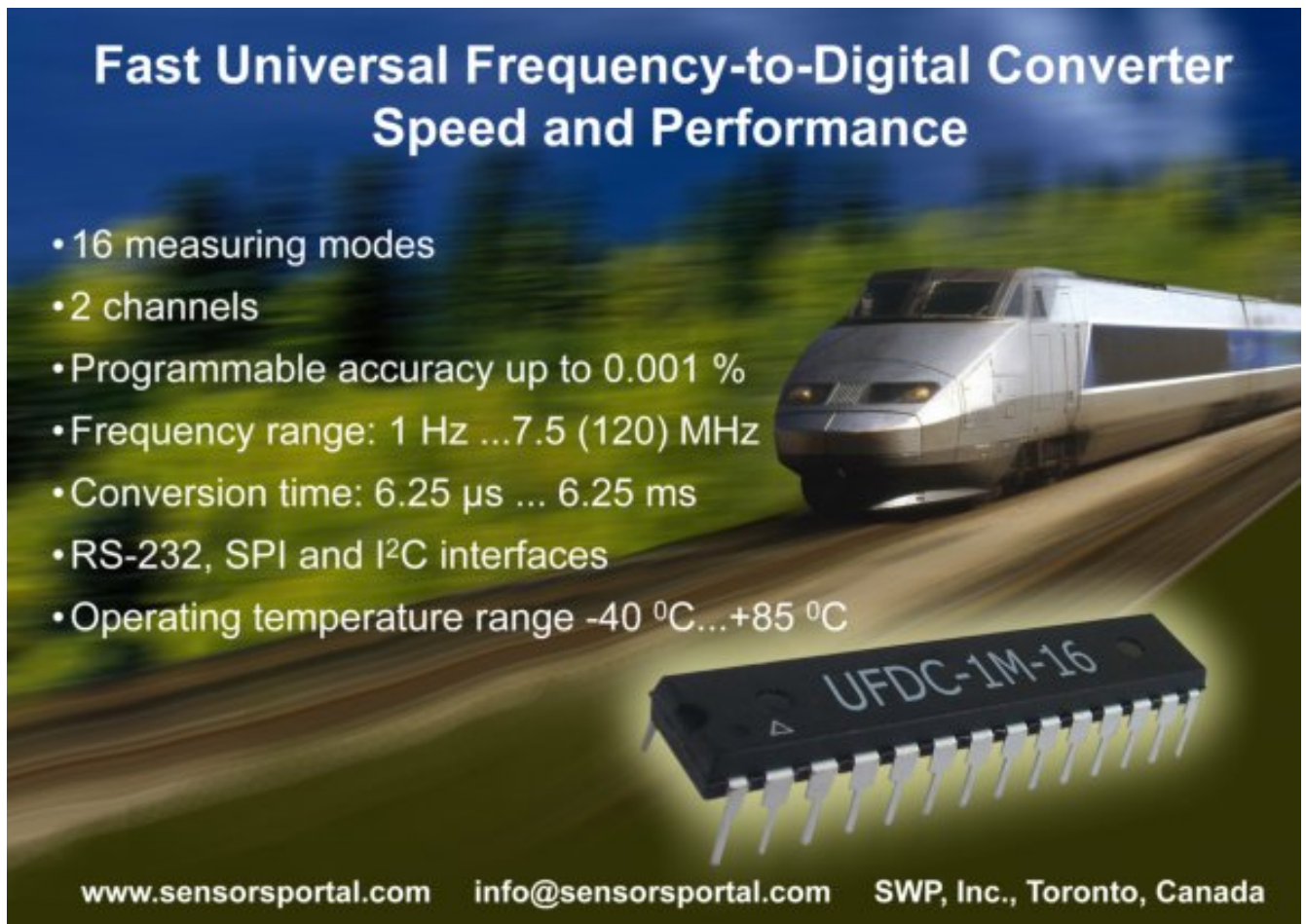
## References

- [1]. Gordon E. Moore, Cramming more components onto integrated circuits, *Electronics*, Vol. 38, No. 8, Apr. 1965.
- [2]. <http://www.intel.com/technology/mooreslaw/index.htm>
- [3]. N. Yazdi and K. Najafi, An all-silicon single wafer micro-g accelerometer with a combined surface and bulk micromachining process, *IEEE JMEMS*, 9, 2000, pp. 544-550.
- [4]. C-H. Liu, A. M. Barzilai, J. K. Reynolds, Aaron Partridge, T. W. Kenny, J. D. Grade and H. K. Rockstad, Characterization of a high-sensitivity micromachined tunneling accelerometer with micro-g resolution, *IEEE JMEMS*, 7, 1998, pp. 235-243.
- [5]. S. J. Sherman, W. K. Tsang, T. A. Core, R. S. Payne, D. E. Quinn, K. H. -L. Chau, J. A. Farrash and S. K. Braum, A low cost monolithic accelerometer; product/technology update, *Proceedings IEDM*, 92, pp. 19.1.1-19.1.4.
- [6]. A. A. Seshia, M. Palaniapan, T. A. Roessig, R. T. Howe, R. W. Gooch, T. R. Schimert and S. Montague, A vacuum packaged surface micromachined resonant accelerometer, *IEEE JMEMS*, 11, 2002, pp. 784-793.
- [7]. L. Pakula and P. J. French, A pull-in operation moe accelerometer, *Proceedings IEEE Sensors*, Daegu, Korea, October 2006.
- [8]. L. Pakula and P. J. French, A CMOS compatible SiC accelerometer, *Proceeding IEEE Sensors*, Toronto, Canada, October 2003, CD, pp. 761-764.
- [9]. F. C. M. Pol, H. T. G. van Lintel, M. Elwenspoek and J. H. Fluitman, A thermopneumatic miropump based on micromachining techniques, *Sensors and Actuators*, A21-A23, 1990, pp. 198-202.
- [10]. R. Zengerle, M. Richer, F. Brosinger, A. Richter and H. Sandmaier, Performacnce simulation of microminituarized membrane pumps, *Proceedings Transducers 93*, Yokohama, Japan, pp. 106-109.
- [11]. J. W. Judy, T. Tamagawa and D. L. Polla, Surface-machined micromechanical membrane pump, *Proceedings IEEE MEMS 1991*, Nara, Japan, pp.182-186.
- [12]. H. Ohji, S. Izuo, P. J. French, K. Tsutsumi, Pillar structures with a sub-micron space fabricated by macroporous-based micromachining, *Sensors and Actuators A*, 97-98, 2002, pp. 744-748.
- [13]. O. Piciu, M. vd Krogt, P. M. Sarro and A. Bossche, Fabrication of optical hole-arrays for use in the attoliter titer plate device for single molecule detection, *Proceedings Eurosensors 2005*, Barcelona, Spain, paper WPa25.
- [14]. W. Benecke, L. Csepregi, A. Heubrerger, K. Kühl and H. Seidel, A frequency-selective, peizoresistive silicon vibration sensor, *Proceedings Transducers 95*, Philadelphia, USA, pp. 105-108.
- [15]. J. L. Arlett, J. R. Maloney, B. Gudlewski, M. Muluneh and M. L. Roukes, Self-sensing micro-and nanocantilevers with Attonewton-scale force resolution, *Nano lett.*, 6, 2006, pp. 1000-1006.
- [16]. M. L. Roukes, Nanoelectromechanical systems, *Proceedings Hilton Head*, 2000, pp. 1-10.
- [17]. K. L. Ekinci and M. L. Roukes, Nanoelectromechanical systems, *Review of Scientific Instruments*, 76, 2005, pp. 1-11.
- [18]. K. C. Schwab and M. L. Roukes, Putting mechanics into quantum mechanics, *Physics Today*, July 2005, pp. 36-42.

- [19].M. Li, H. X. Tang and M. L. Roukes, Ultrasensitive NEMS-based cantilevers for sensing, scanned probe and very high frequency applications, *Nature Nanotechnology*, 2, 2007, pp. 114-120.
- [20].C. -K. Yang, A. J. le Fèvre, G. Paundraud, E. van der Drift and P. J. French, Field emission for resonance sensing in MEMS/NEMS, *Proceedings 20<sup>th</sup> International Vacuum Nanoconference*, Chicago, USA, July 2007, pp. 72-73.
- [21].X. T. Zhou, J. Q. Hu, C. P. Li, D. D. D Ma, C. S. Lee and S. T. Lee, Silicon nanowires as chemical sensors, *Chemical Physics Lett.*, 369, 2003, pp. 220-224.
- [22].R. J. Grow, Q. Wang, J. Cao, D. Wang and H. Dai, Piezoresistance of carbon nanotubes on deformable thin-film membranes, *Appl. Phys. Lett.*, 86, 2005, pp. 1-3.
- [23].H. T. M. Pham, C. R. de Boer, P. M. Sarro, Non-Catalyst and Low Temperature Growth of Vertically Aligned Carbon Nanotubes for Nanosensor Arrays, *Proc. Transducers*, Seoul, Korea, June 5-9, 2005, pp. 97-100.
- [24].H. T. M. Pham, C. R. de Boer, P. M. Sarro, invited paper, Nanostructure formation on anodic aluminum oxide nanotemplates, *The Second International Workshop on Nanophysics and Nanotechnology*, IWONN'04, Hanoi, Vietnam, Oct . 22-23, 2004, pp. 8.

---

2007 Copyright ©, International Frequency Sensor Association (IFSA). All rights reserved.  
(<http://www.sensorsportal.com>)



**Fast Universal Frequency-to-Digital Converter**  
**Speed and Performance**

- 16 measuring modes
- 2 channels
- Programmable accuracy up to 0.001 %
- Frequency range: 1 Hz ...7.5 (120) MHz
- Conversion time: 6.25 µs ... 6.25 ms
- RS-232, SPI and I<sup>2</sup>C interfaces
- Operating temperature range -40 °C...+85 °C

UFDC-1M-16

[www.sensorsportal.com](http://www.sensorsportal.com)   [info@sensorsportal.com](mailto:info@sensorsportal.com)   SWP, Inc., Toronto, Canada

## New Trends on MEMS Sensor Technology for Harsh Environment Applications

**Patricia M. NIEVA**

Department of Mechanical and Mechatronics Engineering,  
University of Waterloo, 200 University Ave. West, Waterloo, N2L 3G1  
E-mail: [pnieva@uwaterloo.ca](mailto:pnieva@uwaterloo.ca)  
<http://simslab.uwaterloo.ca>

*Received: 7 September 2007 / Accepted: 19 September 2007 / Published: 8 October 2007*

---

**Abstract:** MEMS and NEMS sensor systems that can operate in the presence of high temperatures, corrosive media, and/or high radiation hold great promise for harsh environment applications. They would reduce weight, improve machine reliability and reduce cost in strategic market sectors such as automotive, avionics, oil well logging, and nuclear power. This paper presents a review of the recent advances in harsh-environment MEMS and NEMS sensors focusing on materials and devices. Special emphasis is put on high-temperature operation. Wide-bandgap semiconductor materials for high temperature applications are discussed from the device point of view. Micro-opto mechanical systems (MOEMS) are presented as a new trend for high temperature applications. As an example of a harsh environment MOEMS sensor, a vibration sensor is presented. *Copyright* © 2007 IFSA.

**Keywords:** MEMS, NEMS, MOEMS, Sensors, Harsh Environments, Fabry-Perot Interferometry

---

### 1. Introduction

Micro and nano electro mechanical systems (MEMS and NEMS) have emerged as a technology that integrates micro/nano mechanical structures with microelectronics, mainly for sensing and actuation applications. Silicon-based MEMS technology has enabled the fabrication of a broad range of sensor and actuator systems. These systems are having a great impact in areas that benefit from miniaturization and increased functionality. They have been commercialized for applications such as ink jet printing, crash sensing, and optical projection to name a few. The main advantage of silicon-based technology is the possibility of integration with microelectronics. A great deal of attention is being drawn to the development of integrated MEMS and NEMS to produce smart devices and systems. In automotive or aerospace for example, a misfiring cylinder has a negative impact on the

health of the engine and the emissions control. When a cylinder misfires, the remaining cylinders operate at abnormally higher loads resulting in excessive cylinder pressure levels, overheating, knock, pre-ignition, and severe engine damage. Misfire is also accompanied with high emissions of unburned hydrocarbons and CO. Smart MEMS sensors capable of operating “in cylinder”, where the temperatures are around 400 °C for automotive engines or up to and above 900 °C for gas turbine engines, could continuously monitor the combustion quality of the cylinders of automotive engines reducing emissions and improving fuel economy. However, the mechanical and electrical properties of silicon (Si) limit their application in harsh environmental conditions. When the environment temperature is too high (>180 °C), conventional microelectronics suffer from severe performance degradation [1]. Hence, they must reside in cooler areas or be actively cooled. The additional components such as longer wires, extra packaging and/or bulky expensive cooling systems, add undesired size and weight to the system, which at the same time impact the overall reliability of the system. They also require extra supply voltage, which is undesirable for HT applications where power source is very limited. It is then clear that further development, in terms of new MEMS/NEMS materials (including new functional layers such as piezoelectric films) and/or new technologies, is needed to minimize these difficulties. This is especially important where high temperature capability is crucial to realizing improved electronic control and reducing weight.

Silicon carbide (SiC) [2, 3] and group III nitride device technologies [5, 6] are promising for smart MEMS/NEMS sensors operating in harsh environments. In the past decade, tremendous progress has been made in the growth of single crystal SiC wafers and epitaxial growth of crystalline SiC layers on Si and/or SiC wafers [2, 10-15]. However, SiC wafers are not (yet) suitable for MEMS and NEMS, as micromachining of these wafers is still a challenge [2-4]. Issues such as high mechanical stress, deposition uniformity and low etch rates need to be tackled before high-quality SiC structural films can be produced [3]. In addition, the affinity of SiC to form carbides and/or silicides by reacting with metals at temperatures above 600 °C affect metal contacts degrading the performance of SiC MEMS and NEMS sensors [4]. Furthermore, very little is known about the elastic behavior and long-term stability of SiC micro- and nano-structures at elevated temperatures. Hence, despite the obvious benefits of using SiC for the development of MEMS and NEMS for harsh environments, there are still many hurdles that have to be overcome before it becomes appropriate for manufacturing and can be used reliably in commercial applications [2, 3]. Group III nitrides are beneficial as piezoelectric functional components for high temperature operation. For example, Aluminum nitride (AlN) preserves its piezoelectric properties up to 1150 °C [5] and gives the opportunity of building up on-chip smart systems with a high degree of processing control. However, only a few reports exist about such applications [6] and despite of all the progress made in the last few years, they still cannot be used for integrated MEMS or NEMS devices.

Remote sensing through optical signal detection has major advantages for safe signal transmission in harsh environments. It is highly resistant to electromagnetic interference (EMI) and radio frequency interference (RFI) and at the same time, it eliminates the necessity of on-board electronics, which has been one of the main obstacles in the development of smart MEMS sensors for high temperature applications. An economical way to deal with higher temperatures and other aggressive environmental conditions is to build MEMS sensors out of robust materials (e.g. Si, Silicon nitride, SiC) and integrate them with optical signal detection techniques to form MOEMS [7-9]. For instance, Fabry-Perot (FP) microstructures have been used to meet the demand of MEMS sensor systems for harsh environments [7, 8]. In this combination, the small and precise size of the sensing elements offers considerable flexibility in choosing the response range and sensitivity of the final sensors. Optical technology has also been used to power a wireless telemetry module for high temperature MEMS sensing and communication [9]. In this paper, we review the current status and the main obstacles in wide bandgap semiconductor devices and microsystem components for MEMS and NEMS. We also highlight recent advances and trends in MOEMS sensors in the context of using them for high temperature applications. The use of Fabry-Perot microstructures for the development of a new MOEMS

displacement sensor for high temperature applications is discussed. Analysis, modeling and experimental results are presented to show their sensitivity and accuracy.

## **2. Silicon Carbide Semiconductor Devices**

SiC is the most mature and the only wide bandgap semiconductor that has silicon dioxide as its native oxide [10]. This allows for the creation of metal oxide semiconductor (MOS) devices. The outstanding material and electronic properties and chemical inertness of SiC make it a leading candidate for MEMS and NEMS in a variety of harsh conditions [2, 10-17]. Regarding its material properties, SiC has a knoop hardness of 2480 kg/mm<sup>2</sup> compared to that of silicon (850 kg/mm<sup>2</sup>) [12]. In addition, SiC has a Young's Modulus of 700 GPa, as compared to Si (190 GPa) [11a] or other wide bandgap semiconductors such as Gallium Nitride (295 GPa) [13] and AlN (310 GPa) [5]. When compared to silicon, SiC has a larger bandgap (2.3-3.4 eV), a higher breakdown field (30x10<sup>5</sup> V/cm), a higher thermal conductivity (3.2-4.9 W/cm K), and high saturation velocity (cm/s) [12]. Piezoresistive- and capacitive-based sensors are among the most widely used SiC MEMS and NEMS sensing mechanisms.

### **2.1. Piezoresistive-Based Sensors**

The piezoresistive effect in SiC has been used for pressure, force, and acceleration sensors. In general, the piezoresistivity for wide band-gap semiconductors is comparable to that of Si but they can operate at much higher temperatures. However, the contact resistance variation at elevated temperatures can be indistinguishable from the piezoresistance change [16]. In addition, SiC has a relatively low gage factor (30 compared to 90 of Si [11]) which decreases the sensitivity of the sensors as the temperature increases. Okojie et al. [13] developed a piezoresistive pressure transducer which was made of 6H-SiC piezoresistors on a 6H-SiC substrate. The sensor was tested up to 600 °C and 200 psi but due to the significant decrease of the gage factor at high temperatures, the output of the transducer required a temperature compensation scheme above 400 °C. More recently, Wu et al. [14] developed bulk micromachined pressure sensors for HT applications using polycrystalline and crystalline 3C-SiC piezoresistors grown on a Si substrate. The piezoresistors fabricated from poly-SiC films showed -2.1 as the best gauge factor and exhibited sensitivities up to 20.9-mV/V psi at room temperature. Single-crystalline 3C-SiC piezoresistors exhibited a sensitivity of 177.6-mV/V psi at room temperature and 63.1-mV/V psi at 400 °C. Their estimated longitudinal gauge factor along the [100] direction was estimated at about -18 at room temperature but dropped to -7 at 400 °C. Atwell et al. [15] developed a bulk-micromachined 6H-SiC piezoresistive accelerometer for impact applications. The accelerometer was tested up to 40,000 g. Sensitivities ranging from 50 to 343 nV/g were measured for differing sensing elements but non-linear behavior was observed over the shock range relative to a commercial accelerometer (with sensitivity of 1.5  $\mu$ V/g).

### **2.2. Capacitive-Based Sensors**

Capacitive-based sensors have also been used to sense pressure, force, acceleration, and flow rate. They are attractive for HT applications because the device performance is not susceptible to contact resistance variations but they exhibit performance degradation due to the wiring parasitic capacitances and test setup. SiC capacitive sensors are mainly used for pressure sensing and they are mainly fabricated using bulk-micromachining techniques. Young et al. [16] developed a single crystal 3C-SiC capacitive pressure sensor fabricated on a silicon substrate. The sensor demonstrated sensing capabilities up to 400 °C and was tolerant of contact resistance variations. However, it exhibited different responses at different temperatures of operation, which was attributed to trapped air inside the

cavity and thermal mismatch. A promising approach to pressure sensing in corrosive environments was developed by Pakula et al. [17] using post-processing surface micromachining. The sensing membrane was fabricated in low-stress PECVD SiC. To avoid problems related with wiring parasitic capacitances, the sensor was integrated monolithically to a CMOS readout circuit. The sensor showed stable behavior from 10 mbar up to 5 bar.

### **3. Optical MEMS Sensors**

Optical MEMS sensors are highly adaptable to harsh environments, can measure displacement, pressure, temperature and stress, can be easily incorporated into sensor arrays by using multiplexing methods, and are suitable for liquid and gas measurements. In addition, they are highly resistant to electromagnetic interference (EMI) and radio frequency interference (RFI) and at the same time, they eliminate the necessity of onboard electronics. However, simpler processing techniques and therefore lower manufacturing costs are desirable. Moreover, simplification of the sensing elements and the fabrication processes will be helpful for their mass production and commercialization. Fiber-Optic MEMS and MOEMS sensors are lately being developed for harsh environmental conditions [7, 18-20].

#### **3.1. Fiber-Optic MEMS Sensors**

Fiber-optic MEMS are robust, highly resistant to EMI and RFI, and can potentially detect displacements on a sub-nanometer scale. However, their performance depends on mechanical-thermal noise, photodetector noise, fabrication imperfections, and assembly. From all these, the main disadvantage is the need to adjust the optical interrogation system relative to the moving MEMS component. Eklund and Shkel [18] demonstrated that the finesse of a Fiber Optic Fabry-Perot MEMS can decrease up to one order of magnitude due to surface roughness, curvature or a slight deviation from parallelism, thus greatly reducing the resolution of the sensor. Xiao-qi et al. [19] developed a fiber-optic MEMS pressure sensor for harsh environments based on Fabry-Perot interferometry. A dual-wavelength demodulation method was used to interrogate the sensor and results show that the sensor has reasonable linearity and sensitivity within 0.1 MPa to 3 MPa. However, the fabrication is complicated and expensive. In addition, misalignments between the sensor and the fiber cause an increase of the signal-to-noise ratio due to instability of the reflected signal. To overcome these limitations, integration techniques have to be developed which can be either hybrid (e.g. detachable connection of optical fibers with sensor heads). Another solution could also be the integration into MOEMS employing substrate integrated waveguides. However, one of the disadvantages of these waveguides is that leakage losses can be substantial, especially at high temperatures.

#### **3.2. MOEMS Fabry-Perot Sensors**

Fabry-Perot Interferometric techniques can be easily applied to membranes or cantilevers that, if fabricated with robust materials (e.g. Si, silicon nitride, SiC, etc.), can be utilized to develop contact-free sensor components with high sturdiness in harsh conditions. Compared to sensors that utilize optical fibers or multi-chip structures [18, 19], single-chip Fabry-Perot MOEMS sensors do not require alignment or sophisticated optical stabilization techniques [7, 8, 20]. In contrast to cumbersome and ambiguous fringe-counting optical detection schemes associated with large cavity FP sensors used in the literature, the small cavity length of these sensors (2-3  $\mu\text{m}$ ) allows small intensity shifts to be uniquely related to the relative displacement of the moving mirror. This high resolution results in an improvement of functionality, reliability and sensitivity compared to classical fiber-optic sensors, and make them ideal for the manufacturing of on-chip smart systems at a minimum cost.

Haueis et al. [8] developed a Si-based resonant force sensor packaged with fiber-optic signal detection for high temperature operation. An off-chip capacitive detection system was also used to verify the operation of the sensor up to 175 °C. The optical detection showed a resolution of the resonator deflection to be more than ten times better than the capacitive detection. Wang et al. [20] developed a new Fabry-Perot pressure microsensor which has been successfully tested up to 30 psi and 120 °C. Over the pressure ranging from 0 to 21 psi, very small cross sensitivity to temperature was observed in mid or higher end of the pressure range. However, because of the bridge configuration of the sensor, a corrugated diaphragm needs to be used to alleviate both, the signal averaging effect and the cross-sensitivity to temperature.

#### 4. Fabry-Perot MOEMS Sensor for High Temperature Applications

We have developed the MOEMS Fabry-Perot displacement sensor (MFPD) shown in Fig. 1 that is suitable for high temperature applications and can be easily integrated with standard Si micromachining. Details on the development and fabrication were presented in Ref. [7]. The MFPD consists of a cantilever beam fabricated in low-stress LPCVD silicon nitride. The cantilever beam forms the top mirror of the Fabry-Perot interferometer while the silicon substrate below provides the bottom mirror. As shown schematically in Fig. 4, the two mirrors form an optical microcavity for a monochromatic laser beam incident at the top. For this cavity arrangement, the total interferometric light back-reflected depends on the height of the optical microcavity at the location where the laser beam is directed (spot). When the substrate vibrates, there is a relative deflection of the beam with respect to the substrate and hence a change in the microcavity height. If the mechanical characteristics of the device are known, the amplitude of the substrate motion can be calculated by measuring the back-reflected light.

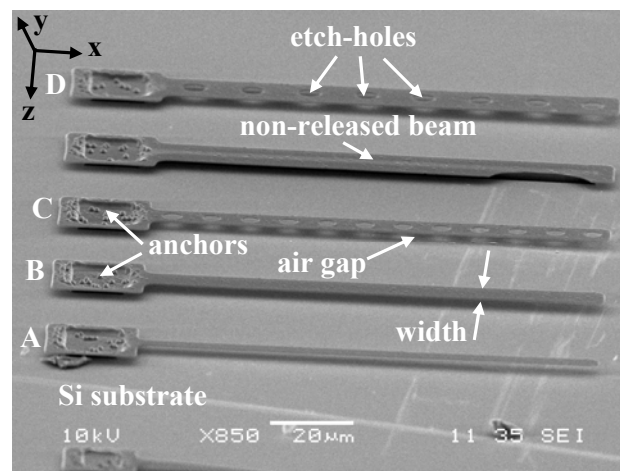


**Fig. 1.** Fabry-Perot MOEMS displacement sensors with a fundamental resonant frequency of ~ 45 kHz [7].

To the best of our knowledge this MFPD sensor is the first surface micromachined Fabry-Perot in the literature that employs a single layered cantilevered structure together with a new extrinsic intensity-modulated optical interrogation method based on the reflectance of the device (and not the transmittance) to measure displacement in high temperature environments. Cantilever beams have advantages over bridge structures because the lowest natural frequency is 16 % of a bridge with the same dimensions, allowing measurement of lower frequencies. Also residual stresses do not significantly affect the resonant frequency of cantilevers [21], but do change the resonant frequency of

a bridge operating at high temperatures [22]. In addition, they eliminate problems due to stress-stiffening effects and variation of the optical path length due to coupled photo-elastic and thermal-optical effects, all of which are critical to the successful realization of sensors for high temperature applications.

#### 4.1. Optical Signal

The optical microcavity of the MFPD corresponds to a Fabry-Perot in reflectance and its optical response is given by the *power reflectance*,  $R$ , of the top of its surface [7]. Assuming no variation in the top mirror thickness ( $t$ ) or the relaxed cavity height ( $h$ ),  $R$  is only a function of the top layer thickness and the time-dependant air cavity height at the location of the laser beam spot. Fig. 3 shows the power reflectance of the MFPD as a function of the relaxed air gap height (dotted curve). This function was obtained from the optical signal shown in Fig. 2, measured for the MFPD type A shown in Fig. 1, vibrating at a frequency of 62 kHz, and fitted to the AC component of the theoretical power reflectance model described in detail in Ref. [7] with  $h$ ,  $\delta_r$ , and  $t_1$  as the fitting parameters. As it can be easily observed, the function is periodic (period  $\lambda/2$ ) and represents the optical transfer function of the microcavity of the sensor.

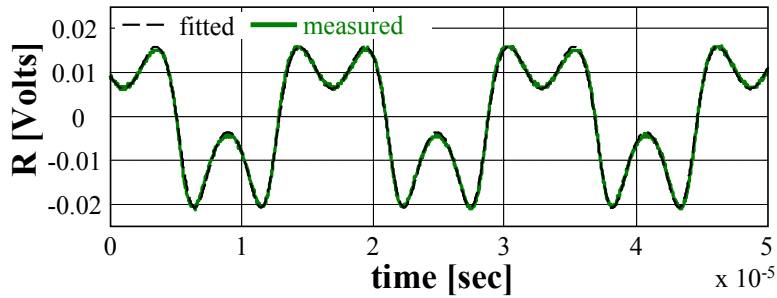


**Fig. 2.** Measured interferometric optical signal from the MFPD cantilever beam A (Fig. 1) vibrating at an amplitude of the relative displacement of  $\sim 143.8$  nm and fitted to the theoretical power reflectance.

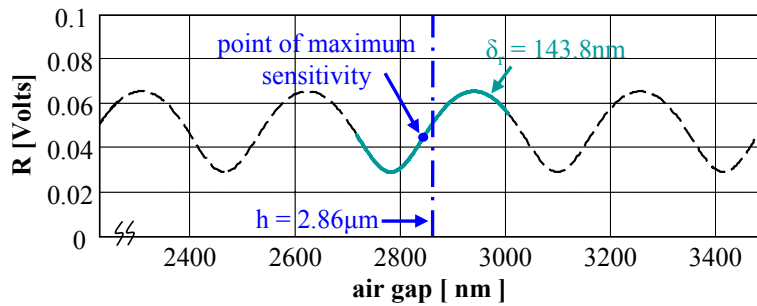


**Fig. 3.** Reflectance of the MFPD type A shown in Fig. 1 as a function of air gap height.

The total displacement of the beam with respect to the substrate is indicated by the solid line. The fitted values of  $h$  and  $t_1$  are within  $\sim 3.3$  % and  $\sim 1.5$  %, respectively, of the measured values listed in Table 1. The static air gap height at the location of the laser beam spot defines the operation point of the sensor which in this case is very close to the point of maximum slope or maximum sensitivity of the transfer function [7]. Motions as small as tenths of nanometers can be resolved using this new extrinsic intensity-modulated optical interrogation method.

**Table 1.** Summary of measured parameters for the Fabry-Perot MOEMS displacement sensors shown in Fig.1.

| Beam Type | Length ( $\mu\text{m}$ ) | Width ( $\mu\text{m}$ ) | Etch-Hole diameter ( $\mu\text{m}$ ) | Air Gap @ spot ( $\mu\text{m}$ ) | Spot Location ( $\mu\text{m}$ ) |
|-----------|--------------------------|-------------------------|--------------------------------------|----------------------------------|---------------------------------|
| A         | 122.5                    | 4.25                    | -                                    | 2.84                             | 5                               |
| B         | 119.6                    | 8.17                    | -                                    | 2.66                             | 17.5                            |
| C         | 123.5                    | 9.31                    | 3.92                                 | 2.60                             | 17.5                            |
| D         | 118.5                    | 13.39                   | 5.56                                 | 2.62                             | 22.5                            |

## 4.2. Frequency Response

The experimental setup used for the determination of the frequency response of the MFPD sensors was described in Ref. [7] and it is presented schematically in Fig. 4. The optical measurement system detects the interferometric optical signal coming from the vibrating Fabry-Perot structure and transforms it into an electrical signal. This electrical signal is then processed to determine the relative deflection of the top mirror with respect to the bottom mirror of the MFPD at the frequency of excitation. The MFPD frequency response is determined by repeating this sequence for the different frequencies in the range of interest.

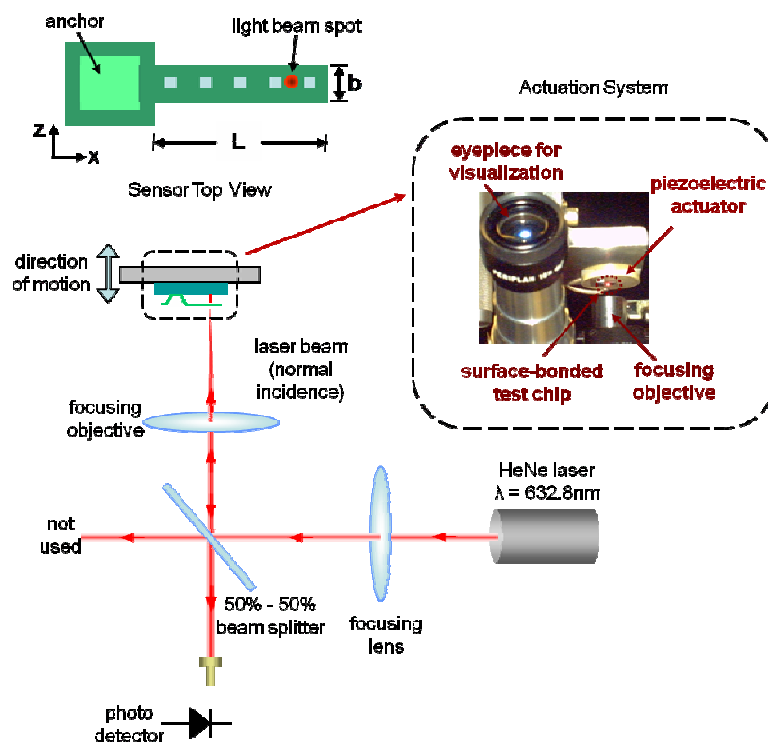


**Fig. 4.** Schematic of the optical setup for the measurement of the interferometric back-reflected light (MFPD sensor shown as mounted).

The experimental frequency response of all the MFPD cantilever beams listed in Table 1 and measured using the technique described above are shown in Fig. 5. These measured frequency responses were measured using a 10 nm amplitude harmonic excitation. The tests were performed at atmospheric pressure (14.7 psi) and room temperature (23 °C). Their average fundamental frequency is  $43.5 \pm 3$  kHz and their total viscous damping factor (mode 1) vary from 0.19 to 0.3. Also shown in this figure are these responses fitted to the analytical vibration mechanical model with the resonant frequency ( $f$ ) and the total viscous

damping factor ( $\zeta$ ) as fitting parameters. The excellent agreement between the experimental measurements and the analytical mechanical models suggests that air viscous damping is the dominant source of dissipation for these structures. For details in the analytical modeling the reader may refer to Ref. [7]. Furthermore, by decoupling the effects of squeeze-film and airflow damping, an array of MFPD microsensors will allow for the simultaneous detection of pressure and temperature in addition to displacement [22]. The primary means of viscous damping differentiation is the dependence of the viscosity and density of the air on temperature and pressure. By microfabricating an array of MFPD structures with different geometries, the air viscous damping effects can be modeled based on the height of the microcavities, resonant frequencies, and temperature and pressure of operation. Thus, successful decoupling of the damping coefficients will result in a sensitive sensor array capable of measuring both temperature and pressure in addition to displacement. Experimental verification of the use of the MFPD as a multifunctional sensor is underway.

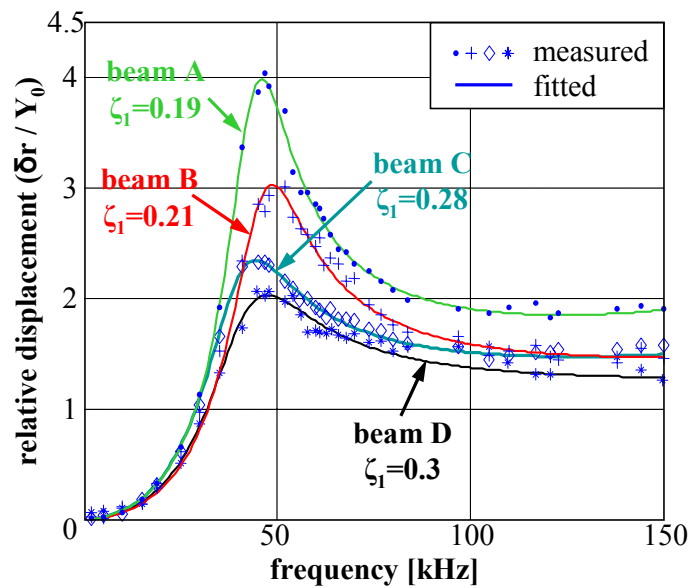


Fig. 5. Measured and fitted frequency response for all MFPD sensors listed in Table 1 [7].

## 4.2. Temperature Dependence

The mechanisms leading to temperature dependence of the MFPD frequency response are mainly due to (1) shift of the resonant frequency arising from the variation of the Young's modulus, density and coefficient of thermal expansion of the  $\text{Si}_x\text{N}_y$  film (2) variation of the take-off angle of the beam curling due to induced uniform stress (3) variation of the viscous damping coefficient due to variation of the density and the viscosity of the air, and (4) changes of the optical path lengths due to the coupled thermal-optical and photo-elastic effects [7].

For the MFPD type A depicted in Fig. 1, a variation of temperature from 23 °C to 600 °C causes a drift in the fundamental resonant frequency of about 6.1 %, which is much less than the 20 % drift reported for bridges in Ref. [23]. For the same MFPD, the take-off angle is  $\sim 5.7$  mrad. Neglecting the effects of stress gradients, the same temperature change produces a variation in the take-off angle of  $\sim 0.38$  mrad. This variant decreases the air gap height at the spot location by about 43 nm moving the point of operation of the sensor about 1.3 % and hence, decreasing the sensor's optical sensitivity [7]. However, if the temperature of operation of the sensor is known, both these effects can be corrected for.

Another mechanism that leads to sensor temperature dependence is the air viscous damping which depends on the viscosity and the density of the air, both of which are dependent on temperature. Fig. 6 shows the variation of the air viscous damping as a function of temperature for the FPMOD type A for the first two modes of vibration and at atmospheric pressure. It can be seen that the variation in viscous damping for a temperature varying from 23 °C to 600 °C is  $\sim 0.14$ . This corresponds to a decrease in relative displacement of  $\sim 2$  and hence, a decrease of sensor sensitivity around the fundamental resonant frequency. However, the same variation of temperature only corresponds to a small variation of the optical path length (around 2.27 nm) due to the coupled thermal-optical and photo-elastic effects. Fig. 7 shows that the effect of the temperature is less significant if the point of operation is close to the point of maximum sensitivity [7].

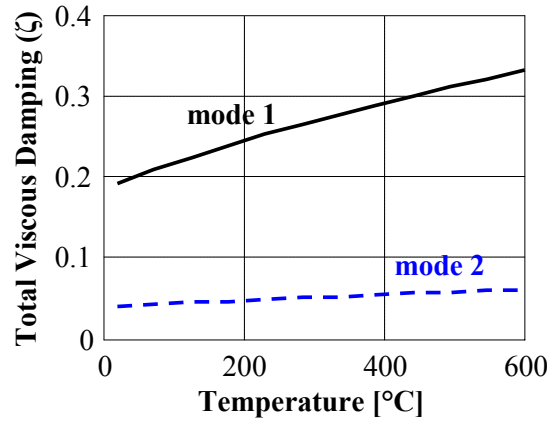


**Fig. 6.** Calculated temperature dependence of the total air viscous damping coefficient ( $n = 1, 2$ ) for MFPD type A.

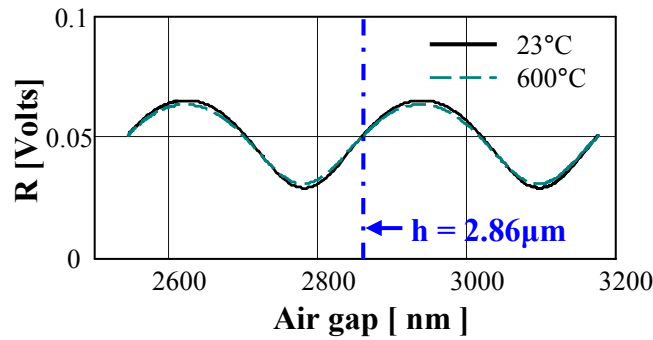


**Fig. 7.** Shift of the optical transfer function of the MFPD type A due to the temperature dependence of the optical path length.

The above results show that the sensitivity of the MFPD at high temperatures is mainly influenced by the effects of the thermally induced stress and the air viscous damping. Thermally induced stress can shift the operation point of the sensor, thus affecting the optical sensitivity, but it has a small effect on the variation of the optical path length. The significant effect that the temperature has on the air viscous damping reduces the overall sensitivity of the sensor, especially in regions around the fundamental resonant frequency. However, if the temperature is known, both of these effects can be compensated. A temperature-controlled sensor chamber is being designed to measure the effect of temperature in the frequency response of the MFPD cantilever beam at high temperatures.

Compared to standard interferometric techniques for the measurement of displacement (e.g.

stroboscopic and laser Doppler interferometers), the MFPD sensor needs neither a reference arm nor sophisticated stabilization techniques. Fig. 6 and Fig. 7 show that the power reflectance of the MFPD is a very sensitive measure of the air gap height. Using the solid MFPD cantilever beam type A, relative displacements as small as  $0.139 \text{ nm}/\sqrt{\text{Hz}}$  were measured [7]. Furthermore, the small size of the sensor, the materials in which it can be built, and its simple construction make it suitable for on-chip integration and ideal for high-temperature applications. Though the optical detection of the frequency response of the MFPD cantilever beam has been implemented for a bare sensor, our experimental results demonstrate the accuracy of the optical interferometric readout on the determination of the frequency response of any free standing micromechanical device at the wafer level. The very simple configuration offered by this optical interferometric system is being considered in the future for integration in the sensor package.

## 5. Conclusions

We have reviewed recent advances in MEMS sensors for harsh-environments focusing on fabricated devices. SiC and group III semiconductor materials such as AlN, are an excellent candidate for the development of MEMS and NEMS for harsh environments. The excellent physical properties of particularly SiC enables its operation in harsh environments (e.g. high temperature, high pressure, high g, radiation and biological or chemical corrosive media). Piezoelectric properties of AlN, and good optical properties of robust materials such as SiC and silicon nitride may allow the improvement of functionality, reliability and sensitivity of classical sensors giving the opportunity of building up on-chip smart systems with a high degree of processing control. The review of different SiC sensor technologies shows unambiguously that although all necessary technology steps are well developed for the fabrication of SiC based MEMS devices, major problems such as reliability, packaging, wiring, and integration issues have to be overcome before they can be manufactured and used reliably in commercial high temperature applications.

The adaptability, resistance to EMI and RFI and high sensitivity make MOEMS sensors ideal for applications in harsh environments. In the past few years, much progress has been made in the development of simpler processing techniques and simplification of MEMS sensing elements. A new Fabry-Perot MOEMS displacement sensor for HT applications was presented. Results show that the small influence of high temperatures on the sensitivity of this sensor offers advantages in terms of size, cost, and operation in high temperature applications. In addition, by microfabricating an array of MFPD structures with different geometries, successful decoupling of the damping coefficients will result in a sensitive sensor array capable of measuring both temperature and pressure in addition to displacement. Finally, the simple configuration of the optical detection system makes it ideal for integration in the sensor package.

## References

- [1]. J. Goetz, Sensors that can take the heat, *Sensors Magazine*, 20-38, June 2000.
- [2]. M. Mehregany, X. Fu and L. Chen, Silicon Carbide Micro/Nano Systems for Harsh Environment and Demanding Applications, *In Proceedings of the NSTI-Nanotech Conference 2006*, 3, pp. 471-474.
- [3]. D. Gao, M. Wijesundara, C. Carraro, R. Howe and R. Maboudian, Recent Progress Toward a Manufacturable Polycrystalline SiC Surface Micromachining Technology, *IEEE Sensors Journal*, 4, 4, 2004, pp. 441-448.
- [4]. C. Jacob, P. Pirouz, H. I. Kuo and M. Mehregany, High temperature ohmic contacts to 3C-Silicon Carbide Films, *Solid State Electronics*, 42, 12, 1998, pp. 2329-2334.
- [5]. R. C. Turner, P. A. Fuierer, R. E. Newnham and T. R. Shrout, Materials for High Temperature Acoustic and Vibration Sensors: A Review, *Applied Acoustics*, 41, 1994, pp. 299-324.

- [6]. D. Doppalapudi, R. Mlcak, J. Chan, H. Tuller, J. Abell, W. Li and T. Moustakas, Sensors based on SiC-AIN MEMS, *Electrochem. Soc. Proc.*, 6, 2004, pp. 287-299.
- [7]. P. Nieva, N. McGruer and G. Adams, Design and characterization of a micromachined Fabry-Perot vibration sensor for high-temperature applications, *J. Micromechanics and Microengineering*, 16, 2006, pp. 2618-2631.
- [8]. M. Haueis, J. Dual, C. Cavalloni, M. Gnielka, and R. Buser, A fully packaged single crystalline resonant force sensor, *J. Micromechanics and Microengineering*, 11, 2001, pp. 514-521.
- [9]. M. Suster, W. Ko and D. Young, An Optically Powered Wireless Telemetry Module for High-Temperature MEMS Sensing and Communication, *J. Microelectromechanical Systems*, 13, 3, 2004, pp. 536-541.
- [10]. S. Dakshinamurthy, N. R. Quick and A. Kar, Temperature-dependent optical properties of silicon carbide for wireless temperature sensors, *J. Physics D: Applied Physics*, 2007, pp. 353-360.
- [11]. M. Mehregany, C. A. Zorman, SiC MEMS: opportunities and challenges for applications in harsh environments, *Thin Solid Films*, 355-356, 1999, pp. 518-524.
- [12]. R. Nowak, M. Pessa, M. Suganuma, M. Leszczynski, I. Grzegory, S. Porowski, and F. Yoshida, *Applied Physics Letters*, 75, 1999, pp. 2070.
- [13]. R. Okojie, G. Beheim, G. Saad and E. Savrun, Characteristics of a Hermetic 6H-SiC pressure sensor at 600 °C, In *Proc. of the AIAA Space 2001 Conference and Exposition, Albuquerque, NM*, 2001, pp. 1-8.
- [14]. C. Wu, C. Zorman and M. Mehregany, Fabrication and Testing of Bulk Micromachined Silicon Carbide Piezoresistive Pressure Sensors for High Temperature Applications, *IEEE Sensors Journal*, 6, 2, 2006, pp. 316-324.
- [15]. A. Atwell, R. Okojie, K. Kornegay, S. Roberson and A. Beliveau, Simulation, fabrication and testing of bulk micromachined 6H-SiC high-g piezoresistive accelerometers, *Sensors and Actuators A*, 104, 2003, pp. 11-18.
- [16]. D. J. Young, J. Du, C. Zorman and W. Ko, High-Temperature Single-Crystal 3C-SiC Capacitive Pressure Sensor, *IEEE Sensors Journal*, 4, 2004, pp. 464-470.
- [17]. L. Pakula, H. Yang, H. Pham, P. French and P. Sarro, Fabrication of a CMOS compatible pressure sensor for harsh environments, *J. Micromechanics Microengineering*, 14, 2004, pp. 1478-1483.
- [18]. E. Eklund and A. Shkel, Factors affecting the performance of micromachined sensors based on Fabry-Perot interferometry, *J. Micromechanics Microengineering*, 15, 2005, pp. 1770-1776.
- [19]. N. Xiao-qi, W. Ming, C. Xu-xing, G. Yi-xian and R. Hua, An optical fibre MEMS pressure sensor using dual-wavelength interrogation, *Meas. Sci. Technol.* 17, 2006, pp. 2401-2404.
- [20]. W. Wang, R. Lin, D. Guo and T. Sun, Development of a novel Fabry-Perot pressure microsensor, *Sensors and Actuators A*, 116, 2004, pp. 59-65.
- [21]. R. A. Buser and N. F. De Rooij, Resonant Silicon structures, *Sensors and Actuators A*, 17, 1989, pp. 145-154.
- [22]. P. M. Nieva, G. G. Adams, N. E. McGruer, Design and modeling of a multifunctional MEMS Fabry-Perot sensor for the simultaneous measurement of displacement, pressure and temperature, In *Proc. of Sensors and Smart Structures Technologies for Civil, Mechanical, and Aerospace Systems 2007*, San Diego, CA, USA, Vol. 6529, 2007, p. 23.
- [23]. M. Fonseca, J. English, M. von Arx and M. Allen, Wireless Micromachined Ceramic Pressure Sensor for High-Temperature Applications, *J. Microelectromechanical Systems*, 11, 2002, pp. 337-343.

## Healthcare for the Healthy People: Miniaturization, Sensing and Actuation Trends and Needs in Preventive and Predictive Medicine

**Alberto SANNA, Marco NALIN, Riccardo SERAFIN**

e-Services for Life & Health, Scientific Institute H. San Raffaele,  
via Olgettina 60, 20132, Milan – Italy,  
Tel.: 02 2643 2919, fax: 02 2643 3997

E-mail: [alberto.sanna@hsr.it](mailto:alberto.sanna@hsr.it), [marco.nalin@hsr.it](mailto:marco.nalin@hsr.it), [riccardo.serafin@hsr.it](mailto:riccardo.serafin@hsr.it)  
[http://www.fondazioneosanraffaele.it/EN\\_home/](http://www.fondazioneosanraffaele.it/EN_home/)

*Received: 7 September 2007 /Accepted: 19 September 2007 /Published: 8 October 2007*

---

**Abstract:** In modern medicine the role of prevention and prediction is acquiring an increasing market share, due to augmented awareness and interest of the population toward these issues, and to the recognition by public bodies that investing on prevention will be the only mean to afford economical sustainability in the future.

Prediction must rely on the dynamic collection of several personal information, not only about the physical condition of the individual, but also about his/her behaviors and the environmental conditions.

Prevention will increasingly imply the ability to modify the detected behaviors. However, monitoring these parameters and acting in response to undesired conditions requires a constant presence in people's everyday life.

The target population for these services is healthy people that possibly won't spend too much in terms of time or money in invasive or costly solutions. For these reasons, we foresee an emerging role for sensing and actuation technologies able to provide miniaturization, pervasiveness and low costs.  
*Copyright © 2007 IFSA.*

**Keywords:** Prevention, Preventive medicine, Predictive medicine, Environmental monitoring, Personal monitoring.

---

## **1. Introduction**

In modern medicine the role of prevention and prediction is acquiring an increasing market share, on one side due to augmented awareness and interest of the population toward these issues, on the other due the recognition by public bodies that investing on prevention will be the only mean to afford economical sustainability in the years to come. To be effective, prediction must rely on the dynamic collection of several personal information, not only about the physical condition of the individual, but also about his/her behaviors and the environmental conditions in which such behaviors are enacted. Prevention will increasingly imply the ability to modify the detected behaviors, actuating both on the environmental conditions and the people life styles. However, monitoring these parameters and acting in response to undesired conditions requires a constant presence in people's everyday life.

This article will provide an overview of the actual trends in preventive and predictive medicine, to allow the reader to understand the potentialities that the healthcare market offers for the sensors and transducers industry.

Then a model of the individual as a complex and dynamic entity will be proposed, divided in exogenous and endogenous determinants of the individual's health status, as a rationale to explain also the complexity of monitoring the individual's vital sign, his daily activities and the environments he lives in.

Finally some application scenarios taken from the Angel [1, 2] European research project will be presented.

## **2. Prevention and Prediction in Modern Medicine**

The modern medicine, in addition to its traditional action fields in the cure and rehabilitation, is more and more oriented toward the development of a preventive and predictive medicine, and the therapy evolves rapidly from a generalized therapy practice to a personalized therapy practice.

This important change of perspective answers to the aspiration toward health protection and a more efficient and effective diseases care. These goals are more and more concrete, thanks to the innovations in the biomedical research, in particular in the genetic sector. Indeed, the comprehension of the molecular mechanisms at the base of the diseases and the mechanisms of transmission of the genetic heritage, environmental factors and reaction to drugs allows more and more to pursue three important objectives:

1. Definition of the diseases risk factors in healthy people;
2. Adoption of lifestyles (with particular reference to nutrition, to life and job environments and to the correct use of the right devices for mental and physical exercises) that allows, on a personalized base, to avoid the rise of diseases in healthy people, but genetically predisposed (primary prevention), and also to avoid the rise of complications in ill people (secondary prevention). It is known nowadays that extra-genetic factors (lifestyle, environment, nutrition...) can influence for more than 50% in avoiding the diseases;
3. Personalization of the therapy on the basis of the major or minor probability of the response to the therapy itself of different persons, affected by the same pathology.

“The Health Systems must nowadays face the commitment to maintain and improve their capacity of offer, performances and services, based on efficiency criteria, effectiveness and quality to lower the costs of the system and to maximize the added value.”[3]

The national health expenditure is raising quickly all around the world: the incidence on the Gross Domestic Product is 9% for Europe and 14% for USA, and the increase of just the hospitals costs from 1989 to 1996 has been of 246% for Germany, 213% for France, 170% for UK and 150% for Italy[3]. These trends are bringing a serious crisis in all national healthcare systems.

The improvement of the diagnostics technologies allows a more and more accurate, personalized and complete definition of the individual risk profile and of the most effective therapeutic conditions or lifestyles. This knowledge must be available to the person during his daily life.

Convergence of the Information and Communication Technologies always sustained by the multimedia information digital management and by the Internet, makes increasingly available and convenient a lot of communication “channels” able to reach the person. The digital terminals, the big and complex computers of some years ago, are more and more present in our daily life, are miniaturized, can be held in one’s pocket, and are embedded in every kind of device that we use, making everything digital and interactive: the mobile phone, the television, the radio, music players, displays (embedded by now everywhere, from the household appliances to the car, from the supermarket carts to the vending machines, from the digital kiosk in the shops, work place, schools etc.). We live in an ecosystem of terminals and devices, personal or shared that ensure and will ensure more in the future, a continuous connection to access and share information, multimedia messages, texts, audio, images, movies, etc.

Together with the terminals, a fast evolution has been registered also in:

- the graphics of multimedia quality of the interfaces, that makes simpler, more intuitive and more user friendly the use of these technologies;
- the quality and spreading of digital devices, supplied with a wide collection of sensors, both of medical nature and, more in general, connected with the person and his activities in the daily life, with lower costs, more and more “invisible”, and in constant communication through wireless connections.

At the same time, knowledge management information technologies allows to store, extract and distribute information and multimedia contents that are rich, complex and personalized. The contents are automatically filtered, assembled and distributed considering the addressee’s characteristics and the interests (the user profile), the relevance of the concepts (semantic engines, information extraction systems), and the coherency with the context in which the person is acting (through the data coming from sensors on the person or in the ambient). In a word our life style, for what concern information access, is more and more individual and digital: we are immersed in environments able to interact with us and helping us to select, among a lot of available information, the ones that are specific, suitable and useful for us in that moment. This context creates progressively optimal condition that allows the citizen the access to relevant and comprehensible information about everything regarding his personal wellness and so to raise the individual awareness.

### **3. Complexity of the Individual**

The “person” as an entity, is much more complex than a set of data stored in a database. It is defined not only by its personal data, personal history, and family history, but also by his culture, his behaviors and his choices in everyday life. The lifestyle is chosen by the person on the basis of his education, his attitude to follow certain behaviors and the particular context in which a decision must be taken.

In particular, as described in Fig. 1, the individual can be mapped in a 3 dimensions schema:

- Genetic factors: how the person is made-up. In this dimension we can include the real “genetic” information that includes for example his attitude toward a particular disease, the metabolism, how the body reacts to diets and drug therapies etc. But also in a wider sense all the characteristics that a person has since his birth or acquires during his life, like allergies, intolerances, chronic diseases (diabetes, heart failure...), etc.
- Behavior factors: how the person acts. Each person has its own culture, beliefs, education, motivation etc, that is the base on which he measures all its experiences and takes daily decisions. Lifestyle factors include also how the person is in a particular moment, and it is determined by a lot of very variable factors. Let’s think for example to the mood, and how well (better drug compliance, better diet compliance...) or badly (anxiety, depression...) it can influence our life. But also the quantity or quality of our eating and drinking, the sleeping quality, the physical activity etc.
- Environment factors: where the person is. The particular context in which a person is can drastically influence his health status and risk profile. Many of these factors are out of the control of the person, and are determined by the physical and social environment. Several studies investigated how the environmental agents can influence the health of a person. For example the temperature and humidity in relation to viruses and bacteria diffusion, but also the air conditioning that is a major cause of obesity [4], or the light management not only for eye safety, but also for treatments of seasonal affective disorders [5, 7] or depression [6]. Besides the physical environment, the individual is involved also in daily social dynamics (family, work place, traffic, school, friendships, neighborhood ...) that can influence directly emotional state too, and so indirectly health status.

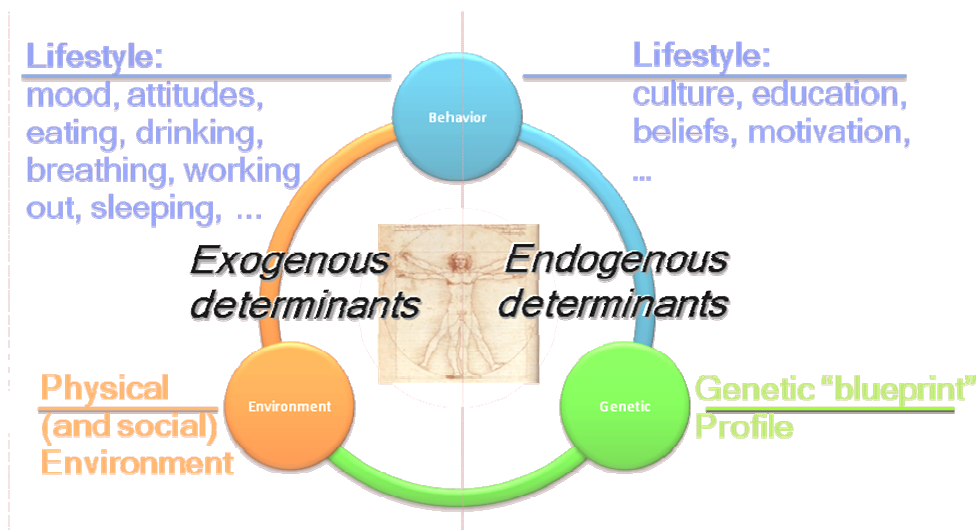


**Fig. 1.** Exogenous and Endogenous determinants.

Some of the described factors, that we can call “Endogenous determinants”, are part of the individual itself and are taken as fixed, with the only exceptions of the children that are still building their own education and culture, and may be at risk for future chronic diseases, but actually healthy. These factors can be just acquired from a system and used as a base to provide suggestions and support.

Other factors, that we can call “Exogenous determinants”, are related to the interaction of the person with the external world, so his lifestyle, his interaction with the environment or his interaction with social groups. On these kinds of factors, it is not only possible to monitor, but also to take some action (i.e. helping the person to increase the physical activity with a step counter etc.).

The division between exogenous and endogenous determinants is shown in Fig. 1. In the field of the “Exogenous determinants”, we can deeper analyze the relation of the individual with the physical environment, as described in Fig. 2. In this way five macro categories can be described:

- Air: considering both the air inhaled by the person (in-take) and the air in contact with skin and eyes (out-take)
- Materials: considering both the materials that may enter in some ways inside our body (in-take), like detergents, paints etc, and the materials that comes in contact with our body (out-take), like furniture, toys, textiles...
- Products: considering both the products that we eat and drink (in-take) and the products that come in contact with our body (out-take), like cosmetics, products for personal hygiene etc.
- Water: considering both the water that we drink and we use to cook (in-take) and the water that we use to wash up (out-take).
- Spectrum & Bio: these two categories have been merged because they represent all the factors to which we are exposed, and most of times they are both outside and inside our body. For example electromagnetic waves, radiations, light, acoustic noise, microbes, allergens etc.

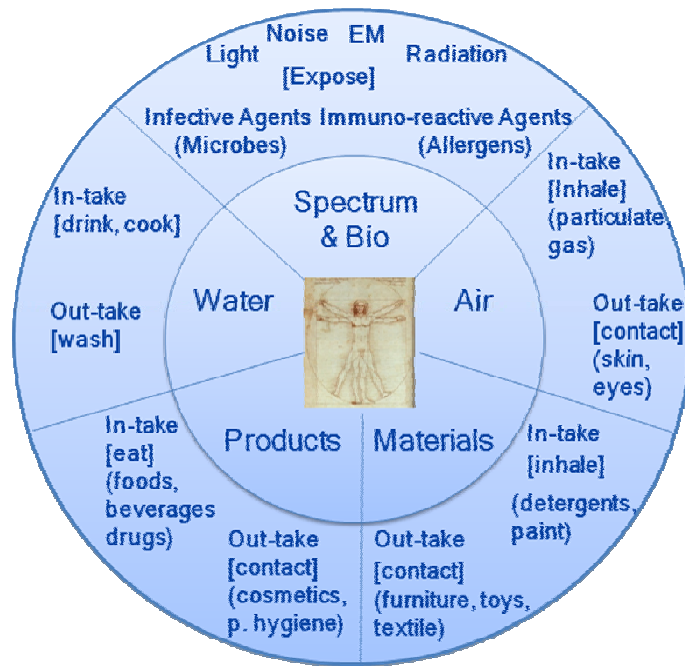


**Fig. 2.** Interaction between the Individual and the Environment.

#### **4. Complexity of Monitoring**

The above described complexity of the individual is directly mapped in a complexity of the monitoring that should be performed over the individual (and over the environments he lives in), in order to provide added value services and support to follow healthier lifestyles.

Modern technology allows preventive monitoring and personalized guidance for people to reduce and manage their own risk of developing some serious diseases (like cardiovascular and metabolic) and to detect disease onset at an early stage. The prevalence of obesity, hypercholesterolemia, hypertension, sedentary lifestyle and type II diabetes, which are increasing across Europe at unsettling rates

especially among young people, have alarmed and become a matter of major concern for public health and health care authorities, health experts, the media and the society. This problem brings up a high degree of complexity both in its scientific and technological dimensions, demanding a multidisciplinary approach for the definition and development of effective and acceptable solutions for a wide range of the public.

The most advanced and innovative interaction technologies are opening new modes and communication channels with the user: a) natural interfaces; b) new virtual scenarios or spaces; c) collaborative web experiences and peer production & support; d) novel home entertainment enhanced devices; e) adaptive smart mobile devices; and f) interactive digital TV, mobile TV and public broadcasting systems.

The new monitoring paradigm must rely on the Ambient Intelligence concept. In an Ambient Intelligence environment it is a must to provide new innovative interaction and communication modalities that relate seamlessly and naturally with the user and react to his needs automatically. The risk management environment should include the flavours of a comprehensive, intensive and unobtrusive interface that adapts itself learning from the same interaction with the different users. The novel concept of ambient intelligence user interface based relies on five principles: a) Multi-modality; b) Nomadic behaviour; c) Gradual adaptation; d) Active learning and e) Natural interaction.

In this line, a new approach of developing interfaces that are actively learning must be pursued. This means to embed in user interfaces various observation mechanism in order to collect information about users' interaction with the system. Such information can be processed in order to enhance the adaptation of the user interface and to anticipate users' actions, improving continuously the interaction between the user and the system.

It is important to build an unobtrusive and non-invasive environment for the individual to perceive that the proposed services are part of his normal life, reducing his possible rejection and enabling a wider range of possible business models, based on the intensive usage and integration of consumer electronics. This means taking profit of the multiple and diverse offers of interaction devices available in the market, well-known and appreciated by the target population.

In this new vision of healthcare, it will become crucial to integrate and adapt common consumer electronic products (video-games consoles, Digital TV, PC, mobile devices, etc) creating a customizable environment that can be configured by the user, just fulfilling a basic set of minimum requirements, to fit his needs, preferences and possibilities.

This adaptation of user interaction devices will be done using innovative technologies that improve the user experience, such as the use of last generation interactive video game consoles to promote physical activity, voice recognition techniques for natural interaction between the system and the user, etc.

The necessity of data collection from the person and from the environments, and the necessity of actuation of some action must be matched with the willingness of healthy people of not being invaded by complex devices, both in terms of configuration and use. From this, the requirements of miniaturization, power saving, seamless interaction, and "invisibility" of the devices, sensors and actuators deployed by the system.

In this Ambient Intelligence for healthcare perspective, sensors are seen as personalized consumer service enablers, in particular for:

- Food Processing Control (Nutrients & Toxic Agents management);

- Food/Beverage Consumption (Nutrients and Energy Intake management);
- Physical Activity (Energy Consumption and Physical Aging management);
- Enhanced Interactivity for Multimedia Content Management (Motivation Stimulation and Cognitive Aging management);
- Smart Interactive Toys & Educational Videogames (Education);
- Indoor Temperature Management (Metabolism & Green Buildings) and Light Management (Mood & Green Buildings);
- Smart Textile (Physiology, Behaviour, Psychology, Socialization).

The market previsions for the sector of wireless technologies, sensors and MEMS/NEMS actuators in healthcare are very optimistic for the next years. The market of wireless technologies in healthcare in the US alone was valued in 2005 at USD 1,8 billion and it is expected to grow to reach USD 7,3 billion in 2010 [8]. If in the analysis we include also the consumer market for healthy people, enabling wellbeing services, it became clear what potential the healthcare sector will offer in the near future.

## 5. Application Scenarios

Wireless sensor networks (WSNs), and in particular body sensor networks (BSNs), promise to enhance quality of life in common human habitats. In this context, application requirements have a strong impact on the WSN architecture, network protocols and even node type and number. The Angel project (ANGEL – *Advanced Networked embedded platform as a Gateway to Enhance quality of Life*, FP6 IST-5-0033506, [1]) aims at providing methods and tools for building complex WSN-based applications in which functional requirements, security aspects, hardware constraints and network interactions are taken into account at early stages of the design flow (Fig. 3). The purpose of the Angel project is to develop and implement new methodologies and tools to create such applications.

The use of networking systems in health-related applications is not new [9, 10] and it is one of the strategic objectives of the European Framework Programs [11]. However, without a deep investigation on the design issues of the involved embedded systems, it may be difficult to develop cost-efficient, reliable, secure and scalable applications.



**Fig. 3.** Angel Platform Usage Scenario.

In the Angel project three scenarios [2] highlighting how a WSN (composed both by sensors and actuators) can really improve the quality of life have been designed:

- 1) “Personalized Indoor Environmental Monitoring & Control for wellbeing”: The first scenario describe an Ambient Intelligence application, with the house of the user monitored, remotely controlled and automatically customized on the user needs and habits. The house is just an example, but the Angel platform can be deployed also in workplaces, schools, etc. All the agents around the person described in Fig. 2 are constantly monitored by the system that will apply some dynamically calculated rules based on the data collected. Indeed, the actuation mechanisms are not static, but will be calculated by the system based on the profile and preferences of the user (or of the users) living in that environment.
- 2) “Post-acute and chronic disease management”: The second scenario highlight how the Angel system can impact on the hospitalization costs, reducing the time a patient need to spend in the hospital in order to recover for post-acute episodes or for chronic diseases. In the scenario, thanks to a set of sensors that the person can wear, some parameters are monitored by the System and eventually (if it is the case) also from an operator in a remote Service Centre. The system is able to detect emergency situations (i.e. fall detection, heart attack detection...) and is able to communicate the alarm to the hospital (both of the problem and of the user position and condition) through a reliable connection. For rehabilitation also smart wound dressing sensors are foreseen in order to better monitor the recovery of the lesion. This scenario shows how such system can empower the unpaired patients (temporary or permanently) to have a normal life.
- 3) “Personal wellness and related enabling services”: The third scenario shows how the same architecture of the second scenarios can be deployed, with less criticality, also to healthy people to enhance the quality of their life. In the scenario a healthy family is described, with two members of the family doing regular physical exercises, the son in order to lose weight in combination with a prescribed diet, and the father just to improve his physical performances. The two are remotely in contact respectively with a physician and a personal trainer that supports them by monitoring their exercises. The mother uses the same system, but in order to control her stress level and sleep quality, and the environment tries automatically to adapt to create the best condition for her to sleep. Finally another application of the system is related to the skin health by monitoring the UV exposure and skin humidity.

The scenarios are designed to provide an overview of what the Angel system can do, and the Angel platform has been designed in order to support all these service and potentially any other service, thanks to its re-configurability, scalability and re-programmability. Some of these applications can be found also as a commercial solution, however the innovation of the Angel platform is the creation of a unique System able not only to support all these services, but also to allow the design of new services in the future, thanks to new sensors and actuators more and more available in the market.

## **6. Conclusions**

Sensors, actuators and wireless technologies in general have seen a significant increase of application in the healthcare sector in the last years, however most of the potentialities of this sector are still unexploited. Recent medical literature and some of the examples we have presented in this article, demonstrate the needs to introduce new monitoring and actuation paradigms, in order to fully exploit the multidimensional personal profile previously presented to provide personalized support both to ill and healthy people. In our vision, in fact, the key for a wider success is to target not only the healthcare sector, but also the wellness sector with the same concepts but with solutions designed for the healthy people, focusing on miniaturization, pervasiveness, usability and low costs. With the same investment will then be possible to reach both the wider consumer market, and the healthcare market,

if the ability to adapt the designed solution also to critical situation, assuring the necessary reliability and quality of service, is retained. The creation of a unique, customizable, and dynamically configurable architecture, able to support a broad range of services, like the one proposed by the Angel project, allows the reduction of costs, the speed-up of the time to market and the decoupling of the dependencies between sensors/devices producers and service providers.

## References

- [1]. Angel Project, Advanced Networked embedded platform as a Gateway to Enhance quality of Life FP6 IST-5-0033506, <http://www.ist-angel-project.eu>
- [2]. M. Nalin, P. Garino, E. Alessio, A. Bragagnini, F. Fummi, G. Perbellini, D. Quaglia, S. Cailotto, L. Cyra, J. Górski, A. Jarzębowicz, J. Miler, M. Olszewski, M. Piechówka, M. Decandia, M. Cristaldi, A. Willig, J. Hauer, A. Huebner, H. Baldus, M. de Gouw, A. Neelen, and J. Bruynen, ANGEL Deliverable D1. 1 – Definition of the ANGEL Platform, January 2007.
- [3]. C. Ruta, Ai Confini della Medicina. Cultura d'Impresa, Egea, 2006.
- [4]. D. Allison, Air-con and lack of sleep promote obesity, In *International Journal of Obesity*, (DOI, pp. 10. 1038/sj. ijo. 0803326), June 2006.
- [5]. Direct brain serotonin measurement validates Light therapy for SAD, In *The Lancet*, Dec. 7, 2002, p. 1840.
- [6]. Lam R. W. Morning light therapy for winter depression: predictors of response, *Acta Psychiatr Scand*, 89, 1994, pp. 97-101.
- [7]. A. Neumeister, N. Praschak-Rieder, B. Besselmann, M. L. Rao, J. Gluck, S. Kasper, Effects of tryptophan depletion on drug-free patients with seasonal affective disorder during a stable response to bright light therapy, *Arch Gen Psychiatry*, 1997, 54, pp. 133-138.
- [8]. Wireless Opportunities in Healthcare, *Kalorama Information*, January 2007.
- [9]. J. Bardram, Hospitals of the future-ubiquitous computing support for medical work in hospitals, In *Proceedings of the 2<sup>nd</sup> International Workshop on Ubiquitous Computing for Pervasive Healthcare Applications (UbiHealth' 03)*, 2003.
- [10]. V. Shnayder, B. Chen, K. Lorincz, T. Fulford-Jones, M. Welsh, Sensor Networks for Medical Care, *Harvard University Technical Report TR-08-05*, April 2005.
- [11]. <http://www.hitechprojects.com/euprojects/myheart>

---

2007 Copyright ©, International Frequency Sensor Association (IFSA). All rights reserved.  
(<http://www.sensorsportal.com>)



### Universal Frequency-to-Digital Converter (UFDC-1)

- 16 measuring modes: frequency, period, its difference and ratio, duty-cycle, duty-off factor, time interval, pulse width and space, phase shift, events counting, rotation speed
- 2 channels
- Programmable accuracy up to 0.001 %
- Wide frequency range: 0.05 Hz ...7.5 MHz (120 MHz with prescaling)
- Non-redundant conversion time
- RS-232, SPI and I<sup>2</sup>C interfaces
- Operating temperature range -40 °C...+85 °C

## Global Environmental Micro Sensors Test Operations in the Natural Environment (GEMSTONE)

**Mark ADAMS, John MANOBIANCO and Matthew BUZA**

ENSCO, Inc 4849 North Wickham Road, Melbourne, FL, 32940, USA

Tel.: (321) 775-7568

E-mail: [adams.mark@ensco.com](mailto:adams.mark@ensco.com)

<http://www.ensco.com>

*Received: 7 September 2007 /Accepted: 19 September 2007 /Published: 8 October 2007*

---

**Abstract:** ENSCO, Inc. is developing an innovative atmospheric observing system known as Global Environmental Micro Sensors (GEMS). The GEMS concept features an integrated system of miniaturized *in situ*, airborne probes measuring temperature, relative humidity, pressure, and vector wind velocity. In order for the probes to remain airborne for long periods of time, their design is based on a helium-filled super-pressure balloon. The GEMS probes are neutrally buoyant and carried passively by the wind at predetermined levels. Each probe contains on-board satellite communication, power generation, processing, and geolocation capabilities.

ENSCO has partnered with the National Aeronautics and Space Administration's Kennedy Space Center (KSC) Weather Office for a project called GEMS Test Operations in the Natural Environment (GEMSTONE). The goal of the GEMSTONE project was to build and field-test a small system of prototype probes in the Earth's atmosphere. This paper summarizes the 9-month GEMSTONE project (Sep 2006 – May 2007) including probe and system engineering as well as experiment design and data analysis from laboratory and field tests. These tests revealed issues with reliability, sensor accuracy, electronics miniaturization, and sub-system optimization. Nevertheless, the success of the third and final free flight test provides a solid foundation to move forward in follow on projects addressing these issues as highlighted in the technology roadmap for future GEMS development.  
*Copyright © 2007 IFSA.*

**Keywords:** Environmental sensors, Atmospheric profile, Buoyant probe

---

## **1. Introduction**

Originally proposed in mid 2000, the Global Environmental Micro Sensors (GEMS) concept leverages technological advancements in micro and nanotechnology for the design and development of a new atmospheric in situ observing system. The initial idea was to deploy large numbers ( $> 10,000$ ) of low-cost, disposable probes as small as 50-100 microns in one or more dimensions. Miniaturizing the electronics and other probe components to dust-sized dimensions was based on realistic projections following Moore's law [1] and recent efforts with so-called "Smart Dust" [2]. At these sizes, the probes would have very small terminal velocities and be lightweight enough to pose virtually no threat to people or property including aircraft. ENSCO, Inc. has been defining and studying the major feasibility issues and enabling technologies for the GEMS system through various internally and externally funded projects since 2001.

During the course of a multi-year study on the GEMS system for the National Aeronautics and Space Administration (NASA) Institute for Advanced Concepts (NIAC; <http://www.niac.usra.edu>), the original idea to pursue miniaturization of the entire probe toward the micron-size was modified based on communication, power, and terminal velocity requirements [3]. First, radio frequency (RF) communication with probes of this size is not practical over the distances of at least several kilometers because their linear dimensions are too small in comparison with radio wavelengths. Second, power generation using solar energy requires areas on the order of hundreds of square centimeters which is impractical with dust-size devices. The final design trade-off favoring larger devices was the requirement to maximize the time probes remain airborne, which is best achieved using a self-contained, super pressure balloon filled with helium to make it neutrally buoyant (i.e. with zero terminal velocity). Although micro-scale devices could be designed to have terminal velocities less than  $10 \text{ cm s}^{-1}$ , they would still fall out of the air in hours to days depending on the altitude where they were released.

When the two-year NIAC phase II project was completed in August 2005, ENSCO began developing GEMS prototypes using commercial-off-the-shelf components as part of internal research efforts. In January 2006, ENSCO and the National Aeronautics and Space Administration (NASA) Kennedy Space Center (KSC) Weather Office responded to a solicitation for dual-use projects implemented through the KSC Technology Transfer Office Innovative Partnerships Program (IPP). The project funded by the IPP was called the GEMS Test Operations in the Natural Environment (GEMSTONE). The goal of the GEMSTONE project was to build and field test prototype probes in the natural environment of the Earth's atmosphere.

The current GEMS super pressure balloons are neutrally buoyant and carried passively by the wind at various predetermined levels in the atmosphere with some perturbation in altitude due to internal heating/cooling and turbulence. Each probe is self-contained with a power source to provide sensing, data processing, geolocation, and communication functions. The probes use one-way RF communication with low-earth orbiting satellites which relay data to ground stations. Each probe contains a micro global positioning system (GPS) unit for accurate wind velocity measurements and micro electro mechanical system sensors for pressure, temperature, and moisture measurements. These sensors are similar to the ones used in dropsondes and radiosondes so GEMS probes can achieve the same measurement precision and accuracy as commercially available instruments. The measurement and communication frequencies can vary within certain limits depending on the specific application.

This paper summarizes key aspects of the GEMSTONE project and is organized as follows. Section 2 describes the GEMS probe and system engineering while Section 3 focuses on data analysis from different laboratory and field tests conducted during the project. Section 4 concludes with a summary and roadmap for future system development.

## **2. Probe and System Engineering**

### **2.1. Mechanical Design**

The GEMS probe features a helium-filled super pressure balloon that is designed to maintain a constant volume when inflated to maximum capacity at sea level pressure. Except for the sensor board, the remaining electronics were initially encapsulated within the helium-filled probe shell. The shell is constructed by placing two pieces of DuPont Mylar™ GL-AE clear film together using Clifton Adhesive HSC-2996 heat sealing glue. A plastic valve is affixed to one side of the balloon with a combination of heat sealing glue and rubber cement. The seams are then heat rolled and pressed to meet glue manufacturer's suggestion of 180 - 240 °C cure temperature. Gore and Tetra designs were considered where multiple pieces of material are attached in an overlapping fashion and then sealed at the top and bottom. However, a face-to-face design was chosen to minimize the number of seams (and potential failure points) as well as lower weight requirements.

When inflated the balloon is pumpkin-shaped measuring ~1.2 m in width by ~0.6 m in height. Initial tests showed that when the electronics were housed within the balloon, the probe was prone to leaking at the seam where the sensor cable passed through shell material. Therefore, the decision was made to place the electronics below rather than inside the balloon. This design modification maintains the integrity of the helium-filled probe but still protects the electronics from water. The electronics are attached to the bottom of the balloon using a separate piece of shell material with adhesive after inflation and prior to launch (Fig. 1). The antenna boards are positioned at the edges of the material and secured from slipping below the electronics package which would obstruct them from transmitting and receiving signals during flight. The sensor board and cable pass through a small opening in the extra shell material so that they are suspended 2-3 cm below the probe and exposed to the free atmosphere during flight.

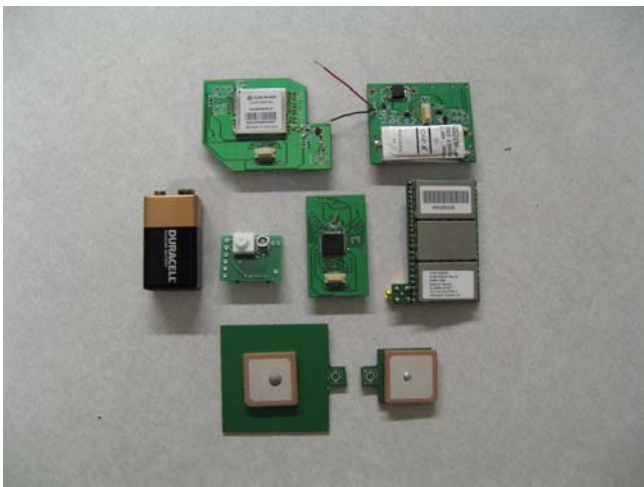
Based on buoyancy calculations, the balloon can lift a 170-gram payload when fully inflated with helium at sea level pressure and temperature in east central Florida. The level of neutral buoyancy can be adjusted using an approximate density profile from a nearby radiosonde to estimate the changes in lift with increased mass. During flight, the level of neutral buoyancy is expected to vary several 100 meters due to horizontal/vertical variations in air density and radiative heating/cooling of the helium inside the balloon.



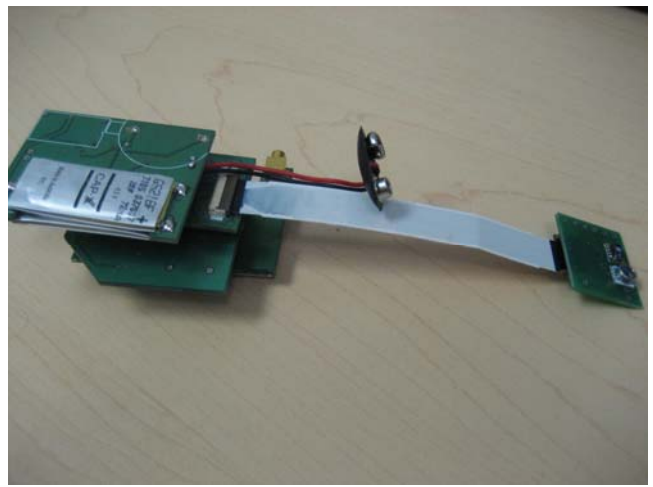
**Fig. 1.** The GEMS probe prior to deployment for the first successful free flight test. Note the electronics mounted on the bottom of the probe with the sensor board hanging below the balloon.

## 2.2. Electronics Design

The electronics package for the GEMS system was designed to be very modular so that hardware and/or software capability could be easily added or removed depending on changing requirements and applications (Fig. 2a). The sensor board has been configured as a switch to activate the electronics once it is plugged into the system. As soon as the electronics are powered up, the system will transmit data at pre-determined time intervals that are software configurable. Each board has a male-female vertical connector that allows the electronics system to be stacked (Fig. 2b). A thin ribbon cable connects the microcontroller board to the sensor board. This cable is passed through the Mylar™ shell material. When completely assembled, the electronics stack weighs ~60 gm with the antenna boards and connector cables adding ~40 gm. The total system payload weighs between 130 - 145 grams depending on the power source as described in section 0.



(a)



(b)

**Fig. 2.** (a) Complete GEMS electronics system with 9-volt battery included for scale. The modules shown from left to right and top to bottom are the global positioning system (GPS), power, sensor, microprocessor, satellite communication (SATCOM), SATCOM antenna, and GPS antenna boards, respectively (b) Complete electronics stack assembled including sensor board cable that passes through the shell material.

### 2.2.1. Power System

The GEMS power board was designed to house primary and secondary power systems. The primary power source is either a standard 9-volt (9V) battery or a 9V thin film solar panel. The decision to use solar cells or batteries depends on requirements for flight duration and time of day as well as frequency of data acquisition primarily related to satellite communications.

The secondary power system consists of two rechargeable Powerstream LIR2450 lithium coin cells. The batteries are connected in series and supply 7.2 V of backup power during night time and cloudy conditions. Two 3.6 V 120 mAh batteries connected in series provide the necessary 5 V required for satellite communication (SATCOM) transmissions during cloudy and night time conditions. The coin cells are used only in conjunction with the solar panels. A microprocessor controls the coin cell recharging circuit. During the day time, the coin cells are constantly charging in order to store energy for night time transmission and supply 120 mAh so the system has enough power to transmit for 5 hours at 15-minute transmission intervals. The solar/coin cell system relies on cycling GPS sleep states to conserve power for night time transmission as discussed in section 0.

The SATCOM transmissions are not powered directly by the batteries or solar cell but from two super capacitors connected in parallel at 5 V and 3.2 Farad (F) capacitance. The super capacitors can source up to 10 amps at 5 V for less than a second. This high current output is needed on quick demand from the SATCOM module. Tests conducted with a standard, plug-in power supply showed that during power cycling, an average of 9 mAh was needed at 15-minute intervals. The current system does not employ power cycling due to the GPS module (section 0) and averages 65 mAh during 15-minute transmissions. The system can maintain this average current with a 9V battery or solar cells in full sun.

### **2.2.2. Microprocessor**

The microprocessor board regulates the GEMS probe and uses a Texas Instruments msp430 microcontroller. The processor controls the timing, data acquisition, SATCOM, and power cycling. Included on the microprocessor board is an operational amplifier to read in the pressure sensor data. All other data are acquired through serial communication ports. Additional analog-to-digital conversion and control lines have been routed to the sensor board through the ribbon cable. This design feature makes it possible to include additional sensors and/or capability on the sensor board. The msp430 microprocessor can function at a minimum of 1.7 V. The remainder of the sub systems operates at a minimum of 3.3 V. This condition means that the microcontroller will continue to execute even if there is insufficient power for these other sub systems. A watchdog timer has been coded into system firmware to reset the main program and avoid infinite loops when power to the sub systems drops below 3 V.

### **2.2.3. Satellite Communications**

The GEMS probe uses the Axonn STX2 satellite transmitter which provides one-way communication to the Global Star network. The STX2 module is the largest electronics component with the SATCOM antenna and SATCOM boards encompassing 40% of the system weight. The SATCOM module has been designed to maximize board space utilizing both top and bottom sides which minimize excess board weight.

Data is compressed to meet the 144-bit STX2 single message requirement and sent via serial communication to the STX2 module. The STX2 uses 1.5 W of power from the super capacitors for 1.4 seconds while transmitting the data to low Earth orbiting satellites through a patch antenna. The STX2 module is configured to meet factory recommended transmission requirements. Axonn suggests that each transmitted message be followed by three subsequent backup messages to achieve >95 % transmission rate. Bench top experiments were completed using a configuration of 5-, 10-, and 20-minute message intervals. Each transmission was accompanied by three backup transmissions as suggested by Axonn. Each test was conducted with a power supply, 9 V battery, and solar cells. The three backup transmissions yielded over 90% success rate compared to <40% for a single transmission.

### **2.2.4. Geo-location**

The GPS receiver board delivers all geo-location data to the microprocessor. The GPS receiver acquires heading, speed, position, and altitude data from GPS orbiting satellites. The Navman Jupiter 30 was chosen for its size, weight and performance characteristics. All tests with the GPS module ran the Jupiter 30 continuously to acquire hot start position fixes and did not conserve power using a GPS sleep mode. Given the focus on daytime probe demonstrations for the GEMSTONE project, this tradeoff does not affect the power cycling but will be important to address for continuous day/night

operation in follow-on efforts. Once at the level of neutral buoyancy, the GEMS probe is assumed to be a passive tracer moving with the wind. Therefore, the instantaneous GPS-derived heading and speed are used to infer horizontal wind velocity. This assumption will not be valid in turbulent flow so it will be necessary in the future to average several high frequency GPS measurements as well as account for vertical probe displacement in order to retrieve accurate wind velocities under diverse weather conditions.

The accuracy of the position, speed, altitude, and heading sent as part of the 144-bit compressed data packet along with the Jupiter 30 specifications for the same quantities is shown in Table 1. The current compression method clearly sacrifices some accuracy that could be obtained using the full resolution measurements from the Jupiter 30. However, the GEMS data record still provides heading and speed measurements accurate to 1 degree and  $0.5 \text{ m s}^{-1}$ , respectively, that is deemed sufficient given the current application and stage of prototype development.

**Table 1.** Comparison between the accuracy of GEMS data record and Jupiter 30 manufacturer specifications for GPS position, speed, altitude, and heading.

|                          | Position | Speed                   | Altitude | Heading     |
|--------------------------|----------|-------------------------|----------|-------------|
| GEMS data record         | 30 m     | $0.5 \text{ m s}^{-1}$  | 10 m     | 1 degree    |
| Jupiter 30 specification | 2.2 m    | $0.05 \text{ m s}^{-1}$ | 0.1 m    | 0.1 degrees |

### 2.2.5. Sensors

The GEMS sensor board is designed to be suspended from the bottom of the balloon. A thin, flat ribbon cable is fed through a small opening in the shell material to connect the microprocessor and sensor boards. Additional control and data lines have been run to the sensor board through this ribbon cable. These extra lines allow for new sensors to be added without having to redesign the sensor board or include multiple boards. The sensor board also features a connection where the microprocessor could be reprogrammed after assembly as needed to adjust or troubleshoot firmware settings, functionality, etc. The sensor package is equipped with an Intersema MS5401-AM analog pressure sensor and a Sensirion SHT14 14-bit temperature/relative humidity (RH) sensor. The Intersema pressure sensor has an accuracy of  $\pm 0.3 \text{ hPa}$  and an operating range of 0 to 1000 hPa. Future projects should explore a pressure sensor with a dynamic range exceeding 1000 hPa to record useful data near the ground when the probes are first launched. The Sensirion temperature (RH) sensor has a resolution of  $\pm 0.02 \text{ }^{\circ}\text{C}$  ( $\pm 0.03 \%$ ) and a range of  $-40 \text{ }^{\circ}\text{C}$  to  $125 \text{ }^{\circ}\text{C}$  (1 % to 99 %) as stated by the manufacturer's data sheet.

## 3. Testing and Analysis

### 3.1. Static Outdoor Test

A static outdoor test was designed to identify any biases in the GEMS Sensirion temperature and RH sensors over the range of ambient conditions near ground level. A National Institute of Standards and Technology (NIST) traceable sensor was purchased from Vaisala to provide accurate validation of the Sensirion sensors during a diurnal cycle. Both the GEMS and Vaisala sensors were located 2 m above ground level adjacent to the ENSCO's Coastal Technology Center (CTC) facility in Melbourne, Florida. Acquired data were analyzed for any bias over three-day periods during November and

December 2006. The validation of the GEMS sensors required placing the sensor board in a louvered plastic housing. Such an arrangement exposed both the GEMS and ground truth sensors to the same environmental conditions and provided radiation shielding and aspiration. A computer workstation was set up to record data from the GEMS sensors.

The diurnal RH tests revealed a bias above 95% and below 65%. As can be seen in Fig. 3a the Sensirion RH measurements are low when the Vaisala sensor reports RH above 95% and the Sensirion measurements are high when the Vaisala sensor reports RH below 65%. The repeatability of the biases suggests that a systematic difference exists between the Vaisala and Sensirion RH sensors. However, no such bias is present with the temperature measurements as the two traces overlap for the same three-day period in November/December 2006 (Fig. 3b). At the end of the test period on 1 December 2006, a rain shower deposited water directly onto the Sensirion sensor that was located close to the edge of the louvered housing. The wetting of the sensor would account for the increase in humidity and decrease in temperature drop relative to the Vaisala measurements.

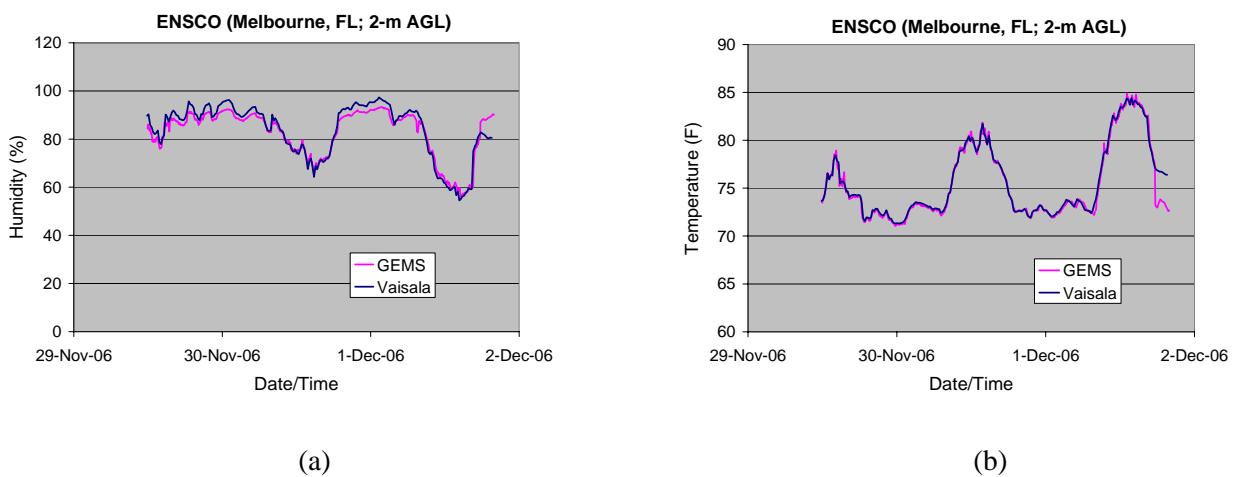


**Fig. 3.** Results comparing (a) relative humidity and (b) temperature measurements between the Vaisala and Sensirion sensors from 29 November 2006 through 1 December 2006 during the outdoor static test at ENSCO's Coastal Technology Center.

### 3.2. Pressure Sensor Calibration

Tests were conducted over a three-day period from 11-13 December 2006 at the NASA KSC environmental testing facility. The facility provided access to a 1.2 x 1.2 x 1.8 m altitude chamber. The chamber was needed to calibrate both the Intersema pressure and Sensirion temperature/RH sensors. The results from the Sensirion sensors are presented below.

The pressure sensors required calibration at multiple values of temperature and pressure to generate realistic calibration curves that would be consistent with conditions at various altitudes and temperatures. The sensors are based upon a resistive bridge coupled to a flexible membrane that deforms as the pressure changes. This deformation is measured as a voltage change across the resistive bridge. The sensor is rated for operation from 0 to 1000 hPa so pressures greater than 1000 hPa generate a nonlinear response. In order to calibrate the sensors, measurements were taken at eight different pressure levels and four different temperatures. Due to limitations of the KSC altitude chamber, it was not possible to record the voltage at or near a zero pressure reading. Therefore, the zero pressure reading was extrapolated from the data acquired. Fig.4 illustrates the sensor response as

a function of pressure.

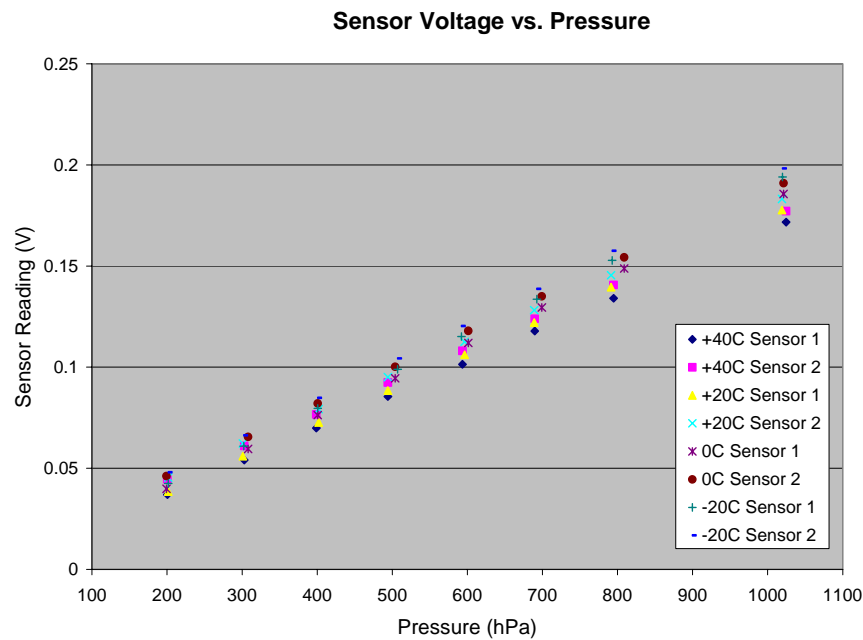


**Fig. 4.** Intersema pressure sensor calibration data from the NASA environmental test chamber.

The temperature in the NASA chamber was varied to measure the thermal coefficient of the resistive bridge. Although the pressure variation induced by temperature is small, it still has an impact on the pressure as seen from the data spread in Fig.4. The bridge's thermal coefficient produces a change in both the slope (delta) and y-intercept of the pressure data. Since the y-intercept/zero pressure reading could not be obtained empirically, an extrapolation was performed. As shown in Fig.4, the spread in the data is also not uniform so regression was used to determine the best fit for both the slope and y-intercept values of the regression line.

The regression yielded excellent results for a linear approximation of slope with a correlation coefficient of 0.99 for both sensors. However, the correlation for the intercept was not as high especially for sensor 1 although the results are acceptable given the minor correction that the intercept actually applies to the pressure calculation (not shown).

### 3.3. Temperature Sensor Calibration

During the pressure sensor calibration process, the Sensirion sensors were also tested to determine their accuracy compared with thermocouples placed throughout the KSC altitude chamber. The initial plan was to test the sensors from -40 to +40 °C; however, the Sensirion sensors are operationally rated at -30 °C and as the temperature descended below -30 °C, the sensors began to fail. The sensor failure was due to icing and resumed correct operation once the ice melted. Due to this constraint, the sensors were tested from -20 to +40 °C with results of the temperature calibration summarized in Fig.5.

As can be seen from Fig 5, both GEMS sensors performed well from 0 to +40 °C over a wide range of pressures with respect to the thermocouple. However, at -20 °C, sensor 2 began to deviate from the reference thermocouples by a substantial amount below 500 hPa. This condition worsened as the pressure decreased. The presence of water on the surface of the sensor could have caused this

degradation. As the temperature was lowered, any water on the surface would have frozen and formed a thin ice layer on the sensing element. As the pressure was decreased, this ice could have applied stress to the temperature element which would have been interpreted as an increased temperature. Further tests would be needed to validate this hypothesis but were not performed since probes deployed during any GEMSTONE free flight tests at altitudes of 1-2km would not experience such low temperatures or pressures.

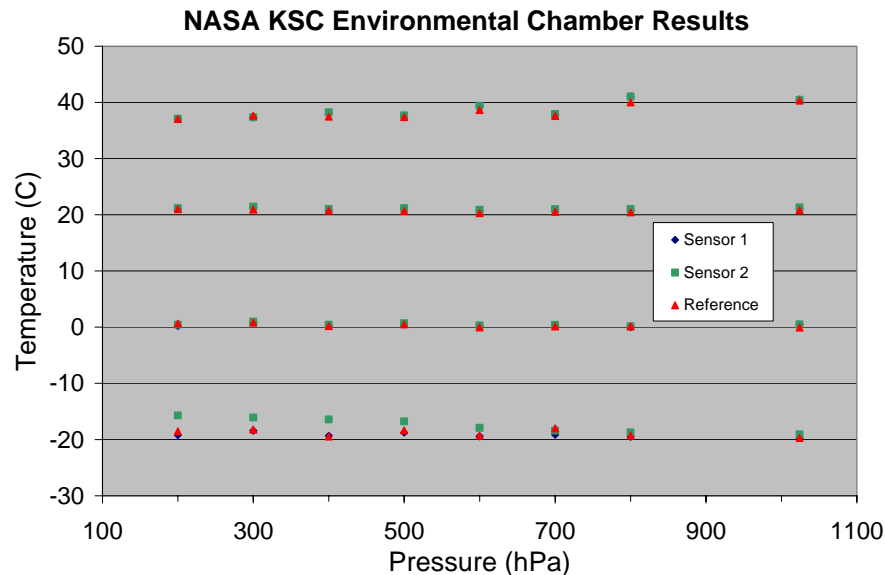


**Fig. 5.** Comparisons between two different Sensirion temperature sensors and the KSC altitude chamber thermocouple located below the test stand. Data were recorded at four different temperatures over a range of pressures from ambient to 200 hPa.

### 3.4. Free Flight Testing

The free flight tests were designed to examine system functionality and robustness in the relevant environment, record sensor data, and document SATCOM reliability. Two free flight tests were attempted during the last week of March 2007 with little success. Problems with the GPS unit not updating position and the balloon having insufficient buoyancy to lift the payload caused premature test failures. The initial GPS problem was linked to using the Callisto receiver that was replaced by the Jupiter 30 module.

A third free flight test was conducted on 19 April 2007 around mid afternoon using a 9 V battery as a power source. For this test, the GEMS probe was released from Melbourne Beach, Florida and traveled in a south, southeast direction (~140 degrees) along the coast for more than 7.5 hours with SATCOM reliability around 75 %. The GPS data stopped updating near Ft. Pierce, Florida after drifting approximately 60 km at average speed of  $7 \text{ m s}^{-1}$ . The loss of real-time GPS data is likely to have occurred when the GPS antenna board came loose and slipped below the main electronics stack preventing the GPS module from acquiring any further signals from the satellite constellation. Before GPS data were lost, the probe altitude ranged from 470 - 1300 m. The limited data from this first successful flight of a GEMS probe are summarized in Fig. 6 and Table 2.



**Fig. 6.** Google Earth™ visual summary of free flight test on 19 April 2007. Data values were entered into the Google Earth™ image including temperature (T), humidity (H), speed (Sp), and altitude (Alt).

**Table 2.** Sample data from a free flight test on 19 April 2007 with deployment from Melbourne Beach, Florida.

| Time  | Latitude (degrees) | Longitude (degrees) | Temperature (C) | Relative Humidity (%) | Altitude (m) | Speed (m s <sup>-1</sup> ) |
|-------|--------------------|---------------------|-----------------|-----------------------|--------------|----------------------------|
| 14:41 | 28.00              | -80.52              | 26.2            | 51.3                  | 10           | 0.0                        |
| 15:16 | 27.87              | -80.48              | 20.5            | 49.5                  | 1300         | 5.1                        |
| 16:10 | 27.75              | -80.43              | 24.1            | 42.3                  | 770          | 6.7                        |
| 16:51 | 27.62              | -80.35              | 24.7            | 43.0                  | 690          | 6.7                        |
| 17:34 | 27.50              | -80.27              | 21.1            | 47.8                  | 1130         | 5.6                        |

## 4. Summary and Roadmap

The GEMS concept leverages technological advancements in micro and nanotechnology for a new atmospheric in situ observing system based on an ensemble of self-contained, low cost disposable probes. During the course of a two-phase study funded by the NIAC, ENSCO, Inc. and collaborators identified the major feasibility issues for the GEMS system and mapped pathways for system development in a technology roadmap.

Follow-on work after the NIAC study included prototype development funded by ENSCO and a cost-sharing project called GEMSTONE sponsored by the KSC Technology Transfer Office. The goal of the GEMSTONE project was to build and field-test a small system of prototype probes in the Earth's atmosphere. This paper summarized highlights from the GEMSTONE project that included probe and system engineering as well as laboratory and field tests from September 2006 through May 2007.

The current GEMS probe design features a super pressure balloon constructed using Mylar™ film that is filled with helium to make it neutrally buoyant at different levels in the atmosphere. Once deployed, the probe measures temperature, pressure, relative humidity, velocity, and position information using micro sensors as it drifts passively with the wind. The electronics system is modular to provide flexibility for future capabilities while optimizing board size to minimize weight. An onboard microprocessor controls all electronic sub systems which are powered by a combination of small

batteries, thin film solar cells, and super capacitors. The data are communicated to ground stations via one-way radio frequency (RF) transmissions to low-earth orbiting satellites.

The various laboratory and field tests conducted during the GEMSTONE project were designed to characterize the sensor suite, the micro GPS, SATCOM capabilities, and overall system performance. Chamber testing was performed to calibrate pressure and temperature sensors. Two free flight tests were attempted during the last week of March 2007 but failed due to problems with the GPS unit not updating position and the balloon having insufficient buoyancy. The third and final free flight test in April 2007 was successful in demonstrating system functionality and robustness in the relevant environment including capability to acquire and transmit useful data in real time.

This section concludes with a roadmap for future development efforts that would be required to yield a fully functional and reliable prototype system (Table 3). The roadmap covers areas related to sensors (dynamic range, aspiration, shielding), SATCOM reliability and coverage, GPS power management / cycling and data processing, balloon construction, and electronics miniaturization. Note that not all of these issues were discussed in the current paper but are covered in the GEMSTONE final report [4]. The successful single-probe flight test provides a solid foundation to move forward and address these outstanding issues in follow-on projects.

**Table 3.** Summary of issues, problems, and areas for future GEMS development along with possible solutions or recommended courses of action that constitute a technology roadmap.

| Classification       | Issue   | Solution or Recommended Course of Action  |
|----------------------|---|---|
| Sensing              | Intersema pressure sensor not rated above 1000 hPa                                  | Research other pressure sensors and combine with or eliminate current device  |
| Sensing              | Sensors not aspirated   | Complete testing and implementation of aspiration using small fans or other methods   |
| Sensing              | Sensors not shielded  | Design and develop mechanical housing for shielding sensors – could be integrated with aspiration scheme  |
| Sensing              | Sensor cable passing through main shell material creates unacceptable failure point | Refine the current design for attaching electronics to the bottom of the probe or redesign the value to accommodate cable pass through.         |
| Communication        | Unreliable Global Star communications   | Explore other satellite providers (e.g. Iridium or ARGOS)   |
| Communication        | Global Star has limited coverage  | Switch to Iridium or other provider with better coverage  |
| Geo-location         | Current microprocessor firmware not configured to use Jupiter 30 GPS sleep mode     | Revise firmware so the GPS unit can use sleep mode to conserve power  |
| Geo-location         | Currently using instantaneous GPS heading and speed                                 | Revise firmware to average higher frequency GPS measurements and account for altitude changes   |
| Power                | Continuous and reliable 24-h probe operation  | Upgrade firmware, optimize power cycling, and test power subsystems   |
| Flight termination   | Hardware (mechanical system) not tested and firmware (GPS ‘fence’) not implemented  | Complete hardware and firmware modifications, bench test, then field test   |
| Balloon construction | Reliability of seams and valves   | Contract with balloon manufacturing company, optimize balloon design, new materials research  |
| Miniaturization      | Reduce system mass  | Integrate separate boards, use flexible electronics and lighter components, redesign SATCOM hardware or choose alternate communication paradigm |

## Acknowledgements

The ENSCO team would like to thank Dr. Francis Merceret (NASA KSC Weather Office Chief Scientist) for his enthusiastic support of the GEMS concept beginning in 2001 and his contributions to the GEMSTONE project as co-investigator. The entire project team acknowledges Rosemary Baize (NASA KSC Technology Transfer Office) for her guidance and support throughout the project as well as ENSCO, Inc. for significant cost sharing that made it possible to complete the effort. The authors appreciate the helpful comments from Mr. Randolph Evans and Mr. Joseph Dreher as well as Mr. Dreher's support of the preliminary free flight tests.

Mention of a copyrighted, trademarked or proprietary product, service, document, or web site does not constitute endorsement thereof by the authors, ENSCO, NASA, or the U.S. Government. Any such mention is solely for the purpose of fully informing the reader of the resources used to conduct the work reported herein.

## References

- [1]. G. E. Moore, Cramming more components onto integrated circuits, *Electronics*, 38, 1965, pp. 114-117.
- [2]. J. M. Kahn, R. H. Katz, and K. S. J. Pister, Emerging challenges: mobile networking for Smart Dust, *J. of Commun. and Networks*, 2, 2000, pp. 188-196.
- [3]. J. Manobianco, et. al, Global Environmental MEMS Sensors (GEMS): A revolutionary observing system for the 21<sup>st</sup> century, phase II Final Report, 2005, [Available from ENSCO, Inc., 4849 North Wickham Road, Melbourne, FL, 32940].
- [4]. J. Manobianco, et. al, Global Environmental Micro Sensors Test and Operations in the Natural Environment (GEMSTONE) Final Report, 2007, [Available from ENSCO, Inc., 4849 North Wickham Road, Melbourne, FL, 32940].

---

2007 Copyright ©, International Frequency Sensor Association (IFSA). All rights reserved.  
(<http://www.sensorsportal.com>)

## **Sensors & Transducers Journal (ISSN 1726-5479)**

Open access, peer review  
international journal devoted to research,  
development and applications of sensors,  
transducers and sensor systems.

Published monthly by  
**International Frequency Sensor Association (IFSA)**



<http://www.sensorsportal.com/HTML/DIGEST/Submition.htm>

## Frequency Domain Modeling of SAW Devices for Aerospace Sensors

<sup>1</sup>William WILSON, <sup>2</sup>Gary ATKINSON

<sup>1</sup>NASA Langley Research Center, Hampton VA, USA, 23681

<sup>2</sup>Virginia Commonwealth University, Richmond, VA, USA, 23284

<sup>2</sup>Tel.: (804) 827-0185, fax: (804) 828-4269

E-mail: [gmatkins@vcu.edu](mailto:gmatkins@vcu.edu)

*Received: 7 September 2007 / Accepted: 19 September 2007 / Published: 8 October 2007*

---

**Abstract:** New Surface Acoustic Wave (SAW) sensors for integrated vehicle health monitoring of aerospace vehicles are being investigated. SAW technology is low cost, rugged, lightweight, and extremely low power. However, the lack of design tools for MEMS devices in general, and for SAW devices specifically, promoted the development of SAW Device Models that will enable integrated design, simulation, analysis and automatic layout generation. A frequency domain model of the SAW device has been created. The model is primarily first order, but it includes second order effects from triple transit echoes. This paper presents the model and results from the model for a SAW delay line device. *Copyright © 2007 IFSA.*

**Keywords:** Modeling, Simulation, Surface acoustic waves microelectromechanical systems, MEMS

---

### 1. Introduction

The lack of integrated design tools for Surface Acoustic Wave (SAW) sensors has led to the development of models for these devices. Frequency domain models have been developed using the time domain analysis within VHDL [1]. The frequency domain analysis is not sufficient for general frequency modeling [2], because the analog extensions to the language use Differential Algebraic Equation (DAE) solvers which do not support transcendentals. A similar issue exists in all analog extended Hardware Description Languages (HDLs) that use DAEs at this time. In the future, non-linear and transcendental solvers may be incorporated into a HDL language [3].

Therefore, to aid in the design and analysis of SAW devices, a SAW delay line model has been created. A dynamic simulator was used for this effort because it provides a graphical interface for the development of dynamic multi-domain (electrical, mechanical and piezoelectric) simulations. This

modeling environment enables both time and frequency domain analysis. Fig. 1 (a) is a diagram of the basic SAW delay line used in the model. It calculates the radiation conductance, the acoustic susceptance, and the frequency response for the system. The model includes optimization for the aperture height. The effects of triple transit echoes have also been included in the model. The model outputs plots for analysis and a text file of parameters that are used for automatic layout generation. The model allows quick design and analysis of SAW delay line devices, followed by automatic layout generation and fabrication.

## 2. Impulse Response Model

The Impulse Response method [4] was used as the basis for modeling the SAW device. This method is valid only for transducers where at least one of the two Inter-Digitated Transducers (IDTs) has a constant aperture or finger overlap [5]. This modeling technique models both the mechanical and electrical behavior of a SAW device and is sufficient for use as a first order model. The model calculates the frequency response, the loss of the system, the admittance, and the electrical parameters for circuit simulators. This model assumes a constant metallization ratio of 0.5 (equal spacing and finger widths). A simple circuit model (Fig. 1 (b)) can be used to convey the basic elements of the Impulse Response Model. The figure shows the source voltage and both the source and load impedances which are not part of the model. In the circuit model  $C_T$  is the total capacitance,  $B_a(f)$  is the acoustic susceptance, and  $G_a(f)$  is the radiation conductance.

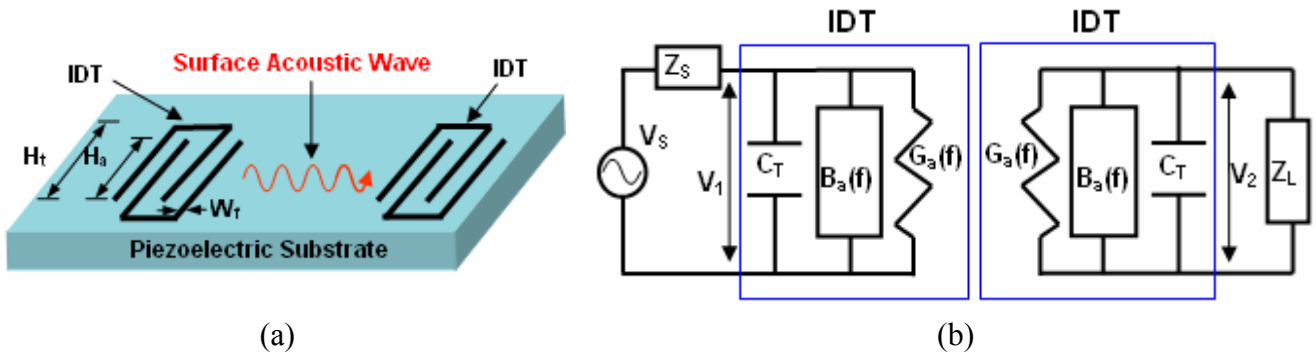


**Fig. 1.** (a) Basic SAW delay line and (b) the circuit model used in the Impulse Response Modeling.  $C_T$  is the total capacitance,  $B_a(f)$  is the acoustic susceptance, and  $G_a(f)$  is the radiation conductance.

From the Impulse Response model one can calculate the wavelength ( $\lambda$ ), and the number of finger pairs ( $N_p$ ) using the following equations:

$$\lambda = \frac{v}{f_0}, \quad (1)$$

$$N_p = \text{round}\left(\frac{2}{NBW} f_0\right), \quad (2)$$

where  $v$  is the acoustic velocity in the media,  $f_0$  is the center or synchronous frequency, and NBW is the Null BandWidth or fractional frequency.

## 2.1. Radiation Conductance

To begin the discussion on the Impulse Response model, first the variable  $X$  is defined as [4]:

$$X = N_p \pi \frac{(f - f_0)}{f_0}, \quad (3)$$

where  $f$  is the frequency. The real part of the input admittance is called the radiation conductance. The radiation conductance is shaped by the sinc function and is found by [4]:

$$G_a(f) = 8k^2 C_s H_a f_0 N_p^2 \left| \frac{\sin(X)}{X} \right|^2, \quad (4)$$

where  $k$  is the coupling coefficient,  $C_s$  is the capacitance per finger pair and unit length, and  $H_a$  is the aperture or overlap height of the fingers. The results of equation (4) are normalized by dividing by the radiation conductance at the synchronous frequency.

## 2.2. Acoustic Susceptance

The second element of the model is the imaginary part of the input admittance which is called the acoustic susceptance. The acoustic susceptance is the acoustic wave modeled as an electrical parameter. The acoustic susceptance is found by taking the Hilbert transform of the radiation conductance and is given by [4]:

$$B_a(f) = \frac{G_a(f_0) \sin(2X) - 2X}{2X^2}. \quad (5)$$

Since the acoustic susceptance at the synchronous frequency is zero, the acoustic susceptance is normalized by dividing by the radiation conductance at the synchronous frequency.

## 2.3. Admittance and Impedance

The total admittance is found by combining the radiation conductance, the acoustic susceptance and the total capacitance [6]. The total admittance is given by

$$Y = G_a + j(2\pi f C_T + B_a). \quad (6)$$

The total static capacitance ( $C_T$ ) for the IDT is found by multiplying the capacitance per unit length for a pair of fingers ( $C_s$ ) times the finger overlap or aperture ( $H_a$ ) times the number of fingers pairs ( $N_p$ ).

$$C_T = C_s H_a N_p. \quad (7)$$

Impedance matching is often used to reduce reflections in high frequency systems. Inverting (6) yields the impedance of the system [4]:

$$Z(f) = \frac{1}{(G_a + j(2\pi f C_T + B_a(f)))}. \quad (8)$$

## 2.4. Frequency Response

For SAW delay line devices the frequency response or transfer response is calculated using [4]:

$$H(f) = 20 \log \left( 4k^2 C_s f_0 N_p^2 \left( \frac{\sin(X)}{X} \right)^2 e^{-j \left( \frac{N_p + D}{f_0} \right)} \right), \quad (9)$$

where D is the delay between IDTs in wavelengths.

## 2.5. Aperture Optimization

An optimal design must match the IDT resistance (real impedance) to the source resistance. The device aperture ( $H_a$ ) is adjusted so that the IDT design achieves the correct resistance, and reduces the reflections caused by impedance mismatches. The following equation is used to optimize the aperture in terms of the source resistance ( $R_{in}$ ):

$$H_a = \frac{1}{R_{in}} \left( \frac{1}{2f_0 C_s N_p} \right) \frac{(4k^2 N_p)}{(4k^2 N_p)^2 + \pi^2}, \quad (10)$$

## 2.6. Second Order Effects

The model has been extended to include the second order effect from triple transit echoes. These occur when a small amount of signal travels from the receiver to the transmitter and then back to the receiver again. The frequency of the signal is  $\frac{1}{2} f_0$  and the amplitude is  $1/64$  of the power of the original [7]. The signal is large enough to cause discernable ripples in the frequency response.

$$H(f) = 20 \log \left( 4k^2 C_s f_0 N_p^2 \left( \frac{\sin(X)}{X} \right)^2 e^{-j \left( \frac{N_p + D}{f_0} \right)} + \frac{1}{64} \sin \left( \frac{f}{0.5} \right) \left( \frac{\sin(X)}{X} \right)^2 \right). \quad (11)$$

## 3. Implementation

The SAW model developed is modular and hierarchical as can be seen in the Impulse Response block (Fig. 2).

The input parameters and material constants are contained in the Inputs block. The frequency variable is generated in the Inputs block as well. The Aperture value is calculated using equation (10) in the  $H_a$  Optimization block. The values for all of the variables are calculated in the Calculations block. Within the Calculations block (Fig. 3) functions and sub-blocks are necessary for the implementation of equations given earlier. The Calculation block also determines the minimum insertion loss, the size of the matching inductor and the total capacitance of the IDT. The parameters necessary for fabrication of the device are all written to a text file in the Outputs block.

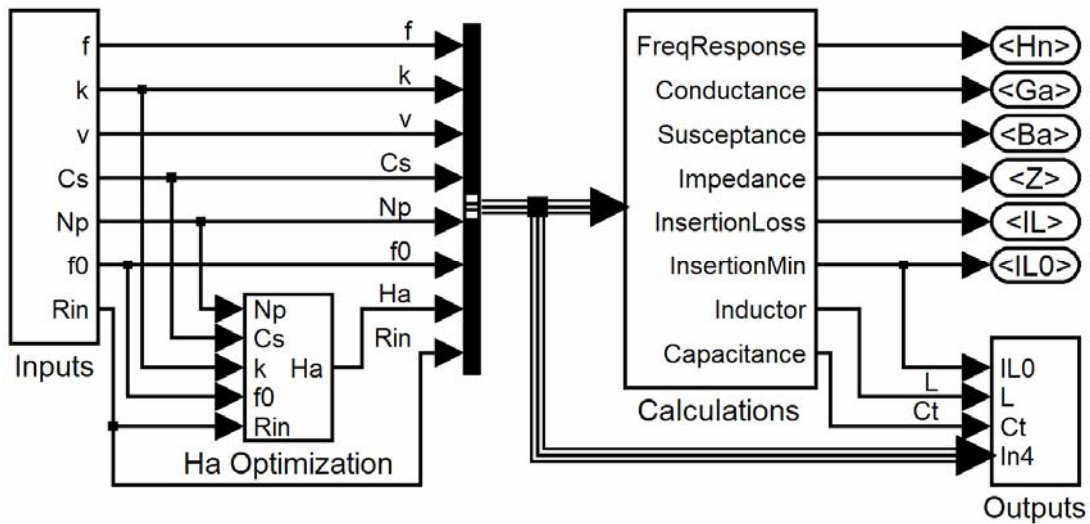


**Fig. 2.** Impulse Response Block.

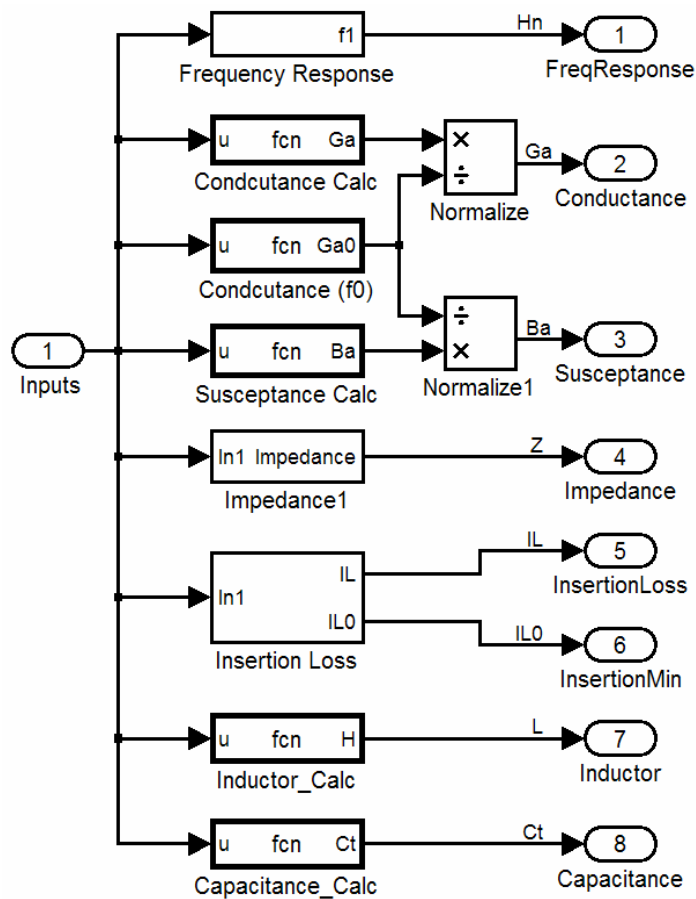


**Fig. 3.** Calculations Block.

The bulk of the calculations occur in the Frequency Response block (Fig. 4). The ideal frequency response is calculated at the top, while the bottom portion is where the triple transit echo (TTE) signal is generated. Both signals are summed and normalized before being output.

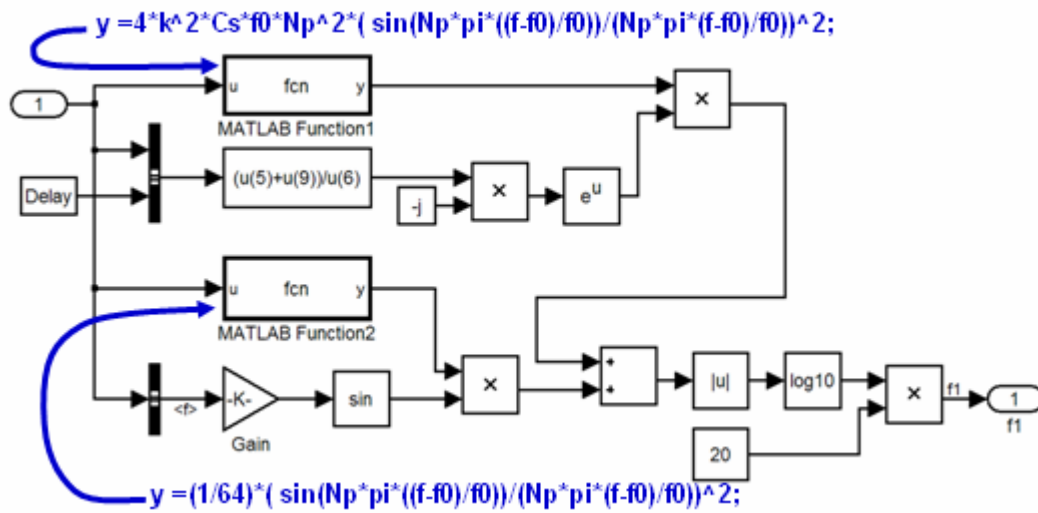


Fig. 4. Frequency Response Block.

#### 4. Saw Delay Line Prototype

To demonstrate the model a simple SAW delay line that consists of two identical IDTs was chosen. The synchronous frequency is 78.95 MHz. The null bandwidth (NBW) or fractional frequency is 1.5 MHz. The delay length between the two IDTs is 5 wavelengths. Both the source and load resistances are assumed to be 50  $\Omega$ , the impedance of the test instrumentation. The substrate is ST cut Quartz, selected for its low thermal expansion coefficient at room temperature. The selection of a substrate material determines the capacitance per finger pair  $C_s = 0.503385$  pf/cm, the piezoelectric coefficient  $k = 0.04$ , and the acoustic velocity  $v = 3158$  m/s for the SAW device [8]. Using these values in equation (11) yields an optimized aperture of 1571.0  $\mu\text{m}$ . For this example the wavelength ( $\lambda$ ) is 40  $\mu\text{m}$ , the finger widths and spaces between the fingers are both 10  $\mu\text{m}$ . The optimal number of finger pairs (105), is calculated using equations (1 and 2).

The model generates plots of the frequency response and of both the normalized radiation conductance and normalized acoustic susceptance (Fig. 5), using the values for the prototype device. The plots are used for analysis of the device design before the device layout is performed.

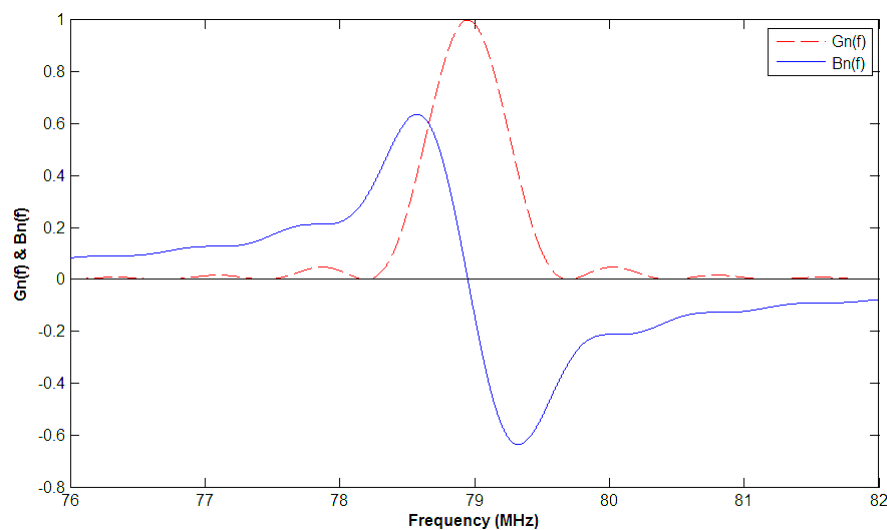
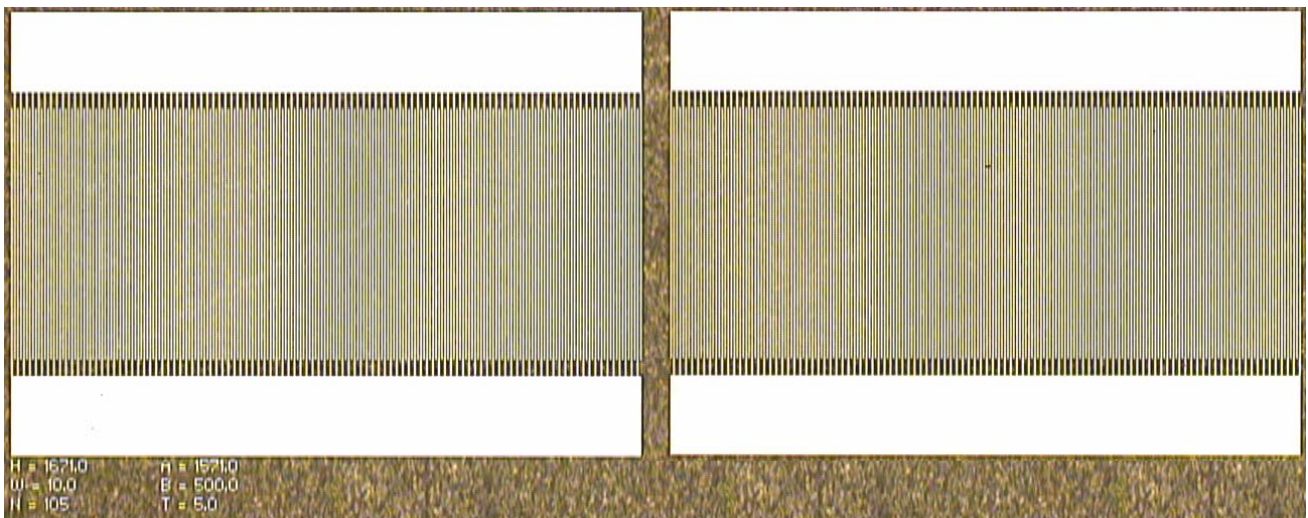


Fig. 5. The normalized Radiation Conductance ( $G_n(f)$ ) and the normalized Acoustic Susceptance ( $B_n(f)$ ) plotted together.

After the modeling tools are used to develop a design concept, the parameters from the model are written into a file that is used by the Layout Editor tools. Parameterizable library components were developed previously that enable automatic layout generation of SAW devices [9] using the Layout Editor tools. This process was used to create a layout of the device. The prototype device was then fabricated from the layout (Fig. 6). Note that the salient parameters of the design are annotated on the layout using the same metal as the fingers. On the layout, H is the height of the fingers, W is the width of the fingers, N is the number of finger pairs, A is the aperture height or length of the overlap between the fingers, and B is the height of the buss bars. The units for all of the parameters mentioned earlier are in microns, the exception is T which is the delay between the two IDTs, and is measured in wavelengths. Note the finger length at 1671  $\mu\text{m}$  is 100  $\mu\text{m}$  greater than the aperture height. This is the non-overlap length of the fingers and the space between the fingers and the bus bars.



**Fig. 6.** Prototype device with 105 aluminum finger pairs per IDT, on a ST-cut Quartz substrate.

The frequency response of the system is calculated using equation (11) and is plotted in (Fig. 7) along with the measured frequency response from a fabricated device. This figure shows that the minimum insertion loss for the system naturally occurs at the synchronous frequency. A comparison between the calculated frequency response and the measured frequency response demonstrates that the first order model captures the main characteristics of the central lobe and the first side lobes. The addition of the triple transit echo signal to the model makes the response more accurate and can be seen as the small ripple on the top of each lobe.

Noise in the measured results has distorted the second and subsequent side lobes. The ripples and peaks on the top of the main lobe are caused by second order effects such as internal reflections. Extensions of this work will include the addition of more second order effects into the frequency response models.

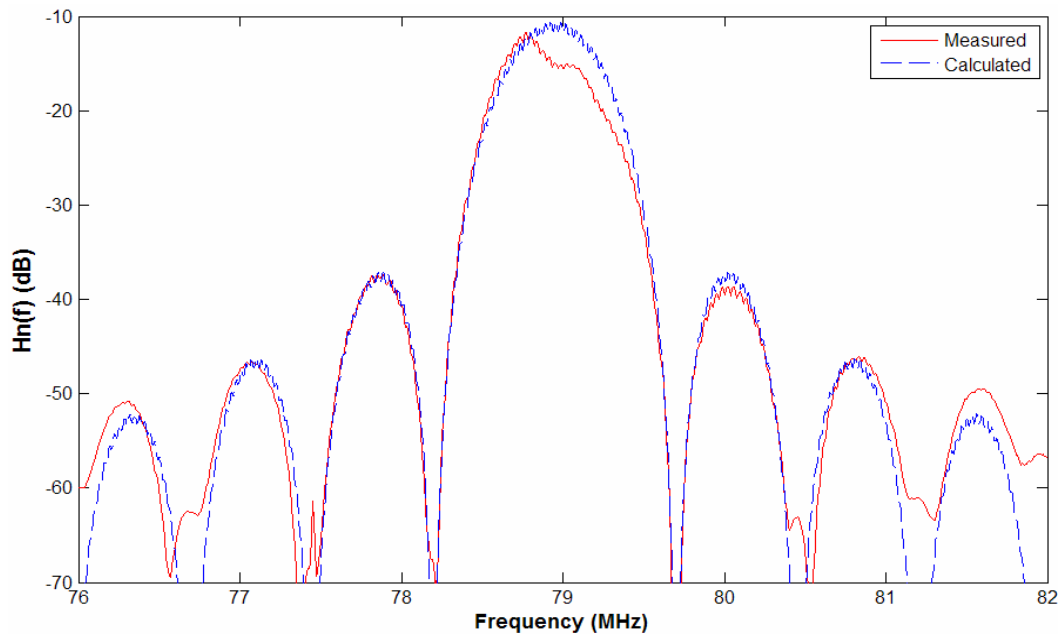


**Fig. 7.** Frequency Response of the SAW Delay line on Quartz ST cut substrate.

## 5. Conclusions

The frequency domain model of a SAW delay line has been created. A dynamical simulator was used because it provides a graphical interface for the development of dynamic multi-domain simulations and does not exhibit any of the issues found in HDLs, thus allowing both time and frequency domain analysis. The model is reasonably accurate for the main lobe and first side lobes of the frequency response. In this region it also captures the ripples upon the main signal caused by the second order effect of triple transit echoes. The model implemented calculates the frequency response, insertion loss, radiation conductance, acoustic susceptance, impedance, total capacitance, and triple transit echo signal.

The model was used to analyze a 78.95 MHz device and to determine the optimal parameters so that a prototype device could be developed. The device was fabricated and the measured results were compared to the model, thus verifying the model's accuracy.

The frequency domain model of SAW devices that has been developed will allow for quick design, analysis and fabrication of prototype SAW devices for aerospace applications such as integrated vehicle health monitoring. In the future, frequency domain models that cover more second order effects will be developed. These models should allow more accurate modeling of internal and external reflections.

## References

- [1]. W. C. Wilson, G. M. Atkinson, Mixed Modeling of a SAW Delay Line using VHDL, In *Proceedings of the IEEE International Behavioral Modeling and Simulation Workshop (BMAS 2006)*, San Jose, CA, 14-15 September 2006, pp. 34-39.
- [2]. E. Christen, K. Bakalar, VHDL-AMS-A Hardware Description Language for Analog and Mixed-Signal Applications, In *IEEE Transactions on Circuits and Systems II: Analog and Digital Signal Processing*, 46, 10, 1999, pp. 1263-1272.

- [3]. K. Einwich, J. Bastian, C. Clauss, U. Eichler, P. Schneider, SystemC-AMS Extension Library for Modeling Conservative Nonlinear Dynamic Systems, In *Proceedings of the 9<sup>th</sup> International Forum on Specification and Design Languages (FDL 2006)*, Darmstadt University, Germany, 19-22 September 2006, pp. 113-118.
- [4]. C. S. Hartmann, D. T. Bell, R. C. Rosenfeld, Impulse Model Design of Acoustic Surface-Wave Filters, In *IEEE Transactions on Microwave Theory and Techniques*, 21, 4, 1973, pp. 162-175.
- [5]. D. C. Malocha, Evolution of the SAW Transducer for Communication Systems, In *Proceedings of the IEEE Ultrasonics Symposium*, 1, Montreal, Canada, 23-27 August 2004, pp. 302-310.
- [6]. K. M. Lakin, T. Joseph, D. Penunuri, Planar Surface Acoustic Wave Resonators, In *Proceedings of the IEEE Ultrasonics Symposium*, 1, Milwaukee, Wisconsin, 11-14 November 1974, pp. 263-267.
- [7]. C. K. Campbell, Surface Acoustic Wave Devices for Mobile Wireless Communications, New York, NY: Academic, 1998.
- [8]. A. J. Slobodnik, Jr., Surface Acoustic Waves and SAW Materials, In *Proceedings of the IEEE*, 64, 5, 1976, pp. 581-595.
- [9]. W. C. Wilson, G. M. Atkinson, Parameterizable Library Components for SAW Devices, In *Proceedings of Modeling and Simulation of Microsystems (MSM 2006)*, Boston, MA, 7-9 May 2006, pp. 570-573.

---

2007 Copyright ©, International Frequency Sensor Association (IFSA). All rights reserved.  
(<http://www.sensorsportal.com>)



Call for Papers

3<sup>rd</sup> International Conference

# smart

materials structures systems

June 8-13, 2008 Acireale, Sicily, Italy

smart materials  
& micro/nano-systems

smart textiles

smart optics

intelligent structures  
mechatronics & robotics

biomedical applications  
of smart materials  
nanotechnology and  
micro/nano engineering

bio-inspired materials  
& bionic systems

[www.cimtecongress.org](http://www.cimtecongress.org)

CIMTEC 2008

The poster features a central collage of images including a DNA helix, a bridge, a satellite, and various microscopic structures, all set against a background of colorful, swirling light trails.

## Development of Materials and Sensors for the U.S. Army's Active Coatings Technology Program

**James L. ZUNINO III**

U.S. Army RDE Command, Bldg 60 Picatinny, NJ 07806-5000

Tel.: 973-724-6773, fax: 973-724-4525

E-mail: [james.zunino@us.army.mil](mailto:james.zunino@us.army.mil)

*Received: 17 September 2007 /Accepted: 19 September 2007 /Published: 8 October 2007*

---

**Abstract:** The ability to custom build and integrate novel technologies into functionalized systems is the driving force towards the creation and advancement of active coatings systems. Active coating systems require the development and advancement of numerous technologies across various energy domains (e.g. electrical, mechanical, chemical, optical, biological, etc.). The U.S. Army is attempting to take these technologies and implement them into an active coatings system through the Active Coatings Technologies Program, thus creating the next generation of coating systems. These technologies give one the ability to work at the molecular level, atom by atom, to create large structures with fundamentally new molecular organization and yield advanced materials that will allow for longer service life and lower failure rates. Novel technologies such as nanotechnology, MEMS, meta-materials, flexible electronics, electrochromics, electroluminescence, etc. are key components in the development of active and reactive materials for the Army. *Copyright © 2007 IFSA.*

**Keywords:** Active Coatings Technologies, Smart Coatings, Army, Nanotechnology, Sensors, MEMS

---

### 1. Introduction

In our ever-changing world, there is a need for materials that can thrive and survive in an almost infinite variety of environments. Most materials are designed to operate in predetermined conditions. Such materials are passive and unable to change in response to its surroundings. With advances in chemistry, physics, engineering, and other related sciences, these passive materials and coatings can and will have the ability to react and respond to their surroundings in real-time. These materials, composites, and coatings are actual systems with numerous components or layers integrated together

to combine functionality and capabilities, limited only by the current state of the technologies of which they are comprised.

The U.S. Army is currently transforming into a lighter yet more lethal “objective force”, all while fighting the War on Terror. New technologies and materials are needed to achieve these transition goals. New platforms must be deployable, be 70 % lighter and 50 % smaller than current armored combat systems, while maintaining equivalent lethality and survivability [1]. To meet the lighter yet more lethal requirements of the Future Combat Systems, Army scientists and engineers need to capitalize on new technologies and breakthroughs in the scientific arena. Novel technologies such as nanotechnology, MEMS, meta-materials, flexible electronics, electrochromics, electroluminescence, etc. are key components in the development of active and reactive materials for the Army.

The coatings currently applied to tanks, helicopters, and other weapon systems need to better protect their structures and crew since design margins are significantly tighter resulting in lower tolerances with regard to material loss/fatigue induced by wear, corrosion, erosion, and battle damage for these lighter vehicles. The U.S. General Accounting Office (GAO) estimates that the total cost for Department of Defense (DOD) corrosion related problems alone is currently \$ 20 billion per year, \$ 4 billion of which is related to painting and de-painting operations [2]. The coatings applied to weapon systems today lack the ability to self-correct when environmental conditions and circumstances change, and they do not have the ability to alert the user of potential anomalies such as corrosion, damage or adhesion problems.

The ability to perform prognostic and diagnostic analyses, in real-time, is a key objective for the DOD. Smart coatings, materials, and structures will allow the military to incorporate these advanced capabilities while maintaining weight and lethality requirements. The ability to custom build and integrate technologies into functionalized systems is the driving force towards the advancement of active coatings systems. These systems will assist the U.S. Army in its transition from scheduled maintenance to condition based maintenance, saving time and money.

Engineers at Picatinny Arsenal, NJ are addressing the issues of military coatings systems by developing coatings capable of collecting, analyzing, managing, and adapting to data from the environment in real-time. If an anomaly such as a scratch or degradation from corrosion is detected, embedded sensors will analyze the data and initiate a response. The response may result in the coating self-healing if a crack exists or the coating’s color patterns may change via electroluminescence and/or electrochromics to visually display corroded areas on the tank, if desired.

There have been major advances in the technologies researched and developed under the Active Coatings Technologies program. These advances include research into MEMS and Nano devices in order to create coating systems that will self correct and identify areas of weakness. These devices will be crucial in the coating process; helping the Army move into the lighter realm. Self correcting coatings will significantly cut costly repairs by limiting the extent of damage through early detection and notification. The research is ongoing and will continue looking at smaller electronics and related technologies that will better help the Warfighter.

## **2. Discussions**

Nanostructured materials yield extraordinary differences in rates and control of chemical reactions, electrical conductivity, magnetic properties, thermal conductivity, strength, and fire safety. The small size allows for numerous systems and functions to be incorporated together and embedded into materials such as metals, polymers, paints/films, composites, etc. This gives one the ability to work at the molecular level, atom by atom, to create smart structures with fundamentally new molecular

organization and yield advanced materials that will allow for longer service life and lower failure rates. These technologies will allow one to develop customizable coatings solutions to meet military user requirements.

Members of ARDEC have assembled a team including university support as well as other military and industry representatives. This team is developing multilayered, modular active coatings with numerous functionalities such as self-repair, visual display, artificial intelligence, self-management, sensing package, and corrosion inhibitors, that can be customized as needed. An illustration of the patented Smart Coatings System is depicted in Fig. 1.

For example, an Active Smart Coatings System will be corrosion resistant and consist of embedded flexible sensors capable of: 1) collecting data from the current surroundings, 2) processing and managing data, and 3) transmitting data real-time to onboard and/ or monitoring sites. When an anomaly or defect occurs, the coating or material will alert the user allowing for condition based maintenance rather than scheduled based, resulting in cost and time efficient repairs. This transition will save the DOD valuable man power, time, supplies, and money.

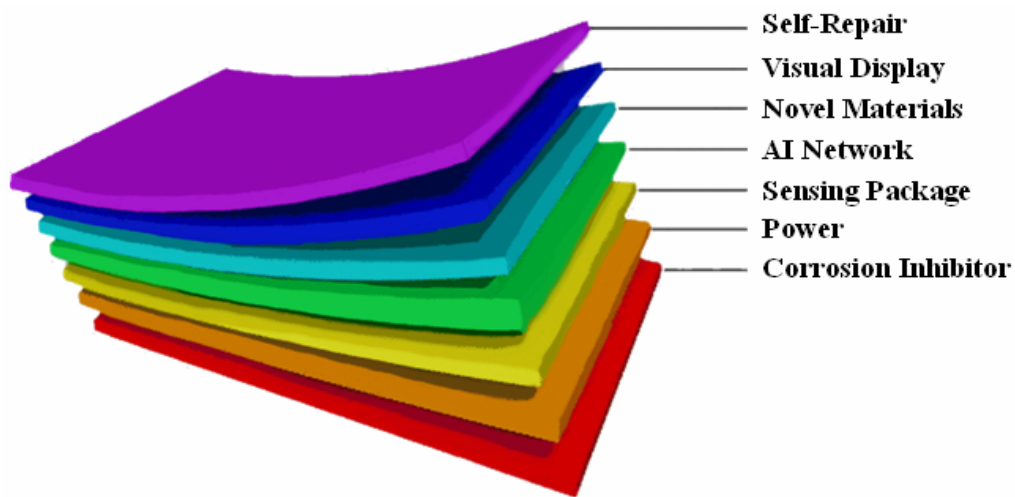


**Fig. 1.** Visual Representation of Patented Smart Coatings System (US 7,244,500 B2).

There are numerous universities and government agencies working on active/reactive materials and active coatings systems. Most are trying to work in specialized areas to develop active coatings for a particular need or application. Some believe that active coatings should be designed to meet a given goal, or perform a set function, while others feel that active coating systems should and can be capable of possessing numerous functionalities in one system. The US Army ARDEC along with researchers from the New Jersey Institute of Technology (NJIT), Clemson University, and several other partners are steadily working towards developing an Active Coating Systems as described above. The multi-disciplined team includes experts in physics, chemistry, engineering, and other sciences trying to develop and integrate revolutionary technologies into an active coating system to meet military needs.

### **Development of Materials and Sensors**

As part of the Army's Smart Coatings and Active Coatings Technologies Programs, a vast array of materials and devices are being research and developed. These developments are key requirements of active/reactive systems, allowing the DOD to increase capabilities by adding functionalities to current

and future systems. To date, several working prototype modules have been developed under these programs. Areas of research have and will continue to include: color modifying coatings, flexible electronics, wireless sensor packages, nanotube development, intelligent nano-clays, alternative fuel/power sources, de-painting/self-repair, material modification, and other technologies capabilities desired by the military. The added capabilities will allow for real-time structural health monitoring of systems, advances in non-destructive evaluation, and cost and time savings for military and commercial sectors.

One area of research involves working with nanotubes and their functionalization, development, and production. Single-walled carbon nanotubes (SWCNT) are being implemented into smart coatings and inks to initiate self-healing, active switching, sensing, color modification, and other functionalities. A corrosion-barrier coating system with an active p-n (positive & negative doped) junction layer below a passive top layer has been fabricated. The resulting charge modulation of the junction coating provides active corrosion protection as well as corrosion sensing capabilities.

Nanotubes are also being utilized for power/fuel cell development and electroluminescence. Functionalized nanotubes can serve as hydrogen storage, or as the electrode material providing more efficient charge transfer. The use of p-n junction SWCNT coatings as photovoltaic modules with the bottom layer functioning as a proton exchange membrane (PEM) fuel cell will provide power while the electroluminescence serves as a modifiable display. Solubility and polymer wrapping of SWCNTs has lead to the ability to functionalize these tubes. Such technological advances have allowed for flexible solar cells to be fabricated using nanotube inks (Fig. 2). Beyond that, is the development of chemistries that enable the production of single-walled nanotubes with precise but tunable dimensions (properties). Functionalized nanotubes are also being investigated to increase strength, add/increase conductivity, reduce signature, negate environmental effects, as well as add additional functionalities to composites and other materials. Increasing the strength to weight ratio of structural materials will allow for more robust systems to be created. Work is also being performed to develop cost effect methods of development and scale-up of SWCNT production reducing the cost and making such materials practical and affordable.

Another area of interest is color modification. Color modification methods include using electrochromics, electroluminescence, intelligent clays (i-clays), nanotubes, and chemical additives to control and adapt color change capabilities on demand. Chromic materials may radiate loose color, become translucent/transparent, or just change properties in response to other external stimuli.



**Fig. 2.** Liquid Ink Solar Cell on Flexible Substrate.

A first level, “proof-of-concept,” prototype has been developed and demonstrated that consists of a thin film strain sensor; N-type/P-type doped single wall carbon nanotube PN junction switch, and color display layer (Fig. 3). The prototype was developed to illustrate the ability to sense a change in the environment (i.e. applied pressure), analyze the change, and alert the user of the anomaly through color changes on the coating (Fig. 4).

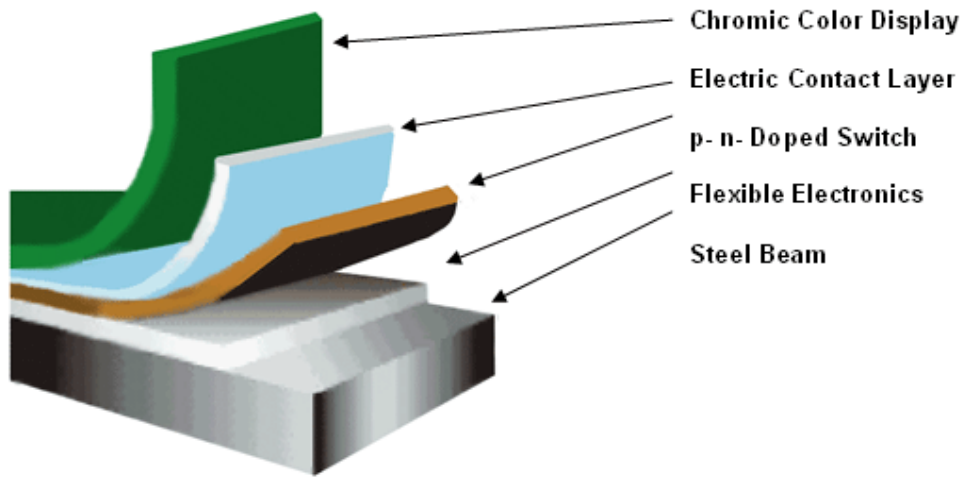


**Fig. 3.** 2005 Smart Coatings Prototype Schematic.



**Fig. 4.** Chromic Color Response.

The prototype system was modeled after the main support members of the Chinook Helicopter and HEMTT vehicle, both of which are susceptible to corrosion and fatigue (Figures 5 and 6).

Typically, weekly inspections of the Chinook include 3 man days to remove floor boards, 2 man days of inspection, and 3 man days to replace floorboards [3]. Utilizing the flexible sensor array and ribbon cables that are accessible in the cockpit or can transmit data wirelessly, technicians can utilize the sensors to determine the structural integrity of the support members without weekly visible inspections. By enabling visible inspections to be conducted less frequently, time and cost savings can be realized.

Another problem is seen in the “loading” of the Heavy Expanded Mobility Tactical Truck (HEMTT). Different payload configurations exist and each has its own set of potential problems. A major problem is present on the fuel version of the vehicle. Common practice is to “half-fill” the fuel tanks since the actual safe load limit is unknown due to material degradation [4]. Active coatings can resolve this problem since the structural integrity and safe load capacity can be known instantly. A color change in the paint or a signal can alert the logistic staff of potential problems. In both cases, the data can be transmitted remotely so the number of visual inspections can be greatly reduced saving time and money.



**Fig. 5.** CH-47D CHINOOK Support Members.



**Fig. 6.** Fuel Version of HEMTT With Corroded Support Beams.

While the chromic materials in these examples revert to their previous state once the stimuli is removed, other chromic materials are used by the ACT Program to change color and remain in that state serving as a marker or warning. Thermochromics are being developed to alert Army logistic staff of dangerous temperature exposures. These active coatings are capable of monitoring elapsed time-temperature/radiation profiles. This is especially of interest for the monitoring of devices and munitions during transportation and storage. Many munitions become unstable when exposed to temperatures beyond their design parameters.

Monomers of conjugated polymers are being optimized to provide color indicators to alert logistic staff when temperature exposures exceed safe levels. An example is a paint band placed on bullets that turns red if the round is exposed to unsafe temperature levels and maybe a safety concern (Fig. 7). The indicators will also provide duration of exposure by quantitative monitoring of light reflection or absorption from the coatings using light from a hand-held laser.

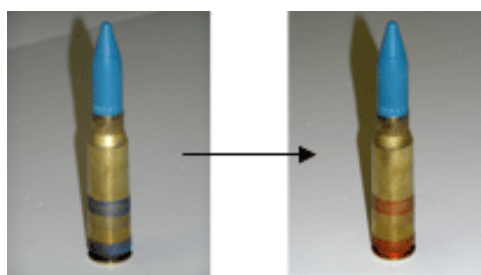


**Fig. 7.** 50 Cal. Round after Exposure Over 157°F.

Nanoclays or micronized minerals may also be incorporated into active systems to add additional capabilities. The “intelligent clay” (*i-clay*) can be incorporated into coating/paint systems. These *i-clays* or smart materials rely on their capabilities to respond to physical, chemical, or mechanical stimuli by developing readable signals. They possess the ability to modify or change their properties and structure, in response to changes in their environment. Responses may range from simple sensing, to advanced corrective action such as self-repair. The addition of *i-clays* and other materials can convert passive coatings into active coating systems. There are numerous applications for *i-clays* including, protection of materials, membranes for controlled drug release, coatings, chromic applications, sensitive and selective sensors. The creation and development of intelligent nanoclays (*i-clays*) for corrosion, humidity, pH, & chem/bio agents via color changes or luminescent properties within active coatings is also underway. These *i-clays* can be incorporated into inks, paints, composites, etc., to add functionalities to current coatings used on Army materiel, automobile, planes, ships, etc.

Active coatings integrated with *i-clays* were tested to demonstrate “early warning of corrosion” sensing capabilities and barrier properties (Fig. 8). The ability to sense corrosion and material degradation, at the molecular level, allows *i-clays* to serve as an early warning system to alert users when and where corrosion occurs. It is hoped that this research will provide solutions to corrosion related problems of military equipment, thus reducing the current multimillion-dollar expenses associated with painting/de-painting operations.

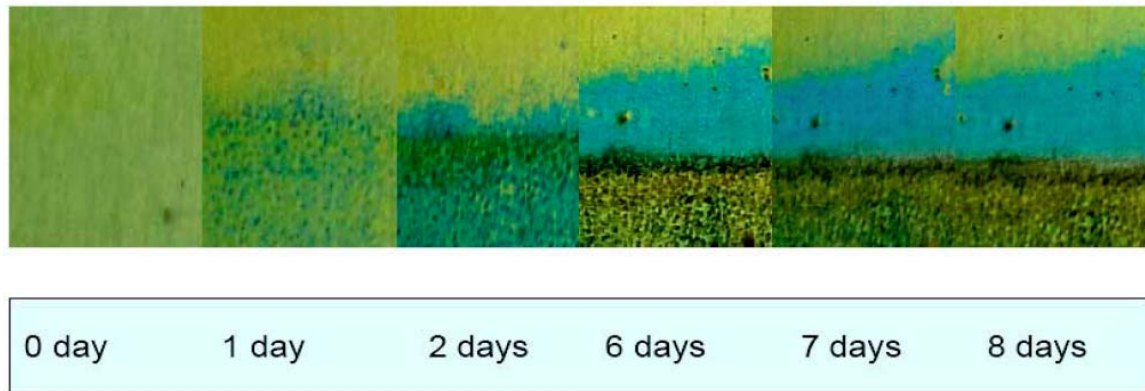


**Fig. 8.** Results of Accelerated Corrosion Testing on i-clays Integrated Coating System.

The ACT and Smart Coatings, as well as others military programs, are developing flexible electronic capabilities for sensing, communication, data collection/storage, and power alternatives. Flexible electronics have been developed allowing us to create several types of sensors. Some of the sensing capabilities include temperature, battle damage, scratch, flow, pressure, strain, impact, shock, pH, humidity, and acoustics. Other sensors capabilities are under development. The sensors will be selected and integrated into a tailorable sensor suite to develop custom systems and smart structures. Added capabilities will allow for real-time structural health monitoring of systems, advances in non-destructive testing, and battlefield damage assessments.

Advances in material printing and nanofabrication have allowed numerous types of sensors and systems to optimized and produced. The ability to cost effectively manufacture sensors on demand will revolutionize our ability to monitor the world around us.

These technologies and modules are designed to be integrated into active coating systems to have these coatings possess desired functionalities. The ability to have active, adaptive coatings systems that act more like a living entity than a typical passive coating system allows the coating to be utilized for military and civilian applications.

Prototype systems have been developed to assist with structural health monitoring, condition based maintenance and damage assessment. The embedded electronics can potentially sense changes in structural materials, in real-time, and alert the user of anomalies such as damage, corrosion, cracks, etc. The data can be collected and saved or used as an early warning system giving real-time status of the material or structures.

### 3. Conclusions

As technologies are developed and advanced, more capabilities can be added into military systems helping the U.S. Department of defense protect both national and international interests. The overall goal is to develop systems to be utilized on current military systems and to transition technologies to the field.

The need to protect our current and future military assets is obvious. It is in DOD's best interest to use the latest technologies to advance the protection of these assets. The current and future advances made in nanotechnology and MEMS are leading to the development of novel materials and systems that ultimately will allow the military to advance into the twenty-first century and beyond. Corrosion, material degradation, and coating failures are a serious cost driver for our military. Current coatings on

military systems are not capable of self-sustainment, or alerting the user of potential anomalies that can cost the DOD billions of dollars per year as well as the loss of equipment and lives.

The Active Coatings Technologies Program is helping to address this issue by integrating state-of-the-art technology into and on military systems. These technologies will result in new and modernized weapons systems fielded globally that are capable of meeting current and potential challenges.

## References

- [1]. Future Combat System (FCS): Article, [www.globalsecurity.org](http://www.globalsecurity.org)
  - [2]. Cost of Corrosion Report to Congress Jan 02: National Association of Corrosion Engineers (NACE), 2002.
  - [3]. Research performed on the Technology Demonstration for the Prevention of Material Degradation Program, U. S. Army Corrosion Office, U. S. Army ARDEC-RDECOM, Picatinny Arsenal, NJ.
  - [4]. Research performed on the Smart Coatings™ Materiel Program, U. S. Army Corrosion Office, U. S. Army ARDEC-RDECOM, Picatinny Arsenal, NJ.
  - [5]. J. Zunino III, et al, U. S. Army Development of Active Smart Coatings System for Military Vehicles, NSTI, Nanotech 2005.
  - [6]. J. Zunino III, et al, Development of Active Sensor Capabilities for the U. S. Army's Active Smart Coatings System, 2005, Tri-Service Corrosion Conference, Department of Defense & NACE.
  - [7]. H. C. Lim, M. Pulickal, S. Liu, G. A. Thomas, J. Zunino, and J. F. Federici, Material corrosion determination via Young's modulus measurement using flexible membrane force sensor, *Sensors and Actuators A*.
  - [8]. T. G. Gopakumar, W. Feng, M-W. Young, J. L. Zunino III, and M. Xanthos, Preparation and characterization of acrylic coatings containing functional nanoclays for sensing corrosion in ferrous and non-ferrous metals, *Journal Polymer Processing Society America*.
  - [9]. Functional Nanoclays as Corrosion Sensors in Smart Polymer Coatings, Research performed on the Active Coatings Technologies Program, U. S. Army Corrosion Office, U. S. Army ARDEC-RDECOM.
  - [10] S. Mitra et al, Wireless Enabled Sensors for Impact, Vibration, and Shock Detection, Active Coatings Technologies Program, 2005.
  - [11] M. Xanthos, J. L. Zunino III, W. Feng, M-Y. Young, S. H. Patel, Smart Polymeric Coatings – Recent Advances, *Advances in Polymer Technology*.
  - [12] J. L. Zunino, H. C. Lim, J. F. Federici, Cyclic thin film flexible strain sensor testing, SPIE Vol. 6463 Reliability, Packaging, Testing, and Characterization of MEMS/MOEMS VI, Jan., 2007, pp. 6463-10.
-

## Microfabrication and Characterization of an Integrated 3-Axis CMOS-MEMS Accelerometer

<sup>1</sup>Hongwei QU, <sup>2</sup>Deyou FANG and <sup>3</sup>Huikai XIE

<sup>1</sup>Department of Electrical and Computer Engineering, Oakland University, Michigan 48309 USA

<sup>2</sup>Freescale Semiconductor, Sensors and Actuators Division, Chandler, Arizona 85224 USA

<sup>3</sup>Department of Electrical and Computer Engineering, University of Florida, Florida 32611 USA

Tel.: (1)248-370-2205

Email: qu2@oakland.edu

*Received: 17 September 2007 /Accepted: 19 September 2007 /Published: 8 October 2007*

---

**Abstract:** This paper reports the fabrication and characterization of a monolithically integrated 3-axis CMOS-MEMS accelerometer with a single proof mass. An improved microfabrication process has been developed to solve the structure overheating and particle contamination problems in the plasma etching processes of device fabrication. The whole device is made of bulk silicon except for some short thin films for electrical isolation, allowing large sensing capacitance and flat device structure. A low-noise, low-power amplifier is designed for each axis, which provides 40 dB on-chip amplification and consumes only 1 mW power. Quasi-static and dynamic characterization of the fabricated device has been performed. The measured sensitivities of the lateral- and z-axis accelerometers are 560 mV/g and 320 mV/g, respectively, which can be tuned by simply varying the amplitude of the modulation signal. The over-all noise floors of the lateral- and z-axis are 12  $\mu\text{g}/\sqrt{\text{Hz}}$  and 110  $\mu\text{g}/\sqrt{\text{Hz}}$ , respectively when tested at 200 Hz. *Copyright © 2007 IFSA.*

**Keywords:** CMOS-MEMS, Integration, Accelerometer, Microfabrication, Characterization

---

### 1. Introduction

Monolithic 3-axis accelerometers have drawn great interests from both industry and academia [1-6]. Capacitive sensing is widely employed in these accelerometers due to its high sensitivity. Most of the commercially available 3-axis accelerometers are based on thin-film microstructures and majority of them use hybrid packages, whose performances are normally limited by the structure thickness, residual stress and parasitics [1, 4-6]. The noise floors of these reported 3-axis accelerometers are normally on the order of hundreds of  $\mu\text{g}/\sqrt{\text{Hz}}$ . By using some uncommon bulk micromachining

process, some 3-axis accelerometers with high resolutions have been demonstrated [3, 7]. High cost is a major concern for these devices due to the dedicated process steps.

A single-crystal silicon (SCS) 3-axis accelerometer was developed using CMOS-MEMS technology to achieve high resolution, small size and low cost simultaneously [8]. But it has two drawbacks. First, although most of the sensing structures are made of single-crystal-silicon (SCS), the z-axis sensing still employs Al/SiO<sub>2</sub> thin-film spring beams, which has poor temperature performance. Second, the silicon undercut for electrical isolation of substrate silicon also undercuts the silicon underneath comb fingers, which increases the comb-finger gap and in turn reduces the sensitivity and signal-to-noise ratio. Recently, a new sensor design and fabrication process were proposed by Qu *et al* [9] to overcome the drawbacks in [8]. Better temperature performance was achieved by employing a torsional SCS-based z-axis spring; and the comb-finger undercut problem was much alleviated by performing the electrical isolation formation and the sensing structures etching separately.

However, there are still two significant issues in [9]. First, the isolation trenches are prone to be contaminated in the following reactive ion etch (RIE) and deep-RIE (DRIE) processes, preventing capacitive comb fingers and other microstructures from being released successfully. Second, the overheating during the dry release step severely undercuts the sensing comb fingers and springs, increasing the comb-finger gaps and even causing device failure.

In this paper, a further modified CMOS-MEMS process is developed to resolve these two remaining issues. The detailed characterization of fabricated 3-axis accelerometers is also presented.

## **2. Structure and Interface Circuit Design**

The 3-axis CMOS-MEMS accelerometer reported in this paper features a single proof mass for 3-axis sensing, in which an imbalanced torsional z-axis sensing element is embedded in the lateral proof mass [9]. A two-stage dual-chopper amplifier (DCA) is integrated with the 3-axis accelerometer for each axis as the continuous-time readout circuit [10]. Detailed structure and circuit design are reported in [9] and [10], respectively.

Fig. 1 shows an SEM micrograph of a fabricated 3-axis accelerometer, where the dimensions of the lateral- and z-axis sensing elements are also given. The thickness of all the structures is about 35  $\mu\text{m}$  and the gap for all the comb-fingers is about 2.1  $\mu\text{m}$ . The length of the lateral- and z- axis sensing comb-fingers are 85  $\mu\text{m}$  and 55  $\mu\text{m}$ , respectively, both having the same width of 4.8  $\mu\text{m}$ . The length and width of z-axis torsional mechanical springs are 400  $\mu\text{m}$  and 4  $\mu\text{m}$ , respectively. The crag-leg springs for lateral axes have the same length and width of 320  $\mu\text{m}$  and 5  $\mu\text{m}$  in both directions. The proof mass has a footprint of 1 mm  $\times$  1 mm.

## **3. Fabrication Process**

The post-CMOS microfabrication reported in [9] improves the device performance by reducing the undercut on comb fingers and mechanical springs. This is accomplished by performing the electrical isolation etch and the final release of comb fingers and mechanical springs separately. Top metal layer (M4 in TSMC 0.35 $\mu\text{m}$  CMOS process that is used in this device) is only used to pattern the electrical isolation structures. After the isolation trenches are formed, as shown in the insets of Fig. 1, M4 is removed by wet or plasma aluminum etch to expose the patterns of other structures of the accelerometer.

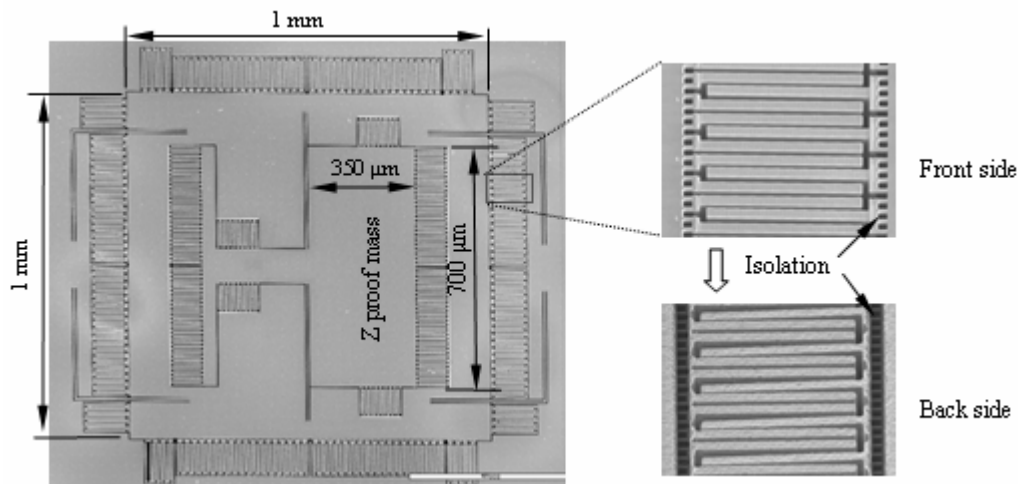


**Fig 1.** SEM photograph of the sensing element of the fabricated CMOS-MEMS 3-axis accelerometer. The insets show front and backside of the electrical isolation structures.

Some negative effects caused by the two-step etch process were observed. The first one is the contamination of the isolation trench formed after the first silicon DRIE. In the following plasma etching steps, including SiO<sub>2</sub> RIE and silicon DRIE, particles and polymers from assorted sources are prone to accumulate on the sidewalls of the isolation trenches. They act as micro masks in the last release DRIE step, preventing the microstructures from being completely etched through. Fig. 2 shows micro connections on the ends of sensing comb fingers. They result from the micro mask effect of the contaminants deposited on the isolation trench sidewall, and connect the rotor and stator sensing comb fingers together, making the proof mass unmovable.

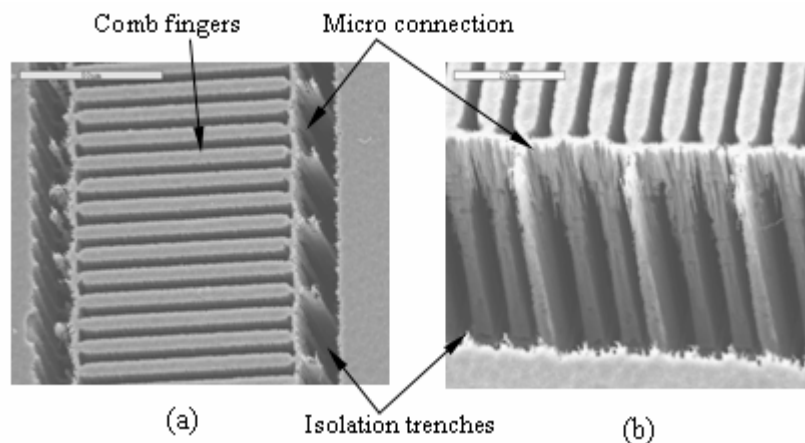


**Fig. 2.** SEM micrographs showing the micro connections caused by the contamination of the isolation trench in plasma etch steps. (a) top view; (b) side.

The second negative effect is the rapid silicon undercut of comb fingers and mechanical springs due to the overheating of these fine structures during the plasma etch. This undercut happens within a very short over-etch after the accelerometer is released. The reason for the severe undercut is the reduced thermal conductance from the comb fingers to the substrate. The heat generated from chemical reaction and ion bombardment in silicon DRIE can not be dissipated effectively, which consequently raises the temperature of the suspended microstructures. This positive feedback eventually leads to

high etching rate and the comb fingers will be undercut very quickly. The same effect was also observed on the z-axis sensing element where the heat can only be transferred through the two long torsional springs.

An improved process, as illustrated in Fig. 3, has been developed to overcome the above two effects.

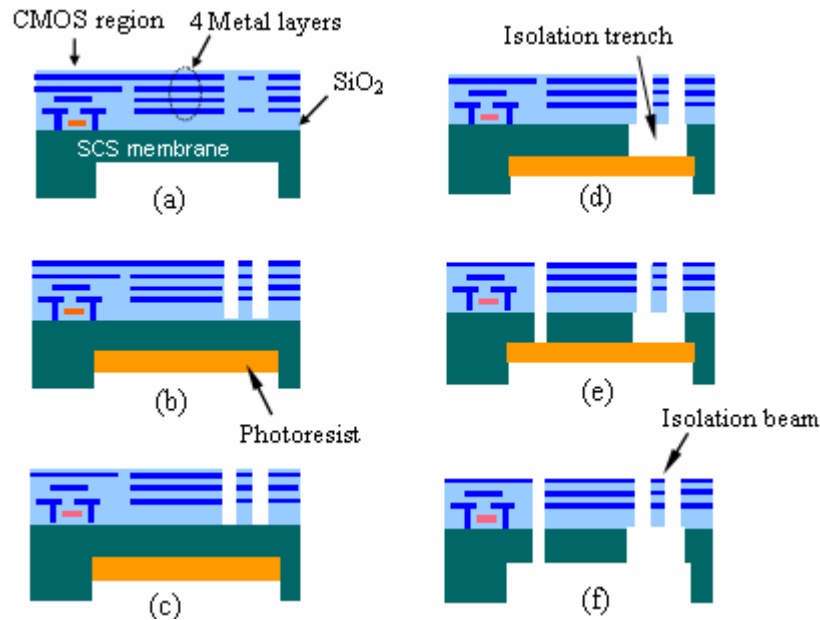
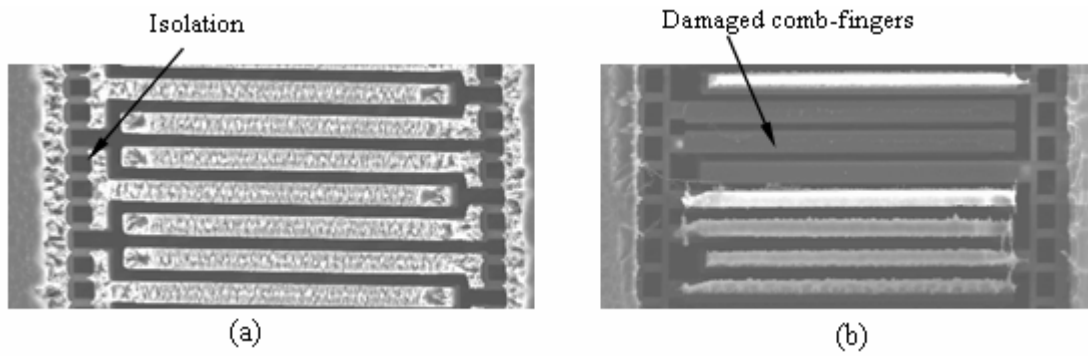


**Fig. 3.** Post-CMOS microfabrication process flow. (a) Backside etch. (b) Backside PR coating followed by front side anisotropic  $\text{SiO}_2$  etch. (c) Top Al etch. (d) Deep Si etch and undercut to form isolation structures. (e) Anisotropic  $\text{SiO}_2$  etch and DRIE Si etch for comb fingers and mechanical springs. (f) PR ashing for final release.

There is only one slight modification to the CMOS-MEMS process used in [9]. After the backside etch that produces a silicon membrane and defines the structure thickness (Fig. 3(a)), a thick sacrificial photoresist (PR) layer ( $\sim 50\mu\text{m}$ ) is applied on the back of the silicon membrane (Fig. 3(b)). After the isolation etching is completed (Fig. 3(c)-3(d)), this PR layer functions as a thermal path during the DRIE silicon etch that forms the entire microstructure (Fig. 3(e)). Finally, the PR is removed by oxygen plasma ashing to release the device (Fig. 3(f)). In Fig. 4, a comparison is made between sensing comb fingers fabricated with and without backside photoresist coating. The undercut of the silicon on comb fingers is greatly reduced and the finger damage is completely avoided by using the modified process (Fig. 4(a)). In contrast, without the PR layer as thermal path, electrical isolation trenches greatly reduce thermal flow from comb fingers to substrate. Consequently comb fingers are overheated and seriously undercut (Fig. 4(b)).

Furthermore, the PR layer helps reducing the backside contamination caused by back scattering. It also helps in tuning the isolation trench profile and relocating the contaminants on the sidewalls. As a consequence, microstructures can be completely released without the micro connections caused by the contaminant particles. This can also be observed in Fig. 4(a).

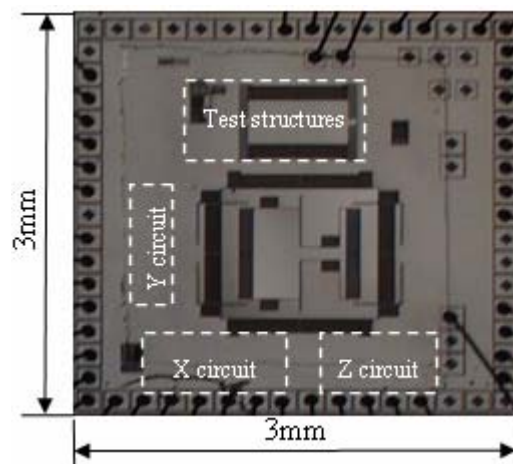
It should be noted that the thermal effect and the modified process described above are valid to many other MEMS devices with structures similar to this 3-axis accelerometer. A proper device design also helps in reducing the thermal problem described above. By considering the aspect-ratio dependent etching effect (ARDE), we can design the device in such a way that the etch-through sequence for different structures can be well controlled.



**Fig. 4.** Comparison of microstructures fabricated with and without backside PR coating. (a) With PR coating, the comb fingers are completely released with slight footing effect; (b) without coating, some comb fingers are completely damaged due to the heating effect.

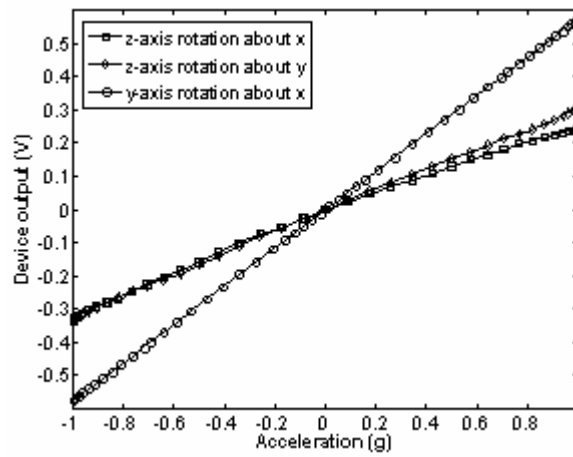
#### 4. Device Characterization

Fig. 5 is the photograph of a wire bonded die showing the locations of the 3-axis sensor and interface circuits. A dummy on-chip interface circuit was tested with an overall gain of 40 dB and a 16 nV/ $\sqrt{\text{Hz}}$  electronic noise floor was measured.



**Fig. 5.** Photograph of the wire bonded die.

The sensitivities in the lateral axes and z-axis were measured as 560 mV/g and 320 mV/g, respectively, at a 1.5 V modulation signal, by using a quasi-static rotation stage. The resonant frequency of z-axis was measured as 1.5 kHz using a Polytech laser vibrometer. It's about 15% lower than the simulated results, reflecting a remaining slight undercut to the mechanical springs in the plasma etch process. The resonant frequencies of lateral axes are still under test. Due to the asymmetry of the z-axis proof mass, the z-axis sensing element has relatively high cross-axis sensitivities which were measured to be 2.1% from the x-axis and 4.7% from the y-axis, as shown in Fig. 6. The noise measurement was conducted using a LDS shake table and SRS network spectrum analyzer. The spectral response of the z-axis output at a 200 Hz, 0.5-g external acceleration is shown in Fig. 7. The overall noise floor of the z element is 110  $\mu\text{g}/\sqrt{\text{Hz}}$ . Although both x- and y-axis have the same number of identical sensing comb-fingers, there is a slight sensitivity difference between these two lateral axes due to the arrangement of the mechanical springs. The spectrum of y-axis output under a 200 Hz, 0.05-g acceleration is shown in Fig. 8. A noise floor of 12  $\mu\text{g}/\sqrt{\text{Hz}}$  is demonstrated.



**Fig. 6.** Static test results of the z- and y- axis using a precision rotary stage.

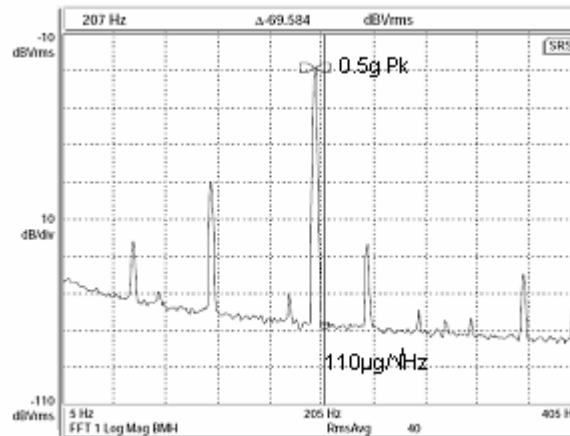


**Fig. 7.** The spectrum of the z-axis output under 0.5g at 200 Hz (RBW = 1Hz).

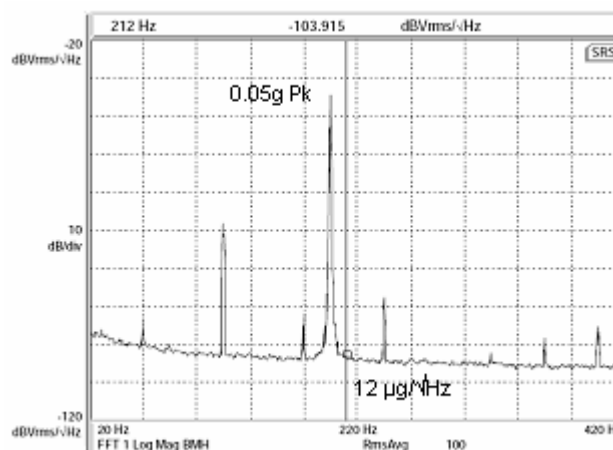


**Fig. 8.** The spectrum of the y-axis output under 0.05g at 200 Hz (RBW = 1Hz).

An overall temperature coefficient of sensitivity (TCS) of approximately 0.28%/°C was measured, which is mainly caused by the gain drifting of the first open-loop amplification stage of the on-chip

amplifier. This is verified by circuit simulation, and a temperature insensitive amplifier is under design. In order to measure the temperature-dependent curling of the sensing comb drives, a band heater was taped on the back of the PLCC-52 sensor package, and the sensor temperature was measured by a spot thermocouple. The vertical curling of the sensing comb fingers was measured using a Wyko optical profilometer. A maximum negative 0.533  $\mu\text{m}$  net curling at the free end of the comb-fingers was measured in a temperature range from room temperature to 96°C. Since the sensor structure thickness is about 50  $\mu\text{m}$ , the corresponding change of the electrode engaged area was approximately 0.23%. Based on these data, a positive 304 ppm/°C temperature coefficient of sensitivity (TCS) of the lateral-axis sensing was derived. Due to the complete SCS structure, temperature-induced structure curling was not observed on the z-axis sensing element.

The measured performance of the device is summarized in Table 1. As a comparison, the performance of ADXL330, a 3-axis accelerometer from ADI, is included.

**Table 1.** Performance summary of the reported device and comparison with ADXL330 from ADI [1].

| Parameters  | Measured values |               |
|---|-----------------|---------------|
|   | This work       | ADXL330       |
| Chip size (mm × mm)   | 3×3             | 4×4 (package) |
| Lateral axes sensitivity (mV/g)                             | 560             | 300           |
| Z axis sensitivity (mV/g)                                   | 320             | 300           |
| Circuit noise floor (nV/ $\sqrt{\text{Hz}}$ )               | 16              | -             |
| Power consumption of each axis (mW)                         | 1               | 0.64~1.15     |
| Lateral axes noise floor ( $\mu\text{g}/\sqrt{\text{Hz}}$ ) | 12              | 170           |
| Z axis noise floor ( $\mu\text{g}/\sqrt{\text{Hz}}$ )       | 110             | 350           |
| Sensitivity temperature drift (%/°C)                        | 0.28            | 0.01          |

## 5. Conclusion

A 3-axis CMOS-MEMS accelerometer with a single proof mass has been demonstrated in this work. The single-crystal silicon incorporated in the device ensures robust sensor structures and high resolution. Low-power consumption (1 mW for each axis) and low-noise floors in all three axes are achieved simultaneously with a compact device size. Compared to the previous processes, this modified post-CMOS microfabrication process has greatly increased the release yield by removing and relocating the contaminants generated in the plasma etching process. It also has increased the process tolerances by providing additional thermal path to the suspended microstructures in plasma etching processes. Though only photoresist was used in this work, there exist many other more suitable materials for the additional heat dissipation. This method can be widely used in micromachining MEMS devices with similar suspended structures. Due to its small size, low power consumption and high resolution, this 3-axis accelerometer has a variety of applications including health monitoring, video games and infrastructure securities.

## Acknowledgements

This project is partially supported by the NASA/UCF-UF Space Research Initiative and University of Florida Startup Fund. The CMOS chip fabrication was supported by MOSIS through its Educational Program.

## References

- [1]. Analog Device, Inc., ADXL330 low-power, 3-axis accelerometer, *Datasheet, Rev. PrA.*, Oct. 2005.
- [2]. M. Lemkin and B. E. Boser, A three-axis micromachined accelerometer with a CMOS position-sense interface and digital offset-trim electronics, *IEEE Journal of Solid-State Circuits*, Vol. 34, 4, 1999, pp. 456-468.
- [3]. J. Chae, H. Kulah, and K. Najafi, A monolithic three-axis micro-g micromachined silicon capacitive accelerometer, *Journal of Microelectromechanical Systems*, Vol. 14, 2, 2005, pp. 235-242.
- [4]. Freescale Semiconductor, *MMA7260Q Datasheet, Rev. 2.*, Mar. 2006.
- [5]. Bosch Sensortec GmbH, *SMB360 Accelerometer Datasheet*, Ver. 1.0-112005, May 2005.
- [6]. ST Microelectronics, LIS3L02AQ3 MEMS linear inertial sensor, May 2005.
- [7]. H. Takao, H. Fukumoto, and M. Ishida, A CMOS integrated three-axis accelerometer fabricated with commercial submicrometer CMOS technology and bulk-micromachining, *IEEE Transactions on Electron Devices*, vol. 48, 9, 2001, pp. 1961-1968.
- [8]. H. Xie, Z. Pan, W. Frey, and G. Fedder, Design and Fabrication of an Integrated CMOS-MEMS 3-Axis Accelerometer, *The 2003 Nanotechnology Conference*, San Francisco, CA, Feb. 23-27, 2003, pp.292-295.
- [9]. H. Qu, D. Fang, and H. Xie, A single-crystal silicon 3-axis CMOS-MEMS accelerometer, *Proceedings of IEEE Sensors 2004*, Vienna, Austria, Oct. 24-27, 2004, pp.661-664.
- [10]. D. Fang, H. Qu, and H. Xie, A 1mW Dual-Chopper Amplifier for a 50- $\mu\text{g}/\sqrt{\text{Hz}}$  Monolithic CMOS-MEMS Capacitive Accelerometer, *Technical Paper Digests of 2006 Symposium on VLSI Circuits*, Honolulu, HI, Jun. 15-17, 2006, pp.59-60.

---

2007 Copyright ©, International Frequency Sensor Association (IFSA). All rights reserved.  
(<http://www.sensorsportal.com>)

## FIRST MEDITERRANEAN PHOTONICS CONFERENCE

*Jolly Hotel, Ischia  
25-28 June 2008*

**A European Optical Society Topical Meeting  
Organized by Italian Optics and Photonics Society**

**General chairman: Prof. Antonello Cutolo  
Co-chairs: Prof. Mario Armenise, Prof.ssa Roberta Ramponi**

### Preliminary list of topics

Polymers, carbon nanotubes and metamaterials  
for photonics  
Post silicon materials, devices and technology  
Micro and nanophotonics devices  
Photonic crystals  
Optical fibers, guided and integrated optics

### *And their applications to*

Telecommunications  
Non linear optics  
Optical sensors  
Optical contactless characterization techniques  
High precision measurements  
Industrial applications  
Aeronautics and aerospace  
Underwater applications  
Structural and environment monitoring  
Biosensors  
Homeland security



**Deadline for submitting a four page summary: March 31st 2008  
Acceptance notification by April 30<sup>th</sup> 2008  
To receive further informations, please, contact:  
[paola.ambrosino@unisannio.it](mailto:paola.ambrosino@unisannio.it)**

## Characterization and Optimization Design of the Polymer-based Capacitive Micro-arrayed Ultrasonic Transducer

**De-Yi CHIOU, Mu-Yueh CHEN, Hsu-Cheng DENG, Ming-Wei CHANG**

RFID and Security Technology Center/Industrial Technology Research Institute  
Rm. 217, Bldg. 52, 195, Sec. 4, Chung Hsing Rd., Chutung, Hsin-Chu 310, Taiwan, R.O.C.  
Tel.: +886-3-5919166

E-mail: [charleschiou@itri.org.tw](mailto:charleschiou@itri.org.tw), <http://www.itri.org.tw/index.jsp>

*Received: 17 September 2007 /Accepted: 19 September 2007 /Published: 8 October 2007*

---

**Abstract:** The polymer-based capacitive micro-arrayed ultrasonic transducers have been investigated using the finite element analysis. The ANSYS Multiphysics solver with sequential approach and the physics environment files are applied for the solution of the electrostatic-structural coupled-field problem. A 2-D electromechanical model is established to characterize the collapse voltage and the resonant frequency of the P-CMUT. Both the numerical and experimental results were in good agreement. An integrated multi-objective design method involving electrical and mechanical characterization was developed to optimize the geometric parameters of the P-CMUT. The optimization search routine conducted using the genetic algorithm (GA) is connected with the ANSYS model to obtain the best design variable. The optimal results show that the proposed approach provides another efficient and versatile numerical tool for multi-objective design and optimization of the P-CMUT. *Copyright © 2007 IFSA.*

**Keywords:** Polymer-based, Capacitive ultrasonic transducer, Finite element method, Optimization

---

### 1. Background

The capacitive micromachined ultrasonic transducer (CMUT) has exists for decades and used for the excitation and detection of acoustic waves [1]. The CMUT has been proven to be an alternative to piezoelectric transducers in terms of superior efficiency and performance. Much works have been done on developing the CMUT by many research groups, such as in Stanford Ginzton Lab, GE Corp., Siemens Corp., and VTT organizations [2, 3].

The polymer-based capacitive micro-arrayed ultrasonic transducer (P-CMUT), pioneered by Chang, et al. since 2005 [4], is proposed for use in air-coupled transmission and detection. The P-CMUT has been demonstrated to be a more attractive alternative to conventional CMUT in terms of “flexibility” that possesses much potential to apply in many areas, ranging from non-destructive evaluation (NDE) to medical-diagnosis imaging system. The market-driving benefits from the batch fabrication capability, low material cost, and flexibility of the device are acquired [5].

Previous research has led to many improvements in CMUT design. Several mathematical models are developed for fast and simple simulation. However, the simplified mathematical models have difficulties when approximating the complex geometric constraints and coupled-field nature is met. To overcome these limitations, many researchers have used the finite element model (FEM) to develop an accurate analysis model to verify both theoretical and experimental results [6, 7]. This paper continues with the use of finite element modeling to investigate the effects of two important factors for P-CMUT operation in view of electrical and mechanical performance simultaneously. These factors are the collapse voltage and the operating frequency, respectively. Moreover, the multi-objective optimization design approach for the P-CMUT using the genetic algorithm (GA) is also presented in this paper.

## 2. Finite Element Modeling

The modeling components of the P-CMUT include the membrane, passivation layer, top electrode, ground electrode, insulation layer, post, and silicon substrate. The suspended membrane is supported at edging post. The major parts of the transducer: membrane, passivation layer, and post are made of an epoxy-type photoresist (SU-8). The passivation layer is used to protect the aluminum (Al) top electrode from ambience wearing and corrosion. A thin insulation layer of silicon oxide ( $\text{SiO}_2$ ) over the grounded electrode of platinum (Pt) prevents short circuit in case of membrane collapse. A thin film of titanium (Ti) is evaporated over the highly doped silicon (Si) substrate as a bonding interface layer between ground electrode and silicon substrate. The air in cavity between the membrane and the substrate is included in the model.

Ideally, a 3-D mesh for the full model should be made, but from a computational efficiency point of view, an axisymmetric 2-D mesh that represents 3-D circular cell structure gives much faster results. Therefore, in this research, a 2-D finite element model was established using the commercial FEM package (ANSYS 9.0, [8]). The finite element model of the P-CMUT was created using APDL (ANSYS parametric design language) programming technique in terms of given parameters or variables. Fig. 1 shows the 2-D finite element model and the corresponding APDL parameters. Table 1 lists the geometric dimensions of the P-CMUT base line model.

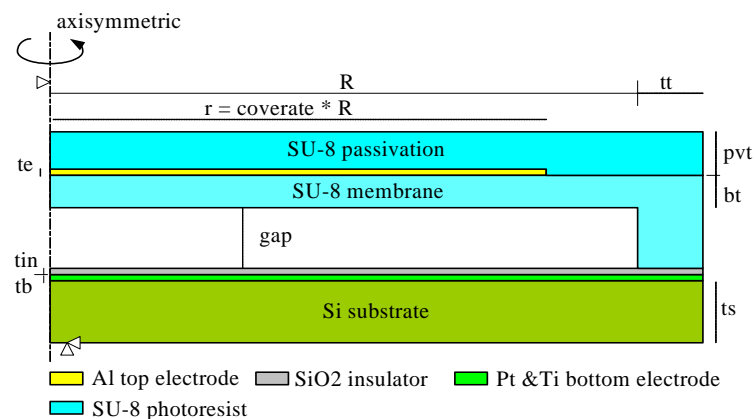


**Fig. 1.** APDL Parameterized P-CMUT base line model.

**Table 1.** Geometric dimensions of the P-CMUT model.

| Component                   | APDL parameter |      |               |
|-----------------------------|----------------|------|---------------|
| Membrane radius             | R              | 50   | $\mu\text{m}$ |
| Top electrode coverage      | cov            | 0.6  |               |
| Top electrode outer radius  | r (=R*cov)     | 30   | $\mu\text{m}$ |
| Passivation layer thickness | pvt            | 2.8  | $\mu\text{m}$ |
| Top electrode thickness     | te             | 0.2  | $\mu\text{m}$ |
| Membrane thickness          | bt             | 2    | $\mu\text{m}$ |
| Cavity gap                  | gap            | 2    | $\mu\text{m}$ |
| Insulator thickness         | tin            | 0.03 | $\mu\text{m}$ |
| Bottom electrode            | tb             | 0.17 | $\mu\text{m}$ |
| Silicon substrate           | ts             | 2    | $\mu\text{m}$ |
| Post thickness              | tt             | 5    | $\mu\text{m}$ |

The ESSOLV macro, an ANSYS built-in iterative solver, is employed for the solution of the electrostatic-structural coupled-field problems. The sequential method is adopted and two Physics Environments files that respectively represent the structural and electrostatic fields are created for a single model. The coupled-field iterations are controlled via the designed convergence criterion and finished when the convergence condition was met.

ANSYS standard elements, PLANE82 and PLANE121, are used for structural and electrostatic Environment files, respectively. The contact-target pair surface elements (CONTA172 and TARGE 169) were used for modeling the contact with the surfaces between membrane and insulation layer. The offset from the insulation layer was set 0.02  $\mu\text{m}$ . to robustly remorph the mesh in the air gap while the membrane is collapsed. In the structural field, the vertical symmetry plane with no displacements in x-direction is applied. In addition, a fully fixed boundary condition on the bottom of the substrate is applied. In the electrostatic field, a nonzero voltage is applied to the borders of the top electrode, and a zero voltage is set on the ground electrode.

The mechanical and electrical properties used in the FEM calculations are listed in Table 2. In this study, the material property testing of SU-8 is performed using a commercial nanoindentation system. The measured elastic modulus of the SU-8 was 5.18 GPa.

**Table 2.** Geometric dimensions of the P-CMUT model.

| Component       | Membrane/<br>Passivation/<br>post | Insulator        | Top<br>electrode | Bottom<br>electrode | Substrate | Air<br>gap | Unit              |
|-----------------|-----------------------------------|------------------|------------------|---------------------|-----------|------------|-------------------|
| Material        | SU-8                              | SiO <sub>2</sub> | Al               | Pt                  | Si        | Air        |                   |
| Young's modulus | 5.18 E9                           | 7.5 E10          | 6.76 E10         | 1.7 E11             | 1.69 E11  |            | N/m <sup>2</sup>  |
| Density         | 1200                              | 2200             | 2700             | 2140                | 2332      |            | Kg/m <sup>3</sup> |
| Poisson's ratio | 0.22                              | 0.17             | 0.3555           | 0.38                | 0.27      |            |                   |
| Permittivity    | 3                                 | 3.9              |                  |                     | 11.8      | 1          |                   |

### 3. Characterization of P-CMUT

The performance of the P-CMUT can be referred to two important factors for CMUT operation. These factors are the collapse voltage and the operating frequency. In this section, the FEM was used to investigate the collapse voltage and resonant frequency with varied bias voltage. The performance is typically dependent on the operating DC bias, which should be close to the collapse voltage. Due to the usage dangers and material breakdown associated with high voltage, the collapse voltage should be limited. Hence, accurate determination of the collapse voltage is necessary. A relationship of the DC bias versus maximum membrane deflection is shown in Fig. 2. As shown in Fig. 2, the displacement asymptotically increases as the bias voltage is increased. The calculated collapse voltage is 551 V. The ZYGO surface profiler (Model NewView 200, ZYGO Corp., Middlefield CT) is used to measure the membrane deflection with bias voltage from 0 V to 280 V. Fig. 3 shows the comparison between the experiment and numerical results, and an agreeable prediction by simulation is obtained.

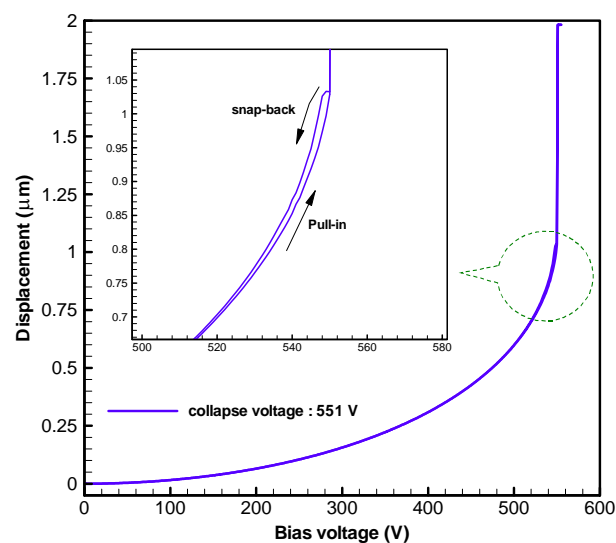


**Fig. 2.** Maximum membrane displacement as a function of applied bias voltage.

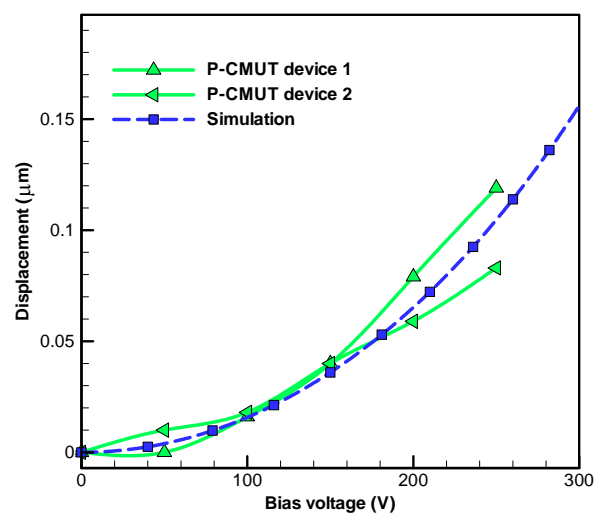


**Fig. 3.** A comparison of the membrane deflection between the numerical and experiment results.

Air-coupled transducers are typically operated at their resonant frequency in order to generate ultrasonic waves that are correctly matched with the acoustic impedance of the air. A receiving transducer should

also be operated at their resonant frequency to increase the overall bandwidth of the device. The FEM is also used to determine the membrane resonant frequency through the use of prestressed modal analysis. The prestressed modal analysis is conducted to calculate the eigenfrequencies of the P-CMUT device.

First, the static deflection due to a bias voltage is calculated. Next, the PSTRESS,ON command is used to introduce prior electrostatic results which will be reused as starting point for future solutions. The resonant frequency of the membrane was then calculated using Block Lanczos solutions and the first modal (resonant) frequency was obtained. Fig. 4 shows the resonant frequency shift as a function of applied bias voltage. It demonstrates a decrease in resonant frequency with increasing voltage. The nonlinear spring softening phenomenon is confirmed. The resonant frequency with bias voltage 250 V was 1.683 MHz. The resonant frequency is also measured by using a heterodyne Doppler laser interferometer. The membrane was electrically excited by single burst of pulse with a peak-to-peak voltage 16V, time interval 50nsec and bandwidth 40 MHz. Fig. 5 shows the vibration response amplitude as a function of frequency. The first resonance peak is found at 1.594 MHz, which is in agreement with the numerical result.

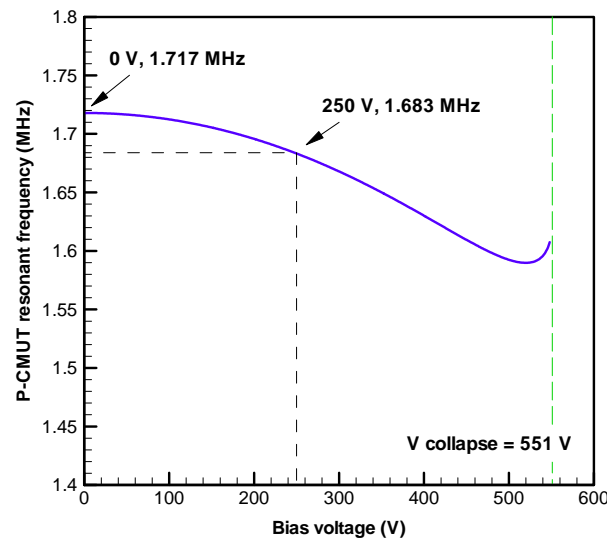


**Fig. 4.** Resonant frequency as a function of applied bias voltage (spring softening effect).

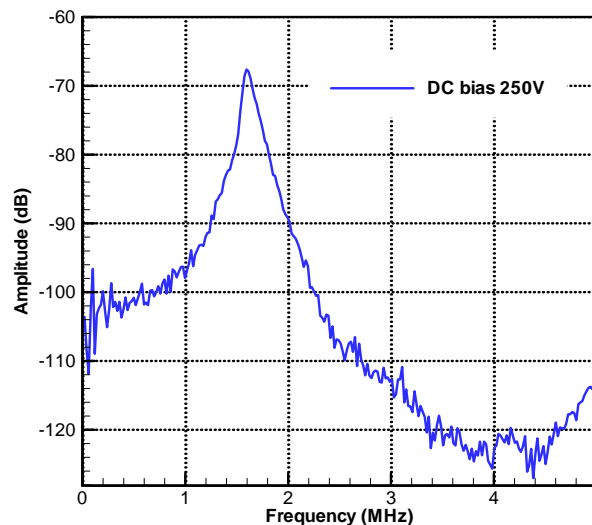


**Fig. 5.** Vibration amplitude excited by single pulse.

#### 4. GA Optimization Design of P-CMUT

From mechanical and electrical qualification viewpoints, the better designing of the P-CMUT is to customize its operating frequency and to reduce the collapse voltage as small as possible. However, these two parameters are mutually affected oppositely and contradictory results are usually encountered. Therefore, considerations with overall physical fields to improve performance and efficiency must be made. To solve this problem of conflict, an integrated multi-objective design approach was applied to optimize the geometric parameters of the P-CMUT.

In this study, the genetic algorithm (GA) is used to search through a large number of possible solutions to discover the best specific solution. It's a problem-solving technique that attempts to evolve the solutions in a random search manner as much as nature does. Much of the original work on GA was done by Holland [9]. Many GA applications and designs coupled with the FEM can be found in [10, 11]. The population is randomly created at the start of the GA search. The GA encodes the values of decision variables in a string called "chromosome". The string is interpreted as simply a string of binary digits. Each bit can be regarded as a "gene" in a chromosome. Each individual represents one possible solution to the problem. The individual's chromosome encodes one set of decision variables and so results in a single point in the solution space. Three operators, selection, crossover and mutation, are used on the population of individuals. Fitness is used to select individuals from the current generation to advance into the next generation. These individuals are recombined and possibly mutated to form the next generation. Search progress evaluation is based on the fitness alone, which keeps the search focused on the actual objective function. The treatment of the objective function is simple; no complex calculation such as derivation is necessary. This search process is continued until there is no change in the best individual in the population.

**Table 3.** The genetic parameters, schemes, and optimal results of the 1 MHz P-CMUT.

| Designated parameter         | Lower Limit | Upper Limit | Optimized result |    |
|------------------------------|-------------|-------------|------------------|----|
| Membrane radius              | 25          | 75          | 65.01276         | μm |
| Passivation layer thickness  | 2.8         | 5           | 2.815943         | μm |
| Top electrode thickness      | 0.1         | 0.5         | 0.213794         | μm |
| Top electrode coverage ratio | 0.1         | 1.0         | 0.867297         |    |
| Fitness                      | 0.00552762  |             |                  |    |
| Number of generation         | 100         |             |                  |    |
| Number of population         | 30          |             |                  |    |

**Objective functions:**

- Minimize the collapse voltage ( $V_{\text{collapse}}$ : 291 V)
- Resonant frequency = 1 MHz

By taking advantages of parametric modeling technique, the optimization search routines [11] can be easily combined with the ANSYS to obtain the best design variables. Four parameters (membrane diameter, passivation layer thickness, top electrode thickness, and top electrode coverage) that mostly affect the collapse voltage and resonant frequency were chosen as design variables and their variation limits were designated. One objective function assigned for electrical characterization is the minimization of the collapse voltage for user safety and energy consumption issues. The other objective function assigned for mechanical characterization is setting the resonant frequency to achieve the desired operation frequency (e.g. 1 MHz). The number of the population and the generation is 30 and 100, respectively. Both the design objectives were given the same weighting. Table 3 lists the design variable optimization results of the P-CMUT. The optimal membrane radius is increased to 65.01 $\mu\text{m}$  and

the top electrode coverage ratio is increased to 0.87. The optimal thickness of passivation layer and top electrode is  $2.82\mu\text{m}$  and  $0.21\mu\text{m}$ , respectively. The solutions show that the optimal P-CMUT design with approached to 1 MHz resonant frequency and lowest collapse voltage (lower to 291V) of demands were acquired. Fig. 6 shows the convergence of the design history involving multi-objective functions over the generations. The fitness value is converged to 0.00552762 at the 48<sup>th</sup> generation. It is concluded that the proposed approach provides another efficient and versatile numerical tool for multi-objective design and optimization for the P-CMUT.

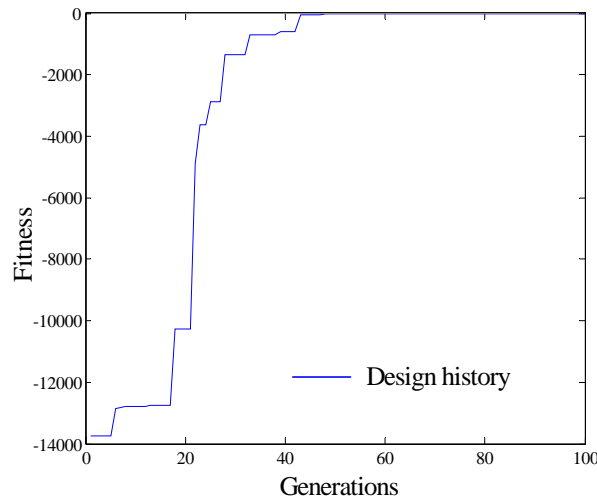


**Fig. 6.** Design history of multi-objective functions versus 100 generations.

## 5. Conclusions

This paper presented finite element modeling developed using ANSYS v.9.0 to illustrate two important operation parameters, the collapse voltage and resonant frequency of the P-CMUT. A 2-D axisymmetric model was built by APDL programming techniques in terms of parameters. It was used to calculate the relationship between membrane deflection and resonant frequency with applied DC bias voltage. The membrane of the P-CMUT is made of SU-8, and its material property is measured using the nanoindentation system. The tested Young's modulus of SU-8 was 5.18 GPa and it was introduced to the FEM model. The calculated maximum displacement of membrane versus DC bias voltage is shown in agreement with that obtained by ZYGO surface profiler. The calculated collapse and snapback voltage is 551V. The prestressed modal analysis produced a resonant frequency of 1.683MHz with biased 250V, which coincides with the experiment results (1.594 MHz) using laser interferometer. The spring softening effect that demonstrates the resonant frequency shift as increasing DC bias voltage is illustrated.

The objective of designing the P-CMUT is to customize its operating frequency and to reduce the collapse voltage as small as possible. In order to make an integral consideration for both electrical and mechanical fields to improve the efficiency and reliability, an integrated design method for the P-CMUT was discussed. A typical genetic algorithm was employed to connect the existed analysis model to conduct the optimization study for obtaining the best design variables using multi-objective functions. The membrane radius was  $65.01\mu\text{m}$  with a 30% increase from the original design. The top electrode coverage ratio was increased to 0.87. The passivation layer and top electrode thickness is  $2.82\mu\text{m}$  and  $0.21\mu\text{m}$ , respectively. The optimal solutions show the two designated objective functions were successfully attained. The corresponding resonant frequency is 1MHz and the collapse voltage is reduced to 291V. A complete and powerful optimal window for P-CMUT design was thus established.

## Acknowledgements

The authors would like to thank the Industrial Technology Research Institute (ITRI) and the Ministry of Economic Affairs (MOEA), R.O.C., for financially supporting this research under grant No.6365C52200. The authors also acknowledge Professor B. T. Khuri-Yakub at the Ginzton Lab., Department of Electrical Engineering, Stanford University in U.S.A., for his helpful inputs and assistance on measurements during this research

## References

- [1]. M. I. Haller and B. T. Khuri-Yakub, A surface micromachined electrostatic ultrasonic air transducer, In *Proceedings of IEEE Ultrasonic Symposium*, Vol. 2, 1994, pp. 1241-1244.
- [2]. D. M. Mills and L. S. Smith, Real-Time In-Vivo. Imaging with capacitive micromachined ultrasound transducer (cMUT) linear arrays, In *Proceedings of IEEE Ultrasonic Symposium*, Vol. 1, 2003, pp. 568-571.
- [3]. A. Lohfink, P.-C. Eccardt, W. Benecke and H. Meixner, Derivation of 1D CMUT model from FEM results for linear and nonlinear equivalent circuit simulation, In *Proceedings of IEEE Ultrasonic Symposium*, Vol. 1, 2003, pp. 465-468.
- [4]. M. W. Chang, T. M. Deng, T. J. Gwo, J. D. Mai, E. Hsu, Polymer-based capacitive micromachined ultrasonic transducers (CMUT) for micro surgical imaging applications, In *IEEE-NEMS conference*, 2006, pp. 18-21.
- [5]. G. Harsányi, Polymer Films in Sensor Applications, *Technomic Publishing*, 1995.
- [6]. G. G. Yaralioglu, A. S. Ergun, B. Bayram, T. Marentis and B. T. Khuri-Yakub, Residual stress and Young's modulus measurement of capacitive micromachined ultrasonic transducer membranes, In *Proceedings of IEEE Ultrasonic Symposium*, Vol. 2, 2001, pp. 953-956.
- [7]. I. Ladabaum, X. Jin, H. T. Soh, A. Atalar, B. T. Khuri-Yakub, Surface micromachined capacitive ultrasonic transducers, *IEEE Transactions on Ultrasonics, Ferroelectrics and Frequency Control*, Vol. 52, 1998. pp. 678-690.
- [8]. ANSYS 9.0, ANSYS Inc., Canonsburg, PA.
- [9]. J. H. Holland, *Adaptation in Natural and Artificial Systems*, University of Michigan, 1975.
- [10]. K. Deb and S. Gulati, Design of truss-structures for minimum weight using genetic algorithms, *Finite Elements in Analysis and Design*, Vol. 37, 2001, pp. 447-465.
- [11]. D. S. Liu, C. Y. Ni and C. Y. Chen, Integrated design method for flip chip CSP with electrical, thermal and thermo-mechanical qualifications, *Finite Elements in Analysis and Design*, Vol. 39, 2003, pp. 661-677.

## Fabry-Perot Diaphragm Fiber Optic Sensor (DFOS) for Acoustic Detection

**Yan SUN, Guanhua FENG, George GEORGIU, Edip NIVER, \*Karen NOE  
and Ken CHIN**

Department of Physics, Materials Science Program, New Jersey Institute of Technology

161 Warren St., Newark, NJ 07102, USA

\*PSE&G Corporation, Newark, NJ, USA

Tel.: 1-973-642-7738

E-mail: [ys2@njit.edu](mailto:ys2@njit.edu)

*Received: 17 September 2007 /Accepted: 19 September 2007 /Published: 8 October 2007*

---

**Abstract:** A diaphragm fiber optic sensor (DFOS) solely based on Fabry-Perot multiple beam interference has been designed and fabricated with micro-electric mechanical system (MEMS) technology. The silicon diaphragm with an embossed center was designed with an interference gap width kept accurately. The DFOS was verified to be a truly and purely Fabry-Perot device via a critical test. Parallel testing with a Piezoelectric (PZT) sensor showed that the DFOS had high sensitivity. The Fabry-Perot DFOS also demonstrated excellent performance in on-line monitoring of Partial Discharge (PD) in power transformers. *Copyright © 2007 IFSA.*

**Keywords:** MEMS, Fabry-Perot, Fiber optic, Acoustic, Diaphragm with embossed center

---

### 1. Introduction

A diaphragm fiber optic sensor (DFOS) utilizes a diaphragm as the sensing element to detect static and dynamic pressure (acoustic wave). The fiber is used to deliver a steady probing light and to receive the reflected light modulated by the signals under detection. In recent years a great deal of efforts have gone into developing diaphragm-based fiber optic sensors for static pressure and acoustic signal detection to take advantage of optic sensors' high sensitivity, flexibility, versatility of diaphragm-fiber structure, resistance to electromagnetic interference (EMI) caused noise, and easiness for multiplexing and integration [1-4]. In this research, the silicon diaphragm was designed to have an embossed center

in order to improve efficiency, alignment, linearity, and Q-point stability, which are critical issues in diaphragm-based fiber optic sensor design.

Currently an imminent application of DFOS is detecting partial discharge (PD) in high voltage transformers in the power industry. PD is an electrical discharge that occurs in an insulation system where the discharge does not completely bridge the electrodes. It is a well-known phenomenon and a precursor to complete insulation failure. Partial discharge within the power transformer could lead to degradation of the insulation system that may result in catastrophic failures [5-9]. It is a big concern for the power industry. As a consequence, there is a strong need for a capable sensor to detect and study PD.

## 2. Sensor System Design

The developed DFOS acoustic detection system is illustrated schematically in Fig. 1. It consists of a DFOS, a 1527 nm DFB laser, a 3-port fiber circulator, a photodiode, a filter & amplification circuit, and an oscilloscope. Light from the DFB laser propagates along the single mode fiber to the DFOS through the circulator and interferes inside the DFOS. The modulated light propagates back in the third leg of the circulator and is detected by the photodiode. The optical signal is turned into electric signal, which is then filtered and amplified, and finally processed and collected by the oscilloscope.

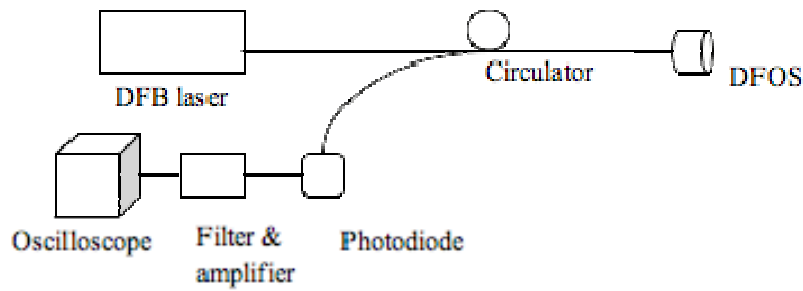


**Fig. 1.** Schematic of DFOS system.

A Fabry-Perot interferometric device is based on the interference of multiply reflected beams. The interference gap  $L$  corresponding to the applied pressure is determined by measuring the inference spectrum. The ratio of optical power output and input is defined as

$$\frac{I^{(0)}}{I^{(i)}} = \frac{2R_a - 2R_g \cos \phi}{1 + R_g^2 - 2R_g \cos \phi}, \quad (1)$$

where  $R_a$  is the arithmetic mean reflectance of the interfaces,  $R_g$  is the geometric mean reflectance of the interfaces, and  $\phi$  is the phase shift of the light propagating across the interference gap  $L$ .

The mechanism of DFOS is usually described by the Fabry-Perot interference of multiply reflected beams between the diaphragm surface and the fiber end surface. The structure of a DFOS is shown in Fig. 2. The diaphragm, as the sensing element, is batch fabricated on a silicon wafer with MEMS technology and soldered to a single mode optic fiber to keep the sensor cavity at Q-point. Fabry Perot interferometry is formed between the fiber end face and diaphragm inner surface. The incident light is partially reflected at the end face of the fiber. The remainder of the light crosses the air gap, gets partially reflected at the inner surface of the diaphragm and transmitted back to the fiber. The acoustic

pressure changes the air gap and modulates the light transmitted back through the fiber. Sensitivity, efficiency and frequency response etc. are determined by the geometry of the diaphragm. Therefore the diaphragm is a critical part of sensor design.

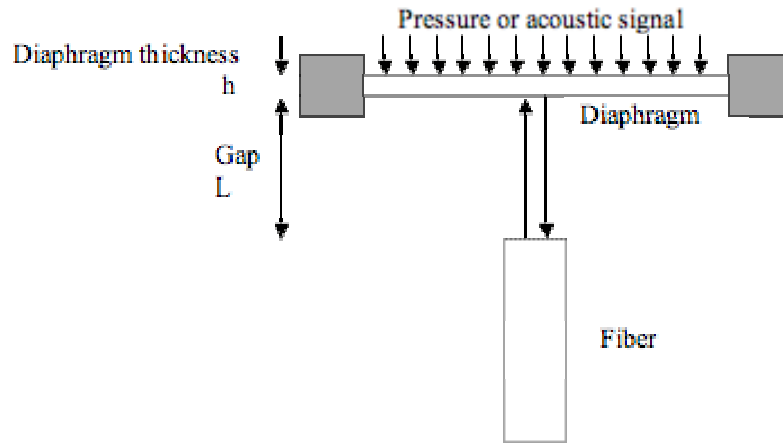


**Fig. 2.** Principle of Diaphragm Fiber Optic Sensor (DFOS).

The selection of diaphragm thickness and side length is based on the pressure range and acoustic frequency at which the device is required to operate. The center deflection  $y_0$  (m) of a flat square diaphragm under pressure may be expressed by Equation 2 [10, 11]:

$$y_0 = \alpha \frac{Pa^4(1-\nu^2)}{Eh^3}, \quad (2)$$

where  $a$  is half side length of the square diaphragm,  $h$  is thickness,  $P$  is applied pressure,  $E$  is Young's modulus, and  $\nu$  is Poisson ratio.

For the diaphragm clamped at its circumference, the resonant frequency is

$$f = \frac{\pi}{a^2} \cdot \left[ \frac{gD}{hw} \right]^{\frac{1}{2}}, \quad (3)$$

where  $D$  is flexural rigidity, and  $w$  is the diaphragm density.

In this research, an embossed center was designed in the diaphragm of DFOS to make the sensor structure and operation more stable and more efficient. The gap between the embossed center and the fiber tip must be kept within several micrometers for near field operation. One advantage of the embossed center is that it prevents lateral misalignment between the diaphragm and the fiber end. Another important advantage is that while the gap between the embossed center and the fiber tip is only a few micrometers, the distance between the diaphragm and the fiber is considerably larger (60  $\mu\text{m}$ ). This geometry increases the air cavity volume, and significantly reduces the air cavity back pressure during diaphragm movement. Diaphragm movement is easier under reduced air pressure, resulting in increased sensor sensitivity. Furthermore, according to mirror symmetry of the electromagnetic wave, the coupling coefficient of the electromagnetic wave back into the fiber increases in reverse proportion to the air gap distance and in proportion to how many times the light is

reflected. Therefore, a smaller interference gap between the embossed center and the fiber increases sensor efficiency and sensitivity.

Femlab software was used for simulation of center-embossed diaphragm deflection for a sensor of 100 kHz resonant frequency for PD acoustic detection. The simulation yielded a diaphragm of 1.9-mm side length and 60- $\mu\text{m}$  thickness with a 0.35mm x 0.35 mm embossed center and a 2- $\mu\text{m}$  interference gap as the optimum parameters.

### 3. Sensor Fabrication

The diaphragm fabrication steps using MEMS technology are shown in Fig. 3. A 220- $\mu\text{m}$  silicon wafer was etched sequentially on both sides in KOH to give a 60- $\mu\text{m}$  thick diaphragm. The embossed center was protected by a layer of silicon oxide to ensure that it remained intact in the etching process. As a result, both ends of the Fabry-Perot cavity (the embossed center and fiber tip) were perfect flat surfaces to reduce speckle noise. The surrounding wall on the embossed-center side of the diaphragm was coated with gold by evaporation. The 2- $\mu\text{m}$  gap between the embossed center and fiber end was accurately determined by the gold film thickness.

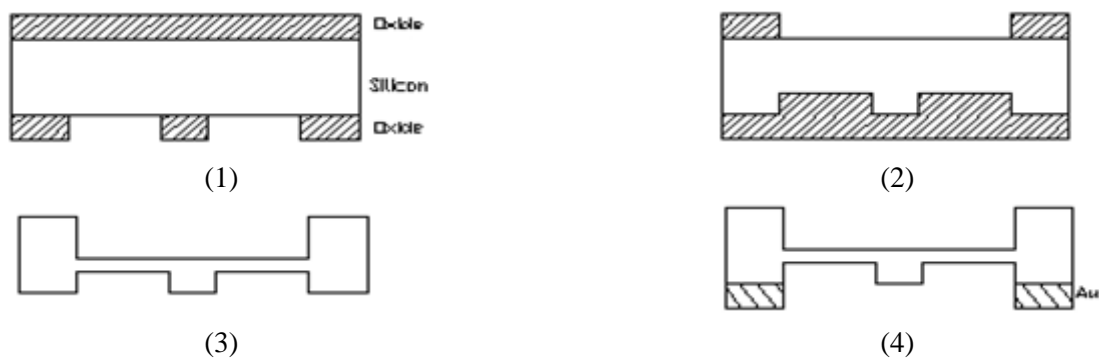


**Fig. 3.** Schematic of diaphragm fabrication steps.

The diaphragm and fiber tip were first clamped together mechanically. The gap between the diaphragm and the fiber was then adjusted while measuring the interference light signal output until it reached linear operation and the highest detection sensitivity, defined as Q-point. After the sensor operation had reached Q-point, the diaphragm and the fiber ferule were soldered together with Ag-Sn-Pb175 under microscope.

## 4. Experimental Results

### 4.1. Static and Dynamic Pressure Testing

This was the first time that static pressure testing was successfully demonstrated in diaphragm-based Fabry-Perot sensors. The static pressure was gradually increased to 9000 Pa. The output signal intensity vs. pressure curve is shown in Fig. 4. Good agreement between the theoretical curve calculated from Equation (1) and experimental data was achieved. Therefore, our DFOS has proven to be a truly and purely Fabry-Perot device.

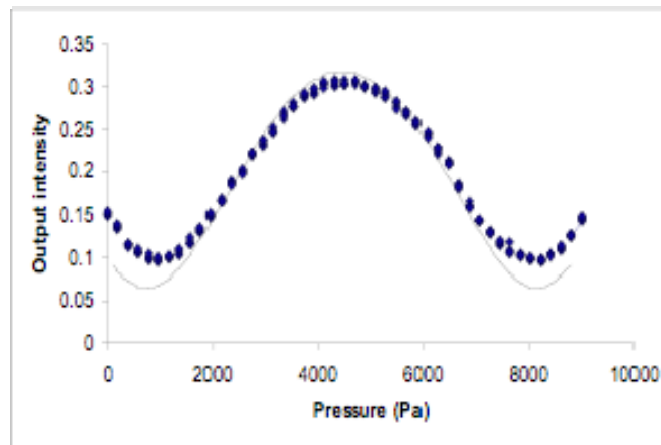


**Fig. 4.** Static characterization of optic output (dotted line) as a function of pressure, in comparison with calculated curve from Equation (1).

In dynamic pressure testing, the DFOS and a PZT sensor were tested in parallel under identical conditions. DFOS and R15 (PZT sensor made by Physics Acoustic Corporation) were immersed in water. The acoustic waves were created by an emitter (pulser R15) placed approximately eight inches away from both sensors. The pre-amp gain of the R15 sensor was set to 20 dB. The DFOS was connected directly to the oscilloscope without any amplification.

The pulser frequency was increased in 5 kHz increments from 75 kHz to 300 kHz. The R15 sensor with 20 dB gain had two bandwidths with peak frequencies at 150 kHz and 230 kHz. The maximum amplitude was about 145 and 185 mV respectively. The DFOS without amplification had a bandwidth with peak frequency at approximately 105 kHz and maximum amplitude of about 140 mV. Fig. 5 (a) and (b) show the waveforms and frequency spectra of the DFOS and R15 when the pulser frequency was 130 kHz. Both sensors exhibited very similar waveform profiles and frequency spectra. The DFOS has shown comparable high sensitivity as the PZT sensor even without signal amplification.

#### 4.2. Partial Discharge Acoustic Detection

The DFOS was placed in the oil inside a retired real utility transformer at various distances from the partial discharge (PD) spark. The PZT sensor was attached to the external tank wall.

In Fig. 6, the purple curves of extremely high frequency are the triggering signals of the PD, which served as the starting point of the PD occurrence. The yellow signals were from the DFOS sensor, and the green signals from the PZT sensor. In the left graph, the PD was far from the two sensors, while it was close to both in the right graph. The time difference between the PD peak to the onset of the yellow/green acoustic signal is the time of flight. Fig. 6 clearly shows the time of flight increased as the sensors were farther away from the spark. The magnitude (sensitivity) of the DFOS signal was higher than the PZT signal.

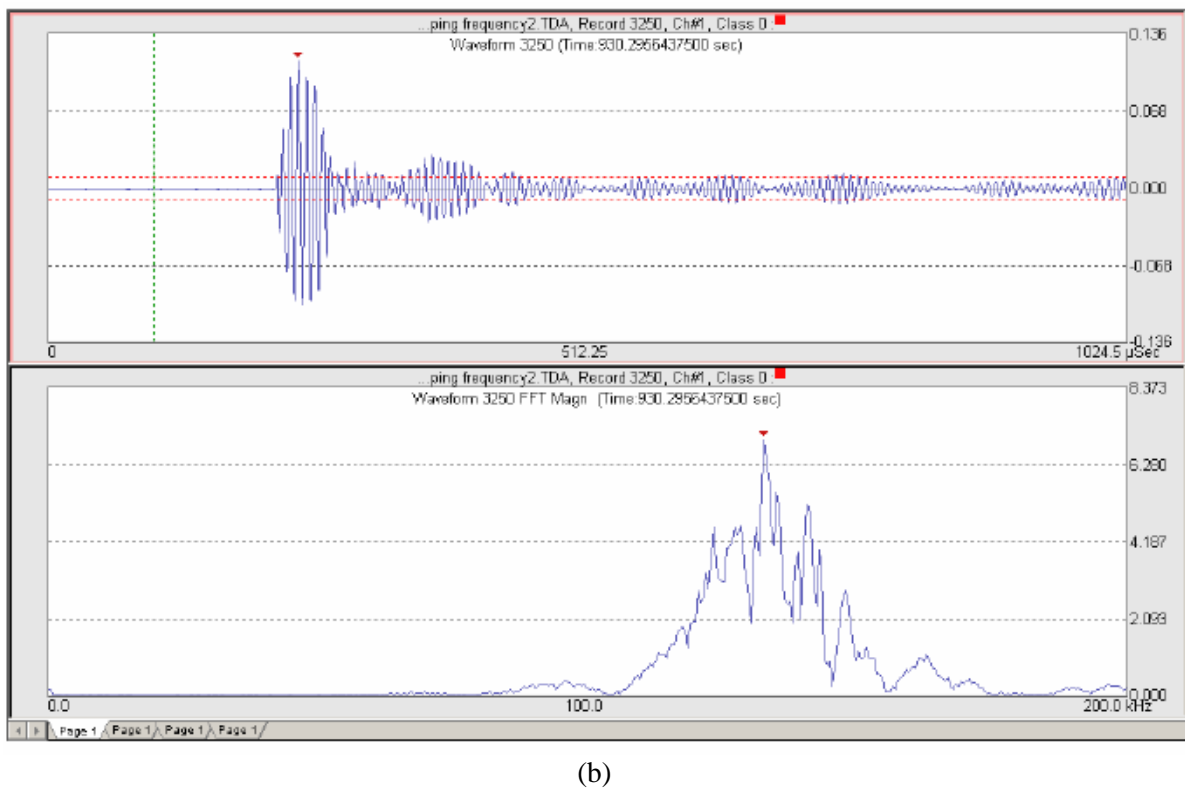
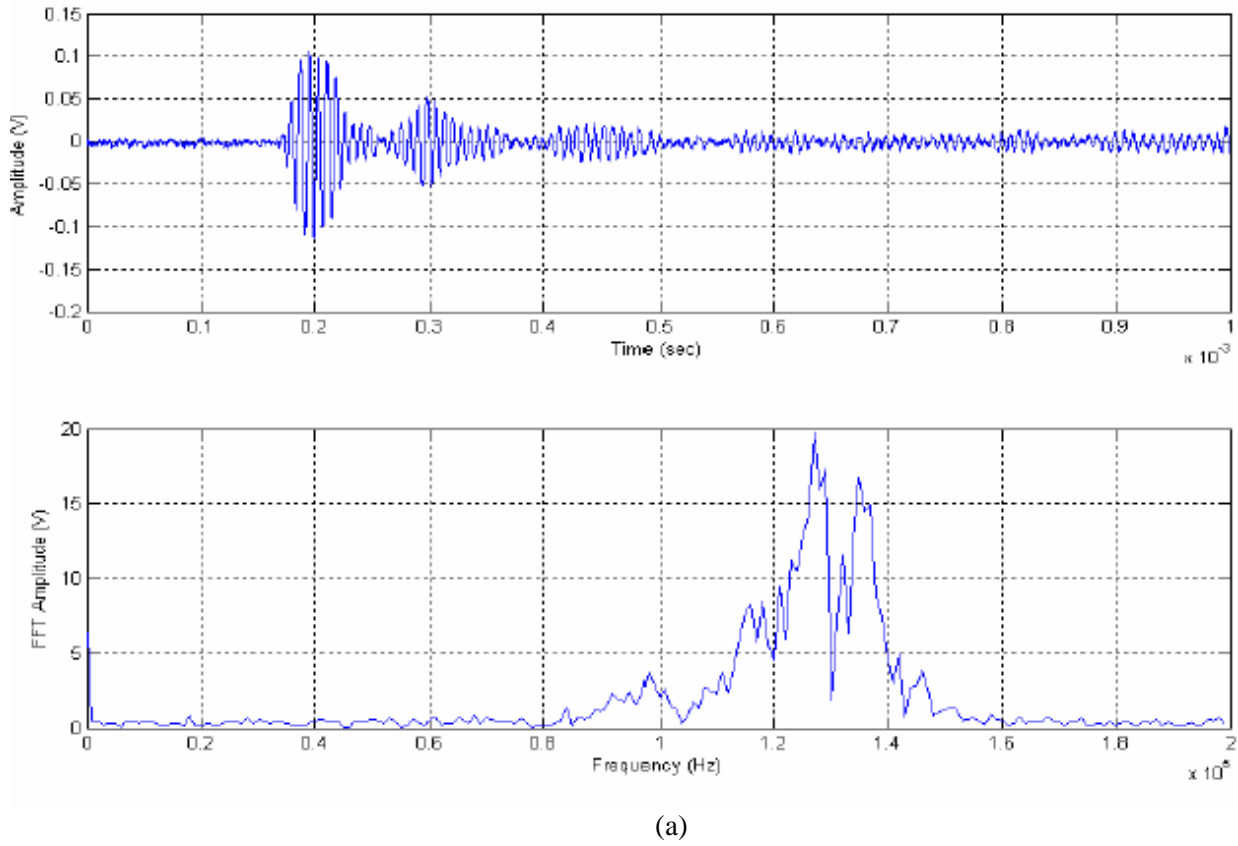


**Fig. 5.** Waveform and frequency spectra when the pulser frequency is 130 kHz.  
(a) DFOS; (b) PZT sensor.

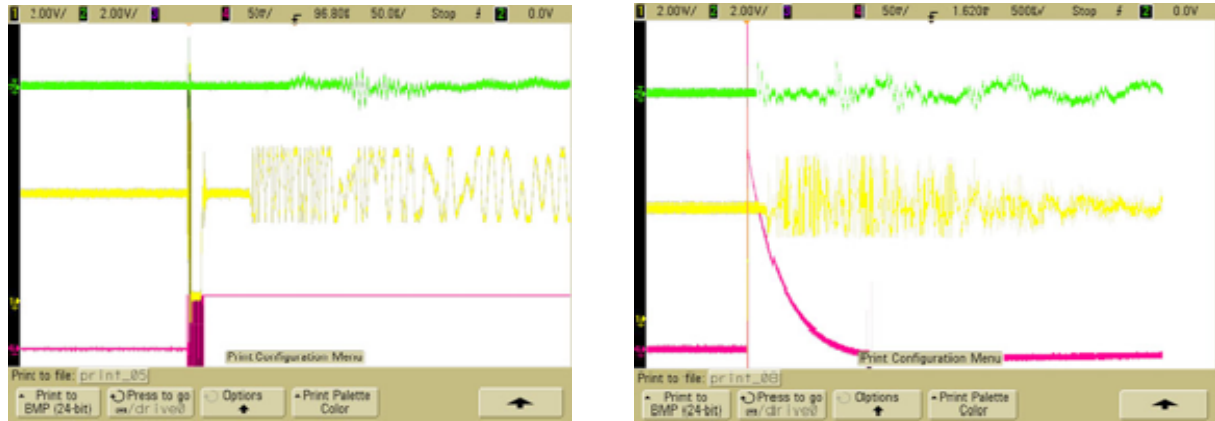


**Fig. 6.** PD in the oil tank of a transformer detected by DFOS and PZT sensor.

## 5. Conclusion

The Diaphragm Fiber Optic Sensor is based on extrinsic Fabry-Perot interferometry. A center embossed diaphragm was designed to serve as the sensing element of the sensor. The bonding and diaphragm processing methods by MEMS technology ensured that the diaphragm and the fiber were aligned both laterally and angularly. The novel DFOS design and fabrication led to better alignment and Q-point stabilization, high efficiency, and reliability. Experimental results from static pressure and dynamic acoustic measurements demonstrated excellent sensor efficiency and stability. High frequency (100 kHz) DFOS showed high sensitivity in comparison testing with commercial PZT sensors.

## Acknowledgements

The authors thank R. Harry, I. Padron, and S. Hsu for valuable discussions. This research was funded by PSE&G Corporation and Foundation of New Jersey Institute of Technology (NJIT).

## References

- [1]. Prototype Fiber-Optic Acoustic Partial Discharge Sensor: Lessons-Learned Documentation and Field Test, Technical Report, *EPRI*, Palo Alto, CA, 2002.
- [2]. K. Totsu, Y. Haga, and M. Esashi, Ultra-Miniature Fiber-Optic Pressure Sensor Using White Light Interferometry, *Journal of Micromechanics and Microengineering*, Vol.15, 2004, pp. 71-75.
- [3]. J. Xu, X. Wang, K. Cooper, and A. Wang, Miniature All-Silica Fiber Optic Pressure and acoustic Sensor, *Optic Letters*, Vol.30, No.24, 2005, pp. 3269-3271.
- [5]. R. Bartnikas, Partial Discharges Their Mechanism, Detection and Measurement, *IEEE Transactions on Dielectrics and Electrical Insulation*, Vol. 9, No. 5, 2002, pp. 763.
- [6]. R. Harrold, Partial Discharge – Part XVI: Ultrasonic Sensing of PD within Large Capacitors, *IEEE Electrical Insulation Magazine*, Vol. 9, No.3, 1993.
- [7]. L. Lundgaard, Partial Discharge – Part XIII: Acoustic Partial Discharge Detection – Fundamental Considerations, *IEEE Electrical Insulation Magazine*, Vol.8, No.4, 1992.
- [8]. L. Lundgaard, Partial Discharge – Part XIV: Acoustic Partial Discharge Detection – Practical Application, *IEEE Electrical Insulation Magazine*, Vol. 8, No. 5, 1992.
- [9]. P. Eleftherion, Partial Discharge XXI: Acoustic Emission-Based PD Source Location in Transformers, *IEEE Electrical Insulation Magazine*, Vol. 11, No. 6, 1995.

- [10].S. Timoshenko and S. Woinowski-Krieger, Theory of Plates and Shells, *McGraw-Hill*, 1959, p. 415.  
[11].M. Giovanni, Flat and Corrugated Membrane Design Handbook, *Mercel Dekker Inc.*, New York, pp. 157-158.

2007 Copyright ©, International Frequency Sensor Association (IFSA). All rights reserved.  
(<http://www.sensorsportal.com>)



Standards  
Certification  
Education & Training  
Publishing  
Conferences & Exhibits

## 54th International Instrumentation Symposium

Hilton Pensacola Beach, Florida, May 5 - 9 May 2008

Sponsored by ISA ASD, TMD, and PMCD Divisions

### Call for Papers

54 YEARS IN THE MAKING...

The 54<sup>th</sup> International Instrumentation Symposium is sponsored jointly by the Aerospace Industries, Test Measurement, and Process Measurement and Controls Divisions of ISA. This symposium has become recognized as the outstanding forum for discussion of new and innovative instrumentation techniques, development and applications. The symposium will include paper sessions, short courses, and tutorials. Papers will be considered for publication in the ISA technical journal.

#### For additional information, contact:

Randy Buchanan  
General Co-Chair  
University of Southern MS  
(601) 266-4949  
[randy.buchanan@usm.edu](mailto:randy.buchanan@usm.edu)

Aubri Buchanan  
General Co-Chair  
NASA SSC  
(228) 688-3973  
[aubri.c.buchanan@nasa.gov](mailto:aubri.c.buchanan@nasa.gov)

Rodney Jones  
(919) 990-9418  
[rjones@isa.org](mailto:rjones@isa.org)

For the following topics, prospective authors are invited to  
a) submit paper for peer review  
b) submit "presentation only" for review

- Electronic Instrumentation
- Wireless, Electromagnetic, & RF Instrumentation
- Geo-science and Remote Sensing
- Automated Measurement Techniques
- Biomedical Instrumentation
- Built-in-Test & Self-Test Instrumentation & Measurement
- Calibration and Uncertainty
- Time/Frequency based and Real-time Measurements Systems
- DCS, SCADA, and Industrial Instrumentation
- Noise, Measurement, and DSP
- Measurement Standards and Metrology
- Aerospace Systems
- Emerging Technology
- Environmental Measurements and Monitoring
- Cyber and Homeland Security
- Student Sessions

#### Guidelines for Submission:

- All Authors/Speakers must pay registration fee
- Intent to Present Application must be submitted **electronically** and in English.
- Must include a 200-500 word abstract.
- Suggested length limit for papers is 10 pages, including figures and illustrations.
- Papers accepted for publication will require copyright transfer to ISA.

The lead author is the main contact. Submit your electronic Intent to Present Application including abstract online to [www.isa.org/ABSTRACTS](http://www.isa.org/ABSTRACTS) and email to [aubri.c.buchanan@nasa.gov](mailto:aubri.c.buchanan@nasa.gov) and [rjones@isa.org](mailto:rjones@isa.org).

Deadlines: **Abstracts:** 15 November 2007  
**Draft Papers:** 15 February 2008  
**Final Papers/Presentations:** 14 March 2008

- Process Measurement and Control
- Green & Renewable Energy Technologies
- Intelligent Instrumentation & Measurement
- Power Systems, Radiation, & Nuclear Instrumentation
- Hardware-in-the-Loop (HIL) Instrumentation
- Safety Instrumented Systems
- Semiconductor and Superconductivity Measurements
- Sensors & Transducers
- Virtual Instrumentation & Systems
- Laboratory & Physical Science Instrumentation
- Nanotechnology, MEMS, NEMS
- Control System Instrumentation
- Temperature, Pressure, Flow & Process Variable Instrumentation
- Field Programmable Gate Arrays(FPGA) Based Systems
- Laser and Electro-Optics Instrumentation

Setting the Standard for Automation™

55-0577

## Micromechanical GaAs Hot Plates for Gas Sensors

<sup>1</sup>Jiri JAKOVENKO, <sup>1</sup>Miroslav HUSAK, <sup>2</sup>Tibor LALINSKY, <sup>3</sup>Milan DRZIK

<sup>1</sup>Department of Microelectronics, Czech Technical University in Prague,  
Technicka 2, 166 27, Prague 6, Czech Republic

<sup>2</sup>Institute of Electrical Engineering, Slovak Academy of Sciences, Bratislava, Slovakia

<sup>3</sup>International Laser Center, Ilkovičova 3, 812 19 Bratislava, Slovakia

E-mail: jakovenk@feld.cvut.cz, <http://www.micro.feld.cvut.cz>

*Received: 17 September 2007 /Accepted: 19 September 2007 /Published: 8 October 2007*

---

**Abstract:** This paper discusses the design, simulation and fabrication of new Micromachined Thermal Hot Plates (MTHPs) based on GaAs, which were designed for Gas sensors. High sensitivity and low power are expected for present metal oxide Gas sensors, which generally work in high temperature mode (which is essential for chemical reactions to be performed between molecules of the specified gas and the surface of sensing material). Because low power consumption is required, even for operation temperatures in the range of 200 to 500 °C, high thermal isolation of these devices are necessary. The problem can be solved by designing free standing micromechanical hot plates. Mechanical stability and a fast thermal response are especially significant parameters that can not be neglected. These characteristics can be achieved with a new concept of GaAs based thermal converter. Copyright © 2007 IFSA.

**Keywords:** Thermal hot plate, Thermo-mechanical simulation, MEMS, Gas sensor

---

### 1. Introduction

Typical micromachined hotplates are based on thin membranes made of silicon nitride and silicon oxide. However, the operating temperature of these hotplates is limited to a maximum of about 350 °C. The micromachined thermal hot plates based on GaAs seem to be very attractive for micro hotplates design operating in high temperature mode. In general, a MTHP integrates GaAs microelectronic devices (high-speed transistors or Platinum resistors as a heater) and temperature sensors on GaAs thermally isolated micromechanical thin membrane. A Pt micro-heater, placed at the top of micro

hotplate, is designed to warm up the sensing surface to operating temperature. Temperature sensors are integrated within the MTHP structure to sense the temperature at precisely defined places.

Thanks to a higher thermal resistance and operation at high temperatures, MTHPs based on GaAs should be able to perform electro-thermal conversion with higher conversion efficiency than well known Si devices. The most considerable advantages of GaAs, over Si, are some intrinsic material properties such as lower thermal conductivity, high temperature performance, heterostructure quantum effects, etc. The HEMT technology creates optimal conditions for MEMS device development which can be fully compatible not only with signal conditioning and driving circuitry, but also with the Monolithic Microwave Integrated Circuits (MMICs). The most of GaAs based MTHP devices were developed to be applied for RF and microwave power sensors and infrared thermal sensors [1, 2]. In this work we are presenting high-quality thermal performance GaAs based hotplate MTHP devices which were designed for gas sensing.

## 2. MTHP Design and Fabrication Process

In order to assure excellent thermal isolation of the MTHP structure, the hotplate devices are mostly designed as free space standing structures. To increase the thermal resistance values, the hotplate has to be designed with the thickness as thin as possible. Furthermore, optimization of the MTHP structure dimensions (the aspect ratio between the MTHP structure length which increase the thermal resistance and MTHP thickness) has to be performed to obtain the best trade-off between thermal resistance and acceptable mechanical stress in membrane structure.

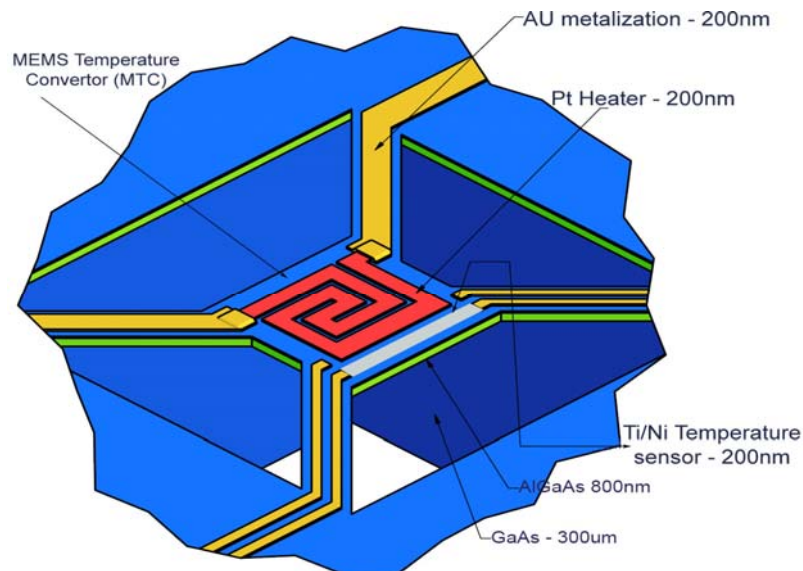


**Fig. 1.** Model of the MTHP suspended membrane structure. GaAs/AlGaAs hotplate is 2  $\mu\text{m}$  thick. SiC barrier layer and gas sensitive NiO layer is not shown.

Fig. 1 shows a schematic view of the GaAs/AlGaAs MTHP. Ti/Pt resistor as a heater and Ti/Ni meander-like thin film as a temperature sensor are monolithically integrated within thermally isolated 2  $\mu\text{m}$ -thick AlGaAs/GaAs island MEMS, which is suspended by the four GaAs cross-bridges. The dimensions of GaAs/AlGaAs hotplate are 150  $\mu\text{m}$  x 150  $\mu\text{m}$ . For FEM numerical simulation, a 3-D GaAs model substrate has been designed 10  $\mu\text{m}$  thick and 100  $\mu\text{m}$  wide. Top view mask layout of MTHP hotplate is shown on Fig. 2. Active devices (temperature sensor and heater) are covered by

500 nm thick SiC barrier layer that electrically isolates the 100 nm thick NiO gas sensitive layer and Pt interdigital electrodes.

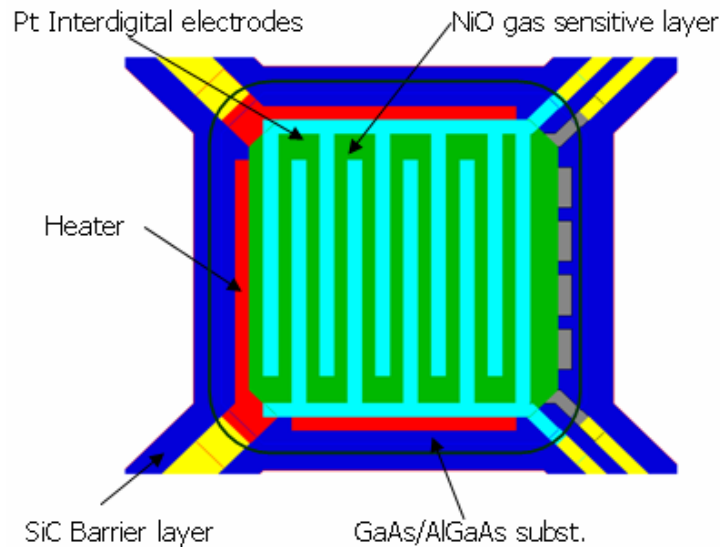


**Fig. 2.** Top view mask layout of MTHP hotplate.

The MTHP fabrication process begins with the front-side processing technology of the micro-heater and temperature sensor. The process must be combined with surface and bulk micromachining of GaAs and must be fully compatible with the processing technology of microelectronic integrated circuits.

The multilayer GaAs/AlGaAs heterostructure active MTHP layers are grown by MBE (Molecular Beam Epitaxy) on GaAs substrate. After this technology step, the double-sided aligned photolithography is carried out to define the etching masks on the both sides of the substrate. Highly selective reactive ion etching (RIE) of GaAs from the front side defines the lateral dimension of the hotplate structure while vertical dimensions are defined by deep back side RIE through a 300  $\mu\text{m}$  thick GaAs substrate to the AlGaAs etch-stop layer. Therefore the hotplate thickness (vertical dimension) is precisely defined by the thickness of MBE grown GaAs layer over AlGaAs etch-stop layer. As the final step, AlGaAs etch stop layer is selectively etched. More technological details can be found in [1].

### 3. MTHP Device Characterization

The design and characterization of MTHP device can be divided into three phases (Fig. 3):

**Preprocessing** – proposition of 3-D model that is derived from 2-D layout which describe shapes of particular functional layers, combining with classification of the technological process. Technology process describes separate deposition and etching steps attributes (layer thickness, etching angle, etc.) Material constants are assigned from material database to each layer. 3-D model is meshed for FEM simulators.

**Processing** – boundary conditions assignment for particular parts and patches of 3-D model. Parameter setting for FEM simulator which should be combined in so called co-solve analysis.

**Postprocessing** – view and analysis of simulation results.

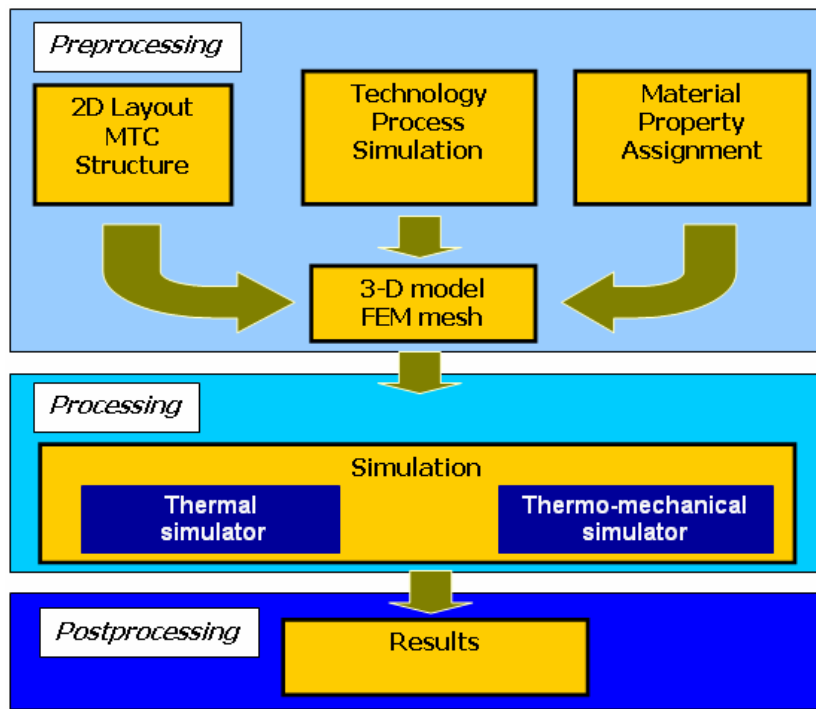


Fig. 3. MEMS simulation general procedure

#### 4. Electro-Thermal Evaluation

Firstly, the temperature sensitivity of Ti/Ni thin film temperature sensor was investigated. Temperature sensor I-V characteristics at constant current biasing were used to convert the temperature into voltage. Fig. 4 shows the measured voltage response to the temperature at constant current biasing of 1 mA. As expected, very good linearity in the sensor voltage response was observed.

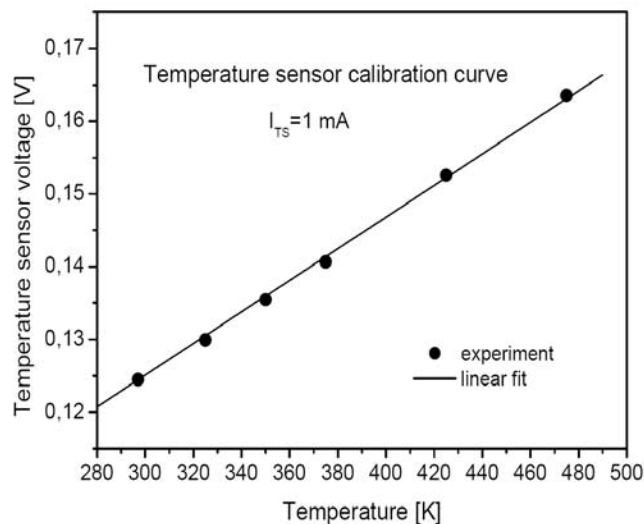
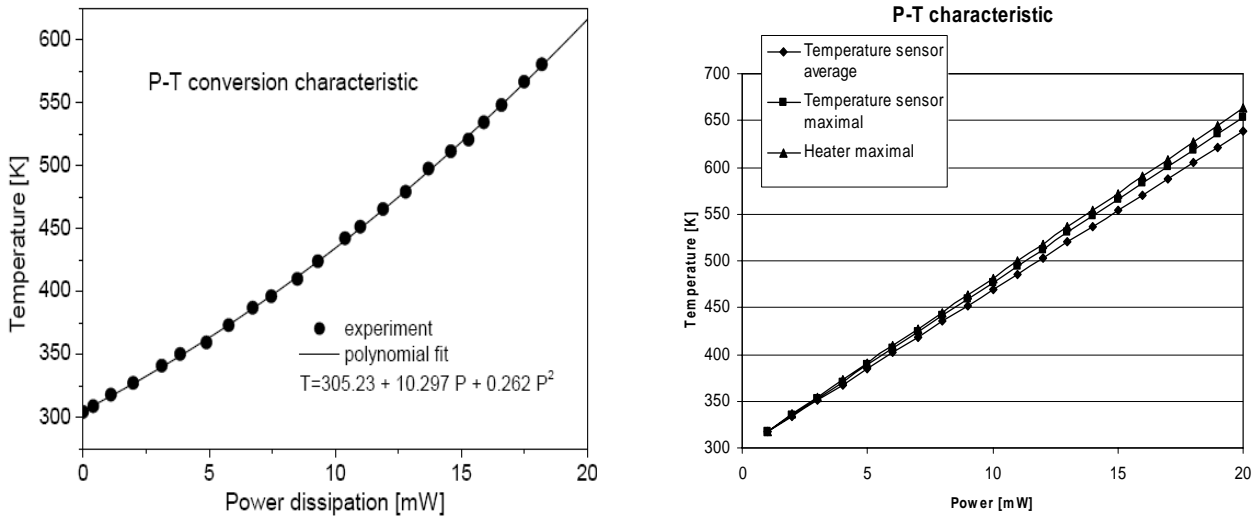


Fig. 4. Measured temperature sensor calibration curve.

The linear fit implemented on the temperature sensor calibration curve in Fig. 4 allows temperature sensor voltage conversion directly to the temperature. Fig. 5 shows the measured power to temperature (P-T) conversion characteristic that can be used to evaluate the conversion efficiency of the MTHP structure.



**Fig. 5.** Measured (a) and simulated (b) P-T conversion characteristic of MTHP device.

As we can see there is a slight difference from a linear dependence. Measured data can be fitted by a quadratic polynomial regression:

$$(T = 305.23 + 10.297 P + 0.262 P^2) \quad (1)$$

It is clear that thermal resistance  $R_{th}$ , defined as  $\partial T / \partial P$ , increases with the power dissipation (temperature increase). At power dissipation in the heater of about 20 mW this value achieves 21 K/mW.

Metal oxide gas sensors generally work in high temperature mode, which is required for chemical reactions to be performed between molecules of the specified gas and the surface of sensing material. Low power consumption is required to obtain the operating temperatures in the range of 500 to 700 K. Uniform temperature distribution in the active sensing area is required to ensure equal sensing properties of the whole surface as well. Operating temperature (650 K) of designed MTHP gas sensor can be achieved by the power dissipation lower than 20 mW.

## 5. Thermo-Mechanical Characterization

For an isotropic homogenous material the steady state heat equation can be written [4]:

$$\nabla^2 T \equiv \frac{\partial^2 T}{\partial x^2} + \frac{\partial^2 T}{\partial y^2} + \frac{\partial^2 T}{\partial z^2} = -\frac{1}{k} Q(x, y, z) \quad (2)$$

where  $Q$  represents generated internal heat,  $k$  denotes the thermal conductivity,  $c_p$  its specific heat and  $T$  its temperature. The steady state temperature analysis has been performed to determine the temperature distributions and thermal resistance of the MTHP device.

For the thermal analysis problem, the essential boundary conditions are prescribed temperatures. Varying thermal and mechanical boundary conditions can significantly modify the analysis performance of thermo-mechanical MEMS devices. Mechanical boundary conditions manage how the device is constrained from movement. Mechanical conditions can be considered fixed for a given MEMS device. Thermal boundary conditions as conduction, convection, and radiation, on the other

hand, depend on the surroundings, packaging, etc. For that reason, careful assessment of thermal boundary conditions is necessary.

Precise thermal analysis that includes the conduction, convection, and radiation effects is necessary to properly predict the behavior of thermo-mechanical devices. Not only quantitative but also qualitative performance can change if thermal boundary conditions are not set correctly.

In many cases convection and radiation losses from the device could be negligible and heat dissipation is entirely due to the heat lost to the substrate. It depends on the shape and dimensions of the device. This is modeled as a constant ambient temperature condition at the base of the substrate or on the side parts and patches of the 3-D model. These boundary conditions are known as Dirichlet [5].

Above mentioned assumption may not be true when the thermal mass of the substrate is not large enough to preserve the ambient temperature or the working temperature is relatively high. At that moment a natural boundary condition (Neumann boundary condition) must be chosen. After completing the thermal analysis we can get no uniform temperature distribution at the base substrate.

The technology process, environment, and the packaging of the MEMS device conclude which boundary condition is suitable. The choice of the type of boundary condition could significantly affect the device behavior.

Because of high temperature operation of MTHP we have used natural boundary condition. The spatial temperature distribution and steady state heat flux were calculated taking into the account the heat transfers to infinity. In the current analysis, according to the application requirement, the fixed thermal boundary is defined for the all side parts of MTHP 3-D model. These walls were kept at the room temperature of 300 K while other sides were adiabatic surrounded by air.

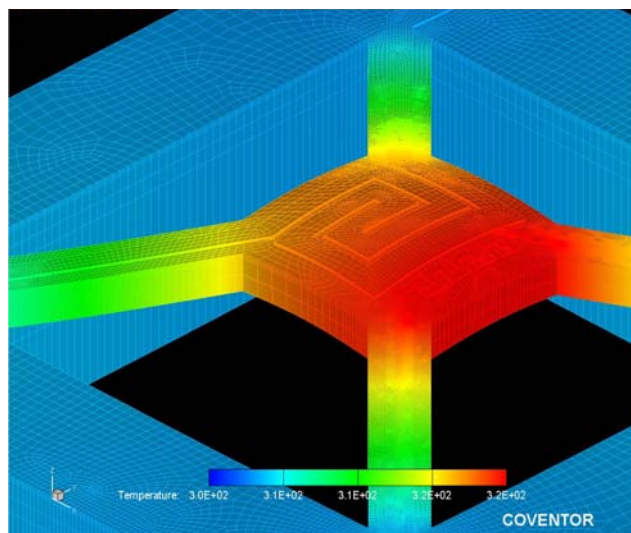
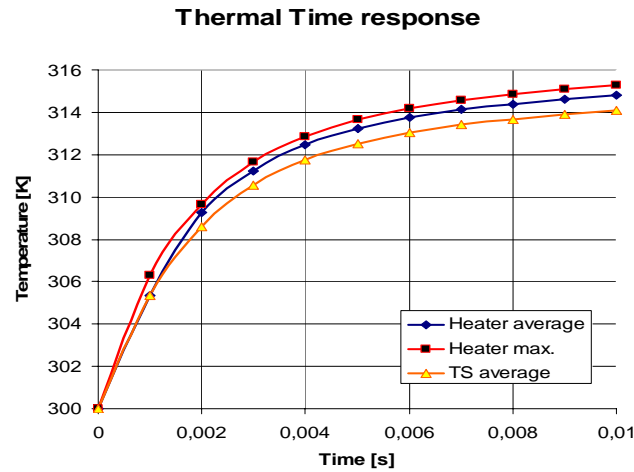


**Fig. 6.** MTHP hotplate temperature distribution (Dissipated power in the heater was 1 mW).

The 3D graph as shown in Fig. 5 gives good overall visualization of the temperature distribution in the suspended island structure of the MTHP device, which is caused by the power dissipation generated in the thin film resistive Pt heater. Thermal analyses were performed for both vacuum ambient and gaseous air around the hotplate. The heat losses, due to radiation, were also taken into account.

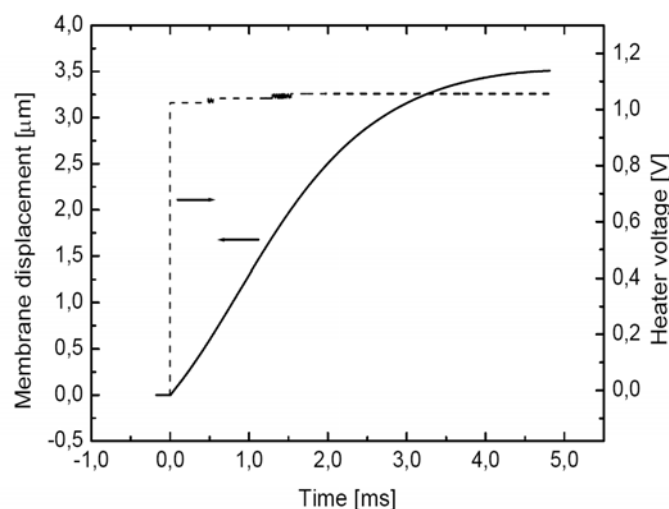
The power to temperature (P-T) conversion characteristics of the MTHP device were also investigated

by the simulation. High electro-thermal conversion efficiency defined by the extracted thermal resistance value ( $R_{th}=17.3$  K/mW (CoventorWare simulation)) was achieved. This value corresponds to the average value obtained from the experiment (see Fig. 5). Transient power characteristics for 1 mW power dissipation are depicted on Fig. 7. There are three transients in Fig. 7. The upper is the maximal temperature of the heater and the bottom dependence reflects average temperature of TS.



**Fig. 7.** The simulated thermal time response for 1 mW power dissipation in the heater.

Thermo-mechanical stability and integrity and a fast thermal response are very important parameters that can not be neglected. An optical measurement method was used to characterize the temperature time response of the MTHP device. It is based on deflection changes measurement of the MTHP hotplate. The deflections are induced due to different thermo-mechanical properties of the multilayer material system. The non-stationary dynamic process of transient heat flow creates also time dependent mechanical movements. To observe these deformation changes we used Laser Doppler Vibrometer (LDV) optical method. The heterodyne interferometrical system of Polytec OFV-303 vibrometer is capable to detect the vibration amplitudes in nanometer range.



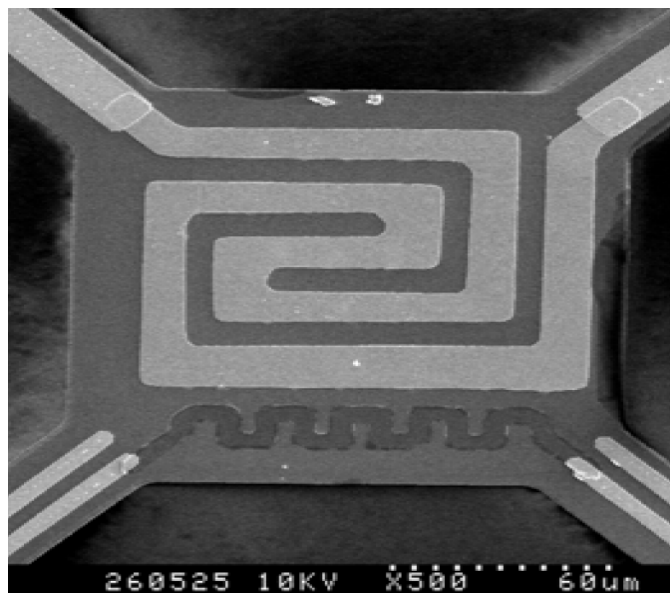
**Fig. 8.** Mechanical time response to the input step-wise heater voltage (temperature increase of 482 K).

Fig. 8 shows the mechanical time response (deflection time dependence) of the suspended hotplate membrane structure obtained by the optical measurement. Extracted thermal time constant value is 1.5 ms and it corresponds to the simulated thermal time constant.

## 6. Conclusions

The main objective of the presented work was the design, modeling and characterization of a micromachined GaAs based MTHP device which is considered to operate with metal oxide gas sensors. The processing technology is fully compatible with the GaAs MESFET or HEMT devices processing. Subsequently, signal processing electronics can be monolithically integrated with the gas sensors.

Comprehensive electro-thermo-mechanical performance analyses of the MTHP hotplate were performed and exhibit very good mechanical integrity and thermal stability. Due to very high electro-thermal conversion efficiency, defined by the extracted thermal resistance values ( $R_{th} \sim 15\text{--}21 \text{ K/mW}$ ), the power consumption can be kept very low. To obtain the operational temperature of the active part of MTHP hotplate in the range of 600-650 K the power consumption was less than 20 mW.



**Fig. 9.** A real view of fabricated MTHP device.

By means of 3-D thermo-mechanical simulation, we optimized MTHP hotplate structure to obtain uniform temperature distribution in the active gas sensitive area. Simulated values were compared to experimental values performed by the measurement of real micromachined MTHP device. The thermal time constant of the MTHP device was also estimated by simulation ( $\tau \sim 1.44 \text{ ms}$ ) and compared to experimental measurement ( $\tau \sim 1.5 \text{ ms}$ ) using LDV method.

The processing technology for the described gas sensor based on the MTHP device is in progress. The process flow is now focused to define gas sensitive area based on polycrystalline NiO thin films with a dense fine-grained microstructure.

## References

- [1]. T. Lalinský, M. Držik, J. Jakovenko, M. Husák, *MEMS/NEMS handbook: Techniques and applications, Chapter 3*, Ed. C. T. Leondes, 2006, pp. 49-109.
- [2]. J. Jakovenko, M. Husak, T. Lalinsky, Design and simulation of micromechanical thermal converter for RF power sensor microsystem, *Microelectronics Reliability*, Elsevier, ISSN 0026-2714, Vol. 44, 2004, pp. 141-148.
- [3]. S. D. Senturia, *Microsystem Design*, Kluwer Academic Publisher, 2001.
- [4]. M. Elwensoekk, R. Wiegink, *Mechanical Mikrosensors*, Springer, 2000.
- [5]. Tai-Ran Hsu, *MEMS and Microsystems Design and Manufacture*, Mc Graw Hill, 2001.

---

2007 Copyright ©, International Frequency Sensor Association (IFSA). All rights reserved.  
(<http://www.sensorsportal.com>)



## Smart Sensors Systems Design

A five-day engineering course  
**5-9 November 2007, Barcelona (Spain)**



### General Information

This course is suitable for engineers who design different digital and intelligent sensors, data acquisition, and measurement systems. It is also useful for researchers, graduate and post graduate students. Course will be taught in English.

### Course Description

An advanced engineering course describes modern developments and trends in the field of smart sensor systems and digital sensors design.

After a general overview of data acquisition methods, modern smart, digital and quasi-digital sensors, smart systems details are discussed. A systematic approach towards the design of low-cost high-performance smart sensors systems with self-adaptation and self-identification possibilities is presented.



### Contact Person

Susana Escriche  
Fundació UPC. Edifici Vèrtex  
Plaça Eusebi Güell, 6, 08034 Barcelona  
Tel.: +34 93 401 08 94  
E-mail: [susana.escriche@fundacio.upc.edu](mailto:susana.escriche@fundacio.upc.edu)

### Course Instructor

Prof. Sergey Y. Yurish,  
Centre de Disseny d'Equips Industrials (CDEI),  
Universitat Politècnica de Catalunya (UPC-Barcelona)  
Tel.: + 34 93 401 74 37, fax: + 34 93 401 19 89  
E-mail: [syurish@sensorsportal.com](mailto:syurish@sensorsportal.com)



**Online Registration:** [http://www.sensorsportal.com/HTML/SSSD\\_Course\\_2007.htm](http://www.sensorsportal.com/HTML/SSSD_Course_2007.htm)  
**Deadline for Registration:** 25 October, 2007



## Integration of Microfluidics and Microacoustics Components for Miniature Flow Cytometry Systems

**\*Surendra K. RAVULA, Darren W. BRANCH, Jennifer SIGMAN,  
Paul G. CLEM, Igal BRENER**

Sandia National Laboratories,  
Building 858EL, Room L3305, 1515 Eubank Boulevard, SE Albuquerque, NM 87123  
Tel.: (505) 845-0540, fax: (505) 284-7690  
E-mail: [skravul@sandia.gov](mailto:skravul@sandia.gov)

*Received: 17 September 2007 /Accepted: 19 September 2007 /Published: 8 October 2007*

---

**Abstract:** Flow cytometry is an indispensable tool in clinical diagnostics, for example in cancer, AIDS, infectious disease outbreaks, microbiology, and others. The cost and size of existing cytometers preclude their entry into field clinics, water monitoring, agriculture/veterinary diagnostics, and rapidly deployable biothreat detection. Much of the cost and footprint of conventional cytometers is dictated by the high speed achieved by cells or beads in a hydrodynamically focused stream. This constraint is removed by using ultrasonic focusing in parallel microfluidic architecture. In this paper, we describe our progress towards a microfabricated flow cytometer that uses bulk and microfabricated planar piezoelectric transducers in glass microfluidic channels. In addition to experimental data, initial modeling data to predict the performance of our transducers are discussed. *Copyright © 2007 IFSA.*

**Keywords:** Microfluidics, Microacoustics, Flow cytometry

---

### 1. Introduction

There is currently great interest in portable and rapidly deployable biothreat detection and characterization platforms, both in the context of biowarfare and field diagnostics for soldiers. Current flow cytometers represent one of the most widespread technologies in biological analysis. However, they are complex and expensive instruments (~250 K) that require trained technicians and significant manual handling. A portable cytometry system will have significantly lower throughput compared to conventional systems, but the reduced cost and simplification of operation will enable the system to be

fielded in clinical settings around the world, especially in remote locations where trained technicians are unavailable.

Over the last fifty years, commercial flow cytometers have become commonplace in clinical and laboratory settings for cellular analyses; however, these complex systems are bulky and expensive. Recently, flow cytometry systems based on microfluidics have brought hope for less expensive and portable alternatives to conventional systems [1-8]. These systems take advantage of the ability of microtechnology to pattern small features and integrate multiple sensing modalities (optical, electrical, mechanical) onto a single platform. In addition, microfluidics offers the ability to build complex interrogation channels that can focus cells into narrow single-file columns for downstream optical interrogation. However, underlying issues (e.g., cell clumping, adhesion to the channel) with appropriate routing of the particles to necessary points in an integrated system remain problematic. Here, we seek to address some of these issues by integrating acoustic pressure waves into microfluidic channel systems to focus particles for optical detection.

## 2. Methods

For metallization, 1.5 in. diameter circular PZT discs were sputtered with Cr/Au (200Å/2000Å) on both sides and lithographically patterned on the top side. In this approach, AZ 5740 photoresist was spin coated (Headway Research Inc., Garland, TX) at 5000 rpm for 30 s (~6 µm thickness) and soft baked for 10 min at 90°C. An optical aligner (Oriel Corporation, Stanford, CT) was used to expose the photoresist and was subsequently developed in Microposit 454 developer (Rohm and Haas, Philadelphia, PA). Finally, liftoff was used to remove the photoresist and pattern the top metal surface (see Fig. 1). The transducer was poled at 300 V DC to actuate in the thickness dimension. Finally, a glass microchannel (Micronit Microfluidics BV, Netherlands) was bonded to provide the conduit for microparticle flow and the area where an acoustic standing wave can be created. The microchannels on this chip were 10 mm x 750 µm x 250 µm. The height of the channel was chosen to be 250 µm to support a half-wavelength resonance at 3 MHz and the width was chosen to support a  $3\lambda/2$  resonance (a harmonic of the halfwavelength resonance) at 3 MHz.

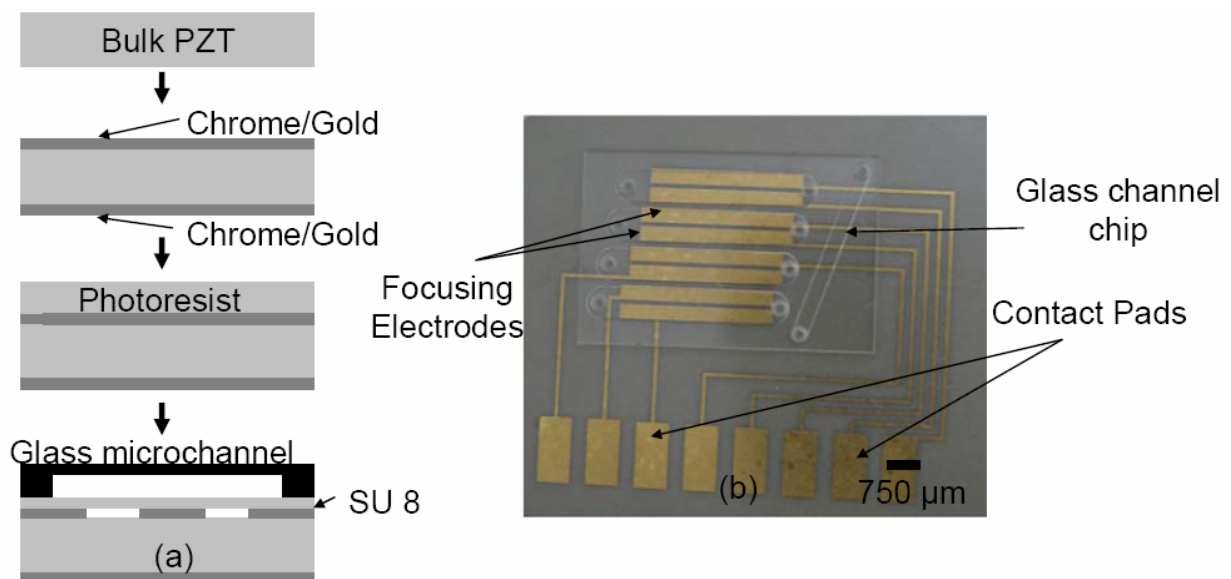


**Fig. 1.** Technique for metallization of PZT substrates. (a) In this scheme, a 1.5 in. PZT disc (500 µm thick) is patterned with a top electrode metal layer using a liftoff procedure. (b) Fabricated device using the technique shown in (a).

An alternate technique for the microfluidic manifold involved a two layer SU 8 process (see Figs. 2 and 3). SU 8 2100 was patterned (150  $\mu\text{m}$  thickness) on top of the PZT substrate to form the bottom channel layer. Then SU 8 2100 was again patterned (100  $\mu\text{m}$  thickness) to form the top channel layer and the proper levitation height for an acoustic routing zone. Finally, a glass coverslip was pressure bonded to the SU 8 microfluidic structure. In each case, fluidic interconnect (Upchurch Scientific) were then fixed to the structure to allow for the delivery of flow to the sheath inlets and 20  $\mu\text{m}$  microspheres (VWR Scientific) to the center inlet. These beads were delivered to the system at a concentration of  $10^6$  particles/mL at a flow rate of 50  $\mu\text{L/hr}$  using a syringe pump (Harvard Apparatus PHD 2000). In the focusing zone, the circular PZT transducers were driven around 3 MHz with a 10  $V_{p-p}$  sinusoidal signal (Agilent 33250A function generator) and in the deflection zone, the frequency of a second function generator was varied around 4 MHz to determine the optimal capture efficiency.

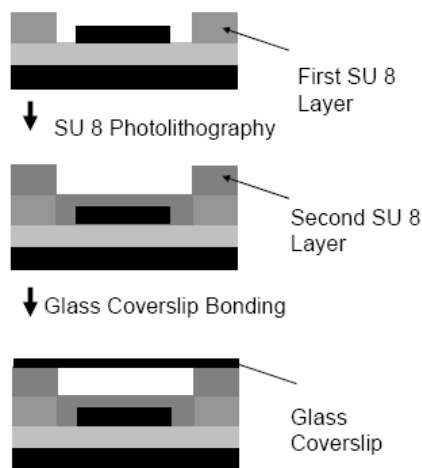


**Fig. 2.** Fabrication process for microfluidic integration using SU 8 photoresist. First, SU 8 2100 was patterned to produce a 150  $\mu\text{m}$  deep, 2mm wide channel on the PZT substrate. Then a second layer of SU 8 2100 was patterned to reduce the depth of the first channel in the acoustic deflection zone and to produce an outlet channel in just the top layer to capture the deflected particles. Finally, a glass coverslip was pressure and heat treated on top of the SU 8 microfluidic structure to create a channel roof.

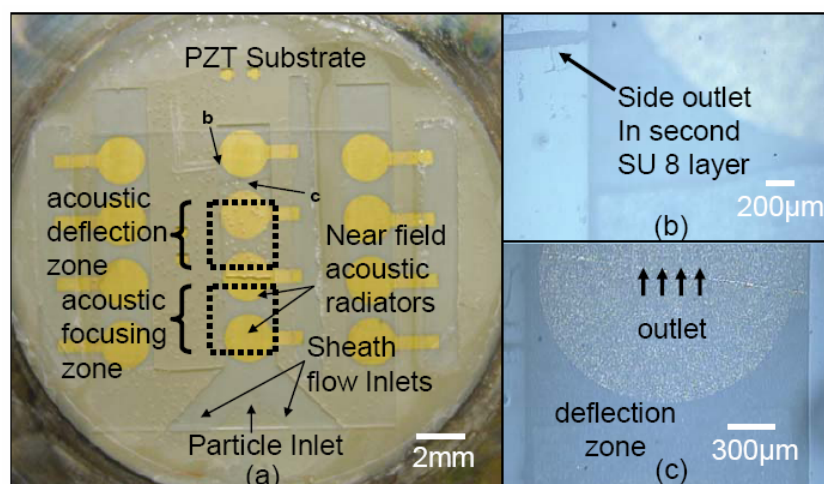


**Fig. 3.** Fabricated SU 8 laminar flow focusing system with integrated acoustic router. (a) SU 8 microfluidic structure showing 2 mm wide microfluidic channels and circular acoustic radiators for near-field focal reinforcement. (b) Zoomed in view of the side channel in the second SU 8 layer that collects deflected particles. (c) Zoomed in view of the deflection zone with different height.

### 3. Acoustic Model of Focal Reinforcement

In designs where we employ focal reinforcement to standing wave systems with near field radiation pressure, we have incorporated micropatterned piezoelectric transducers that could be phased together to achieve three-dimensional focusing within a microchannel. Moreover, the thickness and the surface area of the transducer were chosen to maximize the acoustic efficiency of the standing wave node reinforced with a near field radiation node. Toward this end, we chose PZT transducers with a thickness of 500  $\mu\text{m}$  giving an unloaded resonant frequency of 4.41 MHz. For an optimal design the transducer must be relatively insensitive to drive frequency to avoid power losses from external perturbations such as variation in the fabrication process. To support standing waves in the cavity (i.e. water), a cavity height of  $\lambda/2$  or 170  $\mu\text{m}$  is required in the water. The reflector, however, must be  $\lambda/4$  in the Pyrex or 320  $\mu\text{m}$ . To take advantage of near field effects, the transducer dimension must be chosen to be within the near field limit, given by  $nf \cong a^2 / \lambda$  for a circular transducer, where  $a$  is the transducer radius and  $\lambda$  is the wavelength. In contrast, the far field acoustic radiator acts like a point source which is ideal in beam steering applications. In general, the acoustic pressure field is highly complex for arbitrary transducer geometries and difficult to calculate; however, circular designs have closed-form solutions. In Fig. 4, we show the relative acoustic pressure field from a circular transducer for several values of the radius ( $a$ ) scaled by wavelength, where  $\lambda=340 \mu\text{m}$  as a function of the on-axis distance from the transducer. The key design feature requires that  $a = 5.245\lambda$  such that a pressure minimum exists at  $\sim 85 \mu\text{m}$  or half the cavity height. Though a minima exists when  $a = 1.225\lambda$ , the resulting transducer area is too small for effective impedance matching. Our result causes the standing wave minimum to overlap with the near field minimum from the transducer pressure field. The radius for this design gives  $a = 1.783 \text{ mm}$ . The far field boundary would be over 8.9 mm from a source with this dimension. The transducer area in this design is  $\sim 10^{-5} \text{ m}^2$ .

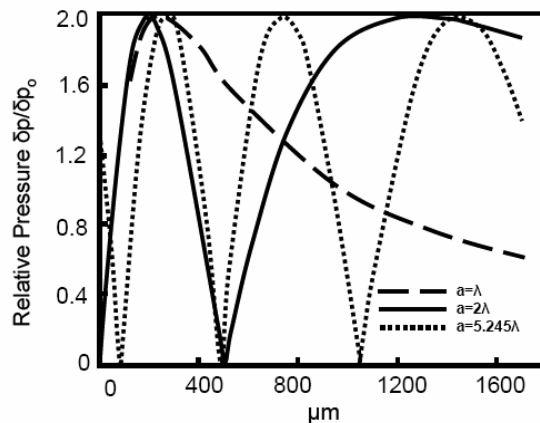
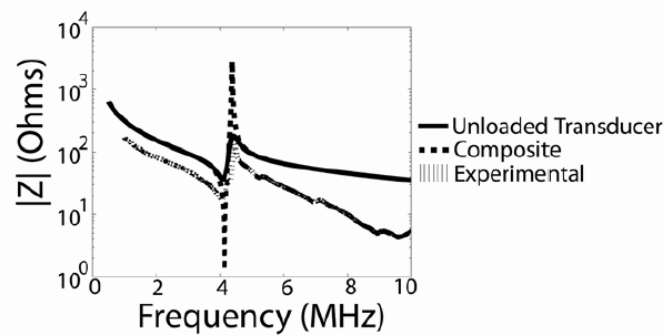


Fig. 4. Relative acoustic pressure in the transducer near field.

### 4. Results and Discussion

For the 500  $\mu\text{m}$  thick PZT disc samples, a 1-D transmission line model and the experimental data taken with an impedance analyzer predict a resonant frequency around 4 MHz (see Fig. 5). The model predicts impedance values slightly higher than those measured experimentally due to secondary acoustic losses through the transducer. For instance, since this model predicts transducer performance only in one dimension, it does not account for losses in the other two.



**Fig. 5.** Modeled and experimental data for the transducer fabricated using the technique in Fig. 1. The curves for the unloaded transducer and the composite show the output of the model for the case in which the transducer is free standing and for the transducer with electroded surfaces. The experimental values were taken with an impedance analyzer.

Fig. 6 shows a photomontage of ultrasonic streams generated for the system in Fig. 1 at various frequencies in the MHz range. While these early system designs did not have the correct geometries for producing single file lines of acoustically focused beads, they did show that beads can be coarsely focused with acoustic pressure waves. By choosing either a  $\lambda/2$  or  $\lambda/4$  thickness glass reflector we have also been able to route the particles at either the top of the microchannel or the middle (see Table 1 a). Table 1 b also summarizes the lateral focusing due to secondary coupling of the primary ultrasonic field.

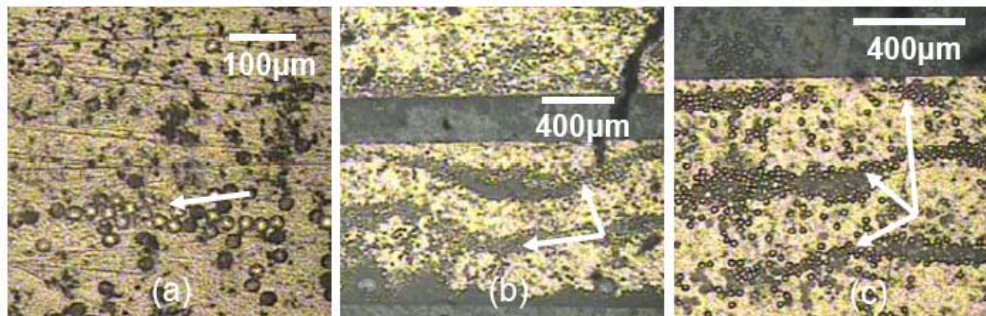


**Fig. 6.** Acoustic streams (arrows) of beads due to lateral focusing in a microchannel. The PZT transducer was driven with a 10 Vp-p sinusoidal signal. The frequency of actuation was 1.2 MHz for (a), 2.1 MHz for (b), and 3.2 MHz for (c).

**Table 1a.** Levitation Height Changes Due to Reflector Thickness (n=6)

| Frequency of Operation (MHz) | Thickness of Roof ( $\mu\text{m}$ ) | Average Levitation Height ( $\mu\text{m}$ ) |
|------------------------------|-------------------------------------|---|
| 2.9                          | 486 ( $\lambda/4$ )                 | 242 $\pm$ 8                                 |
| 3.1                          | 455 ( $\lambda/4$ )                 | 239 $\pm$ 9                                 |
| 3.3                          | 855 ( $\lambda/2$ )                 | 122 $\pm$ 15                                |

Values are mean $\pm$ standard error of measurement.

**Table 1b.** Lateral Focusing Characteristics During PZT Actuation (n=6).

| Frequency of Operation (MHz) | Amplitude of Applied Voltage (V) (peak-to-peak) | Number of Streams | Average Stream Width ( $\mu\text{m}$ ) |
|------------------------------|---|-------------------|--|
| 1.2                          | 10.23   | 1                 | 57 $\pm$ 8                             |
| 2.1                          | 13.14   | 2                 | 32 $\pm$ 9                             |
| 3.2                          | 12.92   | 3                 | 24 $\pm$ 12                            |

Values are mean $\pm$ standard error of measurement.

To produce more tightly focused streams of particles, the system described in Figs. 2 and 3 was fabricated and characterized. The resonant frequency of the acoustic focusing zone in the system was 3 MHz. Flow boundaries for the laminar flow focusing section are shown in Fig. 7 a. Fig. 7 b shows the three dimensional focusing of a stream of beads due to sheath flow and acoustic levitation.

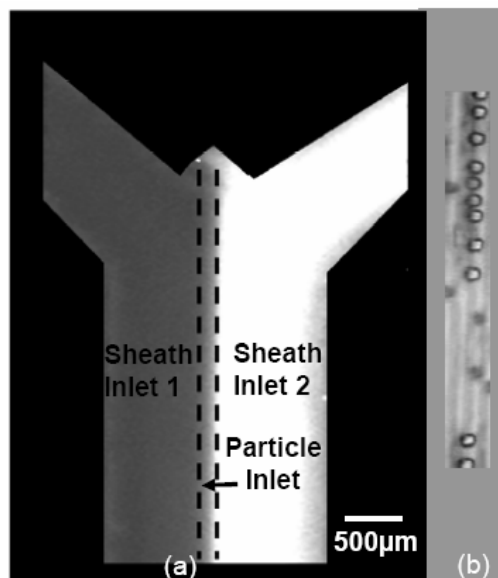


**Fig. 7.** (a) Flow boundaries between the three inlets to the laminar flow focusing portion of the system. Three different color dyes were injected into the three inlets. Flow rate of the particle inlet was 50 $\mu\text{L/hr}$  and for the sheath inlets was 200 $\mu\text{L/hr}$ . (b) 20 $\mu\text{m}$  diameter polystyrene beads being focused due to sheath flow on either side under the flow conditions in a.

Meanwhile, Table 2 summarizes the lateral and axial focusing properties of the system under different flow rates and drive frequencies and shows an optimal drive frequency of 3.2 MHz and sheath flow rate of 200  $\mu\text{L/hr}$ . This design also incorporates circular acoustic radiators that have been designed to establish a near-field radiation pressure minimum at the center along the height of the channel to reinforce the standing wave pressure minimum and obtain tighter z-dimensional focusing (20 % reduction in stream broadening). Finally, Table 3 summarizes the results of a test in which focused beads were fed into the deflection zone. In this experiment, the circular PZT transducers in the deflection zone were always kept on and the deflection distance of beads was measured by changing the focal plane of the microscope. The data suggest an optimal drive frequency of 4.9 MHz for deflecting particles into the capture channel. In future experiments, we will trigger the acoustic router

with an optical interrogation signal for acoustic sorting functions to quantify the throughput of the system. When fully integrated, this microfabricated platform could be a low cost, portable alternative to conventional flow cytometry systems.

**Table 2.** Characteristics of operation for acoustic focusing portion of the system (n=6).

| Frequency of Operation (MHz) | Flow Rate of Sheath Inlets ( $\mu\text{L/hr}$ ) | Average Lateral Location of Focused Stream ( $\mu\text{m}$ ) from left edge of channel | Average Levitation Height ( $\mu\text{m}$ ) from floor of channel |
|------------------------------|---|--|---|
| 2.7                          | 50  | 960 $\pm$ 59   | 116 $\pm$ 14  |
|                              | 100   | 972 $\pm$ 25   | 99 $\pm$ 21   |
|                              | 200   | 985 $\pm$ 9  | 96 $\pm$ 34   |
| 3.2                          | 50  | 925 $\pm$ 42   | 122 $\pm$ 9   |
|                              | 100   | 1022 $\pm$ 38  | 120 $\pm$ 4   |
|                              | 200   | 1006 $\pm$ 5   | 128 $\pm$ 7   |
| 3.7                          | 50  | 992 $\pm$ 52   | 101 $\pm$ 24  |
|                              | 100   | 1008 $\pm$ 24  | 132 $\pm$ 14  |
|                              | 200   | 1001 $\pm$ 4   | 138 $\pm$ 19  |

Values are mean $\pm$ standard error of deviation. Peak to peak drive voltage amplitude for PZT was 10.16 V at 2.7 MHz, 11.56 V at 3.2 MHz, and 9.27 V at 3.7 MHz.

**Table 3.** Characteristics of operation for acoustic deflection portion of the system (n=6)  
Values are mean $\pm$ standard error of deviation.

| Frequency of Operation (MHz) | Amplitude of Drive Voltage (V <sub>peak-to-peak</sub> ) | Average Deflection Height ( $\mu\text{m}$ ) | Capture Efficiency (%) |
|------------------------------|---|---|------------------------|
| 3.7                          | 12.32   | 25 $\pm$ 9                                  | 69                     |
| 4.1                          | 13.11   | 28 $\pm$ 3                                  | 72                     |
| 4.6                          | 9.17  | 40 $\pm$ 6                                  | 97                     |
| 4.9                          | 11.19   | 43 $\pm$ 7                                  | 98                     |
| 5.1                          | 14.56   | 33 $\pm$ 6                                  | 79                     |
| 5.4                          | 12.29   | 29 $\pm$ 6                                  | 76                     |
| 5.7                          | 13.45   | 33 $\pm$ 6                                  | 78                     |

## 5. Conclusions

In this paper we present data on the fabrication, modeling, and characterization of devices that integrate microacoustics with microfluidic systems to focus particles for flow cytometry applications. These systems allow for the creation of standing waves between the boundaries of microchannels to move particles to pressure nulls. By increasing the number of patterned top electrodes interfacing with

the microfluidic channel, we aim to “phase” the acoustic radiation force between two or more strips of electrodes together to achieve more reliable and complicated manipulation of microparticles. By understanding the complex distribution of radiation forces within the system in future work, we will be able to better predict the performance of these devices. In the end, this integrated fabrication scheme has the potential to simultaneously increase functionality and portability while reducing system cost.

Sandia is a multiprogram laboratory operated by Sandia Corporation, a Lockheed Martin Company, for the United States Department of Energy under contract DEAC04-94AL 85000.

## References

- [1]. D. Huh, H. Wei, J. B. Grotberg and S. Takayama, Development of stable and tunable high-speed liquid jets in microscale for miniaturized and disposable flow cytometry, presented at *IEEE-EMBS Special Topic Conference on Microtechnologies in Medicine & Biology*, Madison, WI, 2002.
  - [2]. R. Yang, D. L. Feedback and W. Wang, Microfabrication and test of a three-dimensional polymer hydrofocusing unit for flow cytometry applications, *Sensors and Actuators A*, Vol. 118, 2005, pp. 259-267.
  - [3]. C. Simonnet and A. Groisman, High-throughput and high resolution flow cytometry in molded microfluidic devices, *Analytical Chemistry*, Vol. 78, 2006, pp. 5653-5663.
  - [4]. S. K. Ravula, D. S. Lidke, J. M. Oliver, D. W. Branch, G. Kaduchak, C. D. James, and I. M. Brener, A microfluidic platform with microacoustics and dielectrophoresis for high throughput analyses of spatiotemporal signaling in biological cells, presented at *Transducers*, Lyons, France, 2007.
  - [5]. S. K. Ravula, K. M. Taylor, D. S. Lidke, J. M. Oliver, C. D. James, and I. Brener, A microfabricated flow cytometry system for optical detection of cellular parameters, presented at *Biophysical Society Meeting*, Baltimore, MD, 2007.
  - [6]. S. K. Ravula, D. W. Branch, C. D. James, R. J. Townsend, M. Hill, G. Kaduchak, M. Ward, and I. Brener, A microfluidic system combining acoustic and dielectrophoretic particle preconcentration and focusing, submitted to *Sensors and Actuators B: Chemical*.
  - [7]. S. K. Ravula, D. W. Branch, J. Sigman, C. Arrington, P. G. Clem, I. Brener, Particle positioning in microchannels using ultrasonic standing waves reinforced with radiated near and far field pressure waves, presented at *International Conference on Micro Total Analysis Systems*, Paris, France, 2007.
  - [8]. S. K. Ravula, D. W. Branch, P. Clem, G. Kaduchak, and I. Brener, Microfluidics and microacoustics for miniature flow cytometry, presented at *NSTI Nanotechnology Conference*, Santa Clara, CA, 2007.
-

## Design and Characterization of MEMS Thermal Converter

**Jiri JAKOVENKO, Miroslav HUSAK, \*Tibor LALINSKY**

Department of Microelectronics, Czech Technical University in Prague,  
Technicka 2, 166 27, Prague 6, Czech Republic

\* Institute of Electrical Engineering, Slovak Academy of Sciences, Bratislava, Slovakia

E-mail: jakovenk@feld.cvut.cz, <http://www.micro.feld.cvut.cz>

*Received: 17 September 2007 / Accepted: 19 September 2007 / Published: 8 October 2007*

---

**Abstract:** This paper presents design and characterization of a new GaAs based RF Microwave Power Sensor (RFMPS) microsystem. The main criteria for the RFMPS optimization are to keep the stable thermal distribution and minimize the thermal stress. The concept of absorbed power measurement is based on thermal conversion, where absorbed RF power is transformed into thermal power, inside a thermally isolated system. The Micromechanical Thermal Converter (MTC) spatial temperature dependences, thermal time constant and power to temperature characteristics are calculated from the heat distribution. The temperature changes induced in the MTC by electrical power dissipated in the HEMT (High Electron Mobility Transistor) are sensed by the integrated temperature sensor (TS). The temperature distribution over the sensing area and mechanical stress was optimized by studying different MTC sizes, and topologies of the active HEMT heater and temperature sensor.  
*Copyright © 2007 IFSA.*

**Keywords:** MEMS thermal converter, Thermo-mechanical simulation, GaAs power sensor

---

### 1. Introduction

Transmitted power is the most important measure considered in RF systems. The usual approach to transmitted power measurement is based on the detection of absorbed power waves (incident and reflected) that requires complicated multiple power meter structures and need complex calibration.

An improved method for the absorbed power measurement is based on thermal conversion where, absorbed radio frequency (RF) power is transformed into thermal power inside of a thermally isolated system.

High thermal isolation of the MTC can be reached by the design of a free micromechanical plate which is as thin as possible. We have developed a new GaAs based MTC technological process, which creates optimal conditions for both the monolithic integration of the active HEMT heater and thermal isolation of the microwave sensor elements. Thermo-mechanical numerical modeling and temperature distribution optimization have a significant influence on the performance of the Micromechanical Thermal Converter. MTC structures with diverse sizes and arrangements of the heater and the temperature sensor were studied.

The thermoelectric AC power sensor and microwave power sensor were firstly analyzed by Jaeggy and Kopystinski [1, 2] by using CMOS IC technology. The heater was defined with a polysilicon resistor and a Polysilicon/ Aluminium thermopile was used as temperature sensor. Unfortunately, these sensors can not be integrated with III-V compound semiconductors.

The Gallium Arsenide based Micro-Electro-Mechanical Systems have some advantages over the well-understood Silicon micromachined microsensors. The most considerable advantages are some intrinsic material properties such as lower thermal conductivity, high temperature performance, heterostructure quantum effects, etc. The HEMT technology has been developed for our GaAs based MEMS structures.

## **2. Theory**

The simulation of steady-state and transient dependences of the MEMS devices with embedded thermo-mechanical behavior leads to the solution of three sets of differential equations that govern the electric current (dissipation), thermal, and thermo-mechanical behaviors.

### **2.1. Electric Current and Joule Heat Generation**

Current distribution in the MTC structure for specified voltage boundary conditions is determined by solving the equation for continuity of current:

$$J = \sigma E, \quad (1)$$

where  $J$  is the current density [ $A.m^{-2}$ ],  $E$  is the electric field, and  $\sigma$  is the electric conductivity.

From (1) we can derive Joule heat generation per unit volume is

$$q = JE. \quad (2)$$

Electric field  $E$  can be expressed:  $E = -\nabla V$ , where  $V$  is electric potential (voltage).

### **2.2. Heat Equation**

#### **Conduction**

The steady-state heat conduction equation shown below is solved for temperature distribution for specified thermal boundary conditions, including insulation, natural convection and radiation. The Fourier equation for temperature distribution can be written as follows:

$$\operatorname{div}(\lambda \operatorname{grad} T) = \rho c \frac{\partial T}{\partial t} - p, \quad (3)$$

where  $\lambda$  [ $\text{W m}^{-1} \text{K}^{-1}$ ] is coefficient of thermal conductivity,  $\rho$  mass [ $\text{kg m}^{-3}$ ],  $c$  [ $\text{J kg}^{-1} \text{K}^{-1}$ ] thermal capacity and  $p$  specific heat [ $\text{W m}^{-3}$ ]. Coefficient of thermal conductivity is not constant with temperature differences, however, in most MEMS applications it can be taken as constant. This is also the case here. The value of heat flux can be expressed as:

$$q = -\lambda \cdot \operatorname{grad} T \quad [\text{W.m}^{-2}], \quad (4)$$

If the solid body is heated up by constant power generation and cooled down constantly by the surrounding environment then the temperature distribution will fix. For Cartesian coordinates the temperature distribution can be obtained by solving the following equation [5]:

$$\nabla^2 T(r, t) + \frac{Q(r, t)}{\lambda} = \frac{1}{\alpha} \frac{\partial T(r, t)}{\partial t} \quad (5)$$

## Convection

The ambient of thermal MEMS devices is often various gases or liquids. In such cases the convection effects should be also taken into account. Convection depends on specific dimensions and shapes of the device.

The density of heat flux under the convection is given [5]

$$q = \alpha \cdot \Delta t = \alpha(t_{st} - t_t) \quad [\text{W.m}^{-2}], \quad (6)$$

where  $\alpha$  [ $\text{W.m}^{-2}.\text{s}^{-1}$ ] is heat transfer coefficient given by criteria equation (see below),  $t_{st}$  is wall temperature of solid body,  $t_t$  is gas or liquid surrounding temperature and  $A$  contact area.

Criteria equation can be found in literature in following form for instance [5]:

$$Nu = f(Re, Gr, Pr, \dots), \quad (7)$$

where

$$\begin{aligned} Nu &= \frac{\alpha L}{\lambda_{tek}}, & Re &= \frac{c \cdot L}{\nu}, \\ Pr &= \frac{\nu}{a} = \frac{\eta \cdot c_p}{\lambda}, & Gr &= \gamma \cdot \Delta t \cdot \frac{gL^3}{\nu^2}, \\ Pe &= \frac{c \cdot L}{a} = Re \cdot Pr \end{aligned}$$

Criteria equation for natural convection can be expressed in the form [5]:

$$Nu = C \cdot (Gr \cdot Pr)^n, \quad (8)$$

$C$  and  $n$  constants depends on the value of the product Gr.Pr according Table 1:

**Table 1.** Value of  $C$  and  $n$  depends on Gr.Pr.

| Gr.Pr                    | C     | n     |
|--------------------------|-------|-------|
| $< 1.10^{-3}$            | 0,45  | 0,0   |
| $1.10^{-3} \cong 5.10^2$ | 1,18  | 0,125 |
| $5.10^2 \cong 2.10^7$    | 0,54  | 0,25  |
| $2.10^7 \cong 1.10^{13}$ | 0,195 | 0,333 |

## Radiation

For MEMS devices operating at room temperature the heat losses caused by radiation can be usually neglected. Radiation can have a significant effect for the devices working much above 400 K on the other hand. Therefore for such devices a verification of radiation effects should be conducted.

Heat losses caused by radiation is given by Stefan-Boltzmann emissive law:

$$P_{Rad} = \varepsilon_{1,2} \cdot C_0 \cdot A \sigma T^4, \quad (9)$$

where

$$\varepsilon_{1,2} = \frac{1}{\frac{1}{\varepsilon_1} + \frac{1}{\varepsilon_2} - 1} \quad (10)$$

$\varepsilon$  is emissivity of gray body,  $A$  is the body surface and  $\sigma$  is Stefan-Boltzmann constant =  $5.67 \cdot 10^{-8} [\text{W} \cdot \text{m}^{-2} \text{K}^{-4}]$ .

## 3. MTC Design and Technology Process

The MTC structures used in thermally based MEMS devices are mostly designed as free space standing structures. To increase the thermal resistance values, they have to be designed with the thickness as thin as possible. A new processing technology for a GaAs micromechanical island structure has been developed. The technology process begins with the MBE or MOCVD growth of GaAs heterostructures on semi-insulating substrates (SI-GaAs) (Fig. 1). A front-side processing technology is performed to define Source (S), Drain (D) and Gate (G) of the HEMT. The GaAs surface is completed by Ti (50 nm) / Au (150 nm) metallic transmission lines, which allow connections to the heater and TS.

The next step is the surface micromachining of the cantilever, bridge or island by a masked non-selective wet or plasma etching of the heterostructures up to semi-insulating (SI) GaAs. Surface micromachining is followed by deposition and subsequent thermal forming of a thin top polyimide layer. Finally, a three-dimensional patterning of the micro-mechanical structures is defined by a deep back-side selective reactive ion etching of SI-GaAs through the openings in mask, using AlGaAs together with the polyimide as an etch-stop layer.

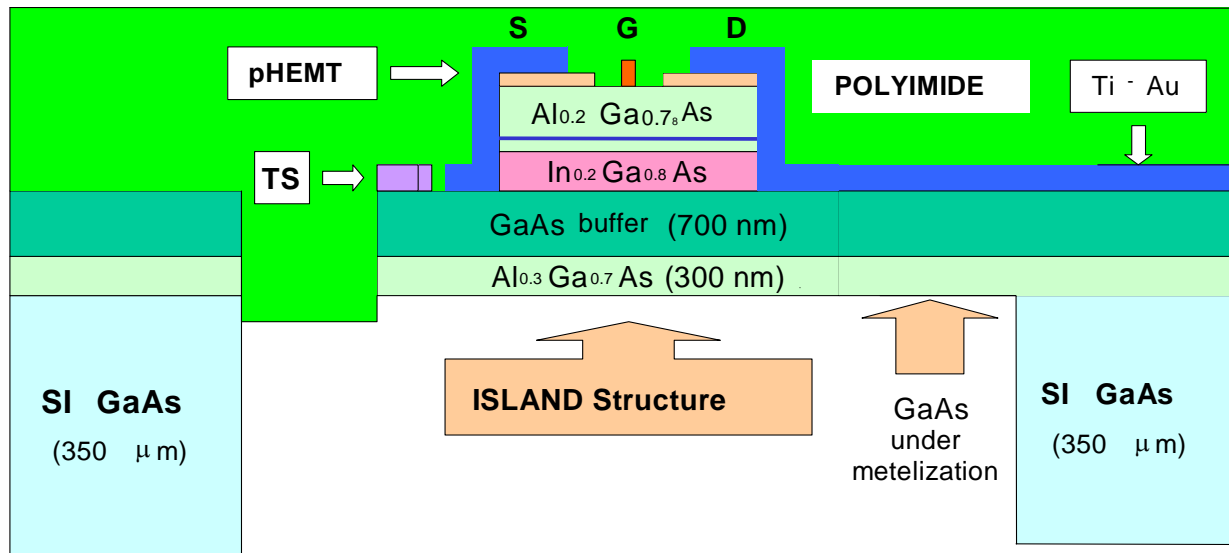


**Fig. 1.** Schematic cross-section through the polyimide-fixed MTC structure to be integrated with HEMT as heater and poly-Si/Pt thin film resistor as temperature sensor TS.

A thin polyimide layer is deposited after the bulk GaAs micromachining and enables the micromechanical structures to be mechanically fixed and thermally isolated in a free space.

A schematic cross-section is shown on Fig. 1. A Silicon delta-doped layer is formed for HEMT design in the  $\text{Al}_{0.22}\text{Ga}_{0.78}\text{As}$  barrier layer. This layer is separated by 3 nm thick undoped  $\text{Al}_{0.22}\text{Ga}_{0.78}\text{As}$  spacer from the  $\text{In}_{0.2}\text{Ga}_{0.8}\text{As}$  channel. A GaAs/ $\text{Al}_{0.3}\text{Ga}_{0.7}\text{As}$  (700 / 300 nm) heterostructure buffer layer under channel was designed to define the thickness of the MEMS structure.

Subsequent benefits of this technology is that the microwave controlled circuit can be also integrated within the MTC microstructure.

Fig. 2 shows the model of the GaAs island structure which has been proposed to increase the sensor thermal resistance. The GaAs island ( $175\ \mu\text{m} \times 125\ \mu\text{m}$ ) floats in  $1\ \mu\text{m}$  thin polyimide membrane ( $225\ \mu\text{m} \times 360\ \mu\text{m}$ ) that mechanically fixes and thermally isolates the GaAs MTC plate. For numerical simulation purposes the GaAs substrate rim has been designed  $10\ \mu\text{m}$  thick and  $50\ \mu\text{m}$  wide. These dimensions ensure sufficient mass for simulator boundary condition setting while keeping the number of simulation nodes at a reasonable level.

#### 4. P-T Characteristic and Steady State Thermal Analysis

Main characteristics for the thermal converters optimization are the temperature distribution over the sensing area, the time response, the sensitivity and the mechanical stresses in the multilayer structure.

The input power dissipation in the heater was defined as heat flux coming through the HEMT gate area ( $10\ \mu\text{m} \times 0.5\ \mu\text{m}$ ). We can use this approximation because the heat dissipation in the HEMT structure is generated in the very thin conduction layer which formed under the gate area.

The spatial temperature distribution of the MTCs and steady state heat flux were calculated taking into the account the heat transfers to infinity. In the current analysis, according to the application

requirement, the fixed thermal boundary is defined for the all side walls of GaAs substrate. These sides were kept at the room temperature of 300 K while other sides were adiabatic.

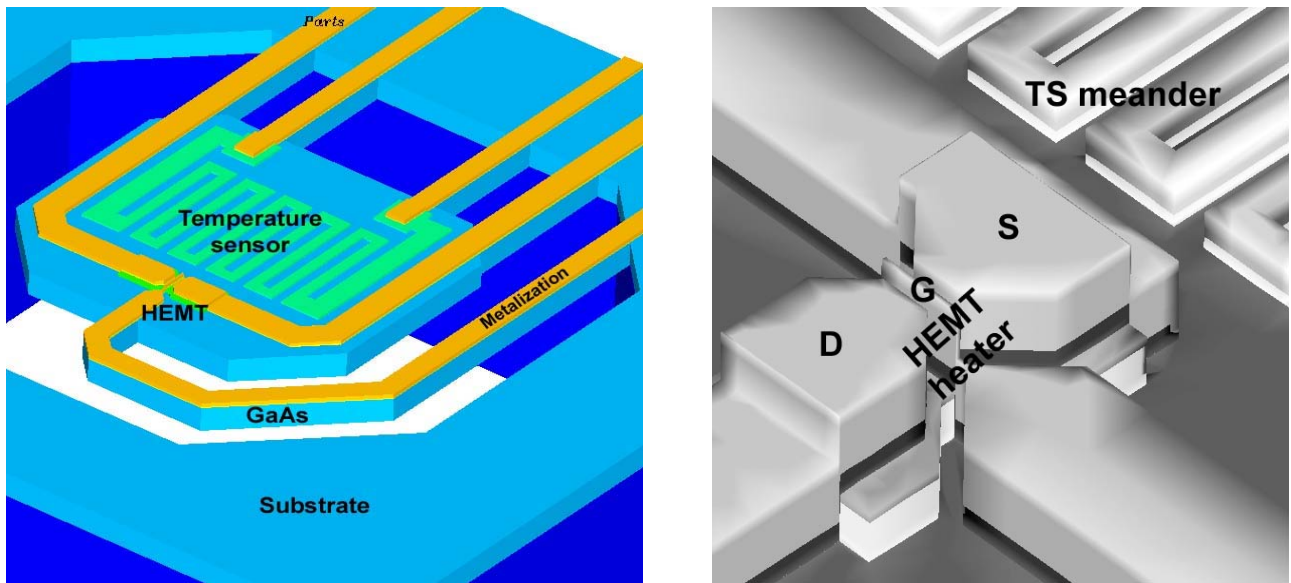


**Fig. 2.** Model of the Island MTC structure. GaAs island is floating” in Polyimide 1  $\mu\text{m}$  thick layer (not visible). The meander-shaped TS is also shown. Z-direction is 20times magnified.  
The Detail of HEMT heater is on the right.

A 3-D diagram gives good overall visualization of the temperature distribution (Fig.3) in the island MTC structure caused by the power dissipation generated by the HEMT heater. Thermal boundary conditions were defined for the side walls of the GaAs substrate. These sides were kept at the room temperature of 300K while other sides were adiabatic. The island is “floating” in the polyimide layer that mechanically fixes and thermally isolates the MTC structure. The polyimide layer is not shown on the figure, but was considered in the simulation.

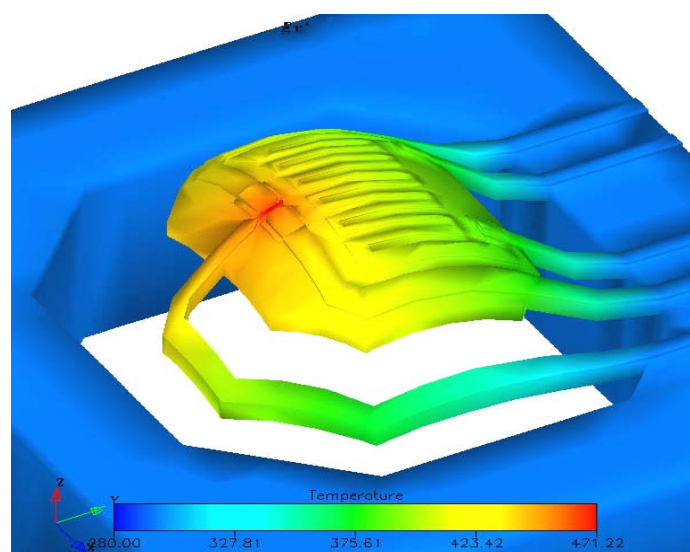


**Fig. 3.** 3-D Plots of temperature distribution of the island MTC structure for power dissipation of 2 mW. The island is “floating” in polyimide layer that mechanically and thermally isolates the MTC structure. Polyimide layer is not shown.

The thermal analyses were performed for both vacuum ambient and non-convective gaseous medium around the MTC structure. The heat losses, due to radiation, were viewed as negligible. The derived power to temperature characteristic is shown in Fig. 4. From the angular coefficient we can express the thermal resistance  $R_{th}$  of the structure which is summarized, for different topologies of the MTC structure, in Table 2.

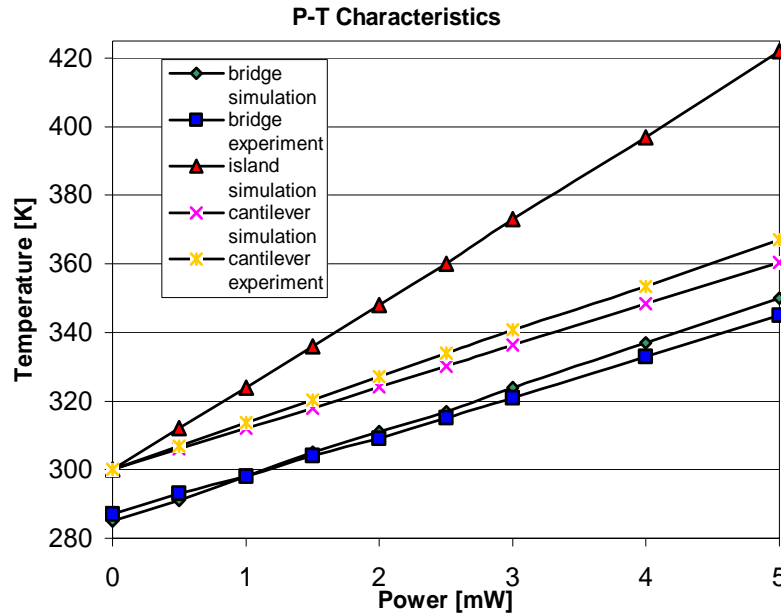


**Fig. 4.** Simulated island, cantilever and bridge Power to Temperature characteristics. Comparison with real micro-machined MTC device. Ambient temperature for bridge MTC was 285 K whereas other two MTCs ambient were 300 K.

The transient on/off power characteristics for the island structure are depicted in Fig. 5. At the beginning (time = 0 s) a power of 2 mW switched ON. At time = 5 ms the power was switched OFF. The thermal time constant of the island structure arrangement is 1.9 ms. There are three transients shown in Fig. 5. The upper one is the maximal temperature of the heater and the bottom dependence reflects the average temperature of TS.

Stress and displacement magnitude evaluation were simulated for BC where the outer substrate rim was set as rigid (non moveable). Fig 3 also shows the mechanical deflection of the island MTC structure for a power dissipation of 2 mW.

## 5. Optimization of MTC Structures

New optimized island structure design reduces the maximal stress caused by temperature changes and minimize the temperature losses that were caused by short supplying metallization to HEMT transistor.

Gate supplying metallization was led around the island in order to lengthen it as much as possible (Fig 3). The temperature losses are minimized by this solution. Another advantage is that all metallization are entering the substrate surface in the same side. Mechanical compressions and stresses are minimized by this solution.

The influence of the gate width on the maximal temperature of the MTC structure has been simulated. Temperature distribution in the HEMT and in the MTC structure for different gate widths (5  $\mu\text{m}$ , 10  $\mu\text{m}$ , 15  $\mu\text{m}$ , 20  $\mu\text{m}$ ) has been obtained. From the simulation results follows that the maximal temperature of the MTC which is located in the gate of the HEMT is inversely proportional to the gate width (Fig. 6).

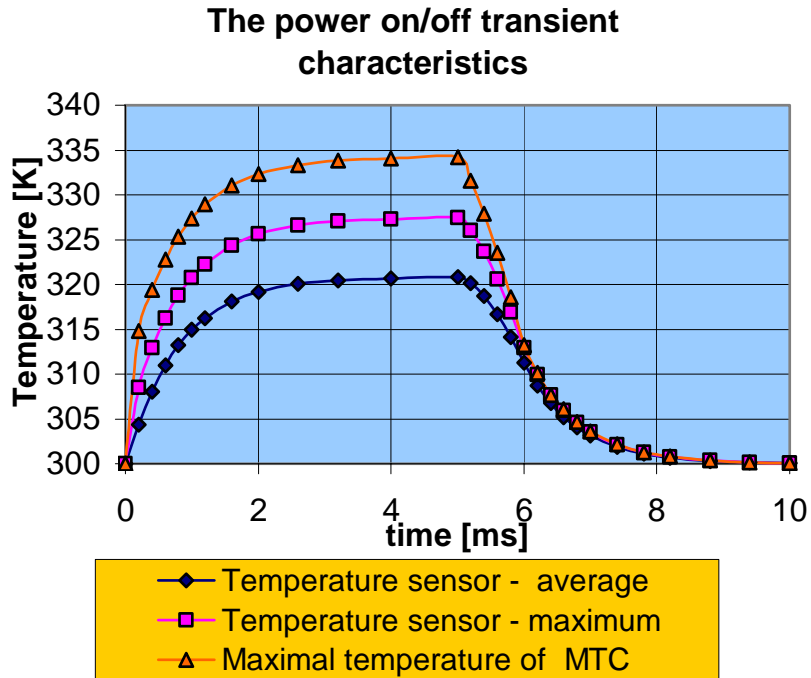


**Fig. 5.** The power on/off transient characteristics for island MTC structure for power ON of 2mW. At the beginning there was power of 2mW switched ON. In the time of 5ms the power was switched OFF.

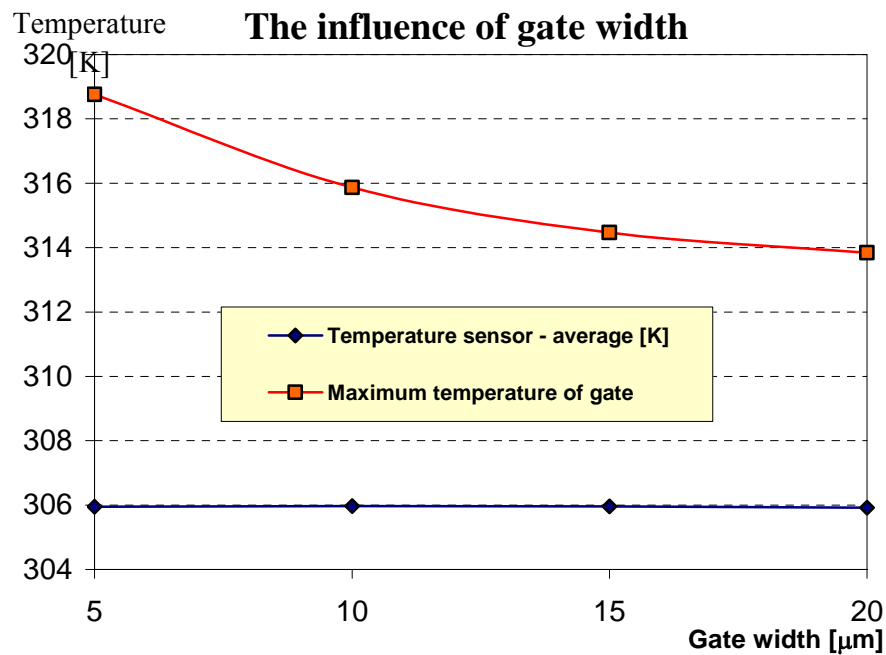


**Fig. 6.** Maximal and average temperature – HEMT gate width dependence. Dissipated power was 0.5 mW.

These analyses have demonstrated that the temperature sensed by the temperature sensor remained the same. It can be concluded that the HEMT gate width does not have any influence on the sensitivity of the MTC, and only influences maximal system temperature changes. In order to minimize maximal temperature of the sensor it is desirable to increase the HEMT gate width. Due to maximal temperature reduction the sensor could be used for a wider field of measured power while the sensitivity remains the same.

A comparison of the designed island MTC structures is summarized in Table 2.

**Table 2.** MTC simulation results summary.

|                                    | Island without GaAs | Island with GaAs | Optimized island with GaAs |
|------------------------------------|---------------------|------------------|----------------------------|
| $R_{th}$ simulation [K/mW]         | 24                  | 13               | 26                         |
| $R_{th}$ measurement [K/mW]        | -                   | 14               | -                          |
| $\tau$ simulation [ ms ]           | 0.9                 | 0.9              | 0.8                        |
| $\tau$ measurement [ ms ]          | -                   | 0.8              | -                          |
| Max. temperature [K] (1mW)         | 332                 | 320              | 336                        |
| Max. displacement [ $\mu$ m] (1mW) | 2.74                | 0.26             | 5.28                       |
| Max. mechanical stress [MPa] (1mW) | 540                 | 434              | 284                        |

## 6. Conclusions

Spatial temperature dependences, thermal time constant, thermal stress and displacement and power to temperature characteristics were calculated from the heat distribution. Temperature distribution, mechanical stresses and displacements of GaAs MEMS device have been simulated using CoventorWare. Using FEM simulations, the layout of the HEMT transistor, temperature sensor and MTC shapes and dimensions were also optimized.

Power to temperature (P-T) conversion characteristics of the MTC devices was simulated and compared with measurements of real micromachined structures. The high electro-thermal conversion efficiency, defined by extracted thermal resistance values ( $R_{th}$ ) 24 K/mW, was achieved for the island structure. As compared with the experimental data, the thermal resistance values are congruent.

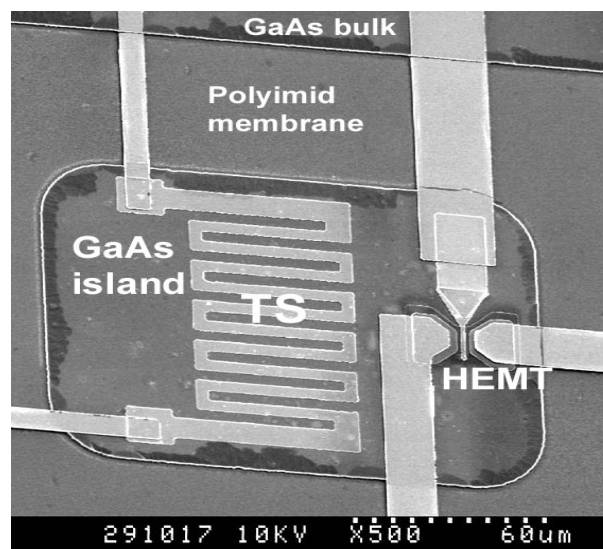


**Fig. 7.** Real micromachined island MTC structure.

## References

- [1]. Jaeggy, H. Baltes and D. Moser, Thermoelectric AC Power Sensor by CMOS Technology, *IEEE Electron Device Letters*, 13, 1992, p. 366.
- [2]. P. Kopystinski, H. Obermayer, H. Delfts, W. Hohenester and A. Loser, Silicon RF Power Sensor from DC to Microwave, *Microsystem Technologies*, 1990, pp. 605.
- [3]. T. Lalinský, M. Držík, J. Jakovenko, M. Husák, MEMS/NEMS handbook: techniques and applications, Chapter 3, Ed. C. T. Leondes, 2006, pp. 49-109.
- [4]. J. Jakovenko, M. Husak, T. Lalinsky, Design and simulation of micromechanical thermal converter for RF power sensor microsystem, *Microelectronics Reliability*, Elsevier, ISSN 0026-2714, Vol. 44, 2004, pp. 141–148.
- [5]. S. D. Senturia, Microsystem Design, *Kluwer Academic Publisher*, book, 2001.
- [6]. M. Elwensoekk, R. Wiegerink, Mechanical Mikrosensors, *Springer*, book, 2000.
- [7]. Tai-Ran Hsu, MEMS and Microsystems Design and Manufacture, *Mc Graw Hill*, book, 2001.
- [8]. A. Dehe, V. Krozer, B. Chen and H. Hartnagel, High-sensitivity microwave Power Sensor for GaAs-MMIC implementation, *Electronics Letters*, 32, 1996, pp. 2149-2150.

---

2007 Copyright ©, International Frequency Sensor Association (IFSA). All rights reserved.  
(<http://www.sensorsportal.com>)



**International Frequency Sensor Association**

is a professional association and Network of Excellence,  
created with the aim to encourage the researches and developments  
in the area of quasi-digital and digital smart sensors and transducers.



For more information about IFSA membership, visit  
**<http://www.sensorsportal.com>**

## Fabrication of a Real Time Reactive Ion Etching Resonant Sensor Using a Low Temperature Sacrificial Polymer

**Bryan G. MORRIS, Paul J. JOSEPH and \*Gary S. MAY**

Georgia Institute of Technology, Atlanta, GA, USA

\*Tel.: (404) 894-2902, fax: (404) 894-4641

E-mail: [gary.may@ece.gatech.edu](mailto:gary.may@ece.gatech.edu)

*Received: 17 September 2007 / Accepted: 19 September 2007 / Published: 8 October 2007*

---

**Abstract:** This paper presents a sacrificial layer process using a low temperature polymer as the sacrificial material for fabricating a surface micromachined reactive ion etching (RIE) resonant sensor. The sensor monitors film thickness and etch rate in the RIE process and will ultimately facilitate closed-loop control. This RIE monitoring methodology exploits the accuracy of resonant micromechanical structures, whereby shifts in the fundamental resonant frequency measure a physical parameter. A majority of these systems require free-standing mechanical movement and utilize a sacrificial layer process as the key technique to develop and release the structure on a substrate. The low temperature sacrificial layer process released the suspended sensor with excellent performance and is capable of fabricating other low cost, high performance and reliable suspended MEMS devices. *Copyright © 2007 IFSA.*

**Keywords:** Resonant sensor, Sacrificial layer process, Reactive ion etching (RIE), In-situ monitoring, Endpoint detection

---

### 1. Introduction

State-of-the-art integrated circuits currently employ upwards of 60 million transistors, six layers of metal, and operate at clock frequencies over 1 GHz. As device dimensions continue to shrink and the speed of computing and communications systems increases, the effect of fluctuations in the manufacturing process becomes critical. Achieving tight specifications, given the continuing trend toward even further miniaturization, represents a major challenge in process control, an issue of critical importance to the semiconductor industry.

Reactive ion etching (RIE) has emerged as a critical step in integrated circuit (IC) fabrication, as it offers high etch directionality, enabling accurate pattern transfer not obtainable with wet etching. Despite its widespread use in the semiconductor manufacturing industry, process control techniques for RIE are inhibited by the inadequacy of existing process sensor technology. Although real-time monitoring techniques exist for the regulation of process conditions such as gas flow, RF power, and chamber pressure, extant process monitoring methods are unable to provide direct, real-time measurements of the actual wafer state during the etch [1].

In this paper, a MEMS device for real-time RIE monitoring is fabricated using a low temperature sacrificial polymer. Ultimately, this device is expected to facilitate closed-loop feedback control. As an application vehicle, process control will be demonstrated in the Plasma Therm SLR series RIE system located in the Georgia Tech Microelectronics Research Center.

## **2. Reactive Ion Etching**

Real-time monitoring of RIE is essential for process control. Ideally, one would like to monitor the RIE process *in-situ* and control outputs such as etch rate, uniformity, and anisotropy directly. However, a complete array of technologies to measure these quantities is not available [2]. Conventional techniques for RIE process monitoring are typically performed off-line. Among the few existing in-situ monitoring techniques are optical emission spectroscopy (OES), residual gas analysis (RGA), and interferometry. The following is a brief review of existing methods for RIE monitoring and control.

### **2.1. Existing Methods of RIE Monitoring**

OES is a bulk measure of the optical radiation of the plasma species. Since emissions come from reactants and products, OES measurements are most often used to obtain the average optical intensity at a particular wavelength above the wafer. By setting an optical spectrometer to monitor the intensity at a wavelength associated with a particular reactant or by-product species, OES serves as an effective endpoint detector. However, the applicability of OES measurements for direct observation of wafer state and/or real-time control remains a challenge. This is because light generated by plasma is rich in emissions from many species that cover a wide spectral range. For some etch chemistries, it is difficult to separate a characteristic line from the intensity background [3].

Another existing scheme for monitoring RIE is to analyze the residual gas composition in the process chamber using mass spectroscopy. An RIE system continuously depletes its chamber gases during etching. At the beginning of etching, the gas in the chamber consists of a mixture of process gas and that resulting from etching. Towards the end, the gas in the chamber will resemble its mixture prior to etching. This information may be used to detect the etch endpoint using RGA. However, RGAs are usually very bulky and require a relatively large work space for mounting. Although new miniature RGA technologies have addressed the size issue, they are still difficult to mount and restrict access to the process chamber, and their small size imposes limits on their ability to separate species with different mass/charge ratios [4].

Laser interferometry gives direct etch rate measurements at the wafer surface by exploiting interference patterns of monochromatic light rays which occur when light is reflected from an upper and an underlying interface. The reflected intensity is a periodic function of film thickness, and its amplitude is a function of the index of refraction of the ambient, film and substrate. At normal incidence, etch rate may be calculated by determining the time between minimum or maximum intensity peaks in an interferogram. Although interferometry works well for endpoint detection, it is

limited in that it covers only a small spot on the surface of the wafer. This technique also only works for translucent films. Alignment, calibration, and mounting of the interferometer are also concerns [5].

### 3. Sensor Technology

The micromachined sensor will be placed in an RIE system to monitor key figures of merit *in-situ*. One of the greatest benefits of micromachining is that the fabrication process can be made compatible with standard IC processing. Mechanical structures can thus be integrated with support electronics to yield a "smart sensor" [6]. This is the approach envisioned for RIE monitoring and control.

One example of a micromachined sensor is the prototype designed at Georgia Tech to assess RIE etch rate [7]. The platform was coated with the same material to be etched from the substrate and positioned above drive and sense electrodes. As etching proceeds, the sensor is excited into resonance. As the mass loading of the platform decreases during etching, its resonant vibrational frequency shifts by an amount proportional to the amount of material remaining, allowing etch rate to be inferred.

#### 3.1 Principle of Operation

The RIE sensor relies on a principle of electrostatic excitation and capacitive detection. This technique requires two electrodes that are in close proximity to a vibrating structure. A voltage applied across the electrodes creates an electrostatic pulling effect on the vibrating element and a displacement current result from the air gap capacitance between the electrodes and the vibrating structure.

The expression for the fundamental resonant frequency of a single-material, flat, thin platform (assuming that air dampening and axial stress are negligible, and that the vibrational amplitudes are small compared to the platform thickness) is:

$$\omega_1 = 2\pi f_1 = \frac{\lambda^2}{\sqrt{12}} \frac{h}{l^2} \sqrt{\frac{E}{\rho(1-\nu^2)}} \quad (1)$$

where  $E$  is Young's modulus,  $\nu$  is Poisson's ratio,  $\rho$  is the density of the platform, and  $\lambda$ ,  $h$ , and  $l$  are the platform's mode constant, thickness, and length, respectively.

Fig. 1 shows the prototype micromachined sensor designed to assess RIE etch rate. During operation, the MEMS platform is coated with the same material to be etched from the substrate and positioned above drive and sense electrodes. As etching takes place, the sensor is excited into resonance by the drive electrodes.

The natural frequency of this prototype sensor was measured by electrostatically exciting the sensor while detecting its movement optically with a vibrometer interfaced with an HP4194A network analyzer. The resonant condition was found to occur at 31.4 KHz, which compares well with the frequency of 38.1 KHz computed using Eqn. (1) (with  $h = 9 \mu\text{m}$ ,  $l = 787 \mu\text{m}$ ,  $\rho = 1400 \text{ kg/m}^3$ , and  $E = 8.3 \text{ GPa}$ ).

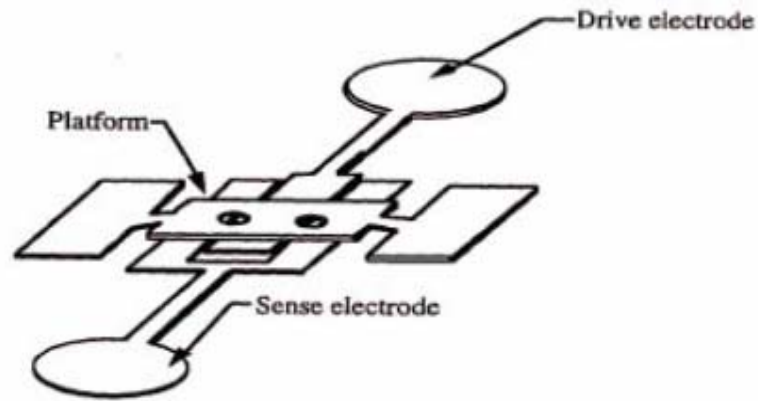


**Fig. 1.** Prototype micromachined sensor showing the platform suspended over drive and sense electrodes.

### 3.2. Finite Element Analysis of New Sensor Design

The RIE sensor has an element vibrating at resonance which must be highly sensitive to changes in the physical or chemical parameters of what is being measured. The newly configured RIE sensor was developed with a high mechanical Q-factor, since the sensor stability and performance is then almost entirely dependent on the mechanical properties of the resonator elements.

The redesigned RIE sensor in [8] was analyzed and optimized by finite element analysis (FEA). This computer-based numerical technique for calculating the strength and behavior of engineering structures was conducted using ANSYS 7.0. The ANSYS parameters are given in Table 1.

**Table 1.** ANSYS parameters for RIE sensor model

| Parameter       | $\mu\text{MKSV}$ units     |
|-----------------|----------------------------|
| Platform Length | 700 $\mu\text{m}$          |
| Platform Width  | 140 $\mu\text{m}$          |
| Platform Height | 9 $\mu\text{m}$            |
| Young's Modulus | 8.3e3 GPa                  |
| Poisson Ratio   | 0.34                       |
| Density         | 1400e-18 kg/ $\mu\text{m}$ |

The sensor was first modeled and meshed using a 2-D element type, and then extruded into the 3-D model shown in Fig. 2.

The RIE sensor was deformed and examined to establish the relationship between applied loads and deflections. We obtained the profile of the first three mode shapes and resonant frequencies and found that the fundament and harmonics were within the expected range. Simulations compare closely with the expected value of 33.3 kHz. The results are summarized in Table 2.

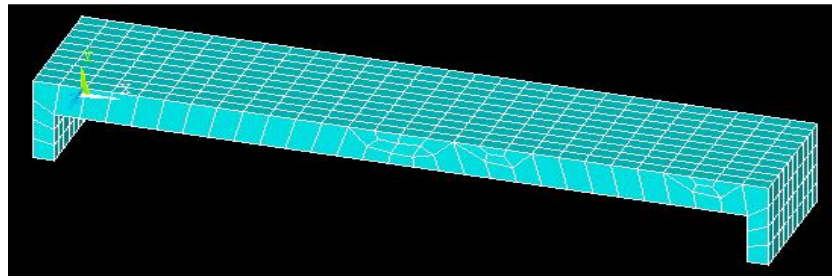


**Fig. 2.** 3-D meshed model of RIE sensor.

**Table 2.** RIE sensor resonant frequencies.

| Harmonics | Frequency |
|-----------|-----------|
| f1        | 50.4 kHz  |
| f2        | 137.3 kHz |
| f3        | 137.3 kHz |

Steady state, transient and random vibration behavior was also analyzed to study the effects caused by the applied load to the sensor. Boundary conditions were employed to indicate where the structure was constrained and restricted against movement or in the case of our symmetric RIE resonant structure when only a portion of the sensor needed to be modeled.

The platform was modeled as a uniform beam with both ends clamped and suspended above a ground plane. To confirm the expected response of the sensor, an electrostatic force was applied. The application of a range of voltages between 10-100 volts caused the platform to deflect. The resonant frequency and displacements varied with the application of the load. Fig. 3 shows that the platform had its maximum deflection at the center, as expected, with a maximum displacement of 0.03216  $\mu\text{m}$ .

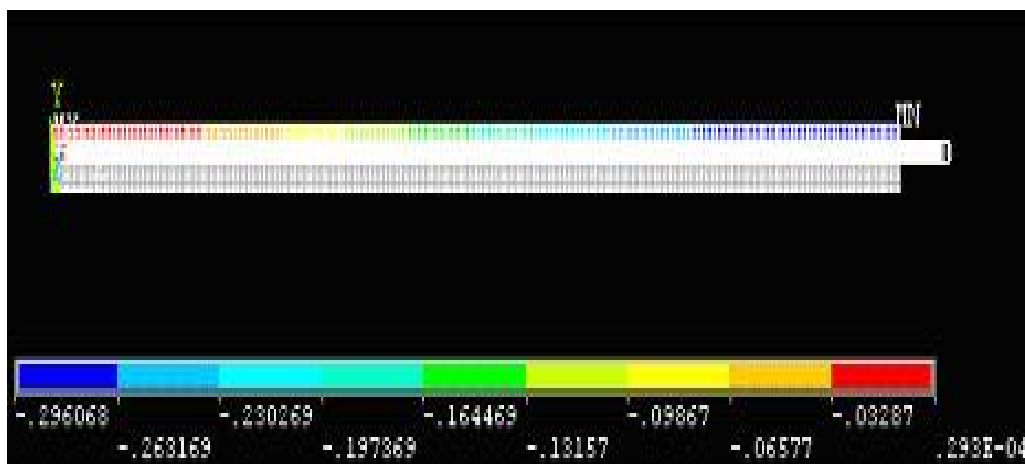


**Fig. 3.** Sensor displacement contour plot showing maximum displacement of 0.0322  $\mu\text{m}$ .

Changes in the mass loading of the platform are simulated by varying the height of the platform which produces a change in the capacitance between the platform and electrodes, resulting in the change in the resonant frequency of the structure. The platform height was varied from  $4\mu\text{m}$  to  $16\mu\text{m}$  to simulate the changes in film thickness that occurs during etching. The height increases as material is etched since there is reduced bending in the middle of the beam due to its own weight. When the height of the platform increased, the resonant frequency shifts to the right on the frequency spectrum and vice versa.

The frequency spectra in Fig. 4 illustrate how changing the height of the platform from  $9\mu\text{m}$  to  $16\mu\text{m}$  affects resonant frequency. The  $9\mu\text{m}$  platform has a resonant frequency of 20.45 kHz and a maximum displacement at the center of  $0.03216\mu\text{m}$ . The resonant frequency occurred at 35.65 kHz for a platform of height of  $16\mu\text{m}$ . This value is closer to the expected resonance frequency of 33.1 kHz. The maximum displacement at the platform center was reduced to  $0.011\mu\text{m}$ . The direct correlation of platform thickness and resonant frequency illustrated in Fig. 5 is evident, potentially providing the desired mechanism for real-time feedback on the wafer state during etching.

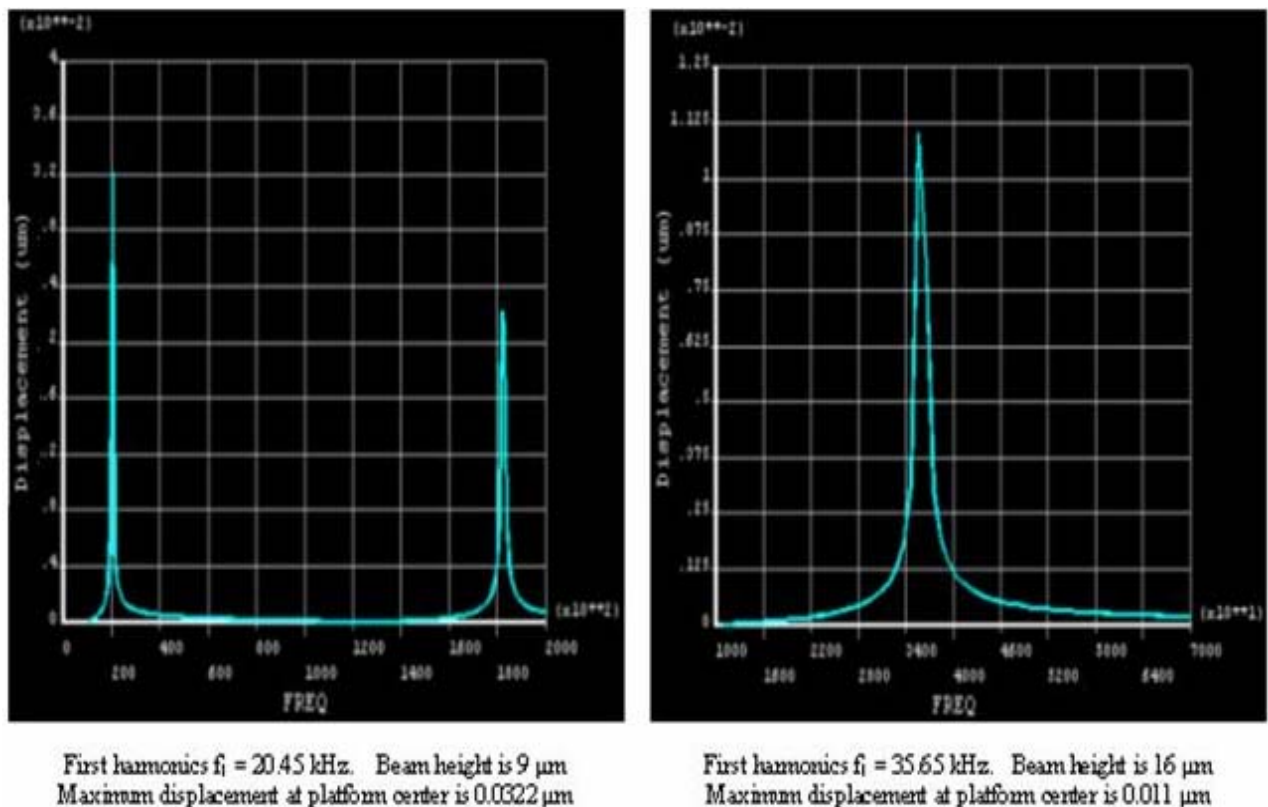


**Fig. 4.** Simulated resonant frequency for varying film thickness.

#### 4. Existing Sacrificial Layer Methods

This RIE monitoring methodology exploits the accuracy of resonant micromechanical structures, whereby shifts in the fundamental resonant frequency measure a physical parameter. A majority of these systems require free-standing mechanical movement and utilize a sacrificial layer process as the key technique to develop and release the structure on a substrate.

**Simulated resonant frequency of the platform as a function of the platform height**

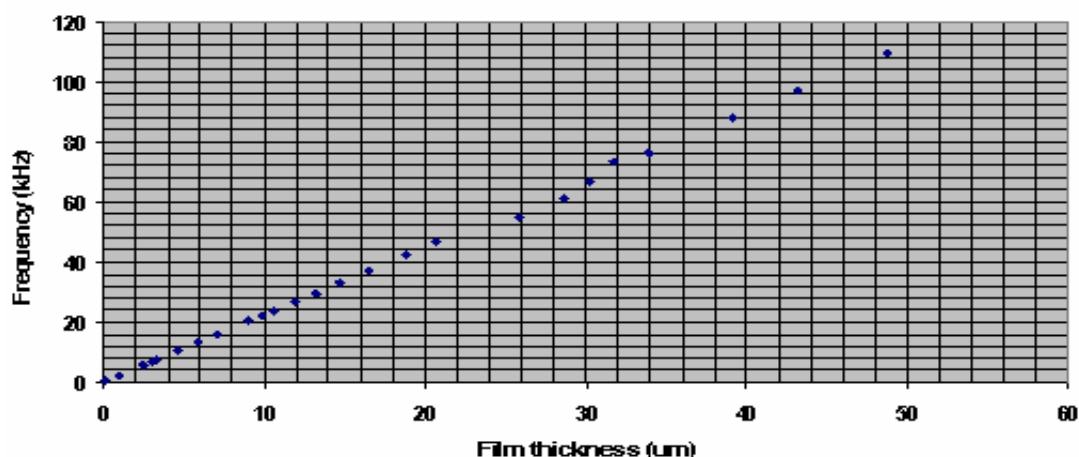


**Fig. 5.** Correlation between film thickness and changes in resonant frequency allows endpoint detection.

Metals have traditionally been used as sacrificial materials. In recent years, the trend has been towards photoresists and polyimide-based sacrificial materials. The difficulties inherent in achieving free-standing micro-structures with the existing sacrificial materials are well documented and include lengthy deposition cycles, slow and expensive release process using hazardous materials, sacrificial thicknesses limits, and the occurrence of stiction [9-11]. The latter is a well-known problem that occurs when the device is removed from the aqueous solution after wet etching of the underlying sacrificial layer (Fig. 6).

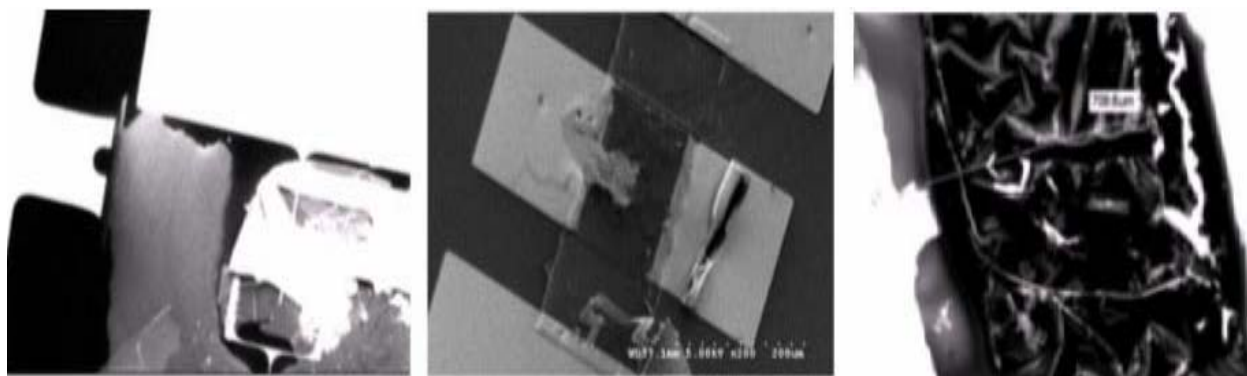


**Fig. 6.** SEM images showing RIE sensor damage observed after development and release using traditional sacrificial materials.

In view of the importance of sacrificial layers in MEMS devices, we demonstrated a sacrificial layer processes that possess the following attributes: (1) the process is simple and reproducible; (2) the coating process is compatible with dry or aqueous etching processes; and (3) the release-stiction problem is alleviated by thermal cure and decomposition of the sacrificial material.

## 5. RIE Sensor Fabrication

The prototype sensor described in this paper consists of three major parts: the drive electrode, the sense electrode, and the platform itself. The sensor was designed such that the end of the electrode was precisely centered beneath the platform. This is very important because the location of the drive electrode will impact the mode being excited. The sense electrode is placed in close proximity of the drive electrode, yet not in contact with it.

The platform has maximum displacement at its center and the capacitance change there is greatest. This implies that not only should the sense electrode be placed near the center of the platform, but the platform should be long compared to the width of the sense electrode. Centering the drive electrode relative to the platform is optimal.

Electrical isolation between the electrodes and the platform is critical. The isolation barrier and resulting air gap is created by utilizing a sacrificial layer material and process to develop and subsequently release the free standing sensor structure.

### 5.1. Fabrication Process

Fig. 7 is an overview of the fabrication process. The RIE sensor measures ( $700\text{ }\mu\text{m} \times 140\text{ }\mu\text{m}$ ) and the sacrificial layer is  $16\text{ }\mu\text{m}$ . The electrodes are etched from the first metallization layer. The sacrificial layer material is the low temperature polymer, Unity 2000P, which is spun on the substrate to the desired thickness. The spin curve in Fig. 8 is utilized to attain sacrificial layer thicknesses between  $2\text{--}80\text{ }\mu\text{m}$ .

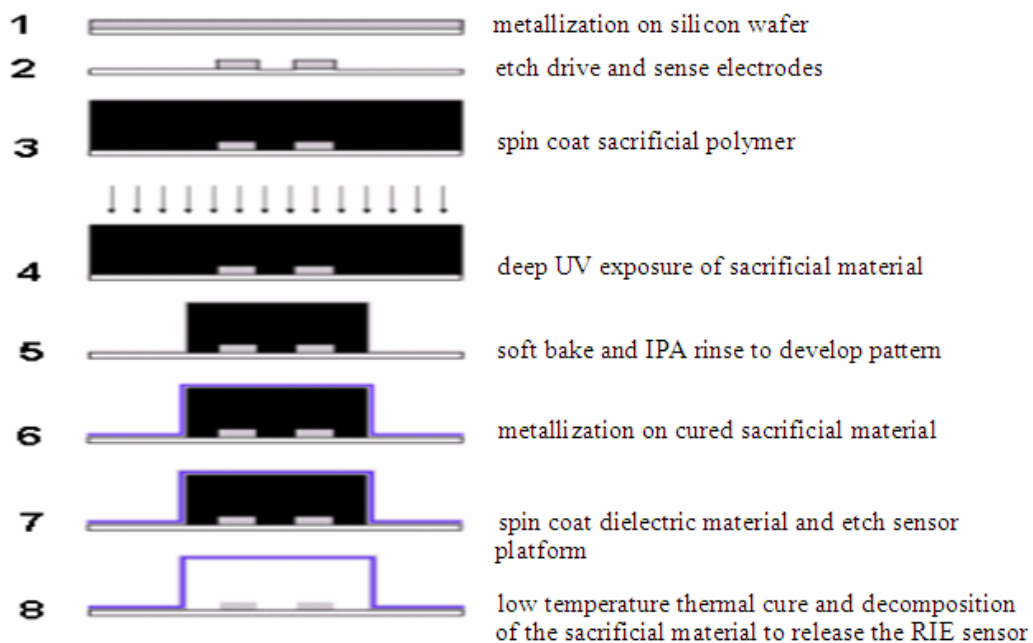


**Fig. 7.** Prototype RIE sensor fabrication process.

A dehydrate bake at  $100\text{ }^{\circ}\text{C}$  on the hotplate is followed by  $1000\text{ mJ}$  dose exposure with a quartz mask. The post exposure bake on the hotplate develops the sacrificial polymer and an IPA rinse removes the unexposed sacrificial material. Metallization and a dielectric coat is patterned and etched to create the

RIE sensor platform. Thermal curing in a 200 °C oven decomposes the sacrificial material and also releases the suspended micromachined resonant sensor.

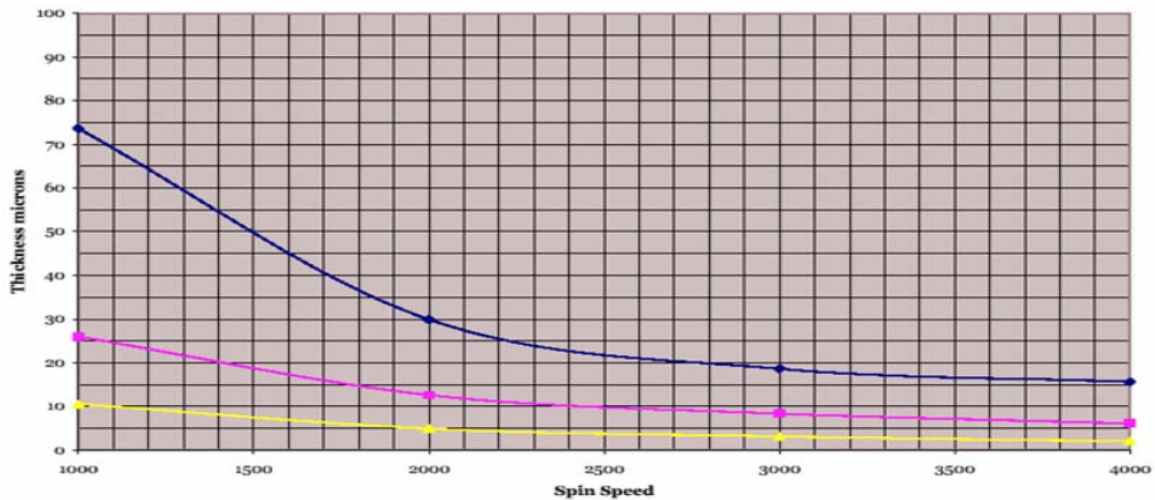


Fig. 8. Unity sacrificial polymer material spin curve.

## 6. Benefits of the New Sacrificial Layer Process

In order to use polymeric materials as clean-release layer, the materials must meet certain requirements. In the current situation, a photoacid generator (PAG) is incorporated in the polymer solution in the composite material which produces an acid on irradiation to UV light. The material should decompose in a narrow range of temperatures leaving little or no solid residue either from the polymer or the PAG. The sacrificial material must have sufficient adhesion to the substrates. The degradation products of the sacrificial material need to be volatile and should have the ability to permeate through the overcoat material. The decomposition temperature of the PAG should be much higher than the process-decomposition temperature of the material so that the UV exposed area only selectively decomposed. Since the polycarbonate-based sacrificial material met these above requirements, they were used as sacrificial material as release layer.

The advantage of using this low temperature sacrificial material and process is dependent on the application. The low temperature sacrificial material is easily coated to the wafer using standard process in a variety of different thicknesses. Thermal curing to convert the sacrificial material and decompose the material releasing the suspended structure is well suited for applications where critical dimension is not easily achieved using the other methods.

The sacrificial material is thermally stable, making the cured properties well suited for most semiconductor fabrication applications. The cured film is also highly resistant in most wet and dry processing chemical used in production, and properties of the cured film can be further optimized for a given application by varying the thickness of the sacrificial material coating.

### 6.1. Improvements in Process

The sacrificial layer material is self-priming, photosensitive and photodefinable, which permits the overcoat material to function without an additional resist masking step. The sacrificial layer material is patterned like photoresist on *I* or *g*-line semiconductor exposure tools. There are also improvements in

the resolution associated with utilizing this semitransparent sacrificial layer polymer material, in contrast with using other sacrificial materials.

Metal sacrificial layers require lengthy deposition cycles to achieve comparable thicknesses. A 16  $\mu\text{m}$  copper sacrificial layer requires 5-14 hrs when coated using the CVC E-beam evaporator or DC sputterer. An additional photoresist process is necessary to pattern the metal prior to the slow and expensive etch and release process using hazardous materials. Metal sacrificial layer materials significantly increase the number of fabrication steps and lengthen the process cycle time.

## **6.2. Reduction in Complexity**

In recent years, the trend has been toward photoresists and polyimide-based sacrificial materials. Polyimides are not inherently photosensitive, but can be made photodefinable with the addition of a methacrylate-based photo-polymerizable additive using an ester. Non-photodefinable self-priming polyimides, such as PI-2555 can be patterned in conjunction with a positive resist to achieve a 3.5  $\mu\text{m}$  polyimide overcoat layer which serves as a sacrificial layer.

Due to the precise pattern definition requirements of single mask processing, the wet etch polyimide process had a narrower process window and needs to be tightly controlled. As a result, critical dimension control is difficult. Cured film thicknesses were limited by resolution requirements to  $< 3 \mu\text{m}$  [12].

The new sacrificial layer polymer offers improved resolution and adhesion compared with the wet etch polyimide process. A photoresist process is unnecessary as the exposed material is developed by heating the substrate in an oven at 110 °C to dry develop the photo defined features. The sacrificial polymer film is then rinsed with isopropyl alcohol (IPA) to remove any remaining residue.

## **6.3. Reduction in Cost**

Photodefinable polyimide sacrificial materials also eliminate the need for a photoresist coat and strip process. The total number of processing steps is reduced when compared with previous sacrificial layer processes. The improved resolution and adhesion characteristics of photodefinable polyimide material permit the application of a thicker sacrificial layer. This increased film thickness, combined with improved adhesion is expected to have good device reliability. The drawback of the photodefinable polymer sacrificial material process is an increase in material costs compared with the other existing sacrificial layer process [13].

Table 3 compares the Unity 2000P sacrificial polymer process with traditional sacrificial materials and techniques typically used to develop and release free-standing resonant systems.

## **7. Process Integration**

Integration of the new sacrificial material process is relatively straightforward. Some key variables that were adjusted are the soft bake time and temperature, exposure energy, post exposure bake, and develop time and technique. The sacrificial material is exposed through a quartz mask.

**Table 3.** Experimental Comparison of Typical Sacrificial Layer Materials.

| Sacrificial Material   | Coating Process   | Development/Release Method  |  |
|--|---|---|--|
| Photoresist<br>S1827   | Spin Coat<br>Film Thickness: 2.5 $\mu\text{m}$  | Soft Bake: 90 sec / Exposure<br>MF-319 Developer: 50 sec<br>Hard bake: 30 min<br>Resist Strip   |  |
| Polyimide<br>PI-2555   | VM651 Primer<br>Spin Coat<br>Film Thickness: 3.5 $\mu\text{m}$  | Polyimide Soft Bake: 30 min<br>Photoresist Overcoat & Soft Bake: 2 min<br>Exposure / MF-319 Developer<br>Polyimide Cure: 2 hrs<br>Resist Strip<br><br><u>Plasma-Therm RIE</u><br>Gases: $\text{CF}_4 / \text{O}_2$ (PI-2555)<br>Etch Rate: 5000 $\text{\AA}/\text{min}$ |  |
| Silicon Dioxide $\text{SiO}_2$<br><br>*additional photoresist<br>masking step required                     | Plasma-Therm PECVD<br>Rate: 400 $\text{\AA}/\text{min}$   | <u>Plasma-Therm RIE</u><br>Gases: $\text{CHF}_3 / \text{O}_2$<br>Etch Rate: 400<br>$\text{\AA}/\text{min}$  | <u>Wet Etching</u><br>HF: $\text{NH}_4\text{HF} \cdot \text{H}_2\text{O}$<br>HF: $\text{HNO}_3$<br>Etch Rate: 20 $\text{\AA}/\text{sec}$   |
| <u>Metals</u><br><br>Aluminum / Copper /<br>Chrome<br><br>*additional photoresist<br>masking step required | <u>CVC E-Beam Evaporator</u><br>Rate: 3 $\text{\AA}/\text{sec}$ (Al /Cu/Cr)<br><br><u>CVC DC Sputterer</u><br>Rate: 6.27 $\text{\AA}/\text{sec}$ (Al)<br>8.21 $\text{\AA}/\text{sec}$ (Cu)<br>6.88 $\text{\AA}/\text{sec}$ (Cr) | <u>Plasma-Therm RIE</u><br>Gases: $\text{BCl}_3 / \text{Cl}_2$<br>(Al)<br>Etch Rate: 500-<br>2000 $\text{\AA}/\text{min}$<br>Gases: $\text{Cl}_2 / \text{O}_2$ (Cr)<br>Etch Rate: 100-200<br>$\text{\AA}/\text{min}$  | <u>Wet Etching</u><br>HCl/ $\text{HNO}_3$ /HF 10 $\text{\AA}/\text{sec}$<br>(Al)<br>$\text{H}_2\text{O}/\text{HNO}_3$ 80 $\text{\AA}/\text{sec}$ (Cu)<br>$\text{H}_2\text{O}/\text{H}_2\text{O}_2$ 40 $\text{\AA}/\text{sec}$ (Cr) |
| Unity 2000P Sacrificial<br>Polymer   | Spin Coat<br>Film Thickness: 2 - 80 $\mu\text{m}$   | Soft Bake: 15 min / Exposure & IPA Rinse<br>Thermal Decomposition: 2 hrs  |  |

The desired sacrificial layer thickness was achieved without the long deposition times of metals. The new overcoat process repeatedly patterned 16  $\mu\text{m}$  sacrificial layer coatings. The underlying layer electrodes are clearly visible in the semitransparent sacrificial material film, which facilitates easier alignment and exposure between the 1<sup>st</sup> and 2<sup>nd</sup> mask steps. The resolution was improved and patterning was insensitive to the underlying wafer topology.

There is improvement in process latitude and room temperature stability between the sacrificial polymer cured film, when compared to a photoresist or polyimide sacrificial coating, as no discernable degradation of pattern quality was noticed between coat, exposure and development. The sacrificial material offered excellent resistance to the etch process gases during the processing and development of the platform metallization and dielectric layers.

Overall process complexity is reduced as the release process is improved. There is no need for the wet etch process to dissolve the sacrificial layer. The release-stiction problem is alleviated by thermal cure and decomposition of the sacrificial material, which results in better sensor performance and reliability.

Scanning electron micrograph images in Fig. 9 show the sacrificial material during the fabrication process. The new sacrificial layer process can be readily integrated into the desired mask process scheme. There are potential improvements in process complexity, steps, and cost using this low temperature sacrificial layer process.

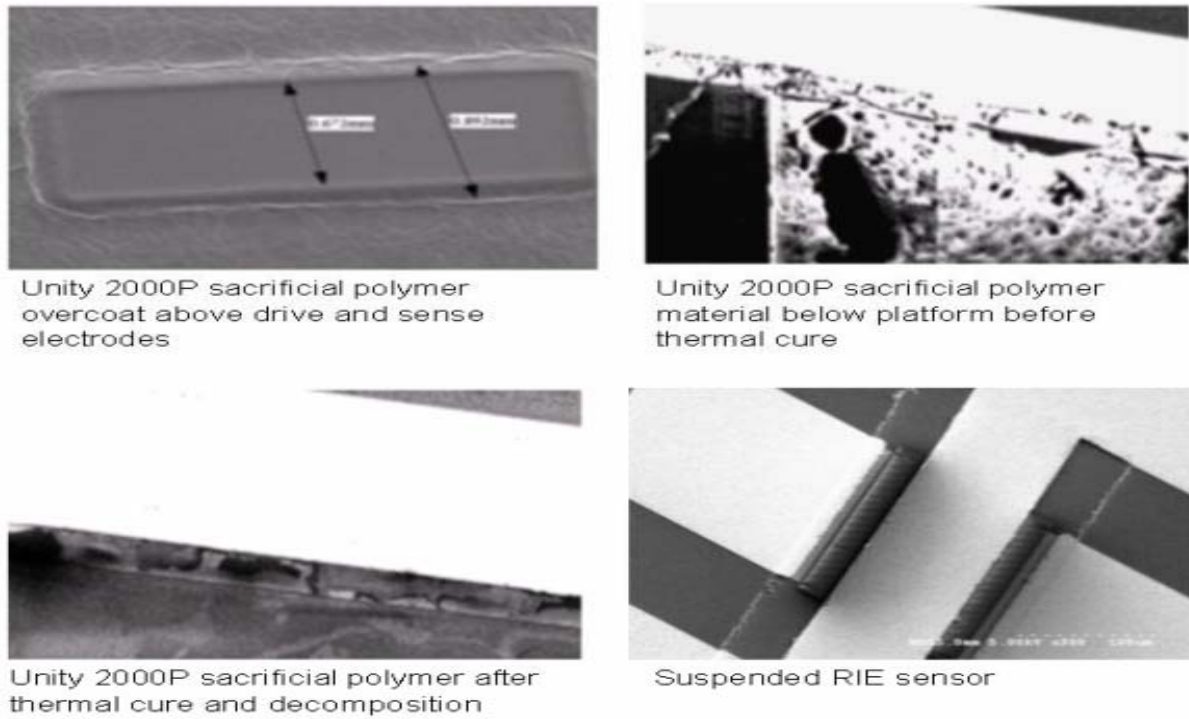


**Fig. 9.** SEM images showing underlying sacrificial polymer material during the spin coat, thermal cure and decomposition to release the suspended micromachined resonant sensor.

## 8. Summary

Sacrificial layers are a proven technology for creating suspended micromachined structures. In view of the importance of sacrificial layers in MEMS devices, we demonstrated a sacrificial layer processes that possess the following attributes: (1) the process is simple and reproducible; (2) the coating process is compatible with dry or aqueous etching processes; and (3) the release-stiction problem is alleviated by thermal cure and decomposition of the sacrificial material.

A low temperature sacrificial polymer was utilized to develop and release a free-standing mechanical RIE resonant sensor. The RIE sensor correlates film thickness with the change in resonant frequency that occurs in the micromachined platform during etching. The micromachined RIE sensor was analyzed and optimized using ANSYS. Simulation shows the direct correlation between platform film thickness and resonant frequency, potentially providing the desired mechanism for real-time feedback on the wafer state during reactive ion etching.

The low temperature sacrificial polymer presents a straightforward alternative to existing sacrificial layer methods. There are improvement in process complexity, adhesion and resolution. The sacrificial layer technique is compatible with other surface micromachining processes and can be applied in fabricating low cost, high performance and reliable MEMS devices.

## References

- [1]. R. Leachman and D. Hodges, Benchmarking Semiconductor Manufacturing, *IEEE Trans. Semi. Manufac.*, Vol. 9, No. 2, May, 1996.
- [2]. C. Himmel, T. Kim, A. Krauss, E. Kamen, and G. May, Real-Time Predictive Control of Semiconductor Manufacturing Processes Using Neural Networks, *Proc. 1995 American Control Conf.*, Vol. 2, June, 1995.

- [3]. D. White, D. Boning, S. Butler, and G. Barna, Spatial Characterization of Wafer State Using Principal Component Analysis of Optical Emission Spectra in Plasma Etch, *IEEE Trans. Semi. Manufac.*, Vol. 10, No. 1, February, 1997.
- [4]. D. Greve, T. Knight, X. Cheng, B. Krogh, and M. Gibson, Process Control Based on Quadrupole Mass Spectroscopy, *J. Vac. Sci. Tech. B*, Vol. 14, No. 1, Jan/Feb, 1996.
- [5]. J. Pope, R. Woodburn, J. Watkins, R. Lachenbruch, and G. Vilorio, Manufacturing Integration of Real-Time Laser Interferometry to Etch Silicon Dioxide Films for Contacts and Vias, *Proc. SPIE Conference on Microelec. Processing*, Vol. 2091, 1993.
- [6]. N. de Rooij, Current Status and Future Trends of Si Microsensors, *IEEE Spectrum*, 1991.
- [7]. M. Baker, F. Williams, and G. May, A Novel In-Situ Monitoring Technique for Reactive Ion Etching Using a Surface Micromachined Sensor, *IEEE Trans. Semi. Manufac.*, Vol. 11, No. 2, May, 1998.
- [8]. B. Morris and G. May, Design and Development of an Integrated MEMS Sensor for Real Time Control of Plasma Etching, in *Proc. NSTI Nanotech. Conf.*, Vol. 1, 2004, pp. 418 – 421.
- [9]. A. Holmes and S. Saidam, Sacrificial Layer Process with Laser-Driven Release for Batch Assembly Operations, *J. Micromech. Microeng.*, Vol. 7, No. 4, Dec. 1998.
- [10]. S. Psoma and D. Jenkins, Comparative Assessment of Different Sacrificial Materials for Releasing SU-8 Structures, *Adv. Mater. Sci.*, Vol. 10, 2005, pp. 149–155.
- [11]. Z. Cui and R. Lawes, A New Sacrificial Process for the Fabrication of Micromechanical Systems, *J. Micromech. Microeng.*, Vol. 7, 1997, pp. 128-130.
- [12]. H. Kazuyuki and T. Yamashita, Photosensitive Polyimides, *Technomic*, 1995.
- [13]. S. Hall and C. Schuckert, Single Mask Wafer Overcoat Process Using Photodefinable Polyimide, *J. Solid State Tech.*, Vol. 7, 1997, pp. 128-130.

---

2007 Copyright ©, International Frequency Sensor Association (IFSA). All rights reserved.  
(<http://www.sensorsportal.com>)



The graphic features a dark blue background with a grid pattern. At the top, the text "SENSORS WEB PORTAL" is written in large, bold, yellow capital letters. To the right of this text is the IFSA logo, which consists of a stylized yellow star and the letters "IFSA" in yellow. Below the main title, there is a list of sensor types in white capital letters, each preceded by a yellow dot: MEMS, NEMS, NANOSENSORS, and SMART SENSORS. To the right of this list is a computer monitor displaying the Sensors Web Portal website. At the bottom of the graphic, the text "All about SENSORS" is written in large, bold, yellow capital letters, followed by the URL "http://www.sensorsportal.com" in yellow.

## **Perturbation Stochastic Finite Element Analysis of Thermoelastic Quality Factor of Micro-Resonators**

**Séverine LEPAGE and Jean-Claude GOLINVAL**

University of Liege, Aerospace and Mechanical Engineering Department, LTAS-VIS

E-mail: [slepage@ulg.ac.be](mailto:slepage@ulg.ac.be)

*Received: 17 September 2007 / Accepted: 19 September 2007 / Published: 8 October 2007*

---

**Abstract:** In the design of micro-electromechanical systems (MEMS) such as micro-resonators, one of the major dissipation phenomena to be considered is thermoelastic damping. The performance of such MEMS is directly related to their thermoelastic quality factor which has to be predicted accurately. Moreover, the performance of MEMS depends on manufacturing processes which may cause substantial uncertainty in the geometry and in the material properties of the device. The aim of this paper is to provide a framework to account for uncertainties in the finite element analysis. Particularly, the influence of uncertainties on the performance of a micro-beam is studied using the perturbation stochastic finite element method. The developed method is applied on the analysis of the thermoelastic quality factor of a micro-beam whose elastic modulus is considered as random.  
*Copyright © 2007 IFSA.*

**Keywords:** Stochastic finite element method, Thermoelastic damping, Micro-resonator, Uncertainty modeling

---

### **1. Introduction**

Micro-electromechanical systems (MEMS) are subject to inevitable and inherent uncertainty in dimensional and material parameters that leads to variability in their performance and reliability. Manufacturing processes due to the small dimensions and high feature complexity leave substantial variability in the shape and geometry of the device while material properties of a component are inherently subject to scattering. The effects of these variations have to be considered and a modeling methodology is needed in order to ensure required MEMS performance under uncertainties.

In the literature, different works are carried out to quantify the effect of the uncertainties on electrostatically actuated MEMS [1-4]. These studies consider material and geometric parameters as random variables and use costly Monte-Carlo methods as well as first and second order reliability methods. Another approach to avoid the detrimental effect of these uncertainties is to design MEMS whose performances are not sensitive to the uncertain design parameters [5-7], but this is not always possible. In this paper, the Perturbation Stochastic Finite Element Method (PSFEM) is used to quantify the influence of uncertain geometric and material property variations on the thermoelastic quality factor of micro-resonators.

The paper is organized as follows. Firstly, the procedure to quantify the thermoelastic quality factor is exposed. An efficient thermoelastic finite element formulation is the key point in order to investigate the influence of uncertainties on the behavior of micro-systems. Then, the perturbation stochastic finite element method is extended to the study of the thermoelastic quality factor. Finally, the results of PSFEM simulations are presented and discussed.

## 2. Thermoelastic Finite Element Formulation

Thermoelastic damping represents the loss in energy from an entropy rise caused by the coupling between heat transfer and strain rate. Analytical models exist for simple configurations such as beams [8-9]. However, a numerical approach is required in order to take into account the spatial variation of the material properties. A thermoelastic finite element formulation is derived in [10] and shows efficiency in order to estimate the thermoelastic quality factor [11].

In order to determine the thermoelastic quality factor, the thermoelastic frequencies  $\lambda$  have to be computed. The eigenvalue problem corresponding to the thermoelastic problem is

$$\begin{pmatrix} -\mathbf{K}_{uu} & -\mathbf{K}_{u\theta} & \mathbf{0} \\ \mathbf{0} & -\mathbf{K}_{\theta\theta} & \mathbf{0} \\ \mathbf{0} & \mathbf{0} & \mathbf{M}_{uu} \end{pmatrix} \begin{pmatrix} \mathbf{x}_u \\ \mathbf{x}_\theta \\ \dot{\mathbf{x}}_u \end{pmatrix} = \lambda \begin{pmatrix} \mathbf{0} & \mathbf{0} & \mathbf{M}_{uu} \\ \mathbf{C}_{\theta u} & \mathbf{C}_{\theta\theta} & \mathbf{0} \\ \mathbf{M}_{uu} & \mathbf{0} & \mathbf{0} \end{pmatrix} \begin{pmatrix} \mathbf{x}_u \\ \mathbf{x}_\theta \\ \dot{\mathbf{x}}_u \end{pmatrix}, \quad (1)$$

where subscripts  $u$  and  $\theta$  refer respectively to the mechanical and thermal degrees of freedom.  $\mathbf{M}$ ,  $\mathbf{C}$  and  $\mathbf{K}$  are respectively mass, damping and stiffness matrices.

If the number of mechanical and thermal degrees of freedom is denoted by  $n_u$  and  $n_\theta$ , respectively, the eigenvalue problem (1) has  $2 n_u$  conjugate complex eigenvalues and  $n_\theta$  real eigenvalues. The  $2 n_u$  eigenvalues correspond to the mechanical frequencies and the  $n_\theta$  ones to the thermal frequencies. Solving the thermoelastic eigenvalue problem with a non-symmetric block Lanczos algorithm allows the calculation of the complex eigenvalues of the thermoelastic structure and hence, the determination of the quality factor of the corresponding mode. The quality factor of the  $n$ th mode is given by

$$Q = \frac{1}{2} \left| \frac{\Im(\lambda)}{\Re(\lambda)} \right|. \quad (2)$$

## 3. Perturbation Stochastic Finite Element Method

Stochastic Finite Element Method (SFEM) can be applied to the thermoelastic problem. The present work focuses on second moment approaches, in which the first two statistical moments, i.e. the mean and the variance, are estimated. The perturbation SFEM is used in order to determine the mean and the

variance of the thermoelastic quality factor of MEMS. The perturbation SFEM [12] consists in a deterministic analysis complemented by a sensitivity analysis with respect to the random parameters. This enables the development of a Taylor series expansion of the response, from which the mean and variance of the response can be derived knowing the mean and variance of the random parameters.

The perturbation method considers that the random design variables  $b_i$  are perturbed from their expectation  $\bar{b}_i$ , so that the random variables  $b_i$  are written as the sum of a deterministic value  $\bar{b}_i$  and a zero mean random variable  $\Delta b_i$ .

The second order Taylor expansion about the nominal value  $\bar{\mathbf{b}}$  with respect to the random variables  $b_i$  is given by

$$Q(\bar{\mathbf{b}}) \approx \bar{Q} + \sum_{i=1}^n Q_{,i} \Delta b_i + \frac{1}{2} \sum_{i=1}^n \sum_{j=1}^n Q_{,ij} \Delta b_i \Delta b_j. \quad (3)$$

where the subscripts,  $i$  and,  $ij$  respectively denote the first and second order partial derivative with respect to  $b_i$  and  $b_j$  computed at the nominal value  $\bar{\mathbf{b}}$ .

Since the random variables  $\Delta b_i$  are zero-mean random variables of known covariance, the expectation of the quality factor is

$$E[Q(\bar{\mathbf{b}})] \approx \bar{Q} + \sum_{i=1}^n Q_{,i} E[\Delta b_i] + \frac{1}{2} \sum_{i=1}^n \sum_{j=1}^n Q_{,ij} E[\Delta b_i \Delta b_j] \quad (4)$$

$$= \bar{Q} + \frac{1}{2} \sum_{i=1}^n \sum_{j=1}^n Q_{,ij} \text{Cov}(b_i, b_j) \quad (5)$$

while the variance of the quality factor has the following expression:

$$\text{Var}[Q(\bar{\mathbf{b}})] = E\left[\left(Q(\bar{\mathbf{b}}) - E[Q(\bar{\mathbf{b}})]\right)^2\right] \quad (6)$$

$$\approx \sum_{i=1}^n \sum_{j=1}^n Q_{,i} Q_{,j} E[\Delta b_i \Delta b_j] \quad (7)$$

$$= \sum_{i=1}^n \sum_{j=1}^n Q_{,i} Q_{,j} \text{Cov}(b_i, b_j) \quad (8)$$

The mean is second-order accurate, while the variance is first-order accurate since the second-order terms vanish. The first and second order derivatives of the quality factor are expressed in terms of the first and second order derivatives of the eigenvalue. Due to the nature of the thermoelastic eigenproblem, this study involves the calculation of eigenvalue sensitivities of a non-symmetric damped system.

Many eigenpair sensitivity methods are restricted to systems whose characteristic matrices are symmetric. However, the thermoelastic damping and stiffness matrices are asymmetric and the eigenpair sensitivity analysis can not be carried out using the previous methods. Many authors [13-15] extend the method of Fox and Kapoor to asymmetric matrices. Murthy and Haftka [16] expose an excellent review on the calculation of the eigenpair sensitivity of asymmetric systems. Brandon [17] presents the modal method for asymmetric damped systems. This method solves the problems due to

asymmetric matrices by using the left eigenvector. However, it has disadvantages in CPU time and storage capacity because it uses state space form to consider damping of systems and requires a lot of eigenpair information to find eigenpair sensitivity. In [18], an N-space method is exposed where the first order eigenvalue and eigenvector sensitivities are simultaneously obtained from one single equation, which is therefore very efficient in CPU time and storage capacity. This method is extended to the computation of second order sensitivities of asymmetric damped systems in order to be applied to the thermoelastic damping case. Its main advantage is that to compute the second order derivatives of the right eigenpair it requires only corresponding right eigenpair information without use of the left eigenvector information so that the computation of the left eigenvector derivatives is avoided.

#### 4. Applications

In numerous micro-resonators, the vibrating part consists in a clamped-clamped silicon beam. In this section, the test case beam has the following dimensions: a length  $L$  of 90  $\mu\text{m}$ , a height  $h$  of 4.5  $\mu\text{m}$  and a width  $w$  of 4.5  $\mu\text{m}$  (Fig. 1). The thermal and mechanical properties of silicon at  $T_0=298$  K are:  $\rho=2300$  kg/m<sup>3</sup>,  $\eta=0.2$ ,  $c_v=711$  J/kgK,  $\alpha=2.5\text{e-}6$  K<sup>-1</sup> and  $k=170$  W/mK. The thermoelastic quality factor is determined for the first bending mode in plane  $OYZ$ .

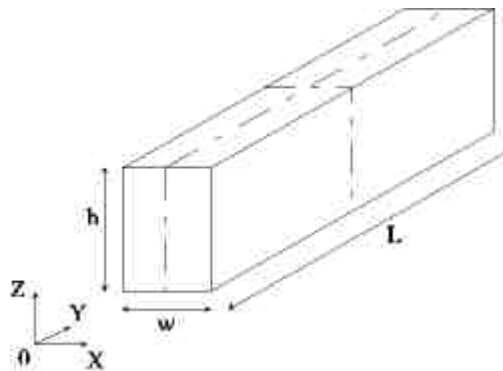
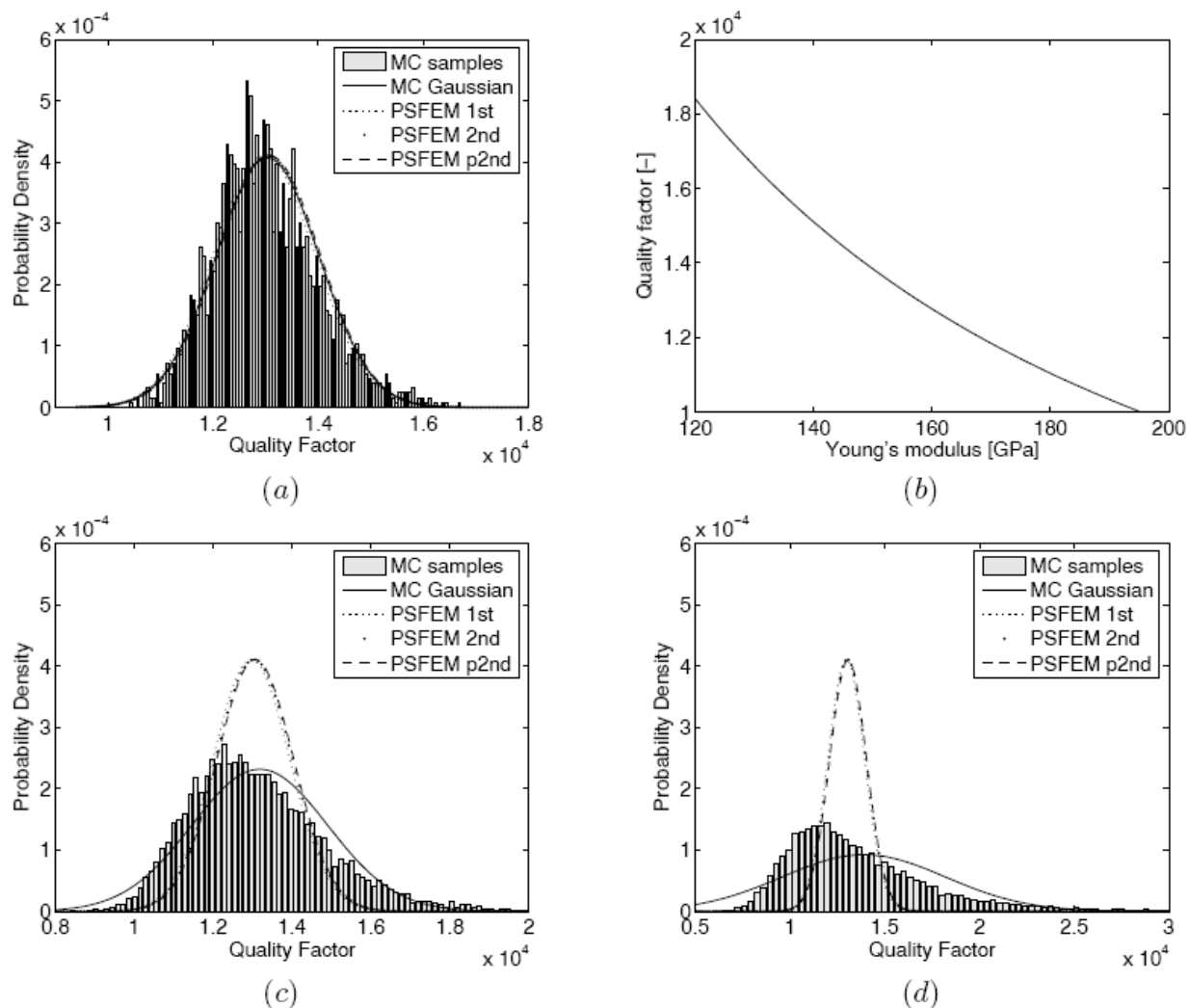


Fig. 1. Beam geometry.

Young's modulus is considered as a Gaussian random variable. Its mean is equal to 158 GPa and its coefficient of variation, i.e. the ratio between the standard deviation and the mean, is set to 6 %, which is a typical value encountered in polysilicon. Direct Monte-Carlo simulations are carried out in order to get a reference solution. 2000 samples are generated.

Table 1 lists the means and standard deviations of the quality factor obtained by different methods. Monte-Carlo results, denoted MC, are considered as reference solutions. First and second order perturbation stochastic finite element methods, denoted PSFEM 1st and PSFEM 2nd, are applied to study the thermoelastic quality factor of the test case. Since the determination of the second order derivative of the eigenvalue can be too computationally demanding, a second order PSFEM in terms of the quality factor but only taking into account the first order derivative of the eigenvalue, denoted PSFEM p2nd, is also investigated. The CPU times for each method are normalized with respect to the CPU time required for one deterministic finite element resolution and are presented in Table 1. MC simulations are a lot more CPU time costly than PSFEM and as the order of PSFEM increases, the CPU time increases. Since the approximation of the standard deviation of the quality factor is first order accurate (Equation 7), the standard deviation has the same value whatever the order of the PSFEM and the relative error with respect to MC standard deviation is less than 1 %. The first order PSFEM gives a mean equal to the deterministic quality factor, i.e. 12967, while MC simulations yield

a higher mean. This is due to the fact that the quality factor is a non-linear function of Young's modulus as shown in Fig. 2 (b). Moreover, due to this non-linear variation, the probability density function of the quality factor is not strictly Gaussian as shown in Fig. 2 (a). In this figure, the bars represent the distribution of the output samples obtained by MC simulations and the solid line plots the Gaussian distribution with a mean and a standard deviation equal to the values of the MC samples. The second order PSFEM approximation of the mean is really good (0.02 % relative error) and the pseudo second order PSFEM approximation has also a good accuracy (0.026 % relative error) at a less computational effort.



**Fig. 2.** Probability density function of the quality factor ( $\text{CoV}(E)=0.06$  (a),  $\text{CoV}(E)=10\%$  (c) and  $\text{CoV}(E)=20\%$  (d)), (b) Variation of the quality factor with respect to Young's modulus.

Table 1 also compares the means and standard deviations of the quality factor corresponding to three different coefficients of variation of Young's modulus, i.e. 6 %, 10 % and 20 %. As the coefficient of variation of Young's modulus increases, the approximations of the mean and standard deviation of the quality factor by PSFEM become less accurate. The second order PSFEM is more accurate than the pseudo-second order PSFEM at the price of a considerably larger computational effort. Figs. 2 (a,c,d) show that as the coefficient of variation of Young's modulus increases, the probability density function drifts away from the Gaussian distribution and PSFEM approximations get worse. Note that as the coefficient of variation increases, the required number of samples in MC simulations increases leading to a larger CPU time ( $n_{\text{samples}}=5000$  for  $\text{CoV}=10\%$  and  $n_{\text{samples}}=10000$  for  $\text{CoV}=20\%$ ).

These analyses show that PSFEM is adequate in order to determine the mean and standard deviation of the quality factor when Young's modulus variation is small (i.e. in this application, a coefficient of variation lower than 10 %). The second order and the pseudo-second order perturbation stochastic finite element methods provide more information than the first order one. Indeed, the first order method does not take into account the variation of the mean due to the non-linear characteristic of the response with respect to the random variable. Moreover, the increase in accuracy from PSFEM p2nd to PSFEM 2nd is not sufficient to justify the increase in computational effort.

**Table 1.** Variation of the mean and coefficient of variation of the quality factor with respect to the coefficient of variation of Young's modulus.

| Method     | CoV(E) [%] | Mean(Q) [-] | $\sigma(Q)$ [-] | CoV(Q) [%] | $t^*_{CPU}$ [-] |
|------------|------------|-------------|-----------------|------------|-----------------|
| MC         | 6          | 13035       | 980             | 7.52       | 2005            |
| PSFEM 1st  | 6          | 12967       | 971             | 7.49       | 1.02            |
| PSFEM 2nd  | 6          | 13037       | 971             | 7.45       | 1.16            |
| PSFEM p2nd | 6          | 13069       | 971             | 7.43       | 1.04            |
| MC         | 10         | 13181       | 1720            | 13.05      | 5015            |
| PSFEM 1st  | 10         | 12967       | 1619            | 12.49      | 1.02            |
| PSFEM 2nd  | 10         | 13161       | 1619            | 12.30      | 1.16            |
| PSFEM p2nd | 10         | 13250       | 1619            | 12.22      | 1.04            |
| MC         | 20         | 13895       | 4313            | 31.05      | 10062           |
| PSFEM 1st  | 20         | 12967       | 3238            | 24.97      | 1.02            |
| PSFEM 2nd  | 20         | 13744       | 3238            | 23.56      | 1.16            |
| PSFEM p2nd | 20         | 14099       | 3238            | 22.97      | 1.04            |

## 5. Conclusions

The Perturbation Stochastic Finite Element Method has been extended to the analysis of a strongly coupled multiphysic phenomenon: thermoelastic damping. The methodology has been validated and its efficiency has been proved on 1-D cases. Therefore, using PSFEM, a numerical method is available to quantify the influence of uncertain property variations on the thermoelastic quality factor of micro-resonators, making available a new efficient numerical tool to MEMS designers.

## Acknowledgements

The author S. Lepage is supported by the Belgian National Fund for Scientific Research (FNRS), which is gratefully acknowledged. This work is also supported by the Communauté Française de Belgique - Direction Générale de la Recherche Scientifique in the framework Actions de Recherches Concertées (convention ARC 03/08-298).

## References

- [1]. M. Allen, M. Raulli, K. Maute and D. Frangopol, Reliability-based Analysis and Design Optimization of Electrostatically Actuated MEMS, *Computers and Structures*, 82, 2004, pp. 1007-1020.
- [2]. J. S. Kong, D. M. Frangopol, M. Raulli, K. Maute, R. A. Saravanan, L. A. Liew and R. Raj, A methodology for Analyzing the Variability in the Performance of a MEMS Actuator Made from a Novel Ceramic, *Sensors and Actuators A*, 116, 2004, pp. 336-244.
- [3]. K. Maute and D. M. Frangopol, Reliability-based Design of MEMS Mechanisms by Topology Optimization, *Computers and Structures*, 81, 2003, pp. 813-824.

- [4]. S. Reh, P. Lethbridge and D. Ostergaard, Quality Based Design and Design for Reliability of Micro-electro-mechanical Systems (MEMS) using Probabilistic Methods, In *Technical proceedings of the 2000 International Conference on Modeling and Simulation of Microsystems*, 2000, pp. 708-711.
  - [5]. R. Liu, B. Paden and K. Turner, MEMS Resonators That Are Robust to Process-induced Feature Width Variations, *Journal of Microelectromechanical Systems*, 11, 5, 2002, pp. 505-511.
  - [6]. A. Mawardi and R. Pitchumani, Design of Microresonators under Uncertainty, *Journal of Microelectromechanical Systems*, 14, 1, 2005.
  - [7]. A. Mawardi and R. Pitchumani, Optimal Design of a Micromachined Force Gauge under Uncertainty, *Journal of Micromechanics and Microengineering*, 15, 2005, pp. 2353-2365.
  - [8]. R. Lifshitz and M. L. Roukes, Thermoelastic Damping in Micro-and Nano-mechanical Systems, *Physical Review B*, 61, 8, 2000, pp. 5600-5609.
  - [9]. C. Zener, Internal Friction in Solids, *Physical Review*, 52, 1937, pp. 230-235.
  - [10]. S. Lepage and J. C. Golinval, Finite Element Modeling of the Thermoelastic Damping in Micro-Electromechanical Systems, In *Acomen 2005, Third International Conference on Advanced Computational Methods in Engineering*, Ghent, Belgium, 30 May-2 June 2005.
  - [11]. S. Lepage, O. Le Traon, I. Klapka, S. Masson and J. C. Golinval, Thermoelastic Damping in Vibrating Beam Accelerometer: A New Thermoelastic Finite Element Approach, In *Caneus 2006*, Toulouse, France, 27 August-1 September 2006.
  - [12]. M. Kleiber and T. D. Hien, The Stochastic Finite Element Method - Basic Perturbation Technique and Computer Implementation, *John Wiley and sons*, 1992.
  - [13]. R. H. Plaut and K. Huseyin, Derivative of Eigenvalues and Eigenvectors in Non-self Adjoint Systems, *AIAA Journal*, 11, 2, 1973, pp. 250-251.
  - [14]. L. C. Rogers, Derivatives of Eigenvalues and Eigenvectors, *AIAA Journal*, 8, 5, 1970, pp. 943-944.
  - [15]. S. Garg, Derivative of Eigensolutions for a General Matrix, *AIAA Journal*, 11, 8, 1973, pp. 1191-1194.
  - [16]. D. V. Murthy and R. T. Haftka, Derivatives of Eigenvalues and Eigenvectors for a General Complex Matrix, *International Journal for Numerical Methods in Engineering*, 26, 1988, pp. 293-311.
  - [17]. J. A. Brandon, Second-order Design Sensitivities to Assess the Applicability of Sensitivity Analysis, *AIAA Journal*, 29, 1, 1991, pp. 135-139.
  - [18]. K. M. Choi, H. K. Jo, W. H. Kim and I. W. Lee, Sensitivity Analysis of Non-conservative Eigensystems, *Journal of Sound and Vibration*, 274, 2004, pp. 997-1011.
-

## A Semi-Analytical Model for Calculating Touch-Point Pressure and Pull-in Voltage for Clamped Diaphragms with Residual Stress

**Anurekha SHARMA and P. J. GEORGE**

Department of Electronic Science  
Kurukshetra University, Kurukshetra-136119, India  
Tel.: +91-1744-238023  
E-mail : anu67s@gmail.com

*Received: 17 September 2007 /Accepted: 19 September 2007 /Published: 8 October 2007*

---

**Abstract:** A closed form model for evaluating touch point pressure and pull-in voltage of clamped square diaphragm with residual stress is proposed. Square diaphragms are used in numerous applications. The design parameters for all these structures are pull-in voltage and/or touchpoint pressure. The materials employed for fabricating diaphragms for these structures are p+ doped silicon, polysilicon, silicon nitride, polyimide etc. All these materials have residual stress, which influences the behavior of the transducer. In addition to this, a capacitive transducer may or may not employ an intervening layer of dielectric on the fixed electrode. Closed form expressions for evaluating touch-point pressure and pull-in voltage have been derived for such a structure by means of semi-analytical model. The method proposed is less complex and less time consuming in comparison with FEM tools. *Copyright © 2007 IFSA.*

**Keywords:** MEMS, Residual stress, Diaphragm, Pull-in, Touch-point pressure

---

### 1. Introduction

A MEMS capacitive sensor is basically an electrostatic transducer employing a parallel plate-structure that depends on electrical energy in terms of constant voltage (voltage drive) or constant charge storage (current drive) to facilitate monitoring of capacitance change due to an external mechanical excitation, such as force, acoustical pressure or acceleration [1]. The parallel plates comprises of one fixed electrode and the other deformable as shown in Fig 1. An intervening layer of dielectric is used

over the fixed electrode in transducers, which have touchmode operation, or to avoid electric short in electrostatic actuators at pull-in. The deformable electrode is usually a clamped diaphragm and can be fabricated using different materials and different geometries, such as, circular, square and rectangular. Square diaphragms are used in numerous MEMS structures because of better area efficiency and process capability using IC lithography [2]. Besides touch-mode capacitive pressure sensors [2], square diaphragms find use in numerous applications like electrostatic valve actuator for high-pressure applications [3], polysilicon micromirrors [4], silicon capacitive microphone [5], micropumps [6] and bio-medical applications [7]. Different materials used are boron doped silicon [8], polysilicon,  $\text{Si}_3\text{N}_4$  [9] and polyimide [10]. All these materials are known to have residual stresses. The residual stress affects the device behavior by influencing its touch-point pressure and pull-in voltage.

The pull-in voltages of micro test structures can be used to extract the material parameters of thin films, such as Young's moduli and residual stresses [11, 12]. Determination of the pull-in voltage is critical in the design to determine the sensitivity, instability in the operational range and the dynamics of devices. Accurate determination of the pull-in voltage is very challenging by virtue of the mechanical–electrical coupling effect and the nonlinearity of electrostatic force. Several methods like FEM (Finite Element Method), lumped model approach and solving coupled PDE's using numerical techniques are available to find the pull-in voltage [13]. Simple fast solutions are available for determination of pull-in voltage of cantilever beams, fixed-fixed beams and circular diaphragms with excellent accuracies and can determine the pull-in voltage for the mentioned structures within 1% agreement with FEM results under certain limitations [11]. However, published analytical or empirical solutions to determine the pull-in voltage for square diaphragm predict pull-in voltage that shows significant error when compared with the finite element analysis results or experimentally measured values [14]. Analytical model [14] based on a linearized uniform approximation model of the electrostatic pressure and a 2-D load deflection model under uniform pressure gives the expression of pull-in voltage by assuming that the pull-in occurs at a critical displacement equal to one-third of the gap between the electrode. A method is proposed in this paper to solve the fourth order partial differential equation by using a trial solution. The closed form expression of pull-in voltage and critical distance are the outcome of the solution. Another distinct feature of the method are that the deflection versus pressure graph depicts a realistic situation as no further deflection takes place after touchpoint pressure is reached.

## 2. Theory

For the plates with residual stress the governing equation is [18]:

$$D\Delta\Delta w(x, y) - \sigma h\Delta w(x, y) = P, \quad (1)$$

where  $\Delta = \frac{\partial^2}{\partial x^2} + \frac{\partial^2}{\partial y^2}$ ,  $w(x, y)$  is the deflection at any point  $(x, y)$  of the diaphragm,  $\sigma$  is the residual stress,  $h$  is the thickness of the diaphragm and  $P$  is the distributed pressure load.  $D$ , the flexural rigidity is given by  $D = \frac{Eh^3}{12(1-\nu^2)}$ , where,  $E$  is the Young's modulus of the diaphragm material,  $h$  is the thickness of the diaphragm and  $\nu$  is the Poisson's ratio. In the presence of applied pressure and applied voltage eq. (1) is modified as

$$D\Delta\Delta w(x, y) - \sigma h\Delta w(x, y) = P + P_{el}, \quad (2)$$

where,  $P_{el}$  is the electrostatic pressure and  $P$  is the mechanical pressure. The electrostatic pressure  $P_{el}$  is given as:

$$P_{el} = \frac{\epsilon_0 \epsilon_r}{2d_0^2} V^2, \quad (3)$$

where,  $d_0$  is distance between the plates,  $\epsilon_r$  is relative permittivity of the medium or the dielectric constant of the medium and  $\epsilon_0$  is permittivity of free space. The diaphragm deflection  $w(x, y)$  with air as dielectric is given by considering that the distance  $d_0$  between the plates changes to  $(d_0 - w)$  due to the displacement  $w$  of the diaphragm in the presence applied pressure and voltage as shown in Fig. 1. Substituting eq. (3) in eq. (2) for diaphragm without the intervening layer of dielectric, the equation becomes:

$$D\Delta\Delta w(x, y) - \sigma h \Delta w(x, y) = P + \frac{\epsilon_0 \epsilon_a}{2(d_0 - w)^2} V^2. \quad (4)$$

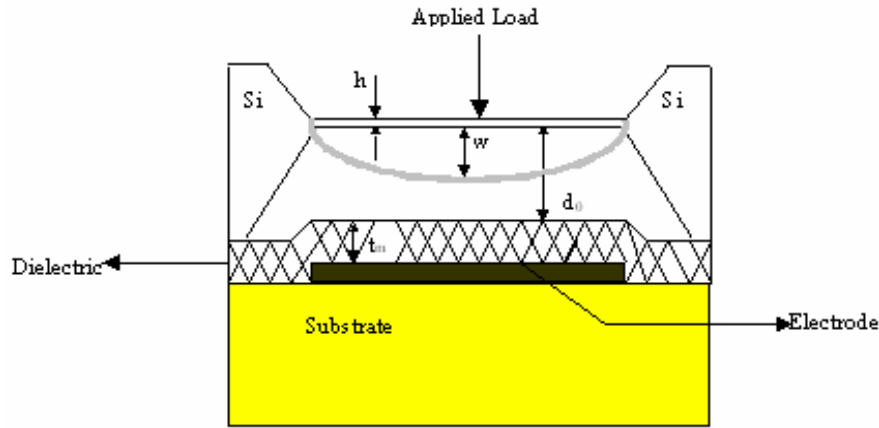


**Fig. 1.** Structure of a capacitive pressure sensor.

For diaphragm with intervening layer of dielectric:

$$D\Delta\Delta w(x, y) - \sigma h \Delta w(x, y) = P + \frac{\epsilon_0 \epsilon_a \epsilon_i^2}{2(\epsilon_a t_m + \epsilon_i (d_0 - w))^2} V^2, \quad (5)$$

where  $d_0$  is zero pressure gap,  $\epsilon_a$  is the dielectric constant of the air,  $\epsilon_i$  is the dielectric constant of the insulator and can be written in a generalized form as:

$$D\Delta\Delta w(x, y) - \sigma h \Delta w(x, y) = P + \frac{\epsilon_0}{2(d_{eff} + d_0 - w)^2} V^2, \quad (6)$$

where  $d_{eff} = t_m / \epsilon_i$  (for a single layer of dielectric) and  $d_{eff} = 0$  for air.

### 3. Semi-Analytical Model

The boundary conditions for the square diaphragm with clamped edges are as follows

$$w(x, y) = 0 \text{ at } x = \pm a, y = \pm a$$

$$\frac{\partial w}{\partial x} = 0 \text{ and } \frac{\partial w}{\partial y} = 0 \text{ at } x = 0, y = 0, x = \pm a \text{ and } y = \pm a,$$

where  $2a$  is the side length of the diaphragm (Fig. 2). The trial solution that satisfies the above given boundary conditions is

$$w(x, y) = \lambda(x^2 - a^2)^2(y^2 - a^2)^2, \quad (7)$$

The value of  $\lambda$  can be found out by the solving the following integral and equating the result to zero [15]

$$\int_{-a}^{+a} \int_{-a}^{+a} w(x, y)(D\Delta\Delta w(x, y) - \sigma h\Delta w(x, y))dxdy - \int_{-a}^{+a} \int_{-a}^{+a} w(x, y)(P + \frac{\epsilon_0}{2(d_{eff} + d_0 - w)^2}V^2)dxdy = 0, \quad (8)$$

The above equation has no closed form analytical solution, and can only be solved numerically. Following methodology is used to find the closed form solutions.

Initially, there is no deflection, therefore  $w=0$ , hence the value of  $\lambda$  from eq. (8) is found as

$$\lambda = \frac{147}{512(27a^4D + 2a^6\sigma h)}(2P + \frac{\epsilon_0}{(d_{eff} + d_0)^2}V^2).$$

Evaluating  $D\Delta\Delta w(x, y) - \sigma h\Delta w(x, y)$  at  $x=0, y=0$ , i.e., at the center of the diaphragm with this value of  $\lambda$ , we have

$$D\Delta\Delta w(x, y) - \sigma h\Delta w(x, y) = \frac{245}{144}((P + \frac{\epsilon_0}{2(d_{eff} + d_0)^2}V^2)) \quad (9)$$

The eq. (9) has to be modified to take into account the new electrostatic pressure every time a deflection  $w$  (xylem) takes place. Hence, the value of  $\lambda$  is re calculated by observing that at the center  $x=0, y=0$ , the following equation should hold well.

$$D\Delta\Delta w(x, y) - \sigma h\Delta w(x, y) = \frac{245}{144}((P + \frac{\epsilon_0}{2(d_{eff} + (d_0 - w(x, y))^2}V^2)), \quad (10)$$

Equation (10) gives a third degree polynomial in  $\lambda$  at  $x=0$  and  $y=0$ , as given below.

$$\begin{aligned}
& \lambda^3 - \lambda^2 \frac{(245a^4 P + 23040(d_0 + d_{eff})D + 2304a^2(d_0 + d_{eff})h\sigma)}{1152a^8(10D + a^2\sigma h)} \\
& + \lambda \frac{(245a^4 P(d_0 + d_{eff}) + 5760(d_0 + d_{eff})^2 D + 576a^2(d_0 + d_{eff})^2 h\sigma)}{576a^{16}(10D + a^2\sigma h)} \\
& - \frac{1}{2304a^{20}(10D + a^2\sigma h)} (490P(d_0 + d_{eff}) + 245\varepsilon_0 V^2) = 0
\end{aligned} \quad (11)$$

This equation has got three roots and only one of them gives a stable value. The value of  $\lambda$  is substituted in eq. (7) to get the deflection at any point (x, y) in terms of applied voltage, pressure and residual stress.

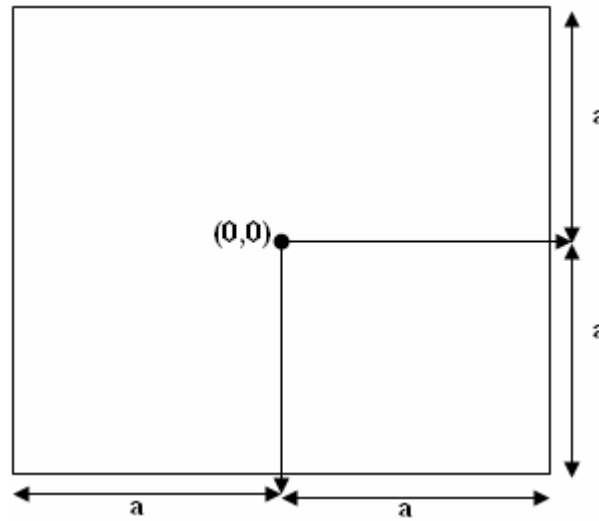


**Fig. 2.** Co-ordinate system and dimensions of square diaphragm.

### 3.1. Pull-in Voltage

Pull-in voltage is determined by differentiating the deflection  $w(x, y)$  at the center, i.e., at  $x=0, y=0$  with respect to voltage at zero mechanical pressure and equating  $dV/dw$  to zero. The critical distance is got by substituting the pull-in voltage for voltage  $V$  in expression for deflection. The closed form expression for pull-in voltage ( $V_{pull}$ ) and critical distance  $w_{cr}$  are

$$V_{pull} = \frac{32\sqrt{(d_0 + d_{eff})^3(10D + a^2\sigma h)}}{7a^2\sqrt{15}\sqrt{\varepsilon_0}}, \quad (12)$$

$$w_{cr} = \frac{(d_0 + d_{eff})}{3} \quad (13)$$

The results of the pull-in obtained from this model are compared with those obtained by simulation or reported experimentally in Table I. For a diaphragm with  $a = 1.2$  mm,  $h = 0.8\mu\text{m}$ ,  $d_0 = 3.5\mu\text{m}$ ,  $\varepsilon_0 = 8.85 \times 10^{-12}$  F/m,  $E = 169$  GPa,  $\nu = 0.3$ ,  $\sigma = 20$  MPa, Fig 3. shows the comparison of deflection with voltage.

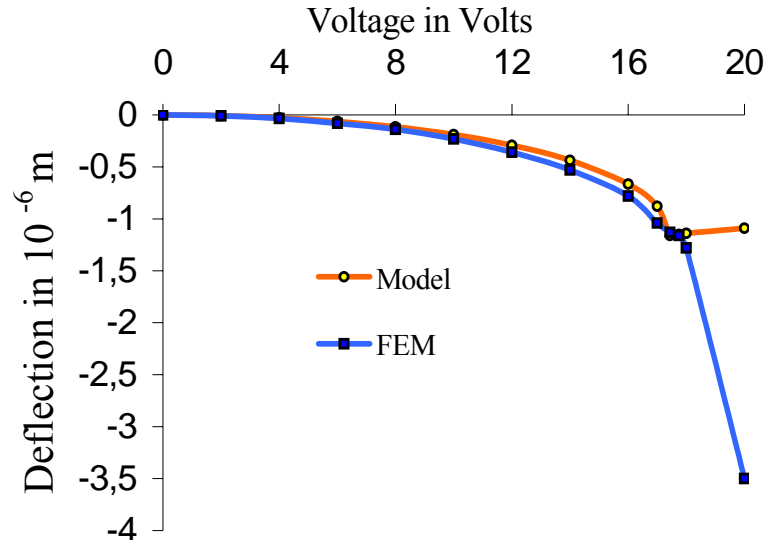


**Fig. 3.** The pull-in voltage from model. Pull-in voltage is represented by discontinuity in the graph.

### 3.2. Touch-point Pressure

Touch-point is defined as the pressure at which the diaphragm just touches the fixed electrode and is of importance for the design of Touchmode Capacitive Pressure Sensors [2]. The touch-point pressure ( $P_{\text{touch}}$ ) is found out by differentiating the deflection  $w(x,y)$  at the center i.e. at  $x=0, y=0$  with respect to pressure  $P$  at zero voltage and equating  $\delta w/\delta P$  to zero, as after touchpoint is reached, there is no further deflection in vertical direction. The closed form expression for touch-point pressure is

$$P_{\text{touch}} = \frac{1152(d_0 + d_{\text{eff}})}{245a^4} (10D + a^2 h \sigma), \quad (14)$$

Table 2 compares the touch-point pressure obtained from this model with that obtained by simulation using Intellisuite®. Figure 4a and 4b compare the deflection with applied pressure as obtained from the proposed model with those simulated using Intellisuite® for a square diaphragm with  $a = 250 \mu\text{m}$ ,  $h = 20 \mu\text{m}$ ,  $d_0 = 8 \mu\text{m}$ ,  $\epsilon_0 = 8.85 \times 10^{-12} \text{ F/m}$ ,  $E = 130 \text{ GPa}$ ,  $d_{\text{eff}} = 0$ ,  $\nu = 0.3$  with and without residual stress

**Table 1.** Comparison of square diaphragm pull-in voltages.

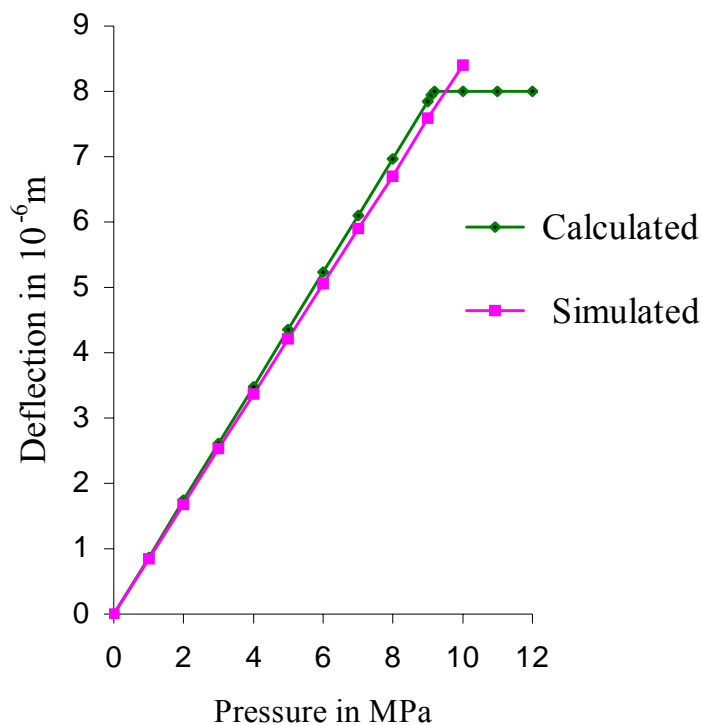
| Reference      | Diaphragm half-side length $a$ | Thickness $h$ $\mu\text{m}$ | Air-gap $d_0$ $\mu\text{m}$ | Stress $\sigma$ MPa | Pull-in Voltage $V_{\text{pull}}$ in Volts |          |
|----------------|--------------------------------|-----------------------------|-----------------------------|---------------------|--|----------|
|                |                                |                             |                             |                     | Present model                              | Reported |
| Osterberg [11] | 12.7 $\mu\text{m}$             | 0.1                         | 0.76                        | 50                  | 46.28                                      | 45.25    |
| Bergqvist [16] | 1 mm                           | 5.1                         | 2.3                         | 6                   | 9.98                                       | 10.0     |
| Sazzadur [14]  | 0.6 mm                         | 0.8                         | 3.5                         | 20                  | 17.43                                      | 17.75    |

**Table 2.** Comparison of square diaphragm Touch-point pressure.

| Reference  | Diaphragm<br>halfside length<br>$a$ | Thickness $h$<br>$\mu\text{m}$ | Air-gap<br>$d_0$ $\mu\text{m}$ | Stress<br>$\sigma$ MPa | Touch-point Pressure MPa |           |
|------------|-------------------------------------|--------------------------------|--------------------------------|------------------------|--------------------------|-----------|
|            |                                     |                                |                                |                        | Present<br>model         | Simulated |
| Pie G.[17] | 250 $\mu\text{m}$                   | 20.0                           | 8.0                            | 0                      | 9.2                      | 9.6       |
| Pie G.[17] | 250 $\mu\text{m}$                   | 20.0                           | 8.0                            | 50                     | 9.8                      | 10.2      |

#### 4. Conclusions

A semi-analytical technique is proposed for calculating the touch-point pressure and pull-in voltage of a square diaphragm with clamped edges in presence of residual stress. The deflection versus pressure studies reported in literature show that the deflection continues to increase beyond the gap  $d_0$  between the diaphragm and fixed electrode. However, in the present study, the deflection gets restricted at the gap  $d_0$ . This enables accurate determination of touchpoint pressure and gives a realistic picture of deflection. The pull-in voltage and critical distance has also been computed. The advantage of this technique lies in its simplicity and speed unlike the FEM tools, which though accurate, take a longer computational time, and requires suitable skills in deciding the mesh size and making the choice of the mesh element. The results are in agreement with the simulated and experimental ones.

**Fig. 4a.** Deflection vs. pressure with residual stress=0 Mpa.

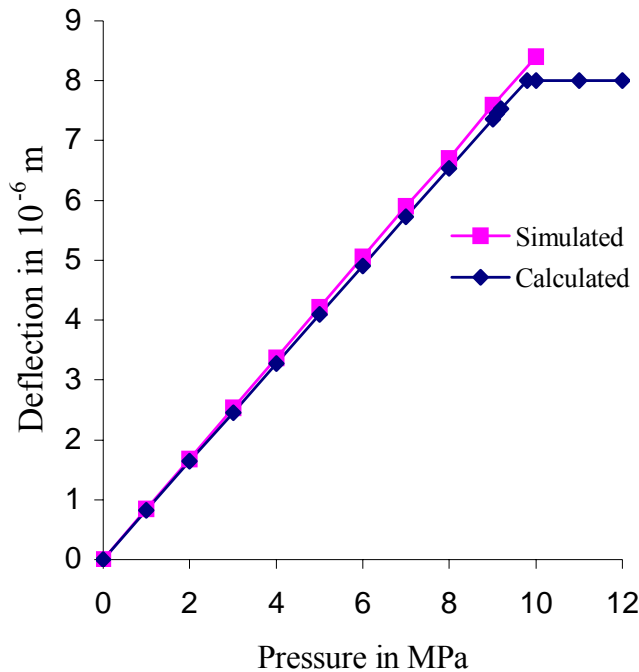


**Fig. 4b.** Deflection vs. pressure with residual stress=50 Mpa.

## Acknowledgements

Author acknowledges the support of CEERI for Intellisuite®. Acknowledgements are due to Mr. Jaideep Gupta, Lecturer, NIT, Kurukshetra for ANSYS® and Mathematica®

## References

- [1]. Robert Peurs, Capacitive Sensors: when and how to use them, *Sensors and Actuators A*, 37-38, 1993, pp. 93-105.
- [2]. Qiang Wang, Wen H. Ko, Modeling of touch mode capacitive sensors and diaphragms, *Sensors and Actuators A*, 75, 1999, pp. 230-241.
- [3]. Wouter van der Wijngaart, Haïkan Ask, Peter Enoksson, Göran Stemme, A high-stroke, high-pressure electrostatic actuator for valve applications, *Sensors and Actuators A*, 100, 2001, pp. 264-271.
- [4]. M. Fischer, M. Giousouf, J. Schaepperle, D. Eichner, M. Weinmann, W. von Minch, F. Assmus, Electrostatically deflectable polysilicon micromirrors – dynamic behaviour and comparison with the results from FEM modeling with ANSYS, *Sensors and Actuators A*, 67, 1998, pp. 89-95.
- [5]. Quanbo Zou, Zhimin Tan, et. al., A novel integrated Silicon Capacitive-Floating electrode Electret Microphone (FEEM), *Journal of Microelectromechanical Systems*, Vol. 7, No. 2, 1998, pp. 224-234.
- [6]. Eiji Makino, Takashi Mitsuya, Takayuki Shibata, Fabrication of TiNi shape memory micropump, *Sensors and Actuators A*, 88, 2001, pp. 256-262.
- [7]. T. Goettsche, J. Kohnle, M. Willmann, H. Ernst, S. Spieth, R. Tischler, S. Messner, R. Zengerle, H. Sandmaier, Novel approaches to particle tolerant valves for use in drug delivery systems, *Sensors and Actuators A*, 118, 2005, pp. 70-77.
- [8]. E. H. Yang, S. S. Yang, The quantitative determination of the residual stress profile in oxidized p+ silicon films, *Sensors and Actuators A*, 54, 1996, pp. 684-689.
- [9]. H. Huang, K. Winchester, Y. Liu, X. Z. Hu, C. A. Musca, J. M. Dell and L. Faraone, Determination of mechanical properties of PECVD silicon nitride thin films for tunable MEMS Fabry-Pérot optical filters, *J. Micromech. Microeng.*, 15, 2005, pp. 608–614.
- [10]. M. Pedersen, M. G. H. Meijerink, W. Olthuis and P. Bergveld, A capacitive differential pressure sensor with polyimide diaphragm, *J. Micromech. Microeng.*, 7, 1997, pp. 250–252.

- [11].P. M. Osterberg and S. D. Senturia, M-TEST: a test chip for MEMS material property measurement using electrostatically actuated test structures, *J. Microelectromech. Syst.*, 6, 1997, pp. 107–18.
  - [12].R. K. Gupta, Electrostatic pull-in test structures design for in-situ mechanical property measurement of microelectromechanical systems, (MEMS), *PhD Dissertation*, Massachusetts Institute of Technology, MA, USA, 1997.
  - [13].Yuh-Chung Hu, Closed form solutions for the pull-in voltage of micro curled beams subjected to electrostatic loads, *J. Micromech. Microeng.*, 16, 2006, pp. 648–655.
  - [14].Sazzadur Chowdhury, M. Ahmadi, W. C. Miller, A new analytical model for the pull-in voltage of the clamped diaphragms subject to the electrostatic force, *Sensor Letters*, Vol. 1, 2003, pp. 116-112.
  - [15].William P. Eaton, Fernando Bitsie, James H. Smith, David W. Plummer, A New Analytical Solution for Diaphragm Deflection and its Application to a Surface-Micromachined Pressure Sensor, *International Conference on Modeling and Simulation of Microsystems*, MSM99, 1999.
  - [16].Bergqvist, Finite-element modeling and characterization of a silicon condensor microphone with a highly perforated backplate, *Sensors and Actuators A*, 39, 1993, pp. 191-200.
  - [17].Pei G.E., Woei Wan TAN, Francis TAY, Theoretical Model of A Three Plates Capacitive Pressure Sensor, *Instrumentation and Measurement Technology Conference*, 2005, 214-219.
  - [18].S. D. Senturia, *Microsystems Design*, Boston, MA: *Kluwer Academic*, 2001, pp. 235-236.
-

## The Development of Chemical Nanosensors

<sup>1</sup>A. J. JIN, \*J. LI, \*Y. LU

Hoda Globe Company, Engineering Division, 800 W El Camino Real,  
Mountain View, CA 94042, USA.

\*NASA, Ames Research Center, Mail Stop 230-3, Moffet Field, CA 94035, USA  
Tel.: 001-650-853-3089  
E-mail: [aj.jin@ieee.org](mailto:aj.jin@ieee.org)

*Received: 17 September 2007 / Accepted: 19 September 2007 / Published: 8 October 2007*

---

**Abstract:** This paper presents a study of the chemical nanosensors (CNS) for space and environmental applications, safety alert devices, etc. The high-resolution nanosensors are applied to detect the rocket fuel hydrazine leak. The CNS detects changes in the electrical conductivity response during the chemical species presence. When the hydrazine is leaked into air, it immediately dissociates into NO<sub>2</sub>. As a result, we are actually detecting the NO<sub>2</sub> gas in the trace amount from the fuel leakage. In more detail, we will discuss the sensor chips preparation and process control in terms of the resistance range control while depositing the nanomaterials on the sensors. Furthermore, there will be detailed studies of the CNS response to the dry NO<sub>2</sub> in the ambient conditions. The inter-digitized electrode sensors are characterized to the variables of NO<sub>2</sub> concentration and nanomaterials. *Copyright © 2007 IFSA.*

**Keywords:** Chemical nano sensors, Hydrazine, Nano technology, Nanosensor stability

---

### 1. Background

Nanoscience and nanotechnology, through the exploration and control of the nanomaterials at the nanometer scale, is considered as one of the key research areas for the future growth of US economy. Many sensor devices are part of our everyday life. More sensor improvements are needed for small size, great sensitivity and selectivity, fast response, minimal power consumption, and reliability demands, etc. Due to the well organized structure in atomic level of nanomaterials and their large surface-to-volume ratio, nanosensors are becoming very attractive for the next-generation of the sensing devices. Chemical nanosensors (CNS) are fabricated for space and environmental applications. For example, we can apply CNS to detect the electrical signal during the chemical species presence.

Fig. 1 is a conceptual diagram where the sensor is placed so that the physical and chemical environment can be monitored and controlled. These conditions include the total gas flow rate, chemical concentration, humidity, chemical interface, temperature, pressure, etc. When chemical gases pass by CNS, the nanomaterials in the sensor platform respond correspondingly. The sensor response by electrical conductivity change is a result of the chemical sensing. Each sensor response is monitored electronically and is recorded in the computer as a sensor signal and for further data processing.

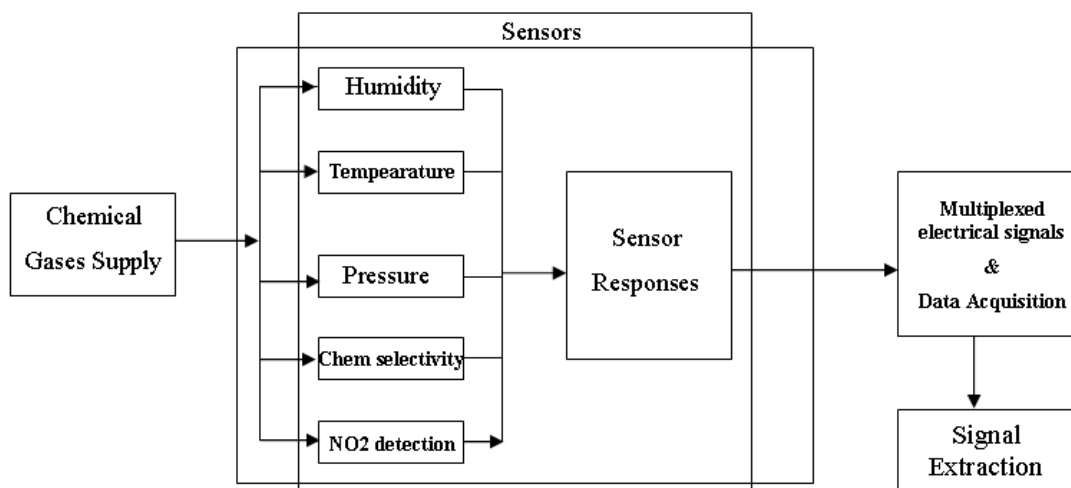


**Fig.1.** The schematic shows the conceptual CNS NO<sub>2</sub> experiments.

The purpose of our CNS project is to monitor the trace amount of NO<sub>2</sub> composed from the leakage of one fuel component, hydrazine. The liquid hydrazine (N<sub>2</sub>H<sub>4</sub>) is an efficient rocket propellant. When the N<sub>2</sub>H<sub>4</sub> is leaked into air, it immediately dissociates and produces NO<sub>2</sub>.

As published in previous literature [1], carbon nanotubes (CNT) is very sensitive to NO<sub>2</sub> and it is therefore a very promising CNS to be employed as a commercial sensor product. The sensor development in this study will focus on the CNS and its NO<sub>2</sub> response in relationship to various NO<sub>2</sub> concentrations. In terms of the dry NO<sub>2</sub> analyte response, we will investigate the CNS on the effects of various variables such as nanomaterials and gap size, etc.

We surveyed many sensing nanomaterials, including - 1) CGNT, 2) CGNT+MPC, 3) CGNT+polymer. The nanomaterials were discussed in Section 2.2, where CGNT is the CVD grown nanotubes. The MPC is monolayer-protected gold clusters (MPC). The polymer is cellulose hydroxypropyl.

We employ the carbon nanotubes (CNT) as the base nanomaterials in the form of the CVD growth. Illustration of Fig. 2 procedures is aimed at preparing a sensor chip before its sensor application.

## 2. Sensor Studies and Optimization

### 2.1. IV Characterization

The IV characteristics of several nanomaterials are studied in the voltage windows and in the reversal voltage as well. Current and voltage characteristics are measured with a semiconductor parameter analyzer.

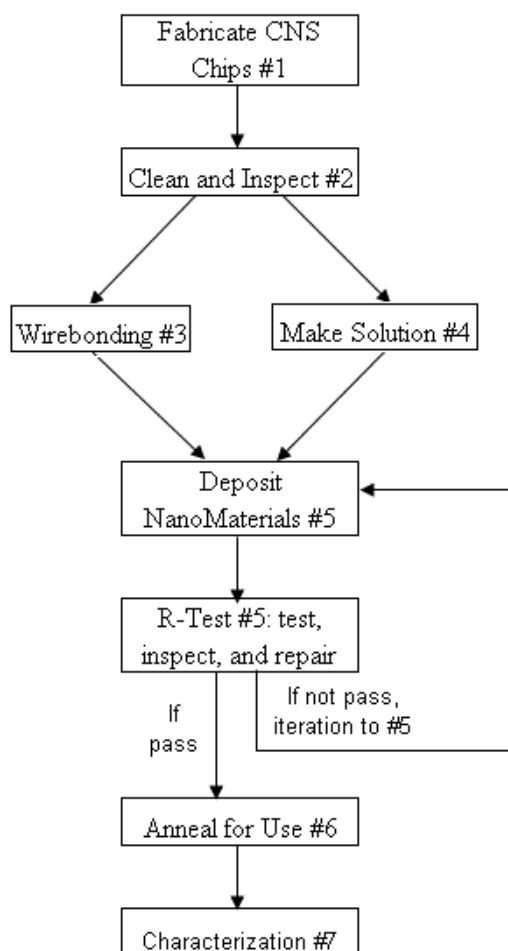


**Fig. 2.** The flow chart shows preparation procedures of the clean CNS chip.

We conducted the current measurement with the DC voltage sweep from  $-2\text{ V}$  to  $2\text{ V}$  with  $0.01\text{ V}$  increment and employed the HP4155B semiconductor parameter analyzer. Some typical IV curves are shown in Fig. 3. For example, we investigated the IV sweep curves from typical sensors with a SWNT/MPC nanomaterial (on the left), a SWNT/cellulose nanomaterial (at middle), and the cast-SWNT nanosensors (on the right). We have plotted a variety of IV curves in Fig. 3 (a), 3 (b), and 3 (c) for the  $4\text{ }\mu\text{m}$  feature gap of three typical interdigitated electrode (IDE) sensors. The non-linearity of the IV curves is also very interesting in order to identify the optimal sensors operating regime.

## 2.2. Bias Voltage Optimization

Moreover, we studied the bias effects by applying different DC bias values. As stated at above, the nanosensors with different nanomaterials show different IV electrical response. The electrical resistance of the CNS may be nonlinear. Therefore, we chose several different dc-bias voltages to measure the sensor response curve at various  $\text{NO}_2$  concentrations (Fig.4).

When the gas flow is the pure air, we only detect the baseline without any signal. Then we expose a sensor by applying on a sensor the chemical/gas flow with a concentration programmed in the same total flow. The change in the electrical signal is measured and the response is extracted from the sensor. Following this step, the sensor is purged to recover.

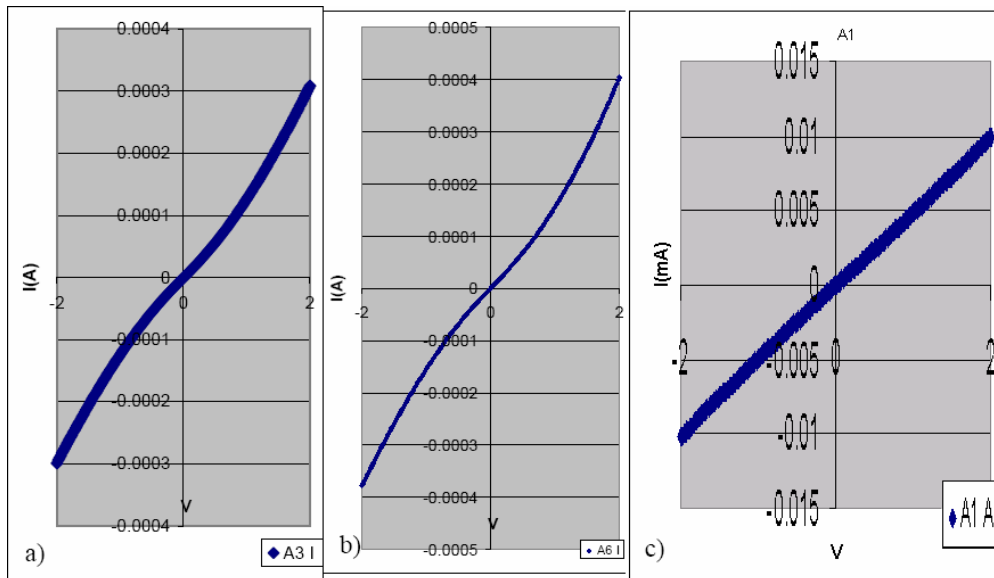


**Fig.3.** The IV curves of the nanosensors are characterized for three nanomaterials.  
(a) CNT/MPC, (b) CNT/polymer, (c) CNT.

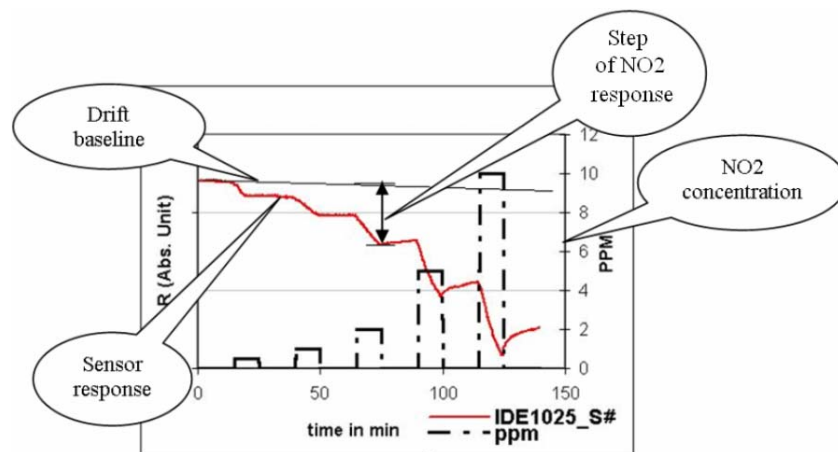


**Fig.4.** Typical data trace of the CNS response to the dry  $\text{NO}_2$  chemical at various concentrations.  
The influence of the various environmental factors will be discussed later.

After having enough purge time, go back and iterate the exposure-purge steps until the sensing process finish. Here is a typical recipe where different gas flow is sequentially applied to the sensor:

15' Air  $\rightarrow$  10' Exposing\_x (x = 0.5-, 1-, 2-, 5-, or 10-ppm)  $\rightarrow$  15' Air... where the time unit is minutes, and the unit of exposure concentration is ppm or parts per million. A typical recipe may contain many exposure-purge cycles by iterating through a given set of concentrations.

Fig. 5 is a typical KAC31 run, where the chip KAC31 is a sensor chip with nanomaterials of CGNT-only, CGNT and MPC composite, and CGNT and polymer composite, respectively. Sixteen sensors are shown to have strong response. We analyzed the data and the relationship between the resistance change and the chemical flow as follows:

- 1) Make a linear fit to the drift baseline (on the initial 15' conditioning);
- 2) The baseline resistance is taken near the end of the recipe step-1 that is the end of the initial conditioning;

- 3) Using linear regression method, extrapolate the baseline as a function of time;
- 4) The response  $dR$  is calculated as the difference between the resistance signal and the baseline at the time immediately after the exposure step. As shown in Fig. 3.2a, the CNS response steps are extracted for every concentration.

Furthermore, the analysis yields the  $dR$  and  $dR/R_0$  dependence upon  $NO_2$  concentration.

By extracting  $dR$ /noise ratio for every sensor at all concentrations, we calculate the sensitivity function and plot this function in Fig. 5 versus the sensors. As a remark, the sensor's resolution in terms of the sensitivity limit,  $S/N$ , can also be derived by an extrapolation method.

**Table 1.** Tabulated is a typical recipe of the dry  $NO_2$  chemical sampling. The sensors chip is conditioned and tested by this recipe. The standard flow rate in total is 400CCM for the most tests. Note that every concentration is diluted by pure air.

| Step number                    | 1   | 2   | 3   | 4   | 5   | 6   | 7   | 8   | 9   | 10  | 11  |
|--------------------------------|-----|-----|-----|-----|-----|-----|-----|-----|-----|-----|-----|
| Mode (F-flow, C-concentration) | F   | C   | F   | C   | F   | C   | F   | C   | F   | C   | F   |
| Time (minutes)                 | 15' | 10' | 15' | 10' | 15' | 10' | 15' | 10' | 15' | 10' | 15' |
| $NO_2$ (ppm)                   | 0   | 0.5 | 0   | 1   | 0   | 2   | 0   | 5   | 0   | 10  | 0   |

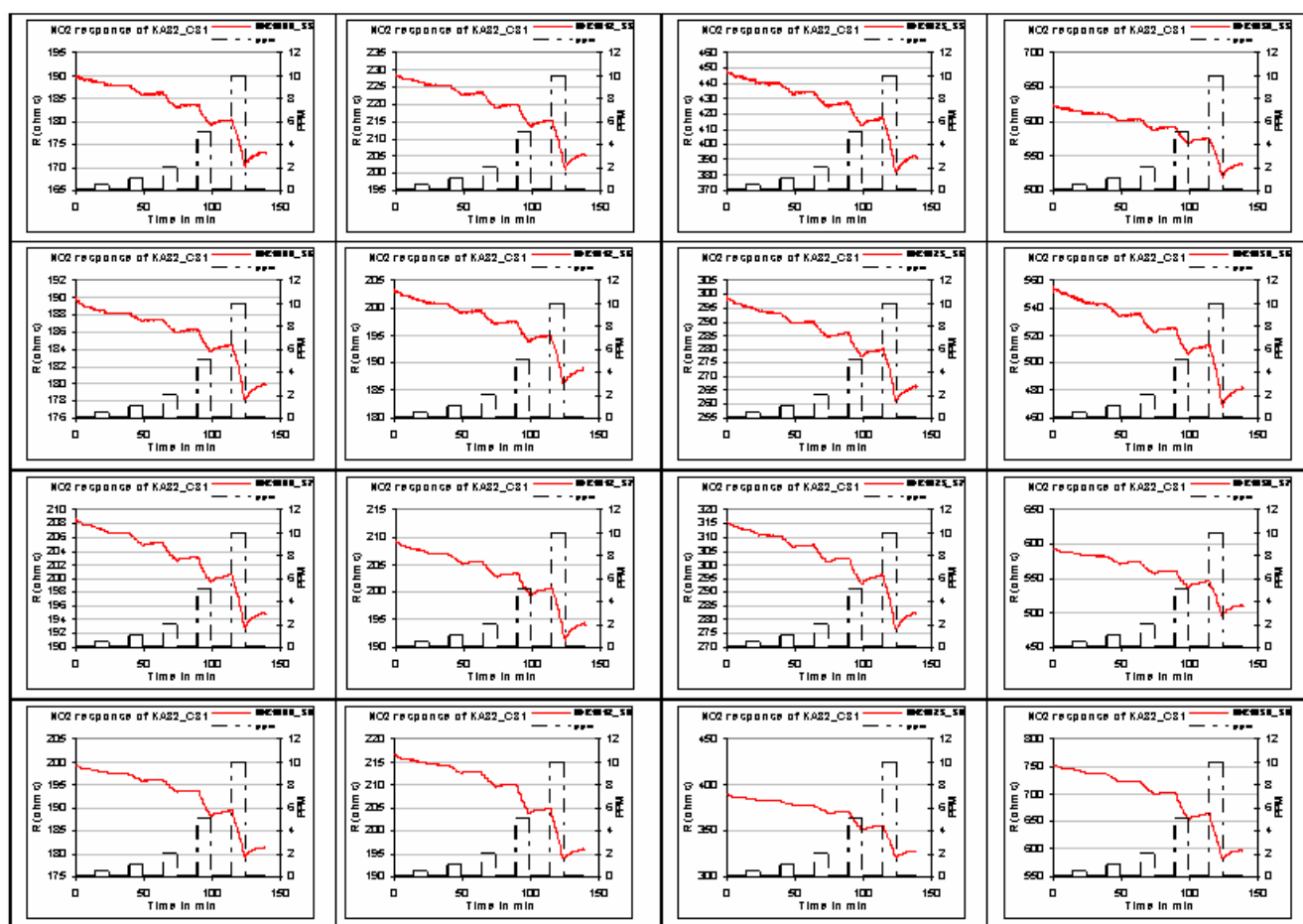


**Fig.5.** Every trace at above shows an individual sensor of KAC31 chip to the  $NO_2$  chemical diluted in air at 400 CCM total flow rate and at ambient conditions. The sensors are labeled. The coordinates are at below: x-axis is the minutes of time; y-axis at left is the electrical signal; the secondary y-axis at right indicates  $NO_2$  levels at 0-, 0.5-, 1-, 2-, 5-, 10-ppm concentrations.

Furthermore, the analysis yields the  $dR$  and  $dR/R_0$  dependence upon  $\text{NO}_2$  concentration. By extracting the  $dR/\text{noise}$  ratio for every sensor at all concentrations, we calculate the sensitivity function and plot this function in Fig. 5 versus both the sensor and the  $\text{NO}_2$  concentration.

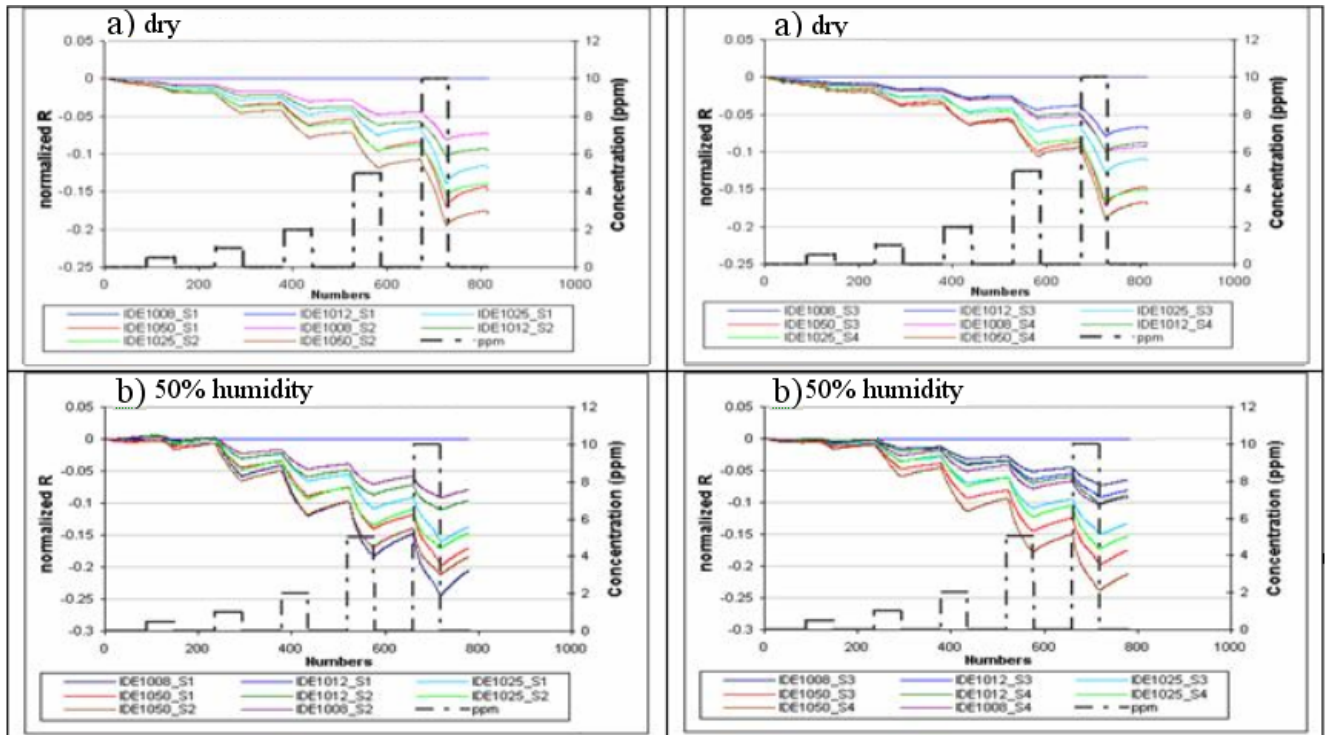


**Fig.6.** These charts show the relative response traces of the KAC31 chip with two RH levels: (a) 0% or dry, (b) 50%. The  $\text{NO}_2$  concentration varies as shown at 0.5-, 1-, 2-, 5-, and 10-ppm.

We have studied the sensor's responses at various humidity values. The humidity tests were set up with the CNS characterization system. The humidifier was calibrated by the factory. We observed that, for the response at low humidity range of 0 % to 30 % RH, the relative sensor response shows that the humidity in this range has quite small effects on the nanosensor response. The  $\text{NO}_2$  response increases with the increasing at a humidity level of 50 % and greater.

### 3. Conclusion

In summary, the CNS has significantly high resolution. We have studied the trace concentration of  $\text{NO}_2$  in sub 1-ppm regime. Further studies are in the progress to characterize the life-expectance of CNS and the effect of temperature, pressure, etc.

### Acknowledgment

The author is indebted to discussions with Dr. Pedro Medelius from ASRC at Kennedy Space Center, Florida, USA.

## References

- [1]. J. Li, Y. Lu, Q. Ye, M. Cinke, J. Han, and M. Meyyapan, *NanoLett.*, 3, 2003, p.929.
  - [2]. J. Li, Y. Lu, Q. Ye, and L. Delzeit, *Electrochemical and Solid-State Letters*, 8 \_11\_ H100-H102 \_2005.
  - [3]. P. Young, Y. Lu, R. Terrill, and J. Li, *Journal of Nanoscience and Nanotechnology*, 5, 2005, p.1.
  - [4]. L. Delzeit, I. McAninch, B.A. Cruden, D. Hash, B. Chen, J. Han, M. Meyyapan, *J. Appl. Phys.*, 91, 2002, p. 6027.
-

## Guide for Contributors

---

### Aims and Scope

*Sensors & Transducers Journal* (ISSN 1726- 5479) provides an advanced forum for the science and technology of physical, chemical sensors and biosensors. It publishes state-of-the-art reviews, regular research and application specific papers, short notes, letters to Editor and sensors related books reviews as well as academic, practical and commercial information of interest to its readership. Because it is an open access, peer review international journal, papers rapidly published in *Sensors & Transducers Journal* will receive a very high publicity. The journal is published monthly as twelve issues per annual by International Frequency Association (IFSA). In additional, some special sponsored and conference issues published annually.

### Topics Covered

Contributions are invited on all aspects of research, development and application of the science and technology of sensors, transducers and sensor instrumentations. Topics include, but are not restricted to:

- Physical, chemical and biosensors;
- Digital, frequency, period, duty-cycle, time interval, PWM, pulse number output sensors and transducers;
- Theory, principles, effects, design, standardization and modeling;
- Smart sensors and systems;
- Sensor instrumentation;
- Virtual instruments;
- Sensors interfaces, buses and networks;
- Signal processing;
- Frequency (period, duty-cycle)-to-digital converters, ADC;
- Technologies and materials;
- Nanosensors;
- Microsystems;
- Applications.

### Submission of papers

Articles should be written in English. Authors are invited to submit by e-mail [editor@sensorsportal.com](mailto:editor@sensorsportal.com) 6-14 pages article (including abstract, illustrations (color or grayscale), photos and references) in both: MS Word (doc) and Acrobat (pdf) formats. Detailed preparation instructions, paper example and template of manuscript are available from the journal's webpage: <http://www.sensorsportal.com/HTML/DIGEST/Submition.htm> Authors must follow the instructions strictly when submitting their manuscripts.

### Advertising Information

Advertising orders and enquires may be sent to [sales@sensorsportal.com](mailto:sales@sensorsportal.com) Please download also our media kit: [http://www.sensorsportal.com/DOWNLOADS/Media\\_Kit\\_2007.PDF](http://www.sensorsportal.com/DOWNLOADS/Media_Kit_2007.PDF)

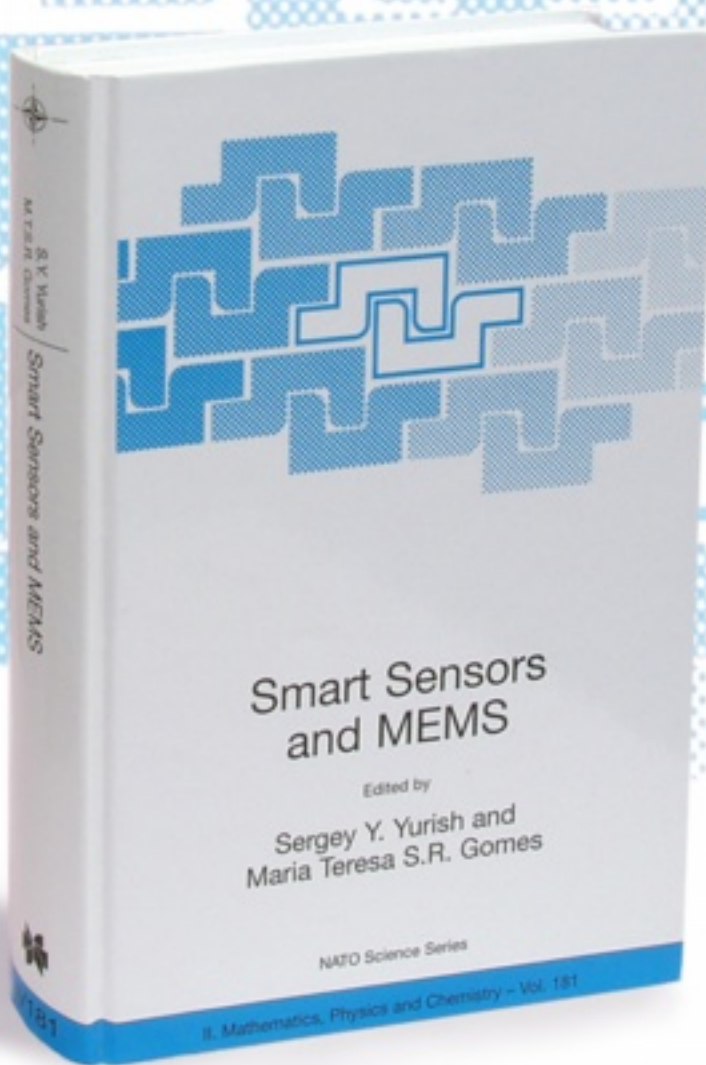
# Smart Sensors and MEMS

Edited by

Sergey Y. Yurish and  
Maria Teresa S.R. Gomes

The book provides an unique collection of contributions on latest achievements in sensors area and technologies that have made by eleven internationally recognized leading experts ...and gives an excellent opportunity to provide a systematic, in-depth treatment of the new and rapidly developing field of smart sensors and MEMS.

The volume is an excellent guide for practicing engineers, researchers and students interested in this crucial aspect of actual smart sensor design.



**Kluwer Academic Publishers**

Order online:

[www.sensorsportal.com/HTML/BOOKSTORE/Smart\\_Sensors\\_and\\_MEMS.htm](http://www.sensorsportal.com/HTML/BOOKSTORE/Smart_Sensors_and_MEMS.htm)

**[www.sensorsportal.com](http://www.sensorsportal.com)**